



University
of Glasgow

Ramanan, Baheerathan (2011) *Quantifying mass transport processes in environmental systems using magnetic resonance imaging (MRI)*.
PhD thesis.

<http://theses.gla.ac.uk/2974/>

Copyright and moral rights for this thesis are retained by the author

A copy can be downloaded for personal non-commercial research or study, without prior permission or charge

This thesis cannot be reproduced or quoted extensively from without first obtaining permission in writing from the Author

The content must not be changed in any way or sold commercially in any format or medium without the formal permission of the Author

When referring to this work, full bibliographic details including the author, title, awarding institution and date of the thesis must be given

Quantifying mass transport processes in environmental systems using magnetic resonance imaging (MRI)

Baheerathan Ramanan

MSc. (Distinction), University of Sussex, UK.

BSc. (Hons), University of Peradeniya, Sri Lanka.

Thesis presented for the degree of Doctor of Philosophy (Ph.D.)

School of Geographical and Earth Sciences,
Glasgow Experimental MRI Centre (GEMRIC), and
School of Engineering,
University of Glasgow.



September, 2011.

Abstract

Understanding the transport behaviour of pollutants is key to enhance remediation strategies and to inform predictive models of pollutant behaviour in environmental and engineered systems. This work investigates magnetic resonance imaging (MRI) as a methodology for imaging heavy metal, molecular and nanoparticle transport in two different saturated porous systems: biofilms and saturated porous geologic media (gravel).

While most renowned for its use in medicine, magnetic resonance imaging (MRI) is enabling us to image the transport of heavy metals, macro-molecules and nanoparticles inside biofilms and porous columns in real time. This is achieved using either ions which are paramagnetic (e.g. Cu^{2+}) or molecules labelled with paramagnetic ions (e.g. Gd^{3+}) or superparamagnetic (e.g. nanomagnetite) nanoparticles. Presence of these tracers causes a concentration dependent shortening of relaxation times (T_1 or T_2) of the surrounding ^1H nuclei and thus creates noticeable changes in the MRI signal. Critically, this enables the transport of (super)paramagnetic ions, molecules or nanoparticles through the biofilm or porous geological media to be imaged. Moreover, the actual concentrations of molecules can be quantified, as changes in relaxation rates have a linear relationship with the concentration of the tracer molecules. Hence, MRI can be used not only to track but also to quantify the transport of (super)paramagnetic molecules inside biofilms and saturated porous columns. The key advantages of MRI over other techniques are its ability to image inside systems opaque to other methods and its ability to collect data non-invasively, hence the system is unperturbed by the analysis.

In this study, the transport of Gd-DTPA, a commonly used MRI contrast agent, was successfully imaged through phototrophic biofilms of 10 and 2.5 mm thicknesses. To improve spatial resolution, for the 2.5 mm thickness biofilm, a bespoke 5 mm diameter RF coil was constructed. The comparison of spatially distributed, time-varying concentrations of Gd-DTPA inside the biofilms with diffusion models illustrated that transport was via both diffusion and advection. This work illustrated the potential of using paramagnetically labelled molecules to quantify molecular pollutant transport and fate in biofilms.

MRI was also used to image heavy metal transport in artificial biofilms (composed of agar and bacteria) to test the suitability of an existing adsorption-diffusion model to represent heavy metal transport and fate in biofilms. While the diffusion coefficients and adsorption constants

estimated were appropriate, discrepancies between the model and the data illustrates models may need to be developed further to incorporate factors such as concentration dependant diffusion or cell lysis.

Finally, the ability to image inside opaque systems was further exploited to image nanoparticle transport inside a coarse-grained packed column. This was undertaken to illustrate the potential for MRI to image nanoparticle pollutant transport in systems relevant to river beds and sustainable urban drainage systems (SUDS). MRI was successfully used to image the nanoparticle transport, with significant transport inhibition was observed in positively charged nanoparticles compared to negatively charged nanoparticles due to permanent attachment.

Acknowledgements

This thesis would not have been possible without the help and support from many people.

I wish to express my sincere gratitude to my supervisors, Dr. Vernon Phoenix, Dr. William Holmes and Prof. William Sloan who were abundantly helpful and offered invaluable assistance, support and guidance throughout this research.

I am very much grateful to the “Lord Kelvin and Adam Smith” scholarship, University of Glasgow for funding this research.

A special thanks goes to Mr. Jim Mullen for his assistance with MRI experiments. Also I wish to express my love and gratitude to my beloved wife and my parents for their understanding & encouragement, through the duration of my studies.

Lastly, I offer my regards to all of those who supported me in any respect during the completion of this thesis.

To all these people this thesis is dedicated.

Author's declaration

I declare that, except where explicit reference is made to the contribution of others, that this dissertation is the result of my own work.

Signature: B. Ramanan.

Print name: BAHEERATHAN RAMANAN

Table of contents

Abstract	II
Acknowledgements	IV
Author’s declaration	V
Table of contents	VI
List of figures	XI
List of tables	XVI
Nomenclature	XVII
Chapter 1 General introduction	
1.1 Biofilms.....	2
1.1.1 Importance of mass transport processes inside biofilms	3
1.1.2 Methods for investigating mass transport inside biofilms.....	6
1.1.3 MRI of mass transport processes inside biofilms	7
1.2 Saturated porous geological media.....	8
1.2.1 Importance of mass transport processes inside porous media.....	9
1.2.2 Methods to investigate mass transport inside porous media	9
1.2.3 MRI of mass transport processes inside porous media	10
1.3 Using MRI contrast agents to quantify mass transport processes inside biofilms and porous media	11
1.4 Modelling mass transport processes inside biofilms and porous geological media	13
1.5 Outline and scope of the thesis.....	15
1.6 References	17
Chapter 2 Magnetic resonance imaging (MRI)	
2.1 Fundamentals of MRI.....	23
2.1.1 Nuclear magnetic moment in a static magnetic field	24
2.1.2 Ensemble of spins	25
2.1.3 Net magnetization.....	26
2.1.4 Application of a radio frequency (RF) pulse	27
2.1.5 Rotating frame of reference	28

2.1.6	Excitation of spins (net magnetization).....	29
2.1.7	Relaxation process	30
2.1.8	Longitudinal relaxation.....	30
2.1.9	Transverse relaxation	31
2.1.10	Field inhomogeneity effect (T_2^*)	32
2.1.11	Mechanism of nuclear spin relaxation	33
2.1.12	MR signal generation.....	34
2.2	MR imaging process	35
2.2.1	Magnetic field gradients.....	35
2.2.2	Two dimensional imaging	36
2.2.3	Slice selection.....	36
2.2.4	Frequency encoding	37
2.2.5	Phase encoding.....	38
2.2.6	Formation of an MR image	38
2.3	Image contrast.....	41
2.4	Pulse sequence	43
2.4.1	Gradient echo pulse sequence	43
2.4.2	Spin echo pulse sequence.....	44
2.4.2.1	Multiple spin echo imaging.....	46
2.4.3	<i>RARE</i> pulse sequence.....	47
2.5	Contrast agents	48
2.5.1	Types of contrast agents.....	48
2.5.2	Quantitative concentration imaging.....	50
2.6	MRI hardware	51
2.6.1	The main magnet.....	51
2.6.2	Shim coils	52
2.6.3	Gradient coils.....	52
2.6.4	RF Coils.....	52
2.6.5	RF oscillator.....	54
2.6.6	RF modulator	54
2.6.7	RF amplifier	54
2.6.8	Duplexer	54
2.6.9	Signal preamplifier	54
2.6.10	Quadrature receiver and analogue to digital converter.....	54
2.6.11	Computer.....	55
2.7	References	55

Chapter 3 Application of paramagnetically tagged molecules for magnetic resonance imaging (MRI) of biofilm mass transport processes

3.1 Summary	57
3.2 Introduction.....	57
3.3 Materials and methods.....	59
3.3.1 Agar and phototrophic biofilm	59
3.3.2 Flow System	60
3.3.3 MRI.....	61
3.3.4 Acquisition of T_1 -weighted images	61
3.3.5 Calculation of T_1 parameter maps.....	62
3.3.6 Calibration of Gd-DTPA concentrations from T_1 parameter maps	63
3.3.7 Determination of relaxivity constant (R) of Gd-DTPA in agar and <i>Phormidium</i> biofilm	64
3.3.8 Estimating the diffusion coefficient of Gd-DTPA inside agar	65
3.3.9 Modelling the mass transport process of Gd-DTPA inside the <i>Phormidium</i> biofilm	65
3.3.10 Visualization of structural complexity of <i>Phormidium</i> biofilm using freeze-substitution TEM.....	66
3.4 Results	67
3.4.1 Relaxivity constant (R) of Gd-DTPA inside agar.....	67
3.4.2 Relaxivity constant (R) of Gd-DTPA inside <i>Phormidium</i> biofilm.....	67
3.4.3 Diffusion of Gd-DTPA inside agar	68
3.4.4 Transport of Gd-DTPA into the <i>Phormidium</i> biofilm	70
3.4.5 Freeze-substitution transmission electron microscopy analysis of biofilm structure	72
3.5 Discussion	72
3.6 References	75

Chapter 4 Magnetic resonance imaging of biofilm mass transport processes and structure using a simple custom made solenoid RF coil

4.1 Summary	79
4.2 Introduction.....	80
4.2.1 MRI of biofilms.....	80
4.2.2 Improving the SNR	81
4.3 Materials and methods.....	84
4.3.1 Agar and phototrophic biofilm	84
4.3.2 Solenoid coil and biofilm frame	84
4.3.3 Estimating the capacitor values of the resonant circuit.....	85
4.3.4 Performance evaluation of the RF coil	88

4.3.5 Flow system.....	88
4.3.6 MRI.....	89
4.3.7 Acquisition of T_1 -weighted images	89
4.3.8 Calculation of T_1 parameter maps.....	89
4.3.9 Calibration of Gd-DTPA concentrations from T_1 parameter maps	90
4.3.10 Determination of the relaxivity constant (R) of Gd-DTPA in agar and <i>Phormidium</i> biofilm	91
4.3.11 Measurement of T_2^* values with different Gd-DTPA concentrations	91
4.3.12 Modeling the transport of Gd-DTPA inside both agar and <i>Phormidium</i> biofilm.....	91
4.3.13 High resolution MRI of biofilm structure	93
4.4 Results	94
4.4.1 Performance evaluation of the RF coil	94
4.4.2 Measured T_2^* values with different Gd-DTPA concentrations.....	95
4.4.3 Diffusion of Gd-DTPA inside agar	96
4.4.4 Transport of Gd-DTPA into the <i>Phormidium</i> biofilm	97
4.4.5 Simple 2D diffusion model of Gd-DTPA transport into the <i>Phormidium</i> biofilm.....	98
4.4.6 MRI of biofilm structure.....	100
4.5 Discussion	100
4.6 References	103
Chapter 5 Investigation of nanoparticle transport inside coarse-grained geological media using magnetic resonance imaging (MRI)	
5.1 Summary	107
5.2 Introduction.....	108
5.3 Materials and methods.....	109
5.3.1 Porous column and nanoparticles.....	109
5.3.2 Transport experiment.....	110
5.3.3 MRI.....	111
5.3.4 Acquisition of T_2 -weighted images	111
5.3.5 Determination of the relaxivity constant (R) of nanoparticles.....	112
5.3.6 Calibration of nanoparticle concentration using T_2 -weighted images.....	112
5.3.7 Modelling the transport of NPs inside the porous column.....	113
5.4 Results	117
5.4.1 The relaxivity constant (R) of <i>Molday ION</i> NPs	117
5.4.2 Transport of <i>Molday ION</i> nanoparticles inside porous column	117
5.4.3 Comparison of experimental data with model data.....	118

5.5 Discussion	120
5.6 References	122
Chapter 6 Investigation of copper immobilisation inside artificial biofilm using magnetic resonance imaging (MRI)	
6.1 Summary	125
6.2 Introduction.....	126
6.3 Materials and methods.....	127
6.3.1 Bacteria	127
6.3.2 Artificial biofilms.....	127
6.3.3 Flow systems.....	128
6.3.4 MRI.....	128
6.3.5 Acquisition of T_2 - weighted images	128
6.3.6 Calculation of T_2 parameter maps.....	129
6.3.7 Calibration of copper concentrations from T_2 parameter maps.....	130
6.3.8 Determination of relaxivity constant (R) of copper in artificial biofilms	130
6.3.9 Modeling the adsorption-diffusion of copper inside artificial biofilms.....	130
6.3.10 Estimating the values for variables used in the model.....	133
6.3.11 Concentration dependent diffusion of copper inside artificial biofilms...	133
6.4 Results	134
6.4.1 Transport of copper inside artificial biofilms	134
6.4.2 Models describing the transport of copper inside artificial biofilms	136
6.4.2.1 Transport of copper modelled with constant diffusion coefficients	136
6.4.2.2 Transport of copper modelled with different diffusion coefficients at different time intervals	137
6.4.2.3 Transport of copper modelled with concentration dependent diffusion coefficient.....	139
6.5 Discussion	142
6.6 References	146
Chapter 7 Concluding remarks	
7.1 Summary of conclusions.....	149
7.2 The future research of MRI of environmental systems	152
7.3 References	155
Appendix.....	158
Papers and Presentations.....	169

List of figures

Figure 1.1. Biofilm formation	2
Figure 1.2. Schematic representation of wastewater treatment using biological membranes. .	5
Figure 1.3. (A) Illustrates the types of organic waste constituents in a typical municipal wastewater. (B) Illustrates the variation of effective diffusion coefficients with respect to the molecular masses of selected solutes inside biofilms.....	6
Figure 1.4. Schematic diagram showing how the MRI scanner was used to conduct transport experiments inside biofilms and porous packed columns.....	12
Figure 2.1. Zeeman splitting with respect to the main magnetic field.....	24
Figure 2.2. Formation of net magnetization when a static magnetic field, B_0 is applied. Here (a) spin up and spin down alignment of magnetic moments, (b) alignment of excess spins along the direction of static magnetic field and (c) formation of net magnetization.	27
Figure 2.3. Stationary and rotating coordinate systems.....	28
Figure 2.4. Schematic illustrating the effect of 90° and 180° RF radiation on individual spins and net magnetization.	30
Figure 2.5.(a) Relaxation of longitudinal component of the net magnetization and (b) the longitudinal relaxation curve.	31
Figure 2.6. (a) Decay of transverse component of the net magnetization and (b) the transverse decay curve.....	32
Figure 2.7. Fluctuating local magnetic field caused by the random tumbling motion of water molecules.	33
Figure 2.8. Excitation and detection of MR signal	34
Figure 2.9. Test specimen placed inside the MRI scanner with respect to the three orthogonal directions (x, y and z).	36
Figure 2.10. Comparison between continuous and modulated RF pulses in time and frequency domains.	37
Figure 2.11. (a) Application of linearly varying magnetic field gradient along x direction. (b) Measured proton density of the sample along the x axis.....	40

Figure 2.12. Illustrates (a) raw data matrix, (b) sample k-space and (c) resulting brain image after the two dimensional inverse Fourier transformation of the k-space.....	40
Figure 2.13. T_2 -weighting image contrast at short and long TE with long TR to minimise the T_1 -weighting.	42
Figure 2.14. T_1 -weighted image contrast at short and long TR with short TE to minimize T_2 -weighting.	42
Figure 2.15. Gradient echo pulse sequence diagram.....	43
Figure 2.16. Spin echo pulse sequence diagram.	45
Figure 2.17. Formation of a spin echo when 180° RF pulse is applied.....	46
Figure 2.18. Continuous formation of echoes using subsequent 180° RF pulses.....	46
Figure 2.19. <i>RARE</i> pulse sequence diagram.	47
Figure 2.20. Illustrates the structure of the Gd-DTPA	49
Figure 2.21. Schematic of (A) amine functional group and (B) carboxyl functional group.....	50
Figure 2.22. Main components of the MRI scanner.....	51
Figure 2.23. Schematic illustrations of coil arrangements used to create magnetic field gradients in x, y, and z directions.....	52
Figure 2.24. Schematic diagram of electronics involved in an MR image formation. Red and blue colour arrows indicate the transmitter and receiver sections respectively....	53
Figure 3.1. Schematic of the flow cell containing agar. Cross sections are (a) along the flow cell and (b) across the flow cell.....	60
Figure 3.2. Schematic of the flow cell containing <i>Phormidium</i> biofilm. Cross sections are (a) along the flow cell and (b) across the flow cell.	61
Figure 3.3. Using T1-weighted images to calculate T1 parameter map inside agar.....	63
Figure 3.4. Illustration of the two dimensional model of <i>Phormidium</i> biofilm constructed using COMSOL Multiphysics. Dimensions are in centimeters	67
Figure 3.5. (A) Variation of $(1/T_{1i})$ values with respect to Gd-DTPA concentration inside agar samples. (B) Variation of Gd-DTPA relaxivity with respect solids contents of several <i>Phormidium</i> biofilm samples.....	68

Figure 3.6. Diffusion of Gd-DTPA into agar was recorded by T_1 weighted images (A-E) and concentration maps (F-J) at selected time intervals.....	69
Figure 3.7. (A) Calibrated Gd-DTPA concentrations at selected time intervals. (B) Calibrated Gd-DTPA concentration profiles curve fitted to the solution of the Fickian one dimensional diffusion equation.....	69
Figure 3.8. Transport of Gd-DTPA into the <i>Phormidium</i> biofilm illustrated as T_1 -weighted images (A-E), concentration maps (F-J) and model results (K-O) at selected time intervals.....	70
Figure 3.9. Gd-DTPA transport inside the <i>Phormidium</i> biofilm is compared between experimental data and (A) model data (modeled at diffusion coefficient of $7.2 \times 10^{-10} \text{ m}^2/\text{s}$) and (B) calibrated diffusion model data.....	71
Figure 3.10. Transmission Electron micrograph of freeze-substituted <i>Phormidium</i> biofilm sample. (A) Cross section of Phormidium filaments embedded in an EPS matrix. (B) Areas where there is little or no EPS between the filaments	71
Figure 4.1. Schematic of flow cell containing agar. Cross sections are (a) along the flow cell and (b) across the flow cell.	84
Figure 4.2. Diagram of the support frame with built-in solenoid RF coil and electronic circuit fixed inside the micro-imaging gradient using the locking mechanism.....	86
Figure 4.3. Photograph of the actual custom made biofilm frame illustrating the flow compartment and electronic compartment.	86
Figure 4.4. Schematic of the solenoid coil used as the RF coil to excite and detect the MR signal.....	87
Figure 4.5. Using T_1 -weighted images to calculate T_1 parameter map and concentration map inside agar.....	90
Figure 4.6. Illustrates the two dimensional model of (A) agar and (B) <i>Phormidium</i> biofilm constructed using COMSOL Multiphysics.....	93
Figure 4.7. Gradient echo images of a cylindrical phantom of aqueous Gd-DTPA illustrates the signal homogeneity of the custom made solenoid coil.	95
Figure 4.8. Transport of Gd-DTPA into the agar illustrated as T_1 -weighted images (A to E), calibrated Gd-DTPA concentration maps (F to J), and diffusion model results (K to O) at selected time intervals	96
Figure 4.9. (A) Calibrated Gd-DTPA concentration profiles inside agar at selected time intervals. (B) Comparison between experimental and model data.	97

Figure 4.10. Transport of Gd-DTPA into the <i>Phormidium</i> biofilm illustrated as T_1 -weighted images (A-E) and concentration maps (F-J) at selected time intervals.....	98
Figure 4.11. Calibrated Gd-DTPA concentrations inside the biofilm along the transect shown by the white dotted line in figure 4.10F at selected time intervals.....	98
Figure 4.12. Transport of Gd-DTPA into the <i>Phormidium</i> biofilm illustrated using the two dimensional diffusion model simulated with the diffusion coefficient of $6.5 \times 10^{-10} \text{ m}^2 \text{ s}^{-1}$ (estimated for agar) at selected time intervals.....	99
Figure 4.13. Comparison between experimental and model data (modeled at diffusion coefficient of $6.5 \times 10^{-10} \text{ m}^2 \text{ s}^{-1}$) at selected time intervals.....	99
Figure 4.14. (a) T_1 and (b) T_2 -weighted images showing the structural heterogeneity of the biofilm. (c) Map of relative apparent diffusion coefficient. (D) Map of relative water density.....	99
Figure 5.1. (a) The Photograph of the experimented porous column. (b) Cross section of the porous column illustrating the diffuser plate and inlet end cap arrangement.	110
Figure 5.2. (a) For the slice along the porous column, (b) T_2 -weighted image, (c) NP concentration map and (d) the two dimensional axis symmetry model.....	115
Figure 5.3. Variation in the change of transverse relaxation rates ($1/T_{2i} - 1/T_{20}$) with respect to both <i>Molday ION Carboxyl</i> and <i>C6Amine</i> NP concentration.	117
Figure 5.4. (a to c) T_2 -weighted images, (d to f) calibrated concentration maps of <i>Carboxyl</i> NP transport inside the column and (g to i) convection-dispersion model results at selected time intervals.	118
Figure 5.5. Averaged concentration profiles of both <i>Carboxyl</i> and <i>C6Amine NPs</i> , along the flow direction at selected time intervals.....	119
Figure 5.6. Variation in the averaged porosity within the area shown in Fig. 5.2c with respect to the column length.	119
Figure 5.7. Transport of <i>Molday ION Carboxyl</i> NPs inside the porous column is compared to the model data.....	120
Figure 5.8. Transport of <i>Molday ION C6Amine</i> NPs inside the porous column is compared to the model data modeled with (A) retardation and (B) retardation and deposition in order to estimate the coefficients of retardation and deposition constant at selected time intervals.....	120
Figure 6.1. Schematic of the flow cell containing the artificial biofilm. Cross sections are (a) along the flow cell and (b) across the flow cell.	128

Figure 6.2 Using T_2 -weighted images to calculate T_1 parameter map and concentration map inside artificial biofilm.....	129
Figure 6.3. Illustration of the two dimensional model of artificial biofilm constructed using COMSOL Multiphysics.....	132
Figure 6.4. Transport of copper into the artificial biofilm of 5:95 mix illustrated as T_2 -weighted images (A-D), calibrated copper concentration maps (E-H), and diffusion-adsorption model results (I-L) at selected time intervals.....	135
Figure 6.5. Transport of copper into the artificial biofilm of 50:50 mix illustrated as T_2 -weighted images (A-D), calibrated copper concentration maps (E-H), and diffusion-adsorption model results (I-L) at selected time intervals..	135
Figure 6.6. Calibrated copper concentration profiles at selected time intervals for (A) 5:95 and (B) 50:50 mix of artificial biofilm.	136
Figure 6.7. Comparison of experimental data with the adsorption-diffusion model data for artificial biofilms made up with (A) 5:95 and (B) 50:50 bacterial pellets and agar mix at selected time intervals.....	137
Figure 6.8. Comparison of experimental data (5:95 mix) to the model data modelled with diffusion coefficients estimated separately for each time interval.....	138
Figure 6.9. Comparison of experimental data (50:50 mix) to the model data modelled with diffusion coefficients estimated separately for each time interval.....	139
Figure 6.10. Comparison of experimental data to the model data modelled with concentration dependent diffusion coefficients for Cu^{2+} inside the artificial biofilm made up with 5:95 agar and bacteria mix at selected time intervals.	140
Figure 6.11. Comparison of experimental data to the model data modelled with concentration dependent diffusion coefficients for Cu^{2+} inside the artificial biofilm made up with 50:50 agar and bacteria mix at selected time intervals.	141

List of tables

Table 2.1. Relaxation mechanisms for different samples of interest.....	34
Table 2.2. Summarises the preferred TE and TR values to generate T_1 , T_2 and proton density-weighted images.	42
Table 2.3. The effect of contrast agents used in this research upon the longitudinal relaxation time (T_1) and transverse relaxation time (T_2) of the surrounding ^1H nuclei.	49
Table 4.1. Variation of T_2^* and $e^{(-TE/T_2^*)}$ values of agar samples with respect to the Gd-DTPA concentrations.	95
Table 5.1. Boundary conditions used in the model to simulate the NP transport inside the column.....	116
Table 6.1. Estimated values of log stability constant, K (for adsorption), constant diffusion coefficient, D_{diff} , forward constant rate, k_f and goodness of fit, R^2 when the model is calibrated for both artificial biofilms (5:95 and 50:50 mix) by considering experimental data obtained at 6, 12, 18 and 24 hour time intervals together. ...	137
Table 6.2. Estimated value of constant diffusion coefficient, D_{diff} and goodness of fit, R^2 when model is calibrated for (5:95) artificial biofilm by considering experimental data separately at 6, 12, 18 and 24 hour time intervals.....	138
Table 6.3. Estimated value of constant diffusion coefficient, D_{diff} and goodness of fit, R^2 when model is calibrated for (50:50) artificial biofilm by considering experimental data separately at 6, 12, 18 and 24 hour time intervals.	139
Table 6.4. Estimated values of base diffusion coefficient, D_0 , unknown constant, b and goodness of fit value, R^2 when model for (5:95 bacteria and agar mix) is calibrated using concentration dependent diffusion coefficient.....	142
Table 6.5. Estimated values of base diffusion coefficient, D_0 , unknown constant, b and goodness of fit value, R^2 when model for (50:50 bacteria and agar mix) is calibrated using concentration dependent diffusion coefficient.....	142
Table 7.1. List of commercially available <i>Molday ION</i> contrast agents.	152

Nomenclature

Gd-DTPA	- Gadolinium diethylenetriamine pentaacetic acid
PFG	- Pulsed field gradient
FLASH	- Fast low angle shot
RARE	- Rapid acquisition relaxation enhancement
SUDS	- Sustainable urban drainage systems
CLSM	- Confocal laser scanning microscopy
FRAP	- Fluorescence recovery after photobleaching
BTC	- Break through curve
CBV	- Cerebral blood volume
CBF	- Cerebral blood flow

Chapter 1

General introduction

1

General introduction

1.1 Biofilms

Micro-organisms are ubiquitous, occurring almost everywhere where there is sufficient water for their survival. Biofilms are the dominant mode of life for these microorganisms in most natural, industrial and clinical environments. As shown in figure 1.1, biofilms form when microorganisms stick to moist surfaces by producing a slimy glue like substance known as EPS (extracellular polymeric substances). Once they stick to surfaces, microorganisms start to reproduce, developing into a dense community of bacteria suspended in the EPS matrix (Wuertz, 2008). Thus, a biofilm can simply be imagined as microorganisms embedded in a gel. Microbial granules or flocs constitute a special case of biofilms. These are communities of microorganisms held together only by EPS without any carrier surface (solid surface) and float freely in suspension (Wuertz, 2008).

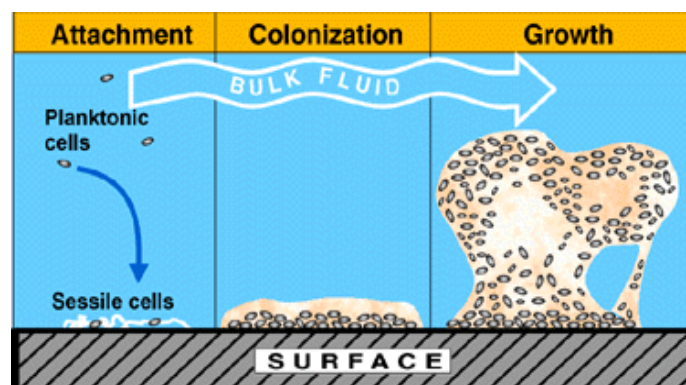


Figure 1.1. Biofilm formation (reproduced from Montana state university, center for biofilm engineering, <http://www.biofilm.montana.edu/resources/images/multicellularextracellular/biofilm-formation-basics.html>)

Depending on the type of microorganisms composing the biofilms, biofilms can have either beneficial or detrimental effects. In industrial environments biofilms are utilized in a wide range of biotechnological processes, such as cleansing municipal and industrial wastewater,

bioremediation of hazardous waste sites, biofuel (H_2 and biogas [CH_4]) and chemical (vinegar) production and the generation of electricity in microbial fuel cells (Logan et al., 2006, Qureshi et al., 2005, Roeselers et al., 2008). In contrast they can also cause equipment damage via bio-corrosion, and energy losses due to pressure and heat transfer losses (Characklis, 1981). Biofilms found in the natural environment play an important role in mediating the geochemistry of the natural environment and can play a role in cleansing natural water resources (Roeselers et al., 2008). In the medical environment, biofilms are responsible for a majority of the infections such as colitis, vaginitis, urethritis, otitis (Davies, 2003) and gingivitis and their accumulation on medical devices, such as urinary, venous and arterial implants and pacemakers can be problematic (Davies, 2003).

Clearly, biofilms have an important impact on an incredibly diverse range of processes. Therefore, controlling their performance in all these processes is essential. Understanding the mass transport processes of relevant substrates inside biofilms is key to control their performance as mass transport of different solutes inside biofilms influences their performance in both beneficial and detrimental processes.

1.1.1 Importance of mass transport processes inside biofilms

For the biofilm to function effectively, the relevant substrates (nutrients) must be transported through the biofilm matrix where they are metabolised. The rate at which these metabolites are transported through the biofilm can be critical in controlling the performance of the biofilm (Bishop et al., 1997, Buffière et al., 1995, de Beer et al., 1994, Qureshi et al., 2005). For example, the ability of biofilms in wastewater treatment plants to treat both industrial and house hold waste via metabolism and biosorption is controlled by the transport properties of different waste constituents as described below.

The harmful organics found in wastewater are degraded into harmless substances by aerobic respiration; a metabolic process of microorganisms which degrades organic carbon in the presence of oxygen. Here the transport rates of both organic waste and O_2 into biofilms control the process efficiency. For example, when metabolic rates are high compared to transport rates, the aerobic degradation will be limited to a narrow outer zone of the biofilm, as oxygen is rapidly consumed. The interior of the biofilm becomes anaerobic and inefficient. Indeed, part of optimizing biofilm design is selection of the optimal biofilm thickness which enables efficient processes to happen at all depths (Beun et al., 1999). Moreover, the inefficient zone

of the biofilm will increase in size if transport rates are reduced due to biofilm density (which reduces diffusion coefficients).

In contrast, systems can be specifically designed for anaerobic digestion of organic waste (this process is becoming increasingly popular due to its ability to generate biogas, a biofuel). Here, only the transport of organics is relevant, as O_2 is not present. However, as in aerobic systems, if transport of organic substrates into deeper biofilm layers is retarded, either due to biofilm density or thickness, then again the system becomes inefficient.

However, many wastewater treatment systems must simultaneously degrade organic waste and ammonia (via combined nitrification-denitrification). This generates a number of challenges relating to mass transport of substrates and metabolism. Nitrification must occur in the presence of oxygen, yet denitrification must occur in its absence. Thus, both oxic and anoxic zones must exist within the biofilm. Moreover, denitrification requires a supply of organic carbon, but as this process must exist in the deeper anoxic layers of the biofilm, the organic carbon has often been depleted by aerobic respiration before it reaches this layer (as organic carbon transport rates are not sufficient to overcome the rapid aerobic degradation rates). One solution is to grow biofilms on a permeable membrane (Walter et al., 2005). This enables O_2 and organic carbon sources to be separated, i.e. O_2 diffuses in at the base of the biofilm through the membrane, while the carbon substrate enters the top of the biofilm from the wastewater. This enables organic carbon to enter the biofilm without rapid aerobic degradation, thus supplying the denitrifying bacteria with a carbon substrate (see Fig. 1.2). Of course, getting such a system to work effectively requires a fundamental understanding of the mass transport rates of all components to ensure correct thicknesses of the oxic and anoxic zones.

The example mentioned above illustrates that the balance between the rates of metabolism and transport of different components controls the efficiency of biological treatment processes. Thus, investigations of mass transport behaviours of such components are essential to optimise the treatment efficiency.

Equally, the rate at which the biofilm can sequester non-metabolizable pollutants such as non-metabolizable heavy metals and recalcitrant organics is also mediated by the transport rate (Carlson and Silverstein, 1998, Phoenix and Holmes, 2008). Here, the faster the transport of non-biodegradable pollutants inside biofilms leads to faster pollutant removal processes if sequestration rate (i.e. adsorption rate) is higher than the transport rate.

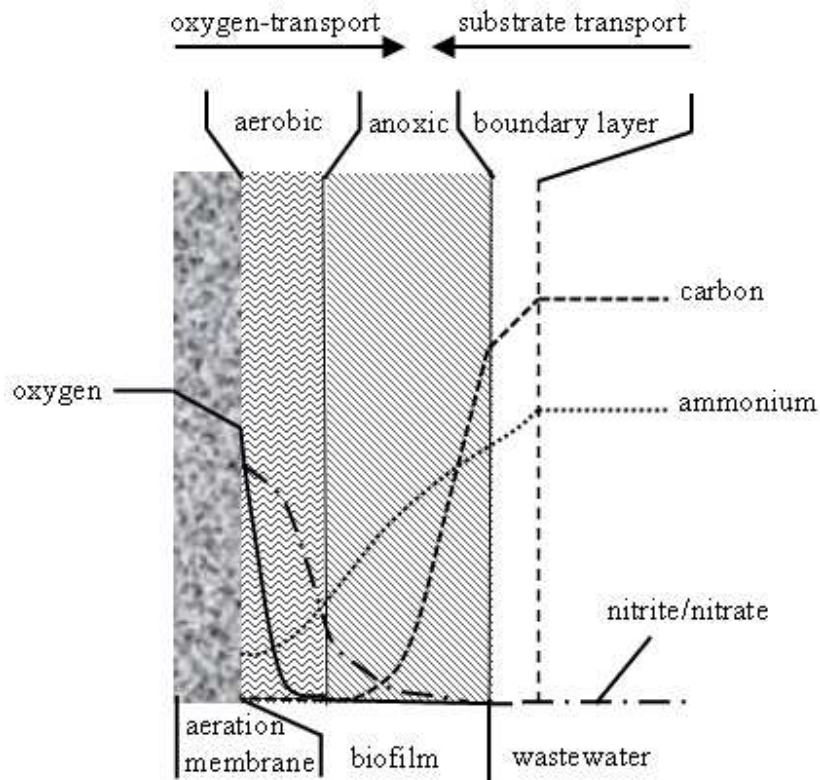


Figure 1.2. Schematic representation of wastewater treatment using biological membranes (reproduced from Walter et al., 2005).

Both industrial and house hold wastes can reach natural water bodies such as rivers and lakes either via direct runoff or from poorly treated wastewater effluents. Hence, the effective transport of relevant substrates inside naturally occurring biofilms is also essential when treatment of wastes depends solely on those biofilms.

Quantifying mass transport is also important in inhibiting detrimental biofilm activity. For example, antibiotics are used to inhibit biofilm function and thus they must also be effectively transported through the biofilm to treat the whole microbial community (Davies, 2003). However, slow transport rates of such molecules inside biofilms due to diffusion limitations limits the migration of antibiotics, thus causing delay in inactivating microorganisms (bacteria).

Previous studies of mass transport inside biofilms show that transport occurs not only by diffusion but also by advection if biofilms contain interconnected channels (Bishop et al., 1997, Carlson and Silverstein, 1998, de Beer et al., 1994, Lewandowski et al., 1995, Stewart, 1998, Stewart, 2003, Yang and Lewandowski, 1995). When transported by diffusion, the properties such as mass, shape and surface charge of the diffusing solute play a key role in mediating transport rate. Generally, the higher the molecular mass of the solute, the lower its

diffusion coefficient (Stewart, 2003) (see Fig. 1.3B). Moreover, the molecular mass and diffusion rates of these solutes vary considerably, ranging from low mass, fast diffusing metabolites such as H_2 and O_2 , to large, slow diffusing organic macromolecules with tens to hundreds of kDa in size. Indeed, high molecular mass molecules and nanoparticles are an important part of the substrate and pollutant load in both wastewater treatment and natural aquatic systems (Logan and Qing, 1990 and Levine et al, 1985) (see Fig. 1.3A). At a certain size, large macromolecules and nanoparticles become too large to diffuse into the dense EPS matrix, although they can still be transported deep into the biofilm along open channels (Carlson and Silverstein, 1998, Stewart, 2003). Moreover, due to the heterogeneous nature of biofilms, substrates can also display significant spatial variation in mass transport rates, such as a decrease in transport rate with biofilm depth (due to increasing biofilm density) (Beyenal and Lewandowski, 2002).

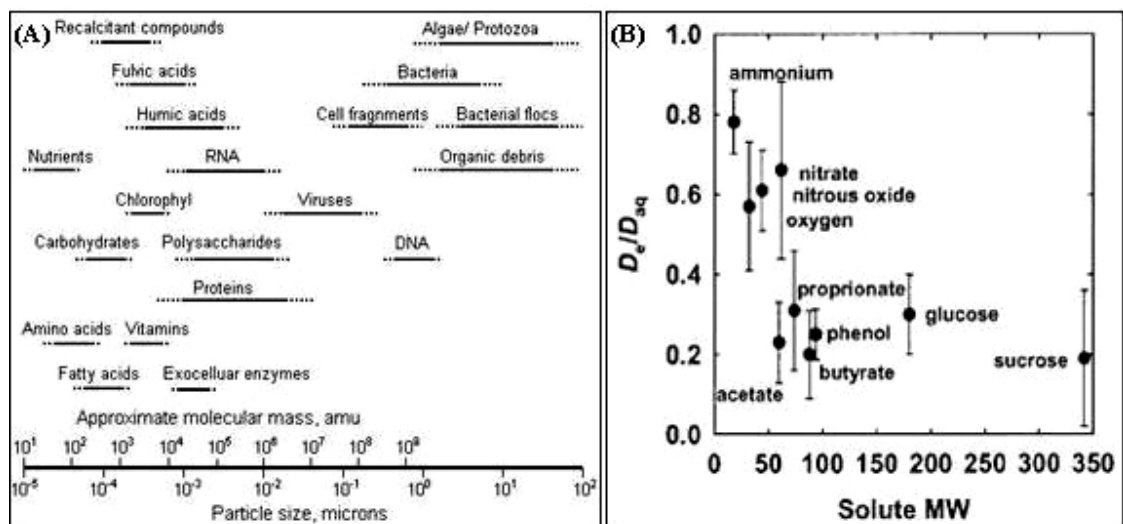


Figure 1.3. (A) Illustrates the types of organic waste constituents in a typical municipal wastewater (edited and reproduced from Levine et al, 1985). (B) Illustrates the variation of effective diffusion coefficients with respect to the molecular masses of selected solutes inside biofilms. (reproduced from Stewart, 2003).

1.1.2 Methods for investigating mass transport inside biofilms

As attempts to investigate biofilm processes are dependent upon accurate mass transport datasets, quantifying the transport behaviours of different molecules inside biofilms is key to allow us not only to understand but also to model real systems more accurately.

Recognizing the importance of mass transport processes inside biofilms researchers have already used a variety of methods. For example, methods such as classic diffusion cell,

microelectrodes, confocal laser scanning microscopy (CLSM), fluorescence recovery after photobleaching (FRAP) and two-photon excitation microscopy have been used to obtain mass transport data in biofilms (Bryers and Drummond, 1998, Damgaard et al., 2001, de Beer et al., 1997). The application of microelectrodes involves the insertion of a narrow (~10 µm) probe into the biofilm which is sensitive to the diffusion or concentration of a specific molecule (Damgaard et al., 2001). This approach has been instrumental in measuring mass transport rates of low molecular mass species, such as oxygen (Wieland et al., 2001) and methane (Damgaard et al., 2001). In contrast CLSM based methods directly visualize the migration of a fluorescently labelled probe through the biofilm and has been used to measure mass transport of high molecular mass compounds (de Beer et al., 1997).

Although these approaches have provided invaluable data on mass transport within biofilms, as with any method, each has certain limitations. For example, the diffusion cell method can only provide an average transport rate and cannot spatially resolve transport properties of the biofilm (Bryers and Drummond, 1998). While microelectrodes are used to measure mass transport of low molecular mass molecules, the detection of particulates and high molecular mass molecules are not possible using this method. Moreover, the insertion of a probe is invasive and thus has potential to disrupt the surrounding material, altering results. This could be problematic when numerous insertions must be made, such as during spatial mapping of diffusion coefficients in heterogeneous biofilms. Conversely CLSM is non-invasive. However, small molecules such as H₂ or O₂ cannot be labelled with the fluorescent probe and thus only the transport of higher molecular weight compounds can be determined. As this method relies on photons penetrating the biofilm, it is limited to both biofilm thickness (< 100µm) and to its density due to optical scattering effects (Paramonova et al., 2007, Vroom et al., 1999). Although the two-photon excitation method can overcome the depth penetration limitation of CLSM by approximately four times (Paramonova et al., 2007) it is not suitable where biofilms exceed these thicknesses. FRAP also suffers similar thickness limitations and light scattering effects. Critically, MRI can overcome many of these issues.

1.1.3 MRI of mass transport processes inside biofilms

Magnetic resonance imaging is being widely used in medical applications as a diagnostic tool since 1981 (Hutchison et al., 1980). The capacity of magnetic resonance imaging (MRI) for completely non-invasive measurement of the transport of both low and high molecular mass compounds and its ability to image inside hydrated biological matrices (Barentsz et al., 1993,

Poncelet et al., 1999), no matter what thickness, means it has significant potential for mass transport analysis of biofilms and can thus be an invaluable additional tool in this research field.

For example, MRI's powerful imaging capability has enabled detailed imaging of internal biofilm structures that are too thick for analysis by CLSM (Wieland et al., 2001, Phoenix and Holmes, 2008). Also, MRI has the ability to spatially resolve water diffusion in biofilms using the pulsed field gradient (PFG) analysis (Lens et al., 1999, McLean et al., 2008, Renslow et al., 2010, Wieland et al., 2001, Phoenix and Holmes, 2008). MRI's sensitivity to ^1H concentration has been exploited to map and quantify the water filled pores available for mass transport in biofilms from lake environments (Wieland et al., 2001). Furthermore, MRI has also been used to reveal processes in metal immobilizing bioreactors, mapping the location of biofilms, metal precipitates and dissolved metal concentrations (Graf von der Schulenburg et al., 2008, Nott et al., 2001). MRI has also been used to examine flow dynamics over biofilm surfaces (Manz et al., 2003, Seymour et al., 2004). Recent work by Phoenix and Holmes has lead to successful quantitative mapping of combined structure, water diffusion and heavy metal transport and adsorption in a real phototrophic biofilm (Phoenix and Holmes, 2008). MRI was subsequently used to investigate transport of trace metals inside real methanogenic granules which are employed in anaerobic wastewater treatment (Bartacek et al., 2009). The paramagnetic property of heavy metals has also allowed MRI to visualize and measure metal adsorption onto alginate gel, immobilized yeast cells, algal biosorbents (Nestle and Kimmich, 1996) and artificial biofilms made up with agar and bacterial pellets (Phoenix et al., 2008).

However, application of MRI in biofilm research is limited due to the relaxation effects, resolution limitations and cost. For example, the metal (e.g. paramagnetic) impurities found in biofilms can inhibit signal detection using MRI and the achievable signal-to-noise ratio may limit the use of MRI to biofilms with thicknesses more than several hundreds of microns.

1.2 Saturated porous geological media

Many natural and engineered water sources such as aquifers, rivers and sustainable urban drainage systems are composed of porous matrices of mineral grains, ranging from sand (0.1 mm) to gravel. These porous aquatic environments display complex heterogeneity in structure, hydrodynamics, geochemistry and microbiology. Once released into the environment pollutants such as organic and inorganic waste, toxic heavy metals and nanoparticles have a

tendency to reach natural and man made water sources via either direct runoff or poorly treated wastewater effluents. Hence, quantifying the transport behaviours of pollutants through porous geological systems is imperative for predicting pollution transport and for the mitigation of contamination in water resources.

1.2.1 Importance of mass transport processes inside porous media

Unlike in biofilms, advection and dispersion of fluid flow dominates the transport of pollutants in geological porous media. The physicochemical properties of both pollutants and porous matrices such as structure, size, composition, surface charge, flow paths and pH influence the fate of pollutants inside porous geological water sources. Recently, there has been considerable concern over the toxicity of nanoparticle pollutants. Nanoparticles (NPs) are particulates that have at least one dimension smaller than 100 nm. Their small size gives them unique surface properties which are exploited in a wide range of industrial and manufacturing processes. Problematically, nanoparticles can show a diverse range of toxic effects once released into the aquatic environment, such as vascular and respiratory injury, brain and liver damage, delayed embryonic development and death (Handy et al., 2008). Due to the extensive use of nanoparticles in a tremendously diverse array of applications, NP pollutants inevitably enter the porous matrices of natural and man made water sources (Dawson, 2008, Handy et al., 2008, Theron et al., 2008).

In contrast to the unintentional release of manufactured NPs, due to their high reactivity and high surface area to volume ratio, engineered NPs are being used for in-situ remediation of pollutants in various water systems (Sánchez et al., 2011, Liu et al., 2005, Zhang, 2003). However, previous studies have shown that a tendency to aggregate and deposition of NPs limits their effective transport, which is normally essential for proper remediation processes. Therefore, the fate of NP pollutants and the efficiency of the remediation processes using engineered NPs are influenced by NP transport behaviours.

1.2.2 Methods to investigate mass transport inside porous media

Break through curve (BTC) analysis has been extensively used to investigate nanoparticle transport inside porous geological media. In this approach, the concentration of nanoparticles eluting from the column outflow is recorded with time. This data can then be used to investigate transport properties such as coefficients of dispersion and retardation using reaction transport models. However, this approach has certain limitations. For example, BTC

analysis is limited to the time-dependent profile of the nanoparticle concentrations either at the column outlet or at a few intermediate sampling points, thus providing no or little information on the spatial heterogeneity of the entire system (Bridge et al., 2006). However, many systems of interest (aquifers, soils, riverbeds and engineered drainage systems) are complex, displaying heterogeneity in structure (Lorente and Bejan, 2006), hydrodynamics, geochemistry (Bhattacharjee et al., 2002) and microbiology (Kim et al., 2010) throughout.

To enable the spatial heterogeneity in the NP transport to be resolved, a range of novel methods have already been developed, such as real-time tracking of fluorescent particles through a translucent packed sand bed (Bridge et al., 2006). This approach, however, relies on sufficient photon penetration and therefore columns that are too opaque for photon-based imaging, either due to the thickness of the matrix or the opaqueness of the grains, cannot be investigated (Shang et al., 2010). Alternatively, two dimensional transport profiles can be extracted using a scanning optical fibre fluorescence profiler (Shang et al., 2010). The profiles, however, must still be inferred from the limited number of fibre optic detectors employed and the presence of buried sensors and fibres inside packed columns may have the potential to disturb natural transport pathways.

1.2.3 MRI of mass transport processes inside porous media

In addition to the traditional use of MRI in medical diagnostic imaging its ability to study structure, diffusion, flow, molecular dynamics, and chemical reactions noninvasively inside porous matrices has been widely utilized in a wide range of applied sciences applications (Callaghan, 1993, Gladden, 2003).

For example, the ability of MRI for characterising structures and fluid flows has already been exploited in chemical engineering to investigate structure of the inter particle pore space and the single-phase flow field in packed beds (Mantle et al., 2001), particle velocities and voidage fractions in bubbling fluidized beds (Holland et al., 2008), and structural and velocity characterization of biofouled membranes (Creber et al., 2010). The ability of MRI to study diffusion has already been applied in food engineering for temperature mapping and evaluation of mixing processes (Gladden, 2003) and dispersion measurements inside porous matrices have also been done using MRI (Khrapitchev and Callaghan, 2003).

MRI has also been used in hydrogeology research to measure water and solute flow and velocities, characterize porous media properties such as grain size and porosity, determine

water and non aqueous phase liquid distribution and evaluate transport mechanisms and reactive transport processes of solutes inside porous matrices (Werth et al., 2010). MRI has significant potential to investigate the transport of NPs inside porous media due to its ability to non-invasively image the movement of molecules and particles that are labelled with a (super)paramagnetic tag, no matter how opaque the porous columns are. Hence, MRI has already been used to observe the transport of several heavy metal ions (Cu^{2+} , Cr^{2+} , Gd^{3+}) in a sandy aquifer matrix (Nestle et al., 2003) and to quantify the transport of paramagnetic colloids (1.3 μm) through a matrix of silica gel (Baumann and Werth, 2005). However, transport of nanoparticles through saturated porous geological media (gravels and sands) has not yet been investigated using MRI.

However, the use of MRI to investigate transport properties of porous media has limitations such as relaxation effects, limited size of the sample, limited spatial resolution and cost. For example the sample size is limited to the bore size of the MRI scanner being used. Also, impurities found in the natural porous matrices can adversely affect the imaging of samples due to relaxation and susceptibility effects.

1.3 Using MRI contrast agents to quantify mass transport processes inside biofilms and porous media

Researchers have shown that MRI can be used to quantify mass transport properties of biofilms and geological porous matrices via measuring diffusion of water inside biofilms and measuring velocity and dispersion of water inside porous matrices. However, pollutants are not water and thus they exhibit transport properties which are different to water. Ions, macromolecules and particles can interact with biological and mineral surfaces, often through electrostatic interaction, resulting in permanent or non-permanent attachment, retarding transport and causing accumulation of the pollutant. Furthermore, as molecular mass increases, diffusion coefficients compared to that of water differ by orders of magnitude (e.g. see Fig 1.3B) (Carlson and Silverstein, 1998, Stewart, 2003), and thus water diffusion becomes decreasingly reliable as a proxy for pollutant diffusion. Thus it is imperative to be able to image the transport of the pollutant itself. The use of MRI contrast agents is a promising alternative to achieve this goal.

MRI contrast agents labelled with paramagnetic or superparamagnetic metal ions/nanoparticles have been developed to improve the potential of MRI in medical diagnostic

imaging as they provide improved contrast (MR signal) in the region of interest. They are used in imaging of tumors, imaging of the breakdown of the blood brain barrier, angiography, and in quantitative assessment of tissue vascularity and myocardial perfusion (Stanisz and Henkelman, 2000, Tofts, 2004), which are otherwise impossible to detect using standard MR imaging techniques.

Contrast agent technology works, not by imaging the actual (super)paramagnetically labelled molecule, but by imaging its effect on the neighbouring ^1H nuclei (see section 2.5). In the case of biofilms and saturated porous media this allows us to image, in-vivo, in-situ and in real time, the transport of these molecules.

The application of (super)paramagnetically tagged contrast agent (tracer) technology to investigate transport of macromolecules and nanoparticles inside biofilms and porous geological media has not been attempted before. Hence, this research will simply focus upon utilizing commercially available MRI contrast agents, such as Gd-DTPA and *Molday ION* nanoparticles. The success of this research could lead to the investigation of transport of a wider range of (super)paramagnetically tagged molecules (whether commercially available, constructed as a surrogate for a specific pollutant or tagged real pollutants) inside such systems.

The MRI scanner cutaway shown in figure 1.4 illustrates the set up used during transport experiments inside biofilms and porous packed columns. This is not an image of the scanner used in this research, but an example for illustrative purposes.

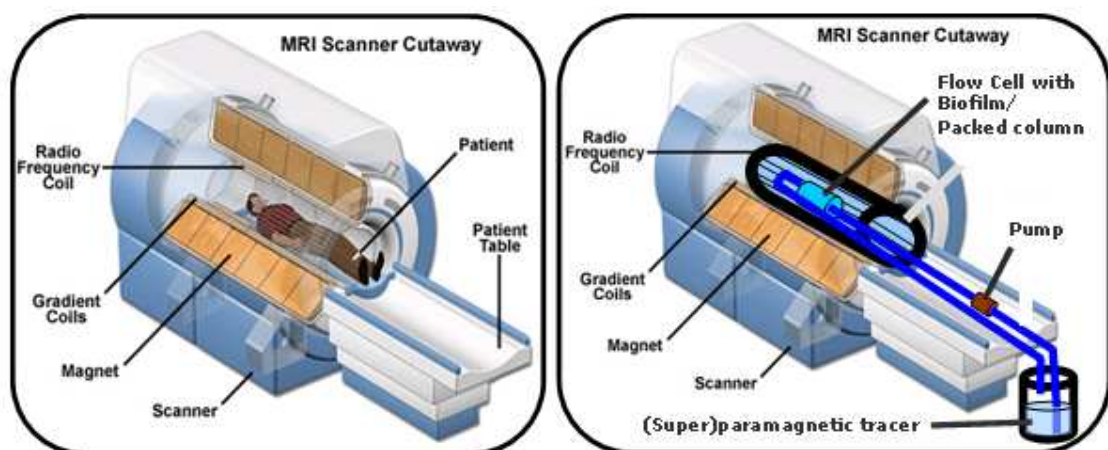


Figure 1.4. Schematic diagram showing how the MRI scanner was used to conduct transport experiments inside biofilms and porous packed columns (reproduced and edited from BIOE 414 Instrumentation Projects).

1.4 Modelling mass transport processes inside biofilms and porous geological media

Mathematical models representing the transport of different molecules of interest inside biofilms and porous geological media are essential to unravel their transport behaviours and quantify mass transport and reaction coefficients. Experimentally quantified transport of molecules using MRI can be compared with mathematical models (representing the transport of molecules) not only to check the accuracy of the MRI methods in quantifying transport, but also to estimate transport and reaction rates of molecules inside biofilms and porous geological media.

In general the transport of molecules inside a biofilm can be represented by a diffusion equation as given below;

$$\frac{\partial C}{\partial t} = \frac{\partial}{\partial x} \left[D_{dif} \frac{\partial C}{\partial x} \right] - rC$$

Equation 1

where C is the solute concentration (M or mg/l), D_{dif} is the molecular diffusion coefficient (m^2/s), x is the distance into the biofilm (m), t is time (s) and r is the reaction coefficient (s^{-1}). r is equal to zero when the transport of non-reactive molecules is considered.

In general the transport of reactive molecules inside a porous geological media can be represented by a convection-dispersion equation as given below;

$$(R) \frac{\partial C}{\partial t} = \frac{\partial}{\partial x} \left[D_{dis} \frac{\partial C}{\partial x} \right] - U \frac{\partial C}{\partial x}$$

Equation 2

where C is the solute concentration (M or mg/l), D_{dis} is the hydrodynamic dispersion coefficient (m^2/s), U is the average pore velocity (m/s), x is the distance into the column (m), t is time (s) and R is the retardation factor. R is equal to one when the transport of non-reactive molecules is considered.

The hydrodynamic dispersion coefficient, D represents the solute spreading caused by both mechanical dispersion and molecular diffusion, and is defined as;

$$D = D_m + D_{dif}$$

Equation 3

$$D_m = kU$$

Equation 4

where D_m is the mechanical dispersion coefficient and D_{dif} is the molecular diffusion coefficient and k is the dispersivity of the porous media.

Solutions for the above mentioned partial differential equations (equations 1 and 2) with respect to their initial and boundary conditions provide spatially and temporally varying concentrations of molecules inside biofilms and porous geological media.

Analytical solutions for these partial differential equations have already been derived by several researchers to study the transport behaviours of solutes inside biofilms and porous media related systems (Baumann and Werth, 2005, Bartlett and Gardner, 1996). However, analytical solutions are limited to simple model geometries and simple boundary conditions. Therefore, numerical simulations were used to represent the transport of molecules inside the irregular domains of biofilms and porous matrices used in this research. Two dimensional finite element models representing mass transport of molecules inside biofilms and a porous column were implemented using *COMSOL Multiphysics* (versions 3.4 and 3.5a).

An optimization routine developed in *MATLAB* was used with *COMSOL* model to estimate transport and reaction rates of molecules inside biofilms and porous media. Estimated transport rates of molecules within test systems (e.g. simple agar) were used to investigate the accuracy of the MRI methods while the estimated transport and reaction rates within real samples (i.e. porous column and biofilms) were used to investigate the behaviours of molecules in those systems.

The detailed description of the use of the above mentioned reaction-transport equations for different experimental purposes are discussed further in their respective chapters.

1.5 Outline and scope of the thesis

Quantifying mass transport of macromolecules and nanoparticles inside biofilms and porous geological matrices is imperative to understand their transport behaviours inside such environmental systems. Mass transport studies using conventional methods such as micro-electrodes, confocal laser scanning microscopy (CLSM), and break through curve analysis have their own limitations as described earlier.

However, the capacity of magnetic resonance imaging (MRI) for completely non-invasive measurement of the transport of ions, macromolecules and nanoparticles using (super)paramagnetic contrast agents and its ability to image inside hydrated systems no matter what thickness and no matter how opaque the system, means that it has significant potential to investigate mass transport processes inside biofilms and porous geological media. Critically, unlike many other approaches, the data is both spatially resolved and the system unperturbed by the analysis. Hence, in this thesis mass transport processes are quantified inside several environmentally related systems using MRI to show its capability as an invaluable additional tool in the environmental research field. As similar to all environmental studies, the work reported here is also highly multidisciplinary, involving the fields of magnetic resonance imaging, mathematical modelling and microbiology.

Aims of this research:

- To introduce the capacity of MRI to investigate transport of macromolecules inside biofilms using Gd-DTPA, a commercially available paramagnetic MRI contrast agent.
- To investigate the influence of biofilm architecture upon its mass transport behaviour with improved spatial resolution using bespoke radio frequency (RF) coils.
- To introduce the capacity of MRI to investigate transport of nanoparticles inside coarse-grained porous media using *Molday ION*, a commercially available superparamagnetic MRI contrast agent.
- To investigate the fate of copper inside artificial biofilms composed of a mix of bacteria and agar using MRI. Thus, testing the suitability of an existing adsorption-diffusion model for predicting heavy metal transport and fate in biofilms.

The thesis is structured as follows:

Chapter 2: MRI theory. This describes the fundamentals and the operational concepts of MRI used in this research to quantify mass transport processes inside biofilms and saturated porous media.

Chapter 3: Application of paramagnetically tagged molecules for magnetic resonance imaging (MRI) of biofilm mass transport processes. This introduces a novel method for mass transport quantification of macromolecules inside biofilms using a commercially available paramagnetically tagged molecule.

Chapter 4: Magnetic resonance imaging of mass transport inside biofilms using a simple custom made solenoid RF coil. This describes the use of a bespoke radio frequency (RF) coil to investigate the influence of biofilm architecture upon its mass transport behaviour with improved spatial resolution. The custom made coil is the simpler and cost effective alternative to image transport of both low and high molecular mass molecules and structure inside biofilms which are otherwise too thick to image using conventional optical microscopy methods such as confocal laser scanning microscope (CLSM).

Chapter 5: Investigation of nanoparticle transport inside coarse-grained geological media using magnetic resonance imaging (MRI). This introduces a novel approach to quantify mass transport of nanoparticles inside coarse-grained porous geological media such as river beds and sustainable urban drainage systems.

Chapter 6: Investigation of copper immobilisation inside artificial biofilm using magnetic resonance imaging (MRI). This describes the use of MRI to investigate the fate of heavy metals inside biofilms, and investigates the suitability of an existing adsorption-diffusion model to predict copper immobilisation inside biofilms.

All the experimental chapters (3, 4, 5, and 6), include their own introduction describing the importance of each study, materials and methods used, results section, discussion and references. The IDL and MATLAB codes used to process MRI data and estimate transport and reaction rates are included in the appendix.

Chapter 7, concluding remarks, includes a general discussion on conclusions being derived and possible future research of environmental systems using MRI.

1.6 References

- BARENTSZ, J. O., RUIJS, S. H. J. & STRIJK, S. P. (1993) The role of mr imaging in carcinoma of the urinary-bladder. *American Journal of Roentgenology*, 160, 937-947.
- BARTACEK, J., VERGELDT, F. J., GERKEMA, E., JENICEK, P., LENS, P. N. L. & VAN AS, H. (2009) Magnetic resonance microscopy of iron transport in methanogenic granules. *Journal of Magnetic Resonance*, 200, 303-312.
- BARTLETT, P. N. & GARDNER, J. W. (1996) Diffusion and binding of molecules to sites within homogeneous thin films. *Philosophical Transactions of the Royal Society of London Series a-Mathematical Physical and Engineering Sciences*, 354, 35-57.
- BAUMANN, T. & WERTH, C. J. (2005) Visualization of colloid transport through heterogeneous porous media using magnetic resonance imaging. *Colloids and Surfaces a-Physicochemical and Engineering Aspects*, 265, 2-10.
- BEUN, J. J., HENDRIKS, A., VAN LOOSDRECHT, M. C. M., MORGENROTH, E., WILDERER, P. A. & HEIJNEN, J. J. (1999) Aerobic granulation in a sequencing batch reactor. *Water Research*, 33, 2283-2290.
- BEYENAL, H. & LEWANDOWSKI, Z. (2002) Internal and external mass transfer in biofilms grown at various flow velocities. *Biotechnology Progress*, 18, 55-61.
- BHATTACHARJEE, S., RYAN, J. N. & ELIMELECH, M. (2002) Virus transport in physically and geochemically heterogeneous subsurface porous media. *Journal of Contaminant Hydrology*, 57, 161-187.
- BISHOP, P. L., GIBBS, J. T. & CUNNINGHAM, B. E. (1997) Relationship between concentration and hydrodynamic boundary layers over biofilms. *Environmental Technology*, 18, 375 - 385.
- BRIDGE, J. W., BANWART, S. A. & HEATHWAITE, A. L. (2006) Noninvasive quantitative measurement of colloid transport in mesoscale porous media using time lapse fluorescence imaging. *Environmental Science & Technology*, 40, 5930-5936.
- BRYERS, J. D. & DRUMMOND, F. (1998) Local macromolecule diffusion coefficients in structurally non-uniform bacterial biofilms using fluorescence recovery after photobleaching (FRAP). *Biotechnology and Bioengineering*, 60, 462-473.
- BUFFIÈRE, P., STEYER, J. P., FONADE, C. & MOLETTA, R. (1995) Comprehensive modeling of methanogenic biofilms in fluidized bed systems: Mass transfer limitations and multisubstrate aspects. *Biotechnology and Bioengineering*, 48, 725-736.
- CALLAGHAN, P. T. (1993) *Principles of nuclear magnetic resonance microscopy*, Clarendon Press.
- CARLSON, G. & SILVERSTEIN, J. (1998) Effect of molecular size and charge on biofilm sorption of organic matter. *Water Research*, 32, 1580-1592.
- CHARACKLIS, W. G. (1981) Bioengineering report. Fouling biofilm development: a process analysis. *Biotechnol Bioeng.*, Vol. XXIII, Pp. 1923-60 (1981).

- CREBER, S. A., VROUWENVELDER, J. S., VAN LOOSDRECHT, M. C. M. & JOHNS, M. L. (2010) Chemical cleaning of biofouling in reverse osmosis membranes evaluated using magnetic resonance imaging. *Journal of Membrane Science*, 362, 202-210.
- DAMGAARD, L. R., NIELSEN, L. P. & REVSBECH, N. P. (2001) Methane microprofiles in a sewage biofilm determined with a microscale biosensor. *Water Research*, 35, 1379-1386.
- DAVIES, D. (2003) Understanding biofilm resistance to antibacterial agents. *Nature Reviews Drug Discovery*, 2, 114-122.
- DAWSON, T. L. (2008) Nanomaterials for textile processing and photonic applications. *Coloration Technology*, 124, 261-272.
- DE BEER, D., STOODLEY, P. & LEWANDOWSKI, Z. (1997) Measurement of local diffusion coefficients in biofilms by microinjection and confocal microscopy. *Biotechnology and Bioengineering*, 53, 151-158.
- DE BEER, D., STOODLEY, P., ROE, F. & LEWANDOWSKI, Z. (1994) Effects of biofilm structures on oxygen distribution and mass transport. *Biotechnology and Bioengineering*, 43, 1131-1138.
- GLADDEN, L. F. (2003) Magnetic resonance: Ongoing and future role in chemical engineering research. *Aiche Journal*, 49, 2-9.
- GRAF VON DER SCHULENBURG, D. A., HOLLAND, D. J., PATERSON-BEEDLE, M., MACASKIE, L. E., GLADDEN, L. F. & JOHNS, M. L. (2008) Spatially resolved quantification of metal ion concentration in a biofilm-mediated ion exchanger. *Biotechnol Bioeng*, 99, 821-9.
- HANDY, R. D., VON DER KAMMER, F., LEAD, J. R., HASSELLOV, M., OWEN, R. & CRANE, M. (2008) The ecotoxicology and chemistry of manufactured nanoparticles. *Ecotoxicology*, 17, 287-314.
- HOLLAND, D. J., MULLER, C. R., SEDERMAN, A. J., MANTLE, M. D., GLADDEN, L. F. & DAVIDSON, J. F. (2008) Magnetic resonance imaging of fluidized beds: Recent advances. *Theoretical Foundations of Chemical Engineering*, 42, 469-478.
- HUTCHISON, J. M. S., EDELSTEIN, W. A. & JOHNSON, G. (1980) A whole-body nmr imaging machine. *Journal of Physics E-Scientific Instruments*, 13, 947-955.
- KHRAPITCHEV, A. A. & CALLAGHAN, P. T. (2003) Reversible and irreversible dispersion in a porous medium. *Physics of Fluids*, 15, 2649-2660.
- KIM, J. W., CHOI, H. & PACHEPSKY, Y. A. (2010) Biofilm morphology as related to the porous media clogging. *Water Research*, 44, 1193-1201.
- LENS, P., VERGELDT, F., LETTINGA, G. & VAN AS, H. (1999) H-1 NMR characterisation of the diffusional properties of methanogenic granular sludge. *Water Science and Technology*, 39, 187-194.
- LEWANDOWSKI, Z., STOODLEY, P. & ALTOBELLI, S. (1995) Experimental and conceptual studies on mass-transport in biofilms. *Water Science and Technology*, 31, 153-162.
- LIU, Y. Q., MAJETICH, S. A., TILTON, R. D., SHOLL, D. S. & LOWRY, G. V. (2005) TCE dechlorination rates, pathways, and efficiency of nanoscale iron particles with different properties. *Environmental Science & Technology*, 39, 1338-1345.

- LEVINE, A. D., TCHOBANOGLOUS, G., ASANO, T. (1985) Characterization of the size distribution of contaminants in wastewater: treatment and reuse implications. *Journal Water Pollution Control Federation*, 57, 805-816.
- LOGAN, B. E., HAMELERS, B., ROZENDAL, R. A., SCHRORDER, U., KELLER, J., FREGUIA, S., AELTERMAN, P., VERSTRAETE, W. & RABAEY, K. (2006) Microbial fuel cells: Methodology and technology. *Environmental Science & Technology*, 40, 5181-5192.
- LOGAN, B. E. & QING, J. (1990) Molecular-size distributions of dissolved organic-matter. *Journal of Environmental Engineering-Asce*, 116, 1046-1062.
- LORENTE, S. & BEJAN, A. (2006) Heterogeneous porous media as multiscale structures for maximum flow access. *Journal of Applied Physics*, 100, 8.
- MANTLE, M. D., SEDERMAN, A. J. & GLADDEN, L. F. (2001) Single- and two-phase flow in fixed-bed reactors: MRI flow visualisation and lattice-Boltzmann simulations. *Chemical Engineering Science*, 56, 523-529.
- MANZ, B., VOLKE, F., GOLL, D. & HORN, H. (2003) Measuring local flow velocities and biofilm structure in biofilm systems with magnetic resonance imaging (MRI). *Biotechnology and Bioengineering*, 84, 424-432.
- MCLEAN, J. S., ONA, O. N. & MAJORS, P. D. (2008) Correlated biofilm imaging, transport and metabolism measurements via combined nuclear magnetic resonance and confocal microscopy. *Isme Journal*, 2, 121-131.
- NESTLE, N., WUNDERLICH, A., NIESSNER, R. & BAUMANN, T. (2003) Spatial and temporal observations of adsorption and remobilization of heavy metal ions in a sandy aquifer matrix using magnetic resonance imaging. *Environmental Science & Technology*, 37, 3972-3977.
- NESTLE, N. F. E. I. & KIMMICH, R. (1996) NMR imaging of heavy metal absorption in alginate, immobilized cells, and kombu algal biosorbents. *Biotechnology and Bioengineering*, 51, 538-543.
- NOTT, K. P., PATERSON-BEEDLE, M., MACASKIE, L. E. & HALL, L. D. (2001) Visualisation of metal deposition in biofilm reactors by three-dimensional magnetic resonance imaging (MRI). *Biotechnology Letters*, 23, 1749-1757.
- PARAMONOVA, E., DE JONG, E. D., KROM, B. P., VAN DER MEI, H. C., BUSSCHER, H. J. & SHARMA, P. K. (2007) Low-load compression testing: A novel way of measuring Biofilm thickness. *Applied and Environmental Microbiology*, 73, 7023-7028.
- PHOENIX, V. R. & HOLMES, W. M. (2008) Magnetic resonance imaging of structure, diffusivity, and copper immobilization in a phototrophic biofilm. *Applied and Environmental Microbiology*, 74, 4934-4943.
- PHOENIX, V. R., HOLMES, W. M. & RAMANAN, B. (2008) Magnetic resonance imaging (MRI) of heavy-metal transport and fate in an artificial biofilm. *Mineralogical Magazine*, 72, 483-486.
- PONCELET, B. P., KOELLING, T. M., SCHMIDT, C. J., KWONG, K. K., REESE, T. G., LEDDEN, P., KANTOR, H. L., BRADY, T. J. & WEISSKOFF, R. M. (1999) Measurement of human myocardial

perfusion by double-gated flow alternating inversion recovery EPI. *Magnetic Resonance in Medicine*, 41, 510-519.

QURESHI, N., ANNOUS, B., EZEJI, T., KARCHER, P. & MADDOX, I. (2005) Biofilm reactors for industrial bioconversion processes: employing potential of enhanced reaction rates. *Microbial Cell Factories*, 4, 24.

RENSLOW, R. S., MAJORS, P. D., MCLEAN, J. S., FREDRICKSON, J. K., AHMED, B. & BEYENAL, H. (2010) In situ effective diffusion coefficient profiles in live biofilms using pulsed-field gradient nuclear magnetic resonance. *Biotechnology and Bioengineering*, 106, 928-937.

ROESELERS, G., LOOSDRECHT, M. & MUYZER, G. (2008) Phototrophic biofilms and their potential applications. *Journal of Applied Phycology*, 20, 227-235.

SÁNCHEZ, A., RECILLAS, S., FONT, X., CASALS, E., GONZÁLEZ, E. & PUNTES, V. (2011) Ecotoxicity of, and remediation with, engineered inorganic nanoparticles in the environment. *TrAC Trends in Analytical Chemistry*, 30, 507-516.

SEYMOUR, J. D., CODD, S. L., GJERSING, E. L. & STEWART, P. S. (2004) Magnetic resonance microscopy of biofilm structure and impact on transport in a capillary bioreactor. *Journal of Magnetic Resonance*, 167, 322-327.

SHANG, J. Y., LIU, C. X., WANG, Z. M., WU, H., ZHU, K. K., LI, J. A. & LIU, J. (2010) In-situ measurements of engineered nanoporous particle transport in saturated porous media. *Environmental Science & Technology*, 44, 8190-8195.

STANISZ, G. J. & HENKELMAN, R. M. (2000) Gd-DTPA relaxivity depends on macromolecular content. *Magnetic Resonance in Medicine*, 44, 665-667.

STEWART, P. S. (1998) A review of experimental measurements of effective diffusive permeabilities and effective diffusion coefficients in biofilms. *Biotechnology and Bioengineering*, 59, 261-272.

STEWART, P. S. (2003) Diffusion in biofilms. *Journal of Bacteriology*, 185, 1485-1491.

THERON, J., WALKER, J. A. & CLOETE, T. E. (2008) Nanotechnology and water treatment: Applications and emerging opportunities. *Critical Reviews in Microbiology*, 34, 43-69.

TOFTS, P. (2004) *Quantitative MRI of the brain: Measuring changes caused by disease* Wiley-Blackwell.

VROOM, J. M., DE GRAUW, K. J., GERRITSEN, H. C., BRADSHAW, D. J., MARSH, P. D., WATSON, G. K., BIRMINGHAM, J. J. & ALLISON, C. (1999) Depth penetration and detection of pH gradients in biofilms by two-photon excitation microscopy. *Applied and Environmental Microbiology*, 65, 3502-3511.

WALTER, B., HAASE, C. & RABIGER, N. (2005) Combined nitrification/denitrification in a membrane reactor. *Water Research*, 39, 2781-2788.

WERTH, C. J., ZHANG, C. Y., BRUSSEAU, M. L., OOSTROM, M. & BAUMANN, T. (2010) A review of non-invasive imaging methods and applications in contaminant hydrogeology research. *Journal of Contaminant Hydrology*, 113, 1-24.

WIELAND, A., DE BEER, D., DAMGAARD, L. R., KUHL, M., VAN DUSSCHOTE, D. & VAN AS, H.

(2001) Fine-scale measurement of diffusivity in a microbial mat with nuclear magnetic resonance imaging. *Limnology and Oceanography*, 46, 248-259.

WUERTZ. S, B. P. L., WILDERER. P.A (2008) *Biofilms in wastewater treatment: An Interdisciplinary Approach*, IWA Publishing.

YANG, S. N. & LEWANDOWSKI, Z. (1995) Measurement of local mass-transfer coefficient in biofilms. *Biotechnology and Bioengineering*, 48, 737-744.

ZHANG, W. X. (2003) Nanoscale iron particles for environmental remediation: An overview. *Journal of Nanoparticle Research*, 5, 323-332.

Chapter 2

Magnetic resonance imaging (MRI)

2

Magnetic resonance imaging (MRI)

This chapter contains a summary of the essential principles of MRI relevant to this thesis. A full description of the theory of MRI can be found in greater detail in the extensive literature that is available. The reader is referred especially to comprehensive sources such as Blumich (2003), Callaghan (1993), Haacke (1999), Levitt (2008), and Tofts (2004).

2.1 Fundamentals of MRI

Atoms consist of sub-atomic particles such as electrons, protons and neutrons. Protons and neutrons create the nucleus of an atom, while electrons orbit around the nucleus. For example, a hydrogen (^1H) atom has a nucleus of one proton and no neutrons with one orbiting electron. In addition to the basic properties like mass and charge, the nucleus may also possess an intrinsic spin angular momentum and magnetic moment.

A nucleus can experience the phenomenon of nuclear magnetic resonance (NMR) if it has a non-zero spin angular momentum (i.e. magnetic moment). The nucleus of ^1H with only one proton has a spin quantum number, I of $\frac{1}{2}$ and is NMR active. On the other hand the nucleus of ^{12}C is NMR inactive, as it has an even number of protons and even number of neutrons resulting a zero spin angular momentum (i.e. $I = 0$).

Saturated porous matrices such as biofilms and packed columns are composed mostly of water and thus ^1H based MRI was utilized in all experiments presented in this thesis. Therefore, only the hydrogen nucleus will be considered in the following explanations and will be referred to as a nuclear “spin”.

Nuclear spins can only take a certain numbers of states since spin is a quantum property. The possible number of states is given by;

$$S = 2 * I + 1$$

Equation 1

where, I is the nuclear spin quantum number.

Therefore, the hydrogen nucleus ($I = \frac{1}{2}$) can only take two discrete states, which are known as spin-up and spin-down. The spin-up state is the lower energy state, as the magnetic moment aligns with the applied main magnetic field, B_0 while the spin-down state is the higher energy state as the magnetic moment aligns against B_0 .

In the absence of a magnetic field these two states have the same energy, while in the presence of a magnetic field the energy levels split. This is known as Zeeman splitting, and is proportional to the applied static magnetic field, B_0 (see Fig. 2.1).

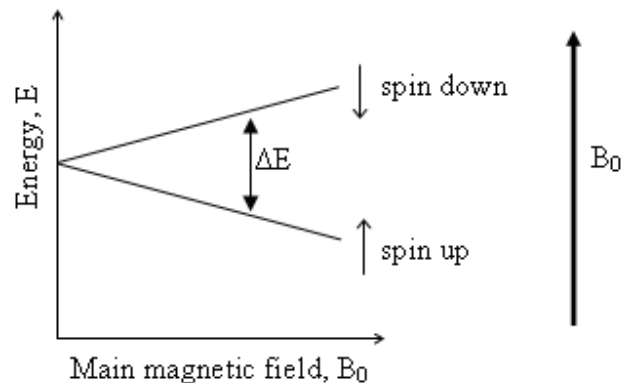


Figure 2.1. Zeeman splitting with respect to the main magnetic field.

2.1.1 Nuclear magnetic moment in a static magnetic field

A nuclear magnetic moment when placed in a static magnetic field will precess about the axis of the field. This is a consequence of the nucleus possessing an intrinsic spin angular momentum. The precessional frequency is known as the Larmor frequency and is proportional to the static magnetic field strength and given by;

$$\omega_0 = \gamma B_0$$

Equation 2

where the proportionality constant, γ , known as the magnetogyric ratio, is a property of the particular nucleus (isotope).

Classically, the motion of a magnetic moment in a magnetic field, i.e; the time rate of change of the angular momentum, p , is equal to the cross product of the magnetic moment, μ , and the magnetic field it is experiencing, B_0 .

$$\frac{dp}{dt} = \mu \times B_0$$

Equation 3

Spin angular momentum and the magnetic moment are proportional to each other and are related by;

$$\mu = \gamma p$$

Equation 4

Substituting equation 4 in equation 3 gives;

$$\frac{d\mu}{dt} = \gamma \mu \times B_0$$

Equation 5

Solving equation 5 for a static field, B_0 , along the z-axis gives;

$$\mu_x(t) = \mu_x(0) \cos(\gamma B_0 t) + \mu_y(0) \sin(\gamma B_0 t)$$

Equation 6

$$\mu_y(t) = \mu_y(0) \cos(\gamma B_0 t) - \mu_x(0) \sin(\gamma B_0 t)$$

Equation 7

$$\mu_z(t) = \mu_z(0)$$

Equation 8

Equations 6 and 7 and equation 8 show the z-component of the magnetic moment does not vary with time, while the x and y components describe a circular motion with time. This demonstrates that the magnetic moment undergoes a precessional motion when placed in a static magnetic field, with a precession frequency equal to γB_0 . A macroscopic analogy for this would be the rotation (precession) of a tilted spinning top about the axis of earth's gravitational field.

2.1.2 Ensemble of spins

The behaviour of a single spin (proton of the hydrogen nucleus) within a static magnetic field (B_0) was outlined in the previous section. However, in practice, samples (e.g biofilms) contain an ensemble (collection) of spins. Therefore, an ensemble of spins within a small volume of a

sample (voxel) will be considered in the following discussion.

2.1.3 Net magnetization

Under normal conditions, the magnetic moments of millions of hydrogen nuclei (spins) present in a small volume (voxel) of a sample (e.g. biofilm) are randomly distributed and will have zero net magnetization. A net magnetization is produced when the sample is placed within a static magnetic field (B_0).

The static magnetic field produces an energy difference between the two nuclear spin states. Due to this energy difference, a slightly larger population of spins will align along the static magnetic field as this has the lower energy level (spin-up state) compared to the higher energy level (spin-down state). The distribution of spins between these two energy states follows the Boltzmann distribution;

$$\frac{N_{\uparrow}}{N_{\downarrow}} = \exp(-\Delta E / kT)$$

Equation 9

where N_{\uparrow} is the number of spins in the spin up state, N_{\downarrow} is the number of spins in the spin down state, ΔE is the energy difference between the two states, k is the Boltzmann constant and T the temperature in the Kelvin scale.

The alignment of excess spins along the direction of the static magnetic field (Fig. 2.2a and b), conventionally termed as the longitudinal direction or z-axis, results a net magnetization (M_0) along that direction (Fig. 2.2c). The randomly oriented transverse component of all magnetic moments (spins) result a zero transverse magnetization.

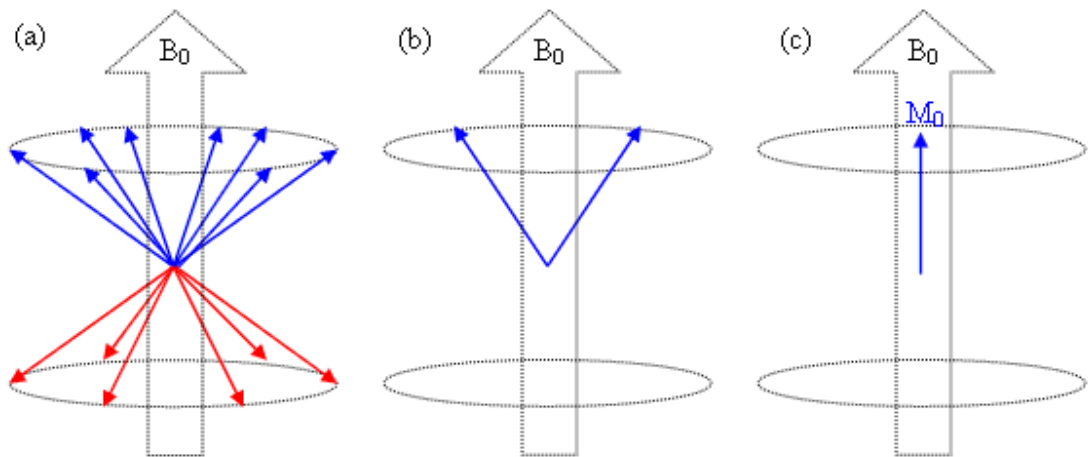


Figure 2.2. Formation of net magnetization when a static magnetic field, B_0 is applied. Here (a) spin up and spin down alignment of magnetic moments, (b) alignment of excess spins along the direction of static magnetic field and (c) formation of net magnetization.

It should be noted here that the net magnetization formed by the ensemble of spins has similar behaviours to that of a single spin, when placed within a static magnetic field. Hence, the equations describing the motion of a single spin can be used to describe the behaviour of the net magnetization as given below.

$$M_x(t) = M_x(0) \cos(\gamma B_0 t) + M_y(0) \sin(\gamma B_0 t)$$

Equation 10

$$M_y(t) = M_y(0) \cos(\gamma B_0 t) - M_x(0) \sin(\gamma B_0 t)$$

Equation 11

$$M_z(t) = M_z(0)$$

Equation 12

Equations 10-12, the Bloch equations illustrate that the net magnetization (M_0) also precesses about the axis of the applied static magnetic field, at the Larmor frequency.

2.1.4 Application of a radio frequency (RF) pulse

Classically, electromagnetic radiation is composed of perpendicularly oriented oscillating electric and magnetic fields. The oscillating magnetic field component of the electromagnetic radiation that matches the precession frequency of the net magnetization (commonly, radio frequency [RF]) is applied perpendicular to the main static magnetic field in order to excite the spins as shown in equation 13. Excitation of spin system is a combination of changing the spin population between the two energy levels and creating phase coherence.

$$\frac{\Delta E}{h} = \gamma B_0 (= \omega_0)$$

Equation 13

where ΔE is the difference in the energy levels, h is the Planck's constant divided by 2π , γ is the magnetogyric ratio, B_0 is the main magnetic field and ω_0 is the Larmor frequency.

As a result the net magnetization is tipped away from its equilibrium position (along the z axis). The energy absorption of a spin (hydrogen nucleus proton) from an electromagnetic radiation at resonance condition is known nuclear magnetic resonance (NMR) effect and this is the underlying phenomenon exploited in magnetic resonance imaging.

2.1.5 Rotating frame of reference

The total magnetic field that the spins (or net magnetization) experience during the application of a RF pulse is the vector sum of B_0 , the static field, and B_1 , the oscillating magnetic component of the RF radiation. Since the precession of net magnetization due to the main magnetic field is constant, it is convenient to introduce a new coordinate system which rotates around the axis of the static magnetic field, B_0 at the frequency of the RF radiation, ω_1 and is known as the Rotating frame (Levitt, 2008). The coordinate system of the rotating frame is represented by primed notation as shown in figure 2.3. Excitation of spins occurs when frequency of the RF pulse, ω_1 matches the precessional frequency of the spin system, ω_0 . This condition is known as on resonance.

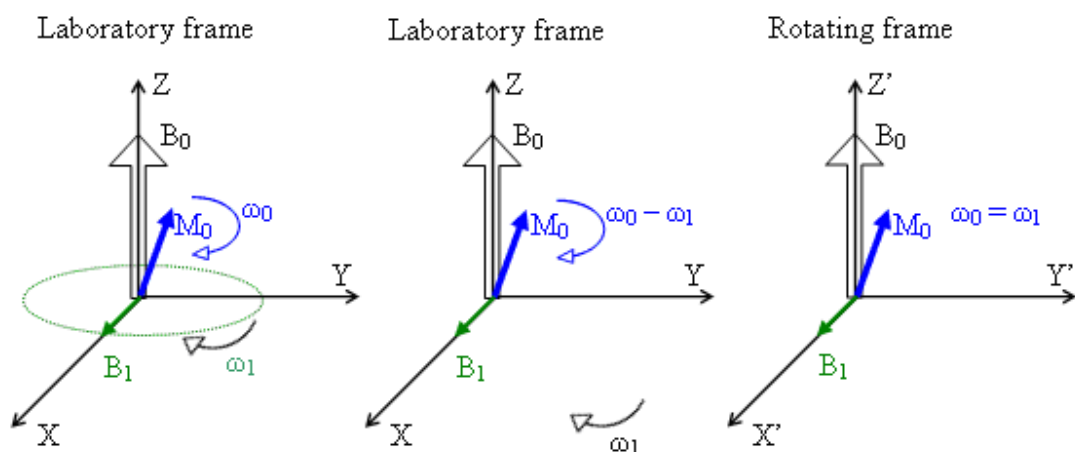


Figure 2.3. Stationary and rotating coordinate systems.

2.1.6 Excitation of spins (net magnetization)

The magnetic field component of the applied electromagnetic radiation is responsible for excitation of spins. Classically, the oscillating magnetic field component of RF pulse (B_1) will exert a torque, F on spin's magnetic moment, μ and is given by;

$$F = \mu \times B_1$$

Equation 14

The generated torque, F is perpendicular to both magnetic moment of the spin and the main static magnetic field, B_0 . As a result the net magnetization is tipped into the transverse plane from its equilibrium position, through an angle known as flip angle, θ , and is given by;

$$\theta = \gamma B_1 t_p$$

Equation 15

where, γ is the magnetogyric ratio, B_1 is the oscillating magnetic field component of the RF pulse and t_p is the time duration of applied RF pulse.

The rotation of the net magnetization (flip angle) depends upon the strength and the duration of the applied RF radiation, B_1 . Application of a 90° RF pulse and 180° rotate the net magnetization respectively onto transverse plane (xy) and $-z$ plane as shown in figure 2.4. This is the semi-classical description, showing individual magnetic moments, in spin-up and spin-down states and the phase coherence following an excitation.

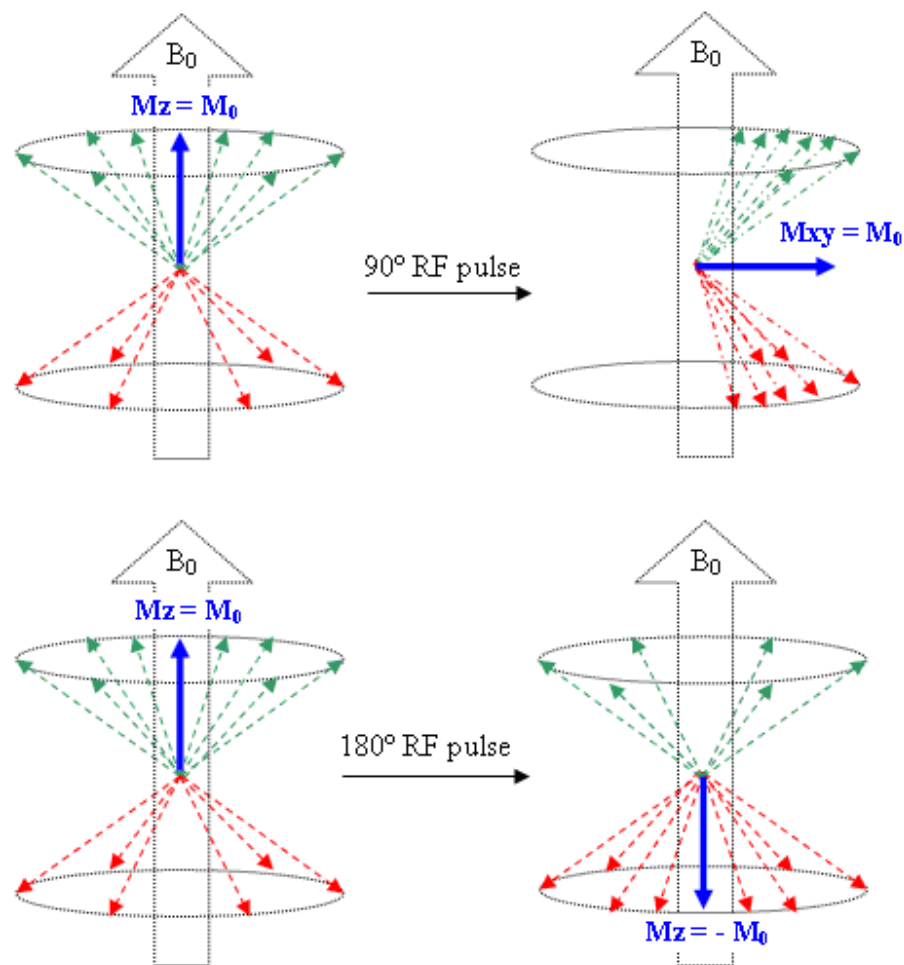


Figure 2.4. Schematic illustrating the effect of 90° and 180° RF radiation on individual spins and net magnetization.

2.1.7 Relaxation process

Following the excitation by an RF pulse, the spin system (or net magnetization) will return to equilibrium; this process is called relaxation. The actual relaxation can be described by two processes; the recovery of the longitudinal magnetization component (T_1 relaxation) and the decay of transverse magnetization component (T_2 relaxation).

2.1.8 Longitudinal relaxation

When excitation pulse is switched off, spins will start to lose the energy they absorbed (during the excitation) to the environment and will return to thermal equilibrium (see Fig. 2.5). This process is known as spin lattice or longitudinal relaxation. This relaxation process is described by the relaxation time constant, T_1 . Following a 90° excitation pulse, the amount of longitudinal magnetization, M_z present at time, t is given by;

$$M_z = M_0(1 - e^{-t/T_1})$$

Equation 16

where M_0 is the net magnetization.

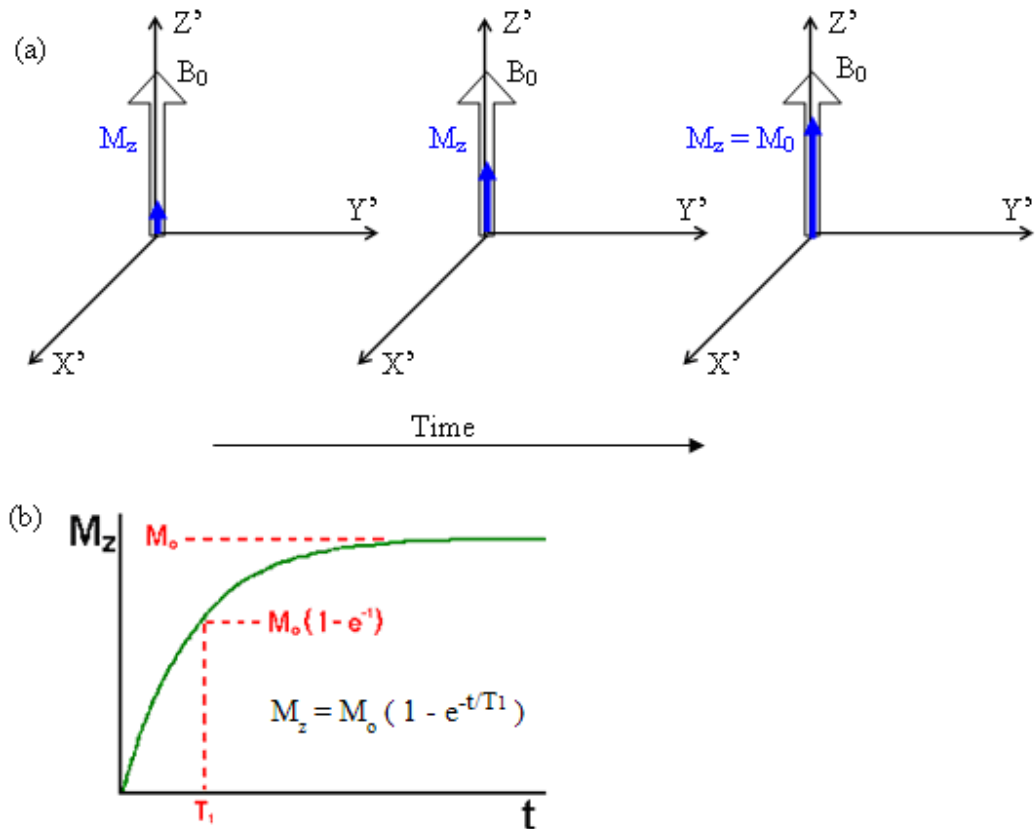


Figure 2.5.(a) Relaxation of longitudinal component of the net magnetization and (b) the longitudinal relaxation curve.

2.1.9 Transverse relaxation

Following the excitation, individual nuclear spins will start to lose their phase coherence, for example via dipole-dipole interaction. This causes the transverse component of the net magnetization to decay with time (see Fig. 2.6) and is known as transverse relaxation or spin-spin relaxation which is described by the relaxation time constant T_2 . Following a 90° excitation pulse, the amount of transverse magnetization, M_{xy} present at time, t , is given by;

$$M_{xy} = M_0 e^{-t/T_2}$$

Equation 17

where M_0 is the net magnetization.

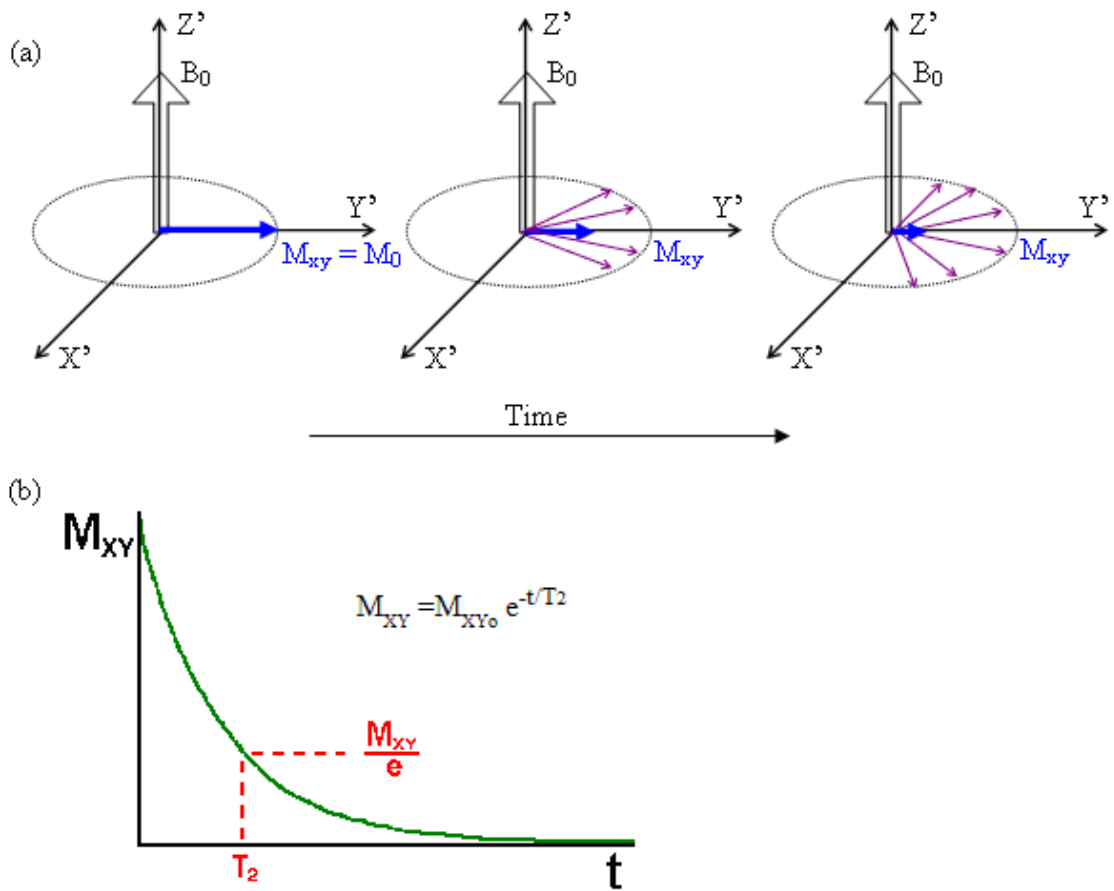


Figure 2.6. (a) Decay of transverse component of the net magnetization and (b) the transverse decay curve.

2.1.10 Field inhomogeneity effect (T_2^*)

In addition to dipole-dipole interactions, the local inhomogeneity of the main magnetic field across the sample also contributes in the decay of the M_{xy} component with a relaxation time constant, T_2' . The combined effects of both dipole-dipole interactions and field inhomogeneity increase the rate of signal loss and the net decay is described by the apparent relaxation time, T_2^* , which is always shorter than T_2 and the relationship is given by;

$$\frac{1}{T_2^*} = \frac{1}{T_2} + \frac{1}{T_2'}$$

Equation 18

The magnetic field inhomogeneities are mainly caused by the differences in the magnetic susceptibility within the sample and any possible paramagnetic impurities found in the sample.

2.1.11 Mechanism of nuclear spin relaxation

The interaction between the magnetic moments of the neighbouring ^1H nuclei is known as dipole-dipole interaction. In the liquid state, water molecules tumble in a random fashion, causing their magnetic moments to generate a randomly fluctuating local magnetic field, $B'(t)$, which is very weak compare to the applied main magnetic field. On a macroscopic scale (space and time) the net effect of the randomly fluctuating magnetic field is zero and known as motional averaging. However, the randomly fluctuating local magnetic field caused due to the dipole-dipole interactions drives the relaxation processes.

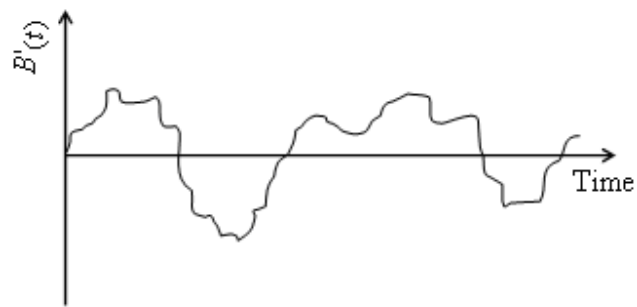


Figure 2.7. Fluctuating local magnetic field caused by the random tumbling motion of water molecules.

The component of the fluctuating local magnetic field along the direction of the applied main magnetic field will cause slight variation in the precessional frequency (Larmor) of the spins. This will create phase difference between spins and thus lead to transverse relaxation process.

The component of the fluctuating local magnetic field perpendicular to the static main magnetic field, which matches the Larmor frequency, will drive transition between spin states thus leading to longitudinal relaxation process.

The time interval between significant fluctuations in the local magnetic field is known as correlation time, τ_c . Therefore, water with short correlation time has long relation times compared to ice which has a longer correlation time.

The relaxation mechanisms for different samples of interest used in this research are summarised in table 2.1.

Sample of interest	Relaxation process	Source of relaxation
Water	Longitudinal relaxation	
	(1) intrinsic	Dipole-dipole interaction
	Transverse relaxation	
	(1) intrinsic	Dipole-dipole interaction
Biofilm	Longitudinal relaxation	
	(1) intrinsic	Dipole-dipole interaction
	(2) surface relaxation	paramagnetic effect > dipole-dipole interaction
	Transverse relaxation	
	(1) intrinsic	Dipole-dipole interaction
	(2) surface relaxation	paramagnetic effect > dipole-dipole interaction
	(3) variations in the Larmor frequency	Magnetic field inhomogeneity
Packed columns	Longitudinal relaxation	
	(1) intrinsic	Dipole-dipole interaction
	(2) surface relaxation	paramagnetic effect > dipole-dipole interaction
	Transverse relaxation	
	(1) intrinsic	Dipole-dipole interaction
	(2) surface relaxation	paramagnetic effect > dipole-dipole interaction
	(3) variations in the Larmor frequency	Magnetic field inhomogeneity

Table 2.1. Relaxation mechanisms for different samples of interest.

2.1.12 MR signal generation

Application of an RF pulse tips the net magnetization onto the transverse plane. The transverse component precesses about the z-axis at the Larmor frequency, ω_0 . The precessing net magnetization generates an oscillating magnetic field, which induces an electro motive force (e.m.f) in the receiver coil placed on the transverse plane. This induced e.m.f (electric current) is the MR signal.

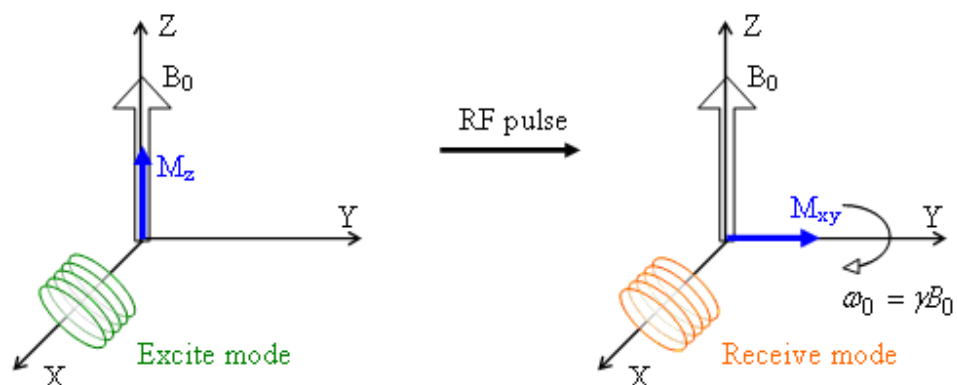


Figure 2.8. Excitation and detection of MR signal

The MR signal generated by the precessing transverse magnetization of a single magnetic moment can be written as;

$$S_{(t)} \propto \exp(i\gamma B_0 t)$$

Equation 19

where $S_{(t)}$ is the time varying MR signal, γ is the magnetogyric ratio, B_0 is the static magnetic field and t is the time after the excitation pulse.

Thus, the generated MR signal from a small volume of a sample (voxel) with a spin density of ρ is given by;

$$S_{(t)} = \rho \exp(i\gamma B_0 t)$$

Equation 20

The next section contains the detailed description on how the MR signal is spatially resolved (encoded) to produce a useful image.

2.2 MR imaging process

2.2.1 Magnetic field gradients

The main magnet produces a uniform magnetic field, B_0 across the sample, thus spins at different spatial positions precess at the same frequency. However, application of pulses of small linearly varying magnetic fields (magnetic field gradients), in addition to the main magnetic field, makes the magnetic field vary across the sample. This causes the spins at different spatial positions to precess at slightly different frequencies, thus labelling their spatial positions. For example, application of a magnetic field gradient along the x-axis (equation 21) will induce small changes in the magnetic field strength, B_z , from point to point along the x-axis as given in equation 22. This will cause the spins to precess at slightly different precession frequencies along the x direction, as given in equation 23.

$$G_x = \frac{\partial B_z}{\partial x}$$

Equation 21

$$B_z = B_0 + x.G_x$$

Equation 22

$$\omega = \gamma B_z = \gamma(B_0 + x.G_x) = \omega_0 + \gamma(x.G_x)$$

Equation 23

where B_0 is the static main magnetic field, G_x is the applied gradient strength, ω is the precessional frequency and γ is the magnetogyric ratio.

Magnetic field gradients are applied as a series of pulses during an MR imaging experiment by using three orthogonal sets of gradient coils. Application of magnetic field gradients to perform two dimensional imaging of a sample is described below.

2.2.2 Two dimensional imaging

Figure 2.9 illustrates the position of a specimen inside the scanner in order to perform a two dimensional MR imaging across the sample. The z axis is chosen along the main magnetic field (longitudinal) direction, which in our scanner is horizontal. Both x and y axes form the transverse plane.

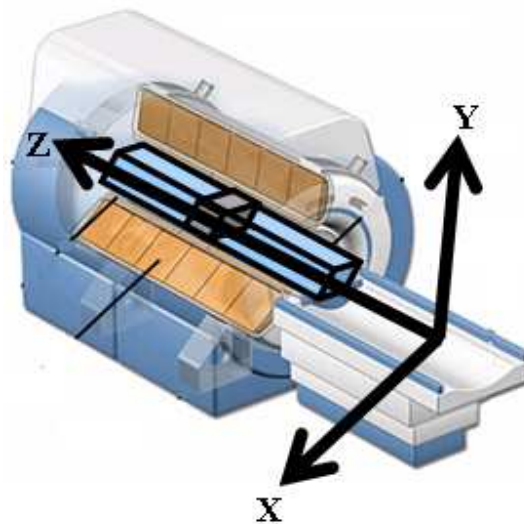


Figure 2.9. Test specimen placed inside the MRI scanner with respect to the three orthogonal directions (x, y and z).

2.2.3 Slice selection

In order to select an imaging slice a magnetic field gradient is applied perpendicular to the desired slice. During the application of a slice selective gradient, the precession frequencies of spins will linearly vary along the gradient direction. Concurrent application of an RF pulse, which has a narrow bandwidth (similar to the precession frequencies of spins inside the slice), will selectively excite the spins with matching precession frequencies. The RF pulse has no effect on spins located outside of the slice. Slice location can be changed by changing the centre frequency of the RF pulse and the slice thickness can be increased either by decreasing

the gradient strength of the applied slice selective magnetic field or increasing the RF band width. Shaped RF pulses; for example a Sinc function in the time domain are used for selective excitation (see Fig. 2.10) as they give better slice definition.

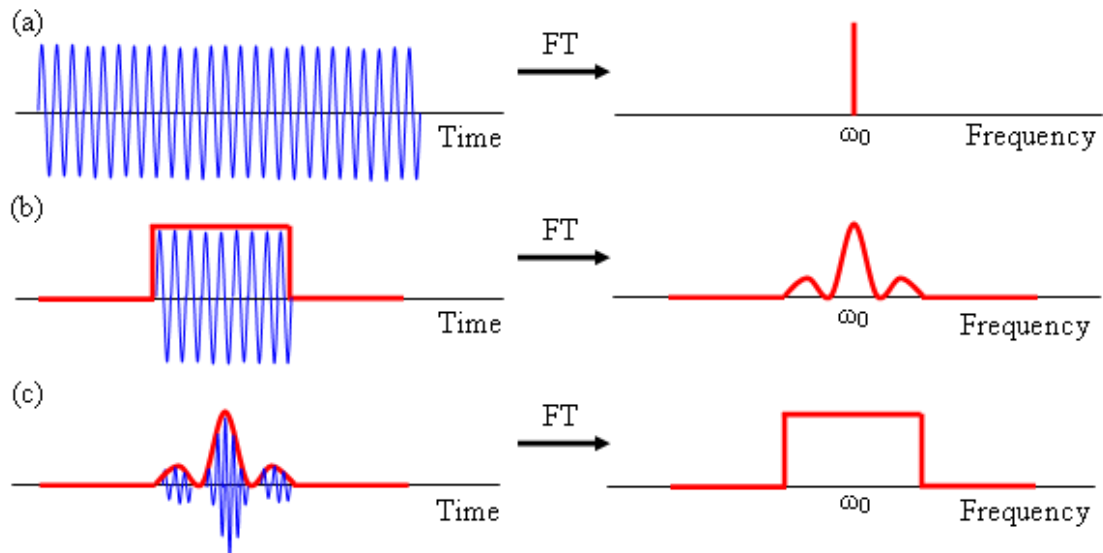


Figure 2.10. Comparison between continuous and modulated RF pulses in time and frequency domains.

As shown in figure 2.10, the continuous RF pulse (a) will have only one resonant frequency while the shaped RF pulses (b) and (c) will have a range of resonant frequencies in the frequency domain. The RF pulse modulated by a hat function in the time domain will produce a sinc distribution of frequencies and thus not suitable for slice selection. However, an RF pulse modulated by a Sinc function in the time domain will produce a hat distribution of frequencies which is more suitable for selection of a rectangular slice.

The net signal produced after applying the slice selective gradient is the summation of signals generated within all the voxels across that slice. This composite signal has to be further spatially encoded to create a two dimensional image. This spatial encoding is done by applying additional magnetic field gradients along the two orthogonal directions to the slice selective gradient as described below.

2.2.4 Frequency encoding

A spatial encoding gradient is applied along the frequency encoding direction after the RF pulse is switched off. This linearly varying magnetic field gradient causes the magnetizations at different positions to precess at slightly different frequencies, thus labelling their spatial positions along the frequency encoding direction.

2.2.5 Phase encoding

Another spatial encoding gradient is applied along the phase encoding direction (perpendicular to frequency encode) during the interval between RF pulse and data acquisition. This applied linearly varying magnetic field gradient along the phase encoding direction causes the magnetizations at different positions to precess at slightly different frequencies. This creates phase differences between the magnetizations depending on their spatial positions, thus labelling their spatial positions along the phase encoding direction.

Generally, one phase encoding step is performed for each excitation-acquisition and the acquired data forms a single line of the raw data matrix, known as k-space. Typically an image requires several data excitation-acquisition to fill the entire k-space and thus the phase encoding procedure is repeated. For example, an image with 256 pixels along the phase encoding direction requires 256 phase encoding steps. The applied magnetic field gradient along this direction is increased (or decreased) at each phase encoding steps in a regular fashion, while gradients of slice selection and frequency encoding remain the same. Note, some MRI techniques such as *RARE*, acquire data from multiple phase encodes but with the same excitation (see section 2.4.3).

2.2.6 Formation of an MR image

By combining equations 20 and 23, the MR signal generated from an element, dx at position x_1 (see Fig. 2.11a) can be written as (Callaghan, 1993);

$$ds(G_x, t) = (\rho(x)dx) \exp[i\gamma(B_0 + G_x \cdot x_1)t]$$

Equation 24

where $\rho(x)$ is the spin density and thus $\rho(x)dx$ denotes the total number of spins available within the element, dx .

Therefore, the total signal generated from the sample is the summation over x and is given by;

$$S(G_x, t) = \int_{-\infty}^{+\infty} \rho(x) \exp[i\gamma(B_0 + G_x \cdot x_1)t] dx$$

Equation 25

The total signal transformed into the rotating frame of reference is given by;

$$S(G_x, t) = \int_{-\infty}^{+\infty} \rho(x) \exp[i\gamma G_x \cdot x_1 t] dx$$

Equation 26

Substitution of the reciprocal space vector k , will convert the signal equation into;

$$S(k) = \int_{-\infty}^{+\infty} \rho(x) \exp[i2\pi k x_1] dx$$

Equation 27

where

$$k = \frac{1}{2\pi} \gamma G_x t$$

Equation 28

Thus, the spin density of the sample can be deduced by the inverse Fourier transform of the equation 27 as given below;

$$\rho(x) = \int_{-\infty}^{+\infty} S(k) \exp[-i2\pi(k \cdot x_1)] dk$$

Equation 29

In the example given in figure. 2.11(a), the resulting projection of spin density on to the x axis would be as shown in figure. 2.11(b).

This relationship between $\rho(x)$ and $S(k)$ can be generalised to two dimensional imaging as given below;

$$\rho(x, y) = \int_{-\alpha-\alpha}^{+\alpha+\alpha} \int S(k_x, k_y) \exp[-i2\pi(k_x x + k_y y)] dk_x dk_y$$

Equation 30

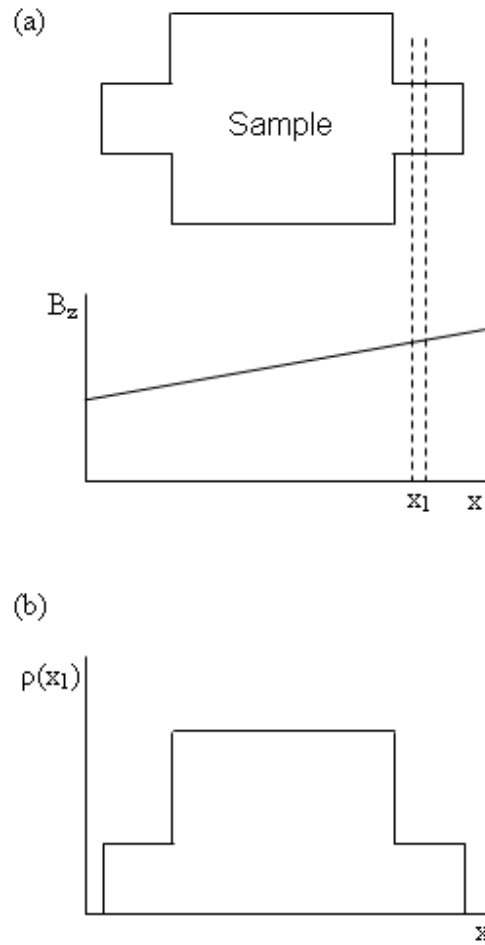


Figure 2.11. (a) Application of linearly varying magnetic field gradient along x direction. (b) Measured proton density of the sample along the x axis.

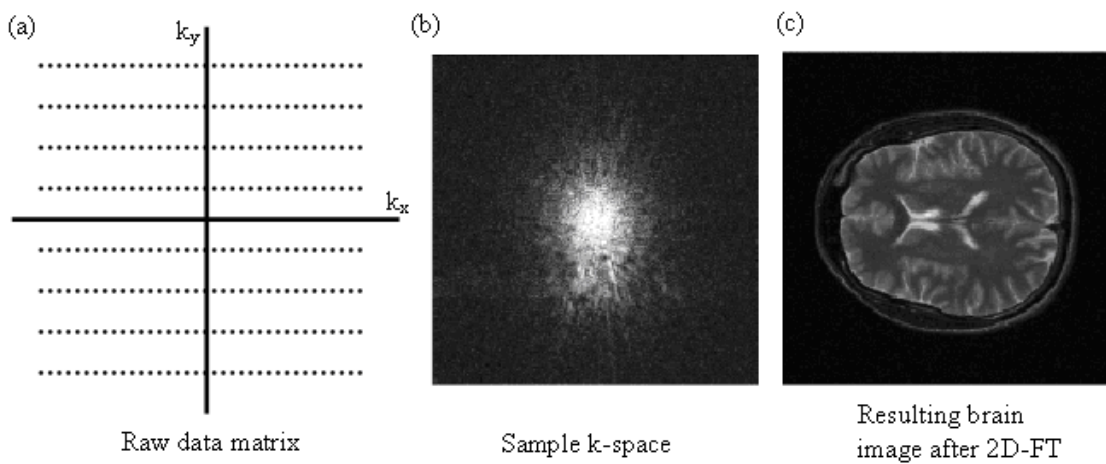


Figure 2.12. Illustrates (a) raw data matrix, (b) sample k-space and (c) resulting brain image after the two dimensional inverse Fourier transformation of the k-space (reproduced from www.ipem.ac.uk).

The digitised MR signal is stored in a complex data matrix known as k-space (see Fig. 2.12a). The two-dimensional inverse Fourier transformation of a (example) k-space (Fig. 2.12b) provides the spin density (or the amplitude) image of the sample (see Fig. 2.12c).

2.3 Image contrast

Spatial variation in the sample properties (e.g. solid content and density of biofilms) generates spatial variation in the MR signal intensity, via different longitudinal relaxation time (T_1), transverse relaxation time (T_2) and ^1H spin density as given below (Haacke, 1999);

$$S = S_0 \frac{1 - e^{-T_R/T_1}}{1 - \cos \alpha \cdot e^{-T_R/T_1}} e^{-T_E/T_2} \sin \alpha$$

Equation 31

where S_0 is the available maximum signal intensity, α is the flip angle of the excitation pulse; T_R denotes the repetition time (the time interval between two successive excitation pulses), T_E is the echo time (the time interval between the excitation pulse and centre of the signal readout centre), T_1 is the longitudinal relaxation time, and T_2 is the transverse relaxation time.

By altering the echo time (TE) or repetition time (TR), the signal contrast can be altered or “weighted”. For example if a long TE is used in combination with long TR, spatial differences in T_2 relaxation times of sample will become apparent, such an image is called a T_2 -weighted image (see Fig. 2.13). Signal from tissues with a long T_2 (e.g. water) takes longer to decay than the signal from tissue with a short T_2 (e.g. biofilm) and thus appear brighter in the image. In a similar manner TR governs T_1 contrast. Tissue with a long T_1 (water) will take a long time to recover back to equilibrium following an excitation. Therefore, short TR interval combination with short TE will make tissue with long T_1 appear dark compared to tissue with a short T_1 (e.g. biofilm), such an image is called T_1 -weighted image (see Fig.2.14). When TE and TR are chosen to minimise both these relaxation weightings (short TE and long TR), the signal contrast will depend mainly on the spin density of a given tissue, and such an image is called proton density-weighted. It should also be noted here that signal measurement with low TE values are essential to reduce the influence of the T_2 effect upon the signal in a T_1 -weighted image, while signal measurement with high TR values are essential to reduce the influence of the T_1 effect upon the signal in T_2 -weighted image.

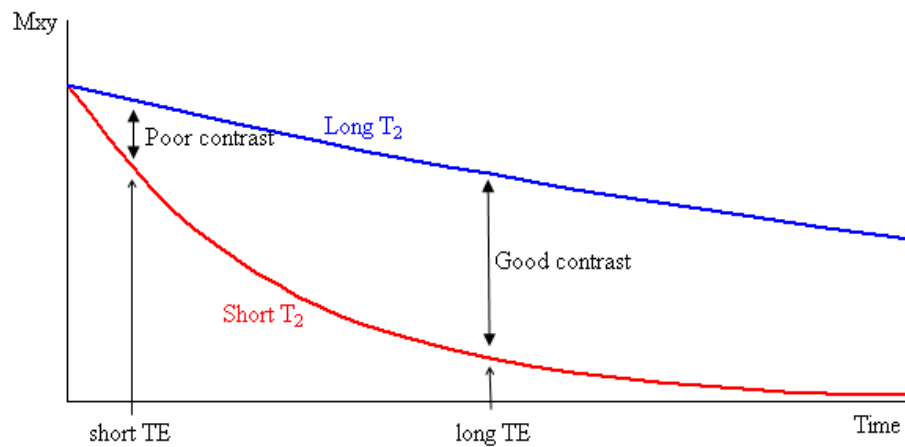


Figure 2.13. T_2 -weighting image contrast at short and long TE with long TR to minimise the T_1 -weighting.

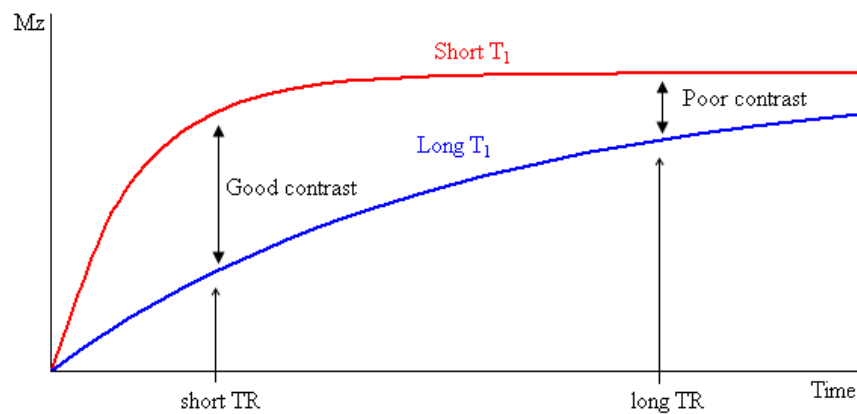


Figure 2.14. T_1 -weighted image contrast at short and long TR with short TE to minimize T_2 -weighting.

Image weighting	TE	TR
T_1 -weighted	Short	Short
T_2 -weighted	Long	Long
Proton density weighted	Short	Long

Table 2.2. Summarises the preferred TE and TR values to generate T_1 , T_2 and proton density-weighted images.

Now it is obvious that the image contrast during an MR imaging experiment depends not only on the spin properties such as relaxation times and spin density, but also on the scan parameters such as TE and TR. There are several types of scans with different operational routines, known as pulse sequences available to create contrast between tissues with different properties.

2.4 Pulse sequence

An MR pulse sequence consists of several concurrent and consecutive events such application of RF pulses, application of magnetic field gradient pulses and data acquisition. The pulse sequence describes the order and exact timings in which these events are executed during an MR imaging experiment.

A large number of pulse sequences have been designed by altering the manner in which the above mentioned events are executed. The types of pulse sequences used in this study are described below (Callaghan, 1993).

2.4.1 Gradient echo pulse sequence

This is a simple form of imaging pulse sequences, based on a gradient echo. The pulse sequence diagram is shown in figure- 2.15.

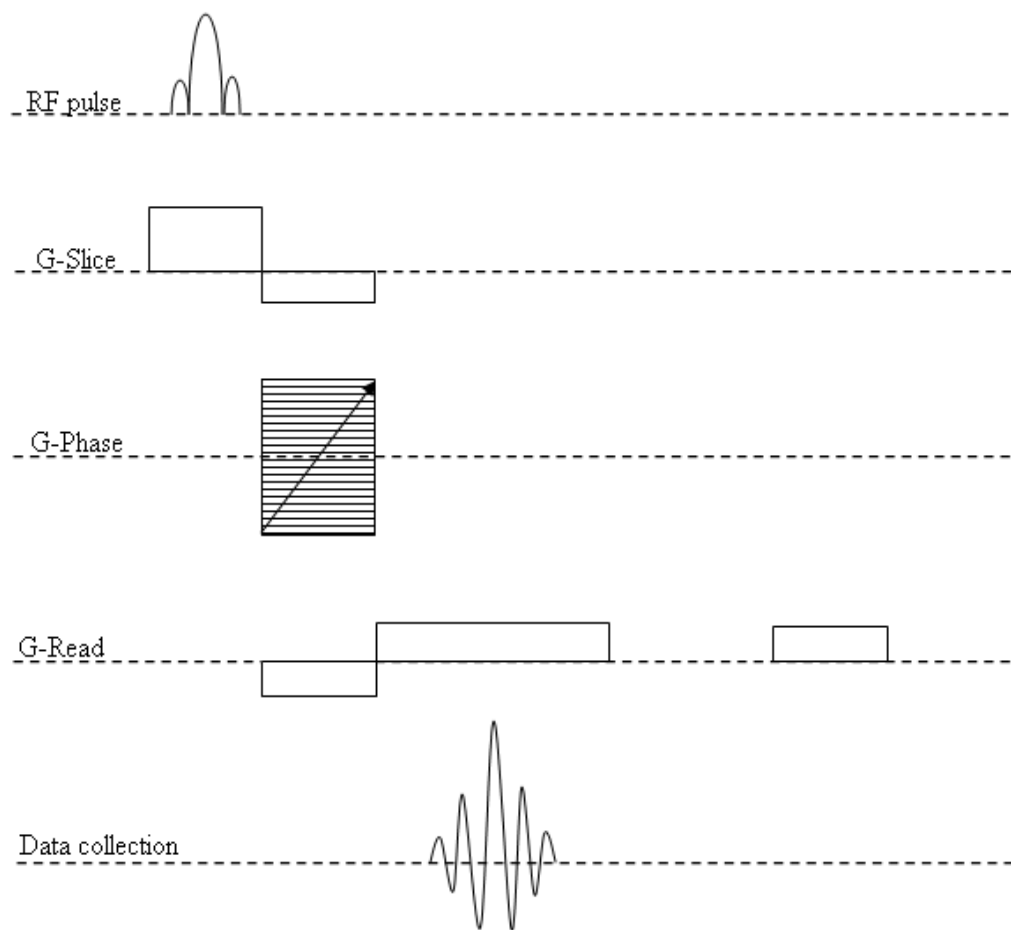


Figure 2.15. Gradient echo pulse sequence diagram.

The basic 2D gradient echo pulse sequence includes the following events. A slice-selective shaped (e.g. sinc function) RF excitation pulse is applied simultaneously as a gradient is applied in the slice-selective direction. Immediately thereafter a gradient is applied in the phase encoding direction, accompanied by a rephasing gradient with opposite sign in the slice-selective direction (that compensates for dephasing throughout the slice), and a preparative dephasing gradient in the frequency encoding direction. Then, a rephasing gradient is applied alone in the frequency encoding direction or 'readout' direction opposite in sign to the preparative gradient, effectively rephasing the magnetization and forming an echo that is then sampled. Magnetization decay during this period is dependent on T_2^* . TE here refers to the time interval from the centre of the RF pulse excitation to the centre of the echo. TR indicates the total time between repetitions of RF excitation pulses. Since this pulse sequence includes a single phase encoding step, it must be repeated several times in order to fill the entire k-space. A spoiler gradient is applied along the frequency encoding direction to destroy any residual transverse magnetizations found in between two successive RF excitations.

2.4.2 Spin echo pulse sequence

The spin echo (SE) pulse sequence is similar to the gradient echo pulse sequence except that an additional 180° RF pulse is used to create a spin echo, in addition to a gradient echo. The pulse sequence diagram in figure 2.16 shows the spin echo pulse sequence.

The spin echo pulse sequence is initiated by a slice-selective shaped (e.g. sinc function) 90° RF excitation pulse applied simultaneously with a magnetic field gradient in the slice-selective direction. This is followed by a rephasing gradient along the slice selection axis, a dephasing gradient in the frequency encoding direction, and, importantly, a gradient is applied in the phase encoding direction whose magnitude is incremented after each excitation. T_2^* effects cause decay of transverse magnetization during this period after the 90°_x RF excitation pulse. At time, TE/2, a second RF pulse, a 180°_y RF pulse is applied accompanied by a second slice-selective gradient. The spin rephasing process caused by the 180°_y RF creates the spin echo at an interval TE/2 after the 180°_y RF pulse.

The total time interval from the issue of the 90° RF excitation pulse to the appearance of the center of the echo is the echo time, TE. The repetition time, TR, indicates the time between repetitions of the 90° excitation pulses. Since this pulse sequence includes a single phase encoding step per TR, it is repeated with varying magnitudes of the phase encoding gradient in

order to fill the entire k-space.

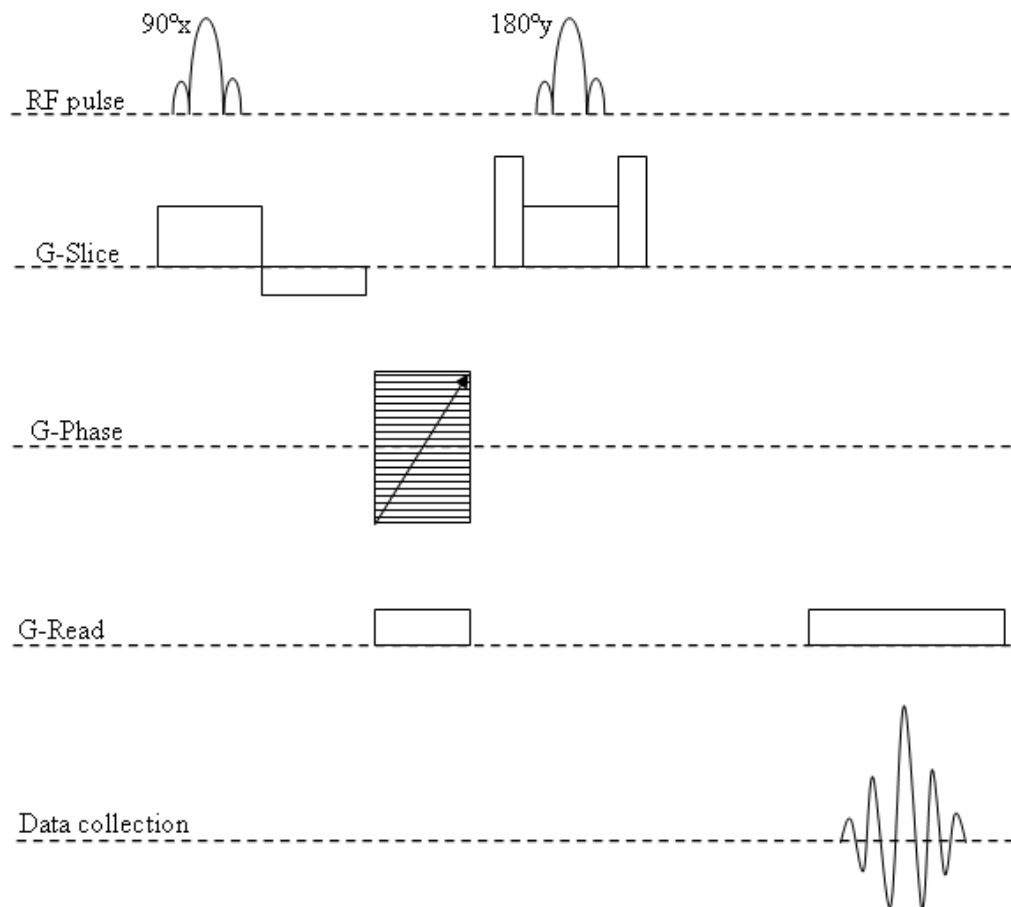


Figure 2.16. Spin echo pulse sequence diagram.

As illustrated in figure 2.17, the initial 90°_x RF pulse along the x-axis, tips the magnetization into the transverse plane (Fig. 2.17a). Tipped magnetizations will precess at slightly different frequencies due to the magnetic field inhomogeneities resulting in a phase difference between the spins (e.g. 1, 2, 3 and 4 in figure 2.17b). The phase differences will increase with time. The application of the 180°_y RF pulse along the y-axis, after time interval of $TE/2$, will cause a 180° rotation of magnetizations around the y-axis (Fig. 2.17c). The magnetizations will continue to precess at the same rate as before, resulting in the rephasing of spins and the creation of a spin-echo signal (Fig. 2. 17d).

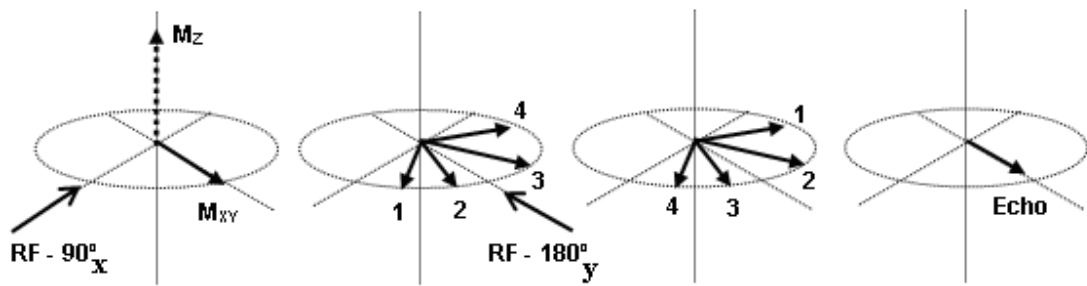


Figure 2.17. Formation of a spin echo when 180° RF pulse is applied

Images formed by the spin echo pulse sequence can reveal T_1 and T_2 and proton density contrast depending on the choice of TE and TR. The refocusing of the magnetization to form a spin-echo makes this pulse sequence less sensitive to magnetic field inhomogeneities than the gradient echo imaging sequence.

2.4.2.1 Multiple spin echo imaging

After the echo is formed by the 180° RF pulse, the net signal will start to decay once again due to the above mentioned field inhomogeneity effect. Subsequent echoes can be formed by repeating 180° RF pulses. However, each echo will be smaller compare to the previous echo due to inherent T_2 decay (see Fig. 2.18). Using more than a 180° RF pulses to create signal echoes is known as multiple spin echo pulse sequence, this can be used to acquires images with T_2 -weighting and is used to obtain a quantitative T_2 parameter image.

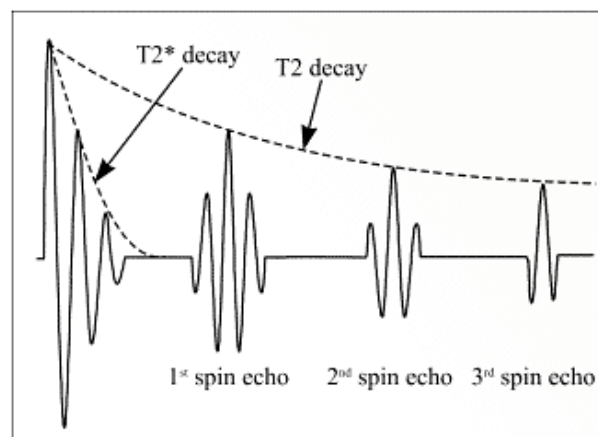


Figure 2.18. Continuous formation of echoes using subsequent 180° RF pulses.

It should be noted, the T_2 values measured using the above method are effective T_2 values, as they depend on the echo time of the multiple echo sequence. This is a result of the diffusion of water molecules within an inhomogeneous magnetic field (Farrar, 1971). The shorter the echo time, the closer the effective T_2 to the pure T_2 value.

2.4.3 RARE pulse sequence

In a conventional spin echo imaging sequence, only a single line of the k-space is filled per excitation-acquisition, requiring longer scan times to produce an MR image. However, in a Rapid Acquisition Relaxation Enhancement (*RARE*) sequence (Henning et al., 1986) multiple spin echoes are generated using a train of 180° pulses after a 90° pulse. Each echo is phase encoded separately to form different lines of the k-space. This multiple acquisition of k-space data (lines) with a single excitation makes the k-space sampling quicker and reduces the total scan time. The *RARE* pulse sequence is shown in figure 2.19.

As the *RARE* sequence contains multiple RF pulses, stimulated echoes are generated in addition to spin echoes. Unlike spin echoes which are refocused via the 180° pulse in the transverse plane, the stimulated echoes are generated by the refocusing of the phase coherence stored as longitudinal magnetization. The regular spacing of 180° pulses in the *RARE* sequence (see Fig. 2.19) results in the simultaneous generation of spin and stimulated echoes (Haacke, 1999).

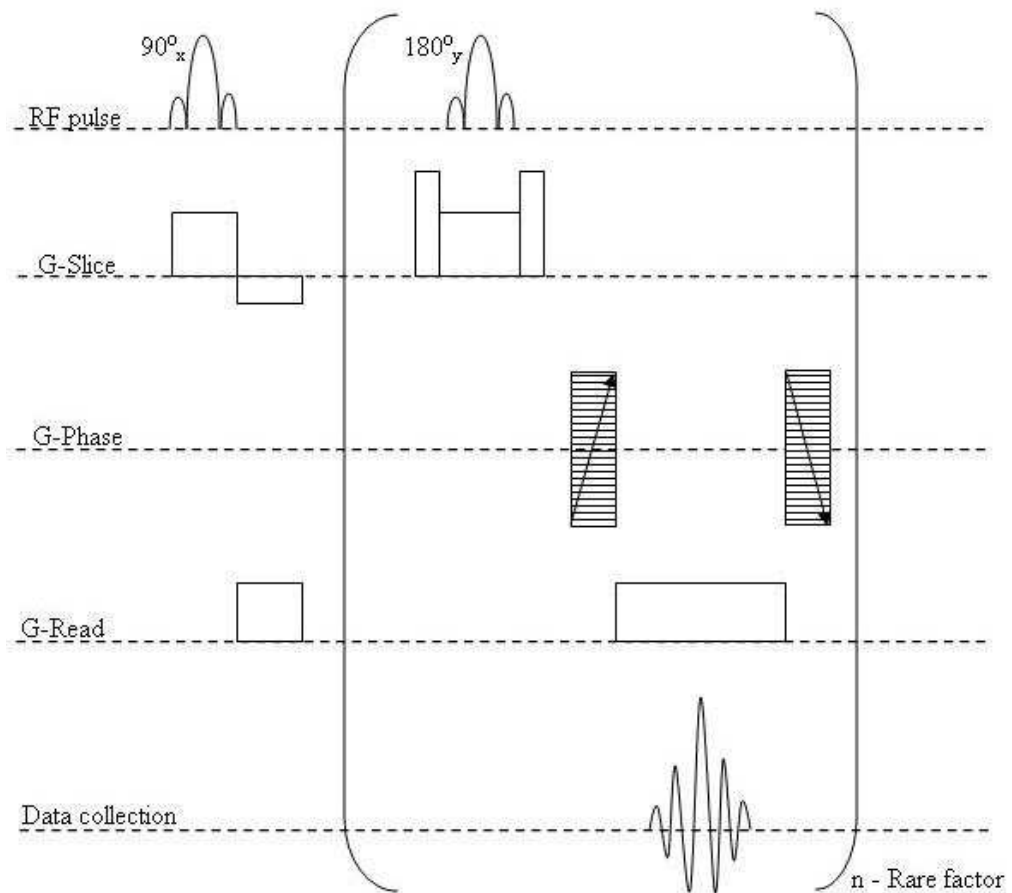


Figure 2.19. *RARE* pulse sequence diagram.

2.5 Contrast agents

Contrast agents have been developed to improve the potential of MRI in medical diagnostic imaging. For example to provide improved contrast in MR imaging of tumours, MR imaging of the breakdown of the blood brain barrier, cerebral blood volume (CBV), cerebral blood flow (CBF), MR angiography, and in quantitative assessment of tissue vascularity and myocardial perfusion, which are otherwise impossible to detect using standard T_1 or T_2 or proton density-weighted imaging (Tofts, 2004).

The presence of contrast agents that contain (super)paramagnetic ions will cause noticeable shortening of both (or either) spin-lattice relaxation time (T_1) and spin-spin relaxation time (T_2) of the surrounding ^1H nuclei. This creates distinguishable differences between tissues, as changes in T_1 and (or) T_2 alters the MR signal.

Paramagnetism generally involves the magnetism (magnetic moments of unpaired electrons) of small isolated ions (e.g. Gd^{3+} , Cu^{2+} , etc) that only behaves as local magnets in the presence of an external magnetic field. Superparamagnetism occurs when crystals (e.g. iron oxide) containing regions of unpaired spins are sufficiently large that they can be regarded as thermodynamically independent, single domain particles. These single domain particles are named magnetic domains. Such a magnetic domain has a net magnetic dipole that is larger than the sum of its individual unpaired electrons. In the absence of an external magnetic field, such magnetic domains are randomly oriented with no net magnetic field. An external magnetic field can cause the magnetic dipoles of the magnetic domains to reorient causing the resultant magnetic moments of such magnetic domains to be greater than that of a paramagnetic substance (Modo and Bulte, 2007).

2.5.1 Types of contrast agents

In general MRI contrast agents are divided into two types:

1. Positive contrast agents –which shorten the longitudinal relaxation time (T_1), and cause increased signal intensity in the region of interest in T_1 -weighted images.
2. Negative contrast agents –which shortens the transverse relaxation time (T_2), and cause decreased signal intensity in the region of interest in T_2 -weighted images.

Table 2.3 summarizes the contrast agents used in this research and their effect upon the longitudinal relaxation time, (T_1) and transverse relaxation time, (T_2) of the surrounding ^1H nuclei.

Contrast agent	Longitudinal relaxation time (T_1)	Transverse relaxation time (T_2)
Gd-DTPA	Shortens	Shortens
Iron oxide nanoparticles	Shortens	Shortens
Copper (Cu^{2+})	Shortens	Shortens

Table 2.3. The effect of contrast agents used in this research upon the longitudinal relaxation time (T_1) and transverse relaxation time (T_2) of the surrounding ^1H nuclei.

Gd-DTPA, a commonly used contrast agent in medical imaging, is a complex of gadolinium (a paramagnetic metal) with the chelating agent diethylenetriamine pentaacetic acid (see Fig. 2.20). Here the chelate complex is used to reduce the toxicity of Gd^{3+} and to tailor the magnetic property of the contrast agent by changing its molecular size and structure. The T_1 and T_2 relaxation times of ^1H nuclei are altered due to the fluctuating magnetic interactions between the electron spins of unpaired electrons of the Gd^{3+} metal ion and the spins of the ^1H nuclei. This interaction depends on the number of unpaired electrons of the metal ion, the proximity of water protons to the metal ion and the rate of tumbling motion of the contrast agent molecules. Similar to Gd-DTPA, Cu^{2+} also alters the T_1 and T_2 relaxation of water due to the interaction between its unpaired electrons and the nuclear spins of the ^1H of water molecules.

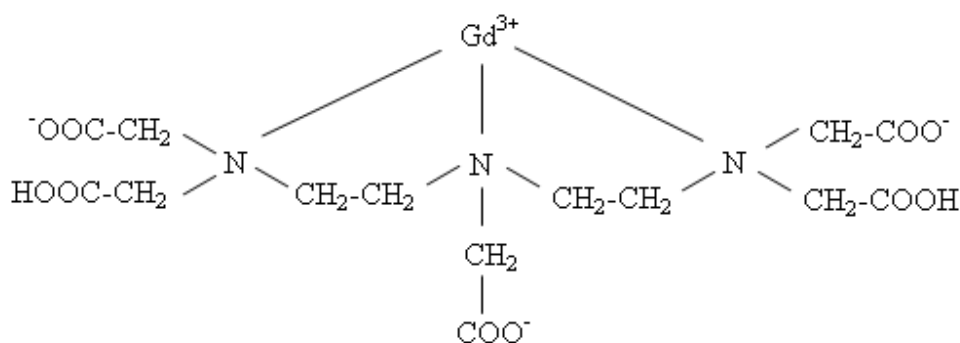


Figure 2.20. Illustrates the structure of the Gd-DTPA (reproduced from http://www.berlex.com/html/products/pi/Magnevist_PI.pdf).

Superparamagnetic nanoparticle contrast agents (e.g. *Molday ION*), shorten T_2 and T_2^* due to their large magnetic moment (Tromsdorf et al., 2007). The relaxation mechanism is related to spins (^1H nuclei) diffusing within the inhomogeneous magnetic field created by the magnetic

clusters of the nanoparticles (Morales et al., 2003). Molday ION™ is an ultra small (e.g. 30 nm in size) iron oxide-based superparamagnetic (USPIO) contrast agent (www.biopal.com). *Molday ION C6Amine* is engineered to have terminal amino groups with a size of ~35 nm, and a zeta potential of about 48 mV. *Molday ION Carboxyl* terminated is engineered to have terminal carboxyl group with a size of ~35 nm, and a zeta potential of about -38 mV.

Amino groups (-NH₂) are common functional groups and often become ionized by the addition of a hydrogen ion (H⁺), forming positively charged amino groups (NH₃⁺). Carboxyl groups are common functional groups and frequently ionize, releasing the H from the hydroxyl group as a free proton (H⁺), with the remaining O carrying a negative charge.

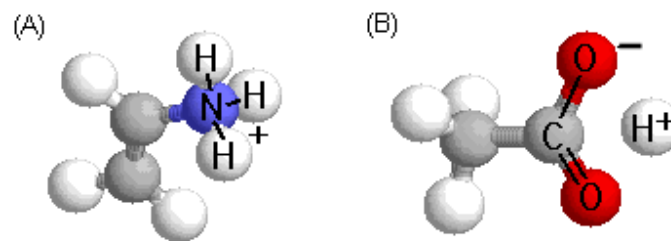


Figure 2.21. Schematic of (A) amine functional group and (B) carboxyl functional group.

The effect of contrast agent on MRI signal intensity is concentration dependent thus allowing us to quantify their concentrations as discussed below.

2.5.2 Quantitative concentration imaging

The presence of MRI contrast agent changes either the T_1 or T_2 relaxation time of the neighboring ¹H nuclei as mentioned above. The actual concentrations of the tracers can be determined, as changes in relaxation rates ($1/T_1$ or $1/T_2$) is linearly related to the concentration of the contrast agent as given in equation 32 (Haacke, 1999).

$$[C] = \left(\frac{1}{T_{1(2),i}} - \frac{1}{T_{1(2),0}} \right) \cdot \frac{1}{R}$$

Equation 32

where $T_{1(2),0}$ is the longitudinal (transverse) relaxation time in the absence of contrast agent, $T_{1(2),i}$ is the longitudinal (transverse) relaxation time in the presence of contrast agent, $[C]$ denotes the concentration of the contrast agent, and R is the relaxivity constant of the contrast agent.

Therefore, construction of spatially resolved T_1 or T_2 parameter maps during the transport of the contrast agent will reveal its transport through biofilms and packed columns. Collecting a T_1 or T_2 based image prior to the contrast agent uptake reveals the impact of properties of the biofilm or saturated packed column on either T_1 or T_2 depending on corresponding relaxation mechanisms (see table 2.1). Any subsequent change in T_1 or T_2 after the uptake of contrast agent can then be attributed to the effect of the contrast agent and used to quantify their spatially resolved concentrations inside biofilms and packed columns using calibration equation 32.

2.6 MRI hardware

This section will briefly introduce the different components of a MRI scanner and their functionality during an MR imaging experiment (Blumich, 2003, Levitt, 2008).

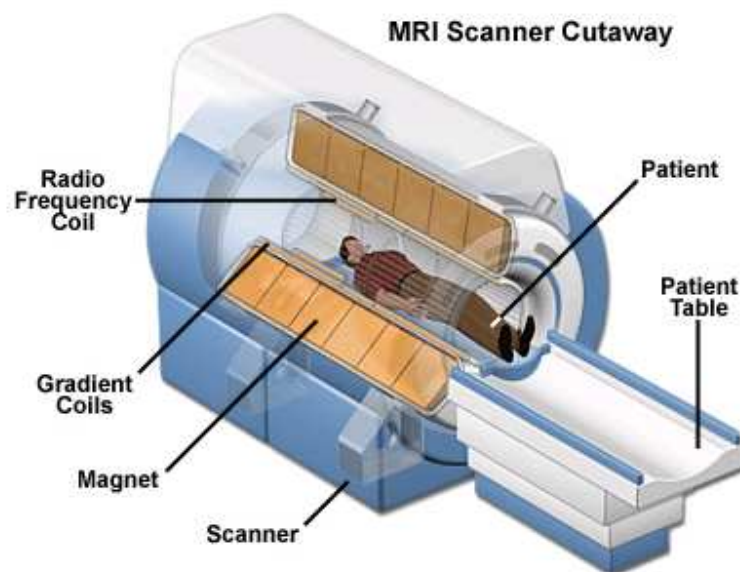


Figure 2.22. Main components of the MRI scanner (reproduced and edited from BIOE 414 Instrumentation Projects).

2.6.1 The main magnet

MRI experiments require a main static magnetic field, B_0 , as discussed in the previous sections. This magnetic field should be homogeneous and stable with time. The larger B_0 the greater the net magnetization and the larger the MR signal.

Superconducting coils are used to produce the main magnetic field. Once charged with current, superconductors allow the current to circulate for a very long time without loss; thus

creating a uniform magnetic field. Superconductor windings are cooled with liquid helium, He (at 4K, the boiling point of liquid He) in order to give negligible electrical resistance. The core of the magnet is known as the bore and samples are placed in the centre of this bore (iso-centre) to experience the largest and most homogeneous magnetic field.

2.6.2 Shim coils

The homogeneity of the main magnetic field inside the bore is altered by the magnetic susceptibility of the sample. Shim coils are additional sets of coils used to improve the homogeneity of the magnetic field over the sample. The homogeneity is optimised by adjusting the current sent through these shim coils.

2.6.3 Gradient coils

Pulsed field gradients are used to spatially encode the MR signal (see section 2.2). Magnetic field gradients are produced during an MRI experiment by applying direct current (dc) through specially designed coils known as gradient coils. Three gradient coils produce magnetic field gradients in x, y and z directions. In this research gradient inserts of (Bruker model BG-6) and (Bruker model BGA-20) were used with a 200-A gradient amplifiers to provide strong linear magnetic field gradient pulses of 1000 mT/m and 200 mT/m respectively.

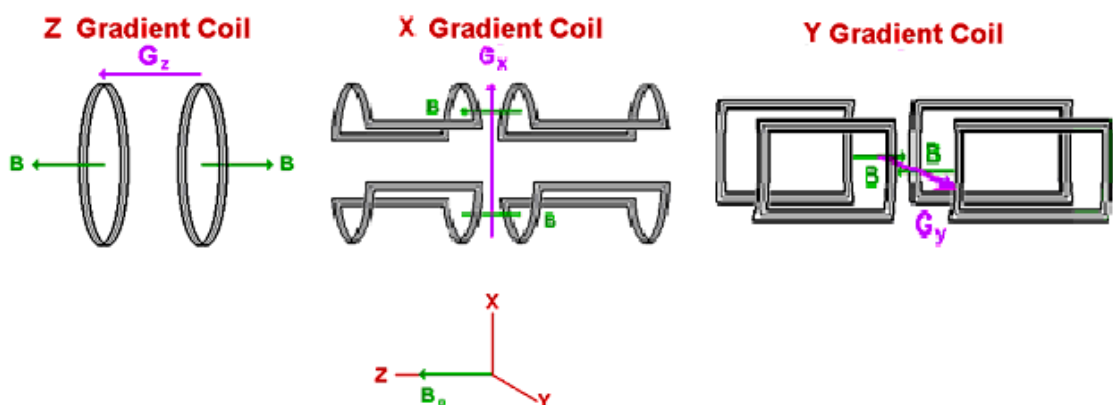


Figure 2.23. Schematic illustrations of coil arrangements used to create magnetic field gradients in x, y, and z directions (reproduced from Magnetic Resonance Imaging by Joseph P. Hornak - <http://www.cis.rit.edu/htbooks/mri/inside.htm>).

2.6.4 RF Coils

Radio frequency (RF) coils are used to produce pulses of RF radiation, these are used perturb (excite) the spin system. RF coils are also used to detect the MR signal. A single RF coil can

be used for both excitation and detection. In some cases different RF coils are used for excitation and detection separately, e.g. volume resonator for excitation with a surface coil for detection.

The oscillating magnetic field, B_1 , produced by the RF coils should be homogeneous and perpendicular to the main magnetic field. Bird cage type coils are commonly used RF coils. Microscopy coils such as solenoid, saddle and Helmholtz made up with simple loops can also be used for MR microscopy of small samples.

Figure 2.24 illustrates the components of a typical MRI scanner.

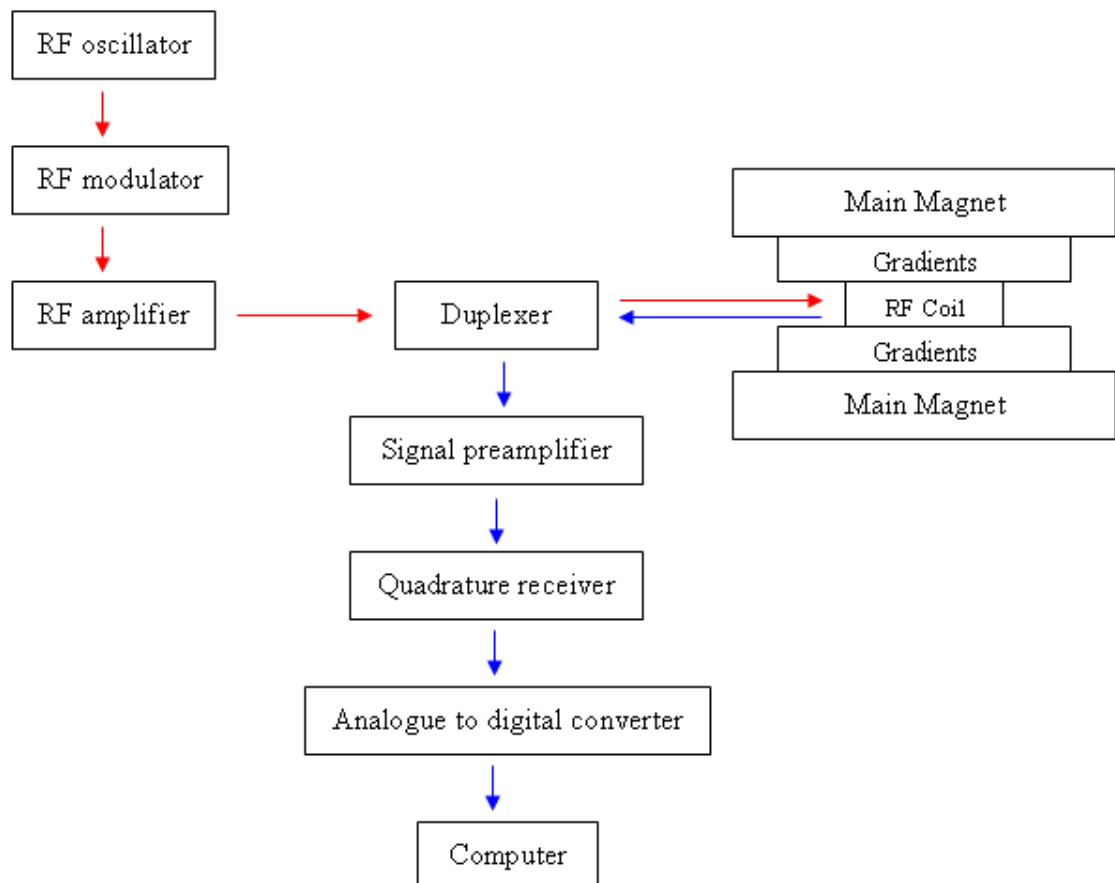


Figure 2.24. Schematic diagram of electronics involved in an MR image formation. Red and blue colour arrows indicate the transmitter and receiver sections respectively.

2.6.5 RF oscillator

RF oscillator produces an oscillating electrical signal at a well defined frequency; the radio frequency (RF) pulse.

2.6.6 RF modulator

The RF modulator is used to modulate the amplitude of RF pulses with time. Shaped RF pulses are used to selectively excite the spins inside a slice, leading to better defined slice profiles.

2.6.7 RF amplifier

RF amplifier amplifies the shaped RF pulse in order to produce large-amplitude RF pulse for transmission to the RF coil.

2.6.8 Duplexer

Duplexer executes two main tasks. It first directs the high power (amplified) RF pulse to the RF coil. The duplexer then directs the weak MR signal to the receiver section. Hence, the duplexer protects the sensitive electronics components in the receiver section from the high power (amplified) RF pulses generated in the transmitter and also sends the entire signal produced by the sample to the receiver section.

2.6.9 Signal preamplifier

The weak RF signal generated by the nuclear spins of the sample is directed towards a preamplifier by the duplexer in order to scale up to a convenient voltage level. Signal preamplifiers are always kept close to the main magnet in order to reduce any signal losses.

2.6.10 Quadrature receiver and analogue to digital converter

The quadrature receiver down converts the raw MR signal from its high frequency (e.g. 300 MHz) to a low value as Analogue to digital converter can only deal with low frequency signals. This is done by comparing the raw signal with a reference signal. Analogue to digital converter converts the analogue MR signal into digital form. This is then processed by the computer.

2.6.11 Computer

The computer system generally consists of an operator console enabling operator input, scan selection and pulse sequence selection. The computer is connected with the real time operating system to control gradients and control RF transmit and receive functions. The computer also handles image reconstruction.

2.7 References

- BLUMICH, B. (2003) *NMR imaging of materials* Clarendon Press.
- CALLAGHAN, P. T. (1993) *Principles of nuclear magnetic resonance microscopy*, Clarendon Press.
- FARRAR, T.C., AND E.D. BECKER (1971) *Pulse and Fourier Transform NMR: Introduction to Theory and Methods*, Academic Press.
- HAACKE, E. M., R. W. BROWN, M. R. THOMPSON, AND R. VENKATESAN (1999) *Magnetic Resonance Imaging: Physical principles and sequence design*, Wiley-Liss.
- HENNING, J., A. NAURTH, AND H. FRIEDBURG (1986) RARE Imaging: A Fast Imaging Method for Clinical MR. *Journal of Magnetic Resonance in Medicine*, 3, 823-833.
- LEVITT, M. H. (2008) *Spin dynamics: Basics of nuclear magnetic resonance*, Wiley-Blackwell.
- MODO, M. J., and J. W., BULTE (2007) *Molecular and cellular MR imaging*. CRC Press.
- MORALES, M. P., BOMATI-MIGUEL, O., DE ALEJO, R. P., RUIZ-CABELLO, J., VEINTEMILLAS-VERDAGUER, S. & O'GRADY, K. (2003) Contrast agents for MRI based on iron oxide nanoparticles prepared by laser pyrolysis. *Journal of Magnetism and Magnetic Materials*, 266, 102-109.
- TOFTS, P. (2004) *Quantitative MRI of the brain: Measuring changes caused by disease* Wiley-Blackwell.
- TROMSDORF, U. I., BIGALL, N. C., KAUL, M. G., BRUNS, O. T., NIKOLIC, M. S., MOLLWITZ, B., SPERLING, R. A., REIMER, R., HOHENBERG, H., PARAK, W. J., FORSTER, S., BEISIEGEL, U., ADAM, G. & WELLER, H. (2007) Size and surface effects on the MRI relaxivity of manganese ferrite nanoparticle contrast agents. *Nano Letters*, 7, 2422-2427.

Chapter 3

Application of paramagnetically tagged molecules
for magnetic resonance imaging (MRI) of
biofilm mass transport processes

3

Application of paramagnetically tagged molecules for magnetic resonance imaging (MRI) of biofilm mass transport processes

3.1 Summary

Molecules become readily visible to MRI when labelled with a paramagnetic tag. Consequently, MRI can be used to image their transport through porous media. In this study, we demonstrated that this method could be applied to imaging mass transport processes in biofilms. The transport of Gd-DTPA, a commercially available paramagnetic molecule, was imaged in both agar (as a homogeneous test system) and in a phototrophic biofilm. The images collected were T_1 -weighted, where T_1 is a MRI property of the biofilm and is dependant on Gd-DTPA concentration. A calibration protocol was applied to convert T_1 parameter maps into concentration maps, thus revealing the spatially resolved concentration of this tracer at different time intervals. Comparing the data obtained from the agar and the phototrophic biofilm experiments with simple diffusion models revealed that mass transport of Gd-DTPA in agar was purely via diffusion with a diffusion coefficient of $7.2 \times 10^{-10} \text{ m}^2 \text{ s}^{-1}$ while its was transported inside the *Phormidium* biofilm by both diffusion and advection with an equivalent transport rate of $1.04 \times 10^{-9} \text{ m}^2 \text{ s}^{-1}$. This technology can be used to explore further mass transport processes in biofilms, either using the wide range of commercially available paramagnetically tagged molecules and nanoparticles, or by using bespoke tagged molecule.

3.2 Introduction

Most MRI procedures utilize the ^1H nuclear magnetic resonance (NMR) signal because H_2O is dominant in biological systems and the ^1H nucleus gives the largest NMR signal. This, however, means that mass transport analysis in biofilms is almost exclusively limited to water which is present in sufficient concentrations (Lens et al., 1999, Wieland et al., 2001). For other

molecules, mass transport analysis is exceptionally difficult due to their much lower concentration which inhibits detection. Fortunately, water diffusivity can be used as a proxy for determining diffusivities of other low molecular mass molecules as there is a close relationship between the diffusivities of water and low molecular mass molecules (Beuling et al., 1998, Vogt et al., 2000, Wieland et al., 2001). However as molecular mass increases, their diffusion coefficients compared to water differ by orders of magnitude and water diffusivity becomes an increasingly less reliable proxy.

Macromolecules (compounds ranging from 1 kDa to hundreds of nanometers) cannot be ignored as they contribute significantly to the pollutant load of wastewater and natural aquatic systems (Logan and Qing, 1990). Consequently, we must pursue alternative ways of determining mass transport of these important larger molecules by MRI.

The aim of this study is to demonstrate this can be achieved by using molecules labelled with a paramagnetic metal ion (e.g. Gd^{3+}). Molecules labelled with paramagnetic metals are readily visible to MRI and thus should enable, in-vivo, in-situ and in real time imaging of the transport of those macromolecules throughout a biofilm. This technology is already heavily utilized in medical diagnostic methods as described in section 2.5.

In this study, a complex of gadolinium (paramagnetic metal) with a chelating agent diethylenetriamine penta-acetic acid (Gd-DTPA) was used. This is a commonly used clinical MRI contrast agent. Not only does this agent provide strong contrast and is thus easy to image, it is also an exceptionally stable complex [log stability constant $K = 20.5$; (Schmitt-Willich et al., 1999)] and hence will not dissociate within the biofilm. Indeed, this high stability enables medical practitioners to inject Gd-DTPA into the human body without fear that the molecule will break down and release toxic Gd^{3+} . It is also one of the simplest commercially available paramagnetic complexes and one which is commonly used to tag other larger molecules.

The presence of Gd labelled molecules, such as Gd-DTPA at any point inside a biofilm will cause noticeable shortening of spin lattice relaxation time (T_1) of surrounding 1H nuclei because of the dipole-dipole interaction between the seven unpaired electrons of the Gd^{3+} and the single proton of the hydrogen nuclei. Therefore, construction of spatially resolved T_1 parameter maps during the mass transport of the Gd labelled molecules reveals their movement through the biofilm. Moreover, the actual concentrations of the tracers can be determined as changes in longitudinal relaxation rate ($1/T_1$) have a linear relationship with the

concentration of the Gd labelled molecule (6, 27, 38). Consequently, the effect of the paramagnetic label upon the MRI signal enables us to not only image the transport of these molecules but also to spatially quantify their concentration in real time. Moreover, this molecule can be used to label larger complexes, and thus construct a range of paramagnetic macromolecules of different masses and reactivities. These bespoke molecules can then be used to explore the impact of such physicochemical parameters upon their transport inside biofilms, as macromolecules and nanoparticles contribute significantly to the pollutant load of wastewater and natural aquatic systems (Logan and Qing, 1990).

A laboratory grown 1-cm thick phototrophic biofilm (composed of the cyanobacteria *Phormidium* sp. strain PP03) was utilised in this study. This was chosen as a simple model biofilm as *Phormidium* biofilm readily grows in the laboratory and phototrophic biofilms of this thickness occur in the natural environment. Phototrophic biofilms also have potential applications in wastewater treatment, bioremediation and biofuel production (Roeselers et al., 2008).

The aim of this first study is to demonstrate the suitability of using paramagnetically tagged molecules for tracing mass transport in biofilms, and hence it's potential for mass transport analysis of a diverse range of mid to high molecular mass molecules and nanoparticles within biofilm structures. Prior to applying this technology to the *Phormidium* biofilm, the technique was applied and validated with a simple system where the transport rate (diffusion coefficient) of Gd-DTPA was quantified inside an 'artificial biofilm' composed simply of agar. The time varying concentration profiles in agar were fitted to the solution of the one dimensional diffusion equation to see if they were consistent with diffusive transport. Moreover, the results from the *Phormidium* biofilm experiment were compared with a simple two dimensional model.

3.3 Materials and methods

3.3.1 Agar and phototrophic biofilm

The artificial biofilm was made up of agar (1.5%). Molten agar was poured into a modified 30ml plastic syringe and allowed to cool such that it produced an agar tube with approximate semi-circular cross-section (see Fig. 3.1).

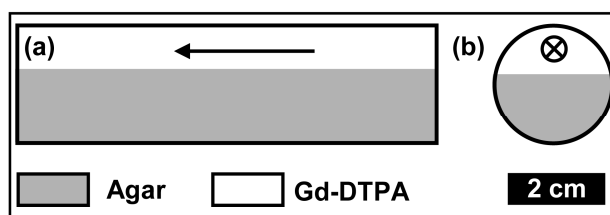


Figure 3.1. Schematic of the flow cell containing agar. Cross sections are (a) along the flow cell and (b) across the flow cell.

The phototrophic biofilm used in this study was 1-cm thick and composed of the cyanobacteria *Phormidium* sp. (strain PP03) from the culture collection of V.R. Phoenix (Phoenix and Holmes, 2008). This phototrophic biofilm was grown in the laboratory in a tray containing BG11 +N liquid media (Rippka et al., 1979) to a depth of 3 cm. This was inoculated with *Phormidium* and placed on a rocking machine at 10 rpm. This was then kept in an incubator and maintained at 28° C, with a constant light intensity of 25 $\mu\text{mol m}^2 \text{s}^{-1}$.

3.3.2 Flow System

During the agar experiment the flow cell containing the agar was positioned inside the MRI bore. The flow cell containing the agar was first connected via silicon tubing to an 18 M Ω water supply and slowly washed with ultrapure water at a flow rate of 2 ml min⁻¹ using a peristaltic pump (see Fig. 3.1). The system was then connected to a 4-liter reservoir of a 1.8 mM Gd-DTPA (molecular mass 547g mole⁻¹; Sigma Aldrich) solution and the solution was pumped through the flow cell at a rate of 2 ml min⁻¹.

During the phototrophic biofilm experiment the *Phormidium* biofilm was carefully positioned in a custom made circular 2.2 cm diameter plastic flow cell with special gasket arrangement such that only the top surface of the biofilm was in contact with the flowing solution. This ensured that transport of Gd-DTPA into the biofilm could only take place from top to bottom of the biofilm (see Fig. 3.2). The flow cell was then positioned inside the MRI bore. Here also the flow cell containing the phototrophic biofilm was first connected via the silicon tubing to an 18 M Ω water supply and slowly washed with ultrapure water. The system was then connected to a 4-liter reservoir of a 5 mM Gd-DTPA solution, which was pumped over the biofilm at a rate of 2 ml.min⁻¹.

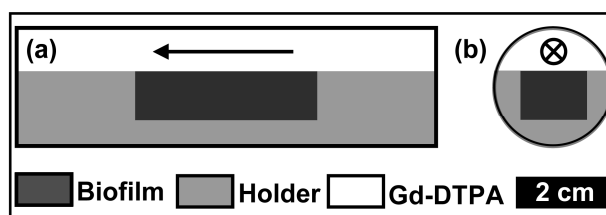


Figure 3.2. Schematic of the flow cell containing *Phormidium* biofilm. Cross sections are (a) along the flow cell and (b) across the flow cell.

3.3.3 MRI

The MRI experiments were performed on a Bruker Avance BioSpec system, using a 30-cm-bore, 7T superconducting magnet (Bruker BioSpec, Karlsruhe, Germany). A Bruker microimaging gradient insert (model BG-6) and 200-A gradient amplifiers were used to provide strong linear magnetic field gradient pulses of up to $1,000 \text{ mT m}^{-1}$, thus allowing the system to perform microimaging experiments. A Bruker 35 mm diameter birdcage RF volume resonator was used to excite and detect the ^1H signal.

Here, MR imaging was used to measure spatially and temporally resolved T_1 values of both agar and *Phormidium* biofilm while Gd-DTPA was transported through these systems. The T_1 value at different biofilm locations is influenced by a number of factors, including biofilm composition, water content, and concentration of paramagnetic ions (Gd-DTPA). Collecting a T_1 -based image of the biofilm prior to Gd-DTPA uptake reveals the impact of biofilm composition and water content on T_1 . The change in T_1 upon Gd-DTPA uptake is then known to be solely due to the Gd-DTPA. Thus, T_1 values can be used to determine concentrations of Gd-DTPA. First, T_1 -weighted images were measured at five different excitation pulse flip angles which highlight only T_1 image contrast. They were then used for calculation of T_1 parameter maps where the image intensity is the actual T_1 value. These parameter maps were then used to obtain quantitative images of Gd-DTPA concentration.

3.3.4 Acquisition of T_1 -weighted images

The transport of Gd-DTPA inside both agar and *Phormidium* biofilm was imaged by acquisition of T_1 -weighted images in the axial plane by using a 2-D Gradient Echo pulse sequence, FLASH (Brookes et al., 1999 and Haacke, 1999). Images were obtained across the samples, with a slice thickness of 1 mm. Both agar and *Phormidium* biofilm experiments were performed with imaging parameters, echo time (TE) of 4 ms and repetition times (TR) of 75 ms for agar and 20 ms for biofilm. The field of view was 3 cm by 3 cm, using an imaging

matrix of 200 by 200 pixels, giving an in-plane resolution of 150 μm by 150 μm . During both experiments T_1 -weighted images were acquired at five different excitation pulse flip angles (10°, 20°, 40°, 60° and 90°). Imaging time at each flip angle was approximately 18 seconds, using a single signal average.

3.3.5 Calculation of T_1 parameter maps

In a gradient echo pulse sequence the local signal intensity is given by (Haacke, 1999);

$$S_{(t)} = S_{0(t)} \frac{1 - e^{-TR/T_1}}{1 - \cos \alpha \cdot e^{-TR/T_1}} e^{-TE/T_2^*} \sin \alpha$$

Equation 1

where $S_{0(t)}$ is the available maximum signal intensity, α is the flip angle of the excitation pulse; TR denotes the repetition time (the time interval between two successive excitation pulses), TE is the echo time (the time interval between the excitation and signal readout centre), T_1 is the longitudinal relaxation time, and T_2^* is the apparent transverse relaxation time.

In equation 1, the term e^{-TE/T_2^*} is considered constant, since TE was a predefined constant throughout the experiment and T_2^* was assumed constant for a particular pixel at a particular time interval. Consequently equation 1 can be reduced as given below,

$$S_{(t)} = K \sin \alpha \frac{1 - e^{-TR/T_1}}{1 - \cos \alpha \cdot e^{-TR/T_1}}$$

Equation 2

where, K is a constant which includes the terms $S_{0(t)}$ and e^{-TE/T_2^*} .

T_1 parameter maps were calculated from the series of five T_1 -weighted images which were acquired at different flip angles (10°, 20°, 40°, 60°, 90°) (see Fig. 3.3A). For each image pixel, the MRI signal intensities, $S_{(t)}$, at different flip angles were fitted to equation 2 using a non-linear least square algorithm (see Fig. 3.3B). This procedure estimates the values for the parameters K and T_1 of that pixel. This procedure was applied to estimate the T_1 value of every pixel within the slice (2D image) (see Fig. 3.3C)

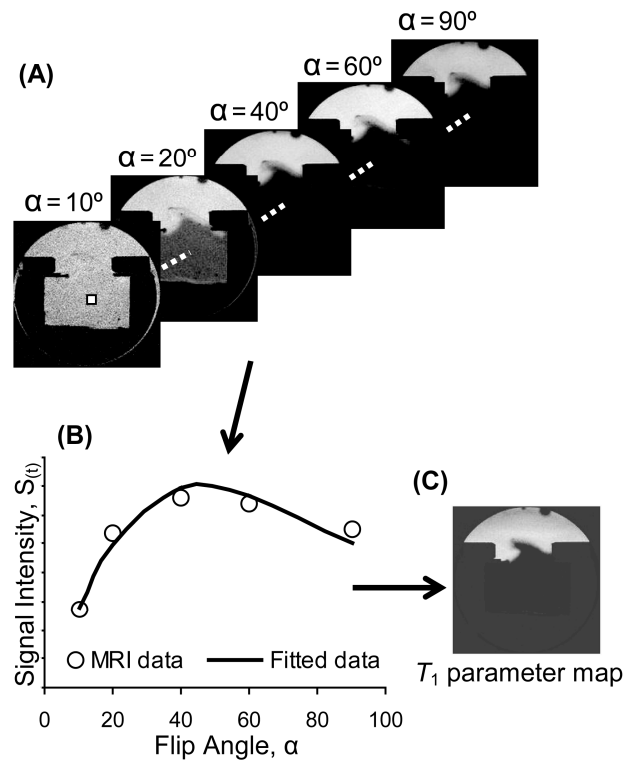


Figure 3.3. (A) For the slice across the biofilm T_1 -weighted images are acquired at five different flip angles. (B) For each pixel, the variation of signal intensity, $S(t)$ with respect to flip angle, α was fitted to the equation 2, giving a T_1 value. (C) Taking the T_1 value of each pixel yields a T_1 parameter map.

3.3.6 Calibration of Gd-DTPA concentrations from T_1 parameter maps

The presence of paramagnetic metal, such as gadolinium, causes a concentration dependent reduction in T_1 . The effect of paramagnetic ions, such as Gd^{3+} (in Gd-DTPA) on the relaxation time of water ^1H is represented by the equation (Stanisz and Henkelman, 2000, Phoenix and Holmes, 2008).

$$[C] = \frac{1}{R} \left\{ \frac{1}{T_{1i}} - \frac{1}{T_{10}} \right\}$$

Equation 3

where T_{10} is the relaxation time in the absence of Gd-DTPA, T_{1i} is the relaxation time in the presence of Gd-DTPA, $[C]$ denotes the concentration of the Gd-DTPA, and R is the relaxivity constant of the Gd-DTPA.

In the current study, T_{10} and T_{1i} are known variables, as they are taken directly from T_1 parameter maps. R , however, is unknown and must be separately determined in order to quantify the concentration measurements.

3.3.7 Determination of relaxivity constant (R) of Gd-DTPA in agar and *Phormidium* biofilm

Recent investigations show, when changes in the T_1 relaxation times are used to quantify the available Gd-DTPA concentrations, the R value of Gd-DTPA depends on the solids content of the sample, with R increasing approximately linearly as solids content increases (Phoenix and Holmes, 2008, Stanisiz and Henkelman, 2000).

Thus, the effect of solids content on Gd-DTPA relaxivity in a *Phormidium* biofilm was investigated. Here, biofilm samples were prepared at four different solid contents by mixing the same amount of biofilm with four different volumes of Gd-DTPA solutions. At each solid content six different samples were made with known Gd-DTPA concentrations (ranging from 0 to 5mM). T_1 values of all samples were measured. Then, plots of $1/T_{1i}$ versus Gd-DTPA concentration were made for samples with similar solid content, and the R values for each solid content was determined by fitting equation 3 to their data using linear least squares method. The percentages of the solids contents of all standards were determined by weighing the mixtures before and after drying to a constant weight at 60° C. Then R values were plotted against solids content and the linear relationship between R and solids content was determined by fitting the data using linear least squares method. At the end of the Gd-DTPA transport experiment, the solids content of the *Phormidium* biofilm was determined by weighing before and after drying the sample to a constant weight at 60° C. The appropriate R value corresponding to its solids content was then determined from the R versus solids content relationship described above. This R value was used in equation 3 to calculate the Gd-DTPA concentrations inside the biofilm from the MRI data collected during the Gd-DTPA transport experiment. This way of estimating the R value of the Gd-DTPA in the experimented biofilm enables the use of a value for R related to the solids content of the biofilm, thus giving a more accurate measurement of Gd-DTPA concentration.

In order to estimate the R value of Gd-DTPA inside the artificial biofilm (agar), agar samples were prepared with five different known concentrations of Gd-DTPA. Then, $1/T_{1i}$ values were plotted against the concentration of Gd-DTPA and R value was estimated by fitting equation 3 to the data using linear least squares method.

3.3.8 Estimating the diffusion coefficient of Gd-DTPA inside agar

Concentration profiles along a straight line through the centre of the flow cell (Fig. 3.6F) were extracted from the data at six discrete points in time (3, 13, 23, 33, 43 and 53 minutes) during the first hour of the experiment. After 1 hour the Gd-DTPA has only penetrated the upper layers of the agar. Therefore, if diffusive transport dominates then the effect of the flow cell boundaries and the irregular domain will be negligible on these central concentration profiles. This would mean that diffusion could be represented by a one dimensional model of Fickian diffusion. To test this we compared the profiles to the solution of the diffusion equation for a semi-infinite one dimensional domain (Crank, 1979). If the concentration on the upper boundary of the agar is assumed to be constant through time ($C = C_0$) and the initial concentration in the remainder of the domain is zero, then the solution is given by

$$C(x,t) = C_0 \operatorname{erfc}(x / \sqrt{4D_{dif}t})$$

Equation 4

where erfc is the complementary error function, D_{dif} is the diffusion coefficient of Gd-DTPA inside agar and t is time. Non-linear least squares fitting of the data to this model allowed the diffusion coefficient to be calibrated.

3.3.9 Modelling the mass transport process of Gd-DTPA inside the *Phormidium* biofilm

To determine whether the concentration profiles of Gd-DTPA measured using MRI were commensurate with purely diffusion driven transport they were compared with those simulated for a mathematical model of diffusion. The morphology of the surface of the biofilm is variable in space and, therefore, it is not possible to represent the transport by a one dimensional diffusion equation. However, there is a degree of symmetry in the shape of the biofilm surface along the axis of flow enabling us to use a two dimensional diffusion model. A two dimensional finite element model for diffusion into the biofilm was implemented using COMSOL Multiphysics (3.4). Diffusion was simulated within the biofilm, the domain Ω shown in figure 3.4, which was determined from the MRI images (Fig. 3.8A). The boundary of the domain was split into two parts (Fig. 3.4) so that $\partial\Omega = \Gamma_1 \cup \Gamma_2$ where Γ_1 is the top surface of the biofilm and Γ_2 includes the walls of the plastic holder and the surfaces of the gaskets inside which biofilm was placed. The concentration of Gd-DTPA in the bulk liquid and hence on the boundary Γ_1 was assumed to be a constant, C^* , through time. No transport was permitted through walls and gasket boundaries, Γ_2 .

Hence the model was defined by;

$$\frac{\partial C(x, y)}{\partial t} = \nabla \cdot (D_{dif} \nabla C(x, y)) \quad x, y \in \Omega$$

Equation 5

$$C(x, y) = C^* \quad x, y \in \Gamma_1$$

Equation 6

$$\frac{\partial C(x, y)}{\partial \bar{n}} = 0 \quad x, y \in \Gamma_2$$

Equation 7

where \bar{n} is the vector normal to the boundaries (Γ_2) and D_{dif} is the diffusion coefficient, which we assume to be constant in time and space. The concentration in the bulk liquid, C^* was 5 mM. For the purposes of the model, the diffusion coefficient was initially assumed to be the same as that calculated for the agar ($7.2 \times 10^{-10} \text{ m}^2 \text{ s}^{-1}$) as both agar and biofilm exhibit very similar solids contents (see sections 3.4.2 and 3.4.3).

The same model was then used to estimate the diffusion coefficient of Gd-DTPA inside biofilm. Here the diffusion coefficient was calibrated using a golden search algorithm in MATLAB, which called the COMSOL model as a subroutine. The objective function was the sum of square errors between observed and simulated concentrations and an optimum diffusion coefficient was estimated at the minimum value of this objective function. The model was undertaken purely for comparative purposes, to determine if transport was dominated by diffusion and to highlight any deviations from diffusion to help evaluate the MRI measurements. I did not develop the complexity of the model further here as this is beyond the scope of this chapter.

3.3.10 Visualization of structural complexity of *Phormidium* biofilm using freeze-substitution TEM

The structural complexity of the *Phormidium* biofilm, such as the presence of EPS and compactness of the filaments, were investigated using freeze-substitution transmission electron microscopy (TEM), with samples prepared by the freeze-substitution method (Tetley et al., 1998). Unlike processing the samples for TEM at room temperature, processing them with the freeze-substitution technique better preserves their structural information (Hunter and Beveridge, 2005).

Note: biofilm sample preparation using freeze-substitution technique and TEM imaging of the

biofilm were done by Dr. Laurence Tetley and Ms. Margaret Mullen of Integrated Microscopy Facility, University of Glasgow.

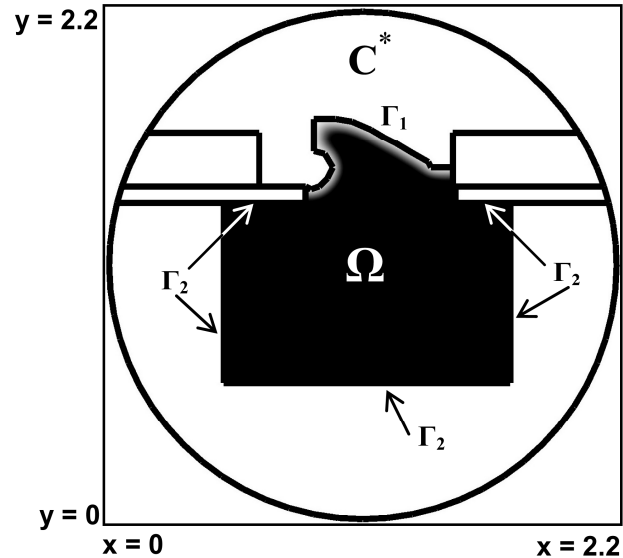


Figure 3.4. Illustration of the two dimensional model of *Phormidium* biofilm constructed using COMSOL Multiphysics. Dimensions are in centimeters

3.4 Results

3.4.1 Relaxivity constant (R) of Gd-DTPA inside agar

The variation of measured T_{1i} ($1/T_{1i}$) values of agar samples with respect to the Gd-DTPA concentrations is shown in Fig. 3.5A. The relaxivity value of Gd-DTPA inside agar was estimated as $3.4 \text{ s}^{-1} \text{ mM}^{-1}$ (with 95% confidence interval of $2.9 - 3.9 \text{ s}^{-1} \text{ mM}^{-1}$) by fitting the data to equation 3.

3.4.2 Relaxivity constant (R) of Gd-DTPA inside *Phormidium* biofilm

The variation of relaxivity of Gd-DTPA with respect to the solids content of the *Phormidium* biofilm is shown in figure 3.5B. A linear least squares fit to this data gives,

$$R = 1.71S + 6.53$$

Equation 8

where S is the solid content of the biofilm. The 95% confidence intervals for both gradient and intercept of equation 8 are (0.1 and 3.4) and (3.2 and 9.8) respectively. The solid content of the actual biofilm sample used during the flow through experiment was measured to be 1.2% and from the above given linear relationship (equation 8) the R value of that biofilm sample was

estimated as $8.58 \text{ s}^{-1} \text{ mM}^{-1}$. This was then used in equation 3 to determine Gd-DTPA concentration inside the biofilm.

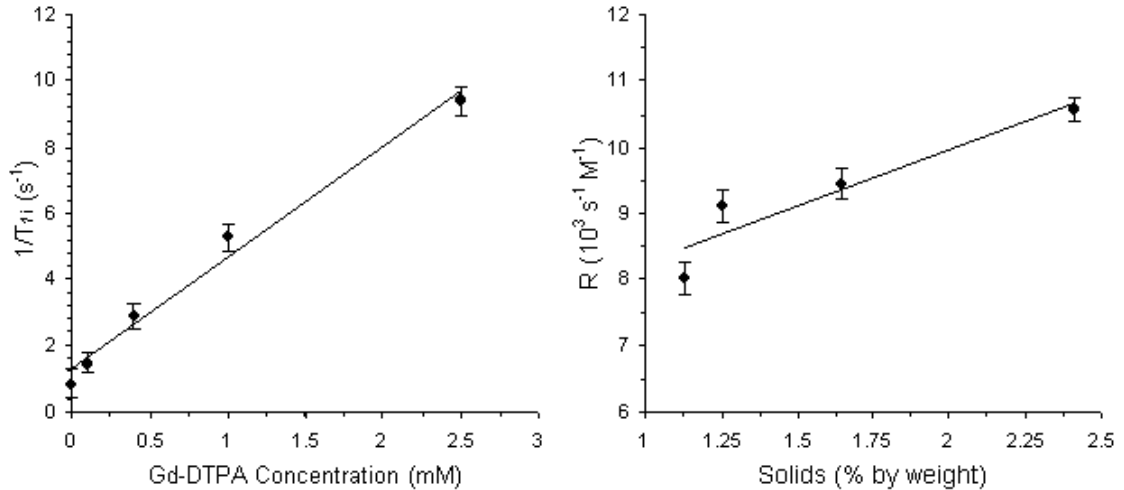


Figure 3.5. (A) Variation of $(1/T_{1i})$ values with respect to Gd-DTPA concentration inside agar samples. (B) Variation of Gd-DTPA relaxivity with respect solids contents of several *Phormidium* biofilm samples.

3.4.3 Diffusion of Gd-DTPA inside agar

In order to test the validity of this MRI method for imaging transport in biofilms, transport of Gd-DTPA in a simpler 1.5% agar test system was imaged. The transport of Gd-DTPA into the agar was recorded by T_1 -weighted images acquired (with a 40° flip angle) at time intervals of 23, 48, 73, 98, and 123 min, as shown in figure 3.6A to E. The transport of Gd-DTPA is shown by the expansion of the brighter region into the agar, as diffusing Gd-DTPA molecules shortens the T_1 value of the surrounding ^1H nuclei, hence increasing the measured MRI signal, which is shown brighter in a T_1 -weighted image.

As the actual concentration of Gd-DTPA is linearly related to the changes in $1/T_1$ values, the calibration protocol (equation 3) was then used to convert the T_1 parameter maps into actual Gd-DTPA concentration maps at time intervals of 23, 48, 73, 98, and 123 min, as shown in figure 3.6F to J. Again, the expansion of the brighter region into the biofilm shows the transport of Gd-DTPA. Concentration profiles along the transect shown by the white line (Fig. 3.6F) at time intervals of 3, 23, 53, and 103 min are shown in figure 3.7A.

By inspecting equation 4 it can be seen that if diffusive transport dominates then if concentrations along the same transect are plotted against the variable, x/\sqrt{t} all of the profiles should collapse onto a single curve. It can be seen from Fig. 3.7B that this is indeed

the case, suggesting that Gd-DTPA was transported by diffusion. The theoretical curve (equation 4) was fitted to the observed using non-linear least squares method and the best fitting diffusion coefficient of Gd-DTPA inside agar was $7.2 \times 10^{-10} \text{ m}^2 \text{ s}^{-1}$. This gave an excellent (R^2) goodness-of-fit value of 0.97 (with 95% confidence interval of 7.0×10^{-10} - $7.4 \times 10^{-10} \text{ m}^2 \text{ s}^{-1}$). The points with zero concentration that do not fit the trend observed on figure 3.7B correspond to the data points with zero concentration on figure 3.7A. These zero concentration points may reflect error in the concentration calibration

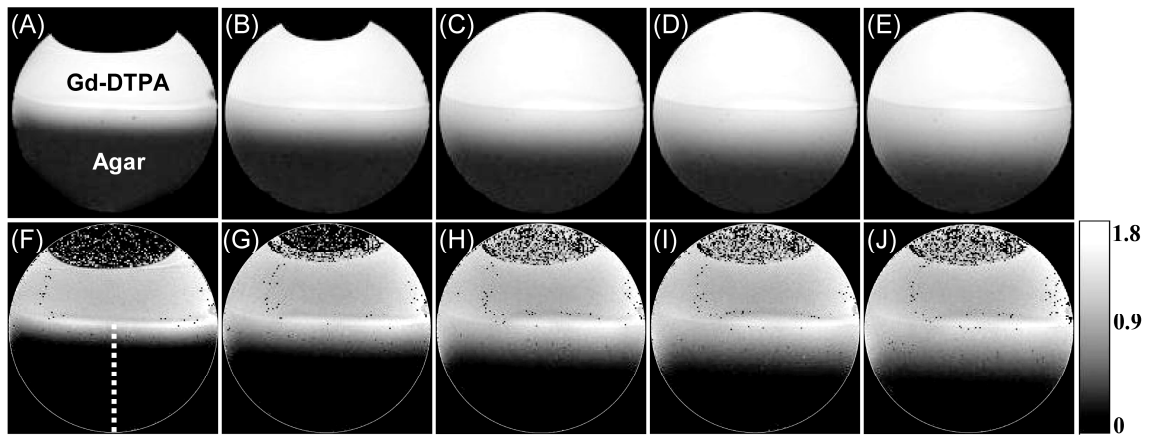


Figure 3.6. Diffusion of Gd-DTPA into agar was recorded by T_1 weighted images acquired at 40° flip angle (A-E) and the calibration protocol (equation-3) was then used to convert the T_1 parameter maps into actual Gd-DTPA concentration maps (F-J) at time intervals of 23, 48, 73, 98 and 123 minutes. The grey scale indicates the Gd-DTPA concentrations (mM) inside agar.

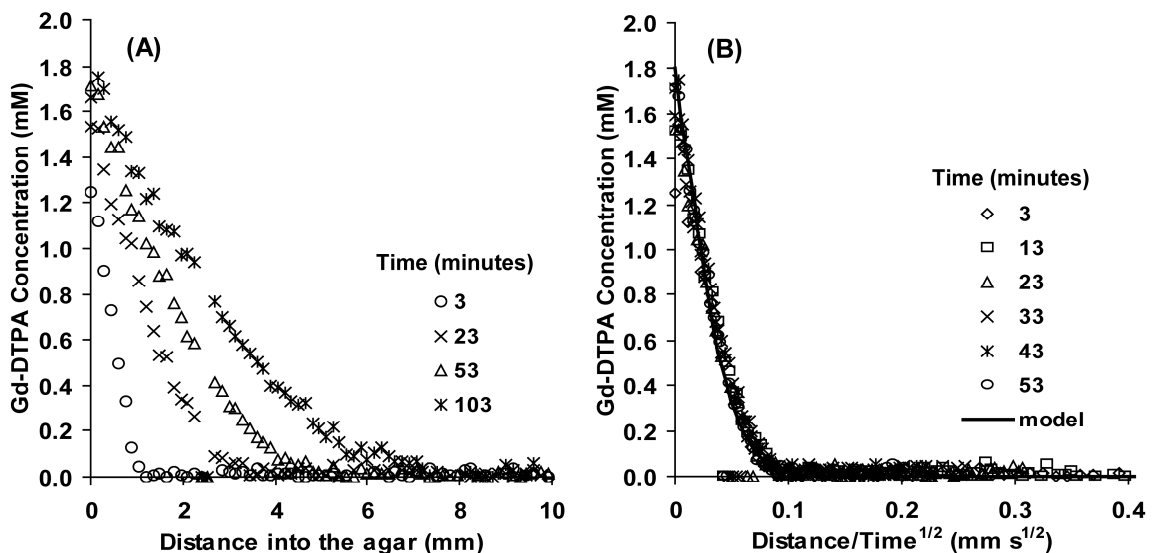


Figure 3.7. (A) Calibrated Gd-DTPA concentrations at time intervals of 3, 23, 53 and 103 minutes along the transect shown by the white line in Fig. 3.6F. (B) Calibrated Gd-DTPA concentration profiles during the first hour of the experiment (3, 13, 23, 33, 43 and 53 minutes), plotted against distance/ $\sqrt{\text{time}}$ and curve fitted to the solution of the Fickian one dimensional diffusion equation to determine the diffusion coefficient of Gd-DTPA inside agar.

3.4.4 Transport of Gd-DTPA into the *Phormidium* biofilm

The transport of Gd-DTPA into the *Phormidium* biofilm was recorded by T_1 -weighted images acquired (with a 40° flip angle) at time intervals of 2, 22, 72, 122 and 172 minutes as shown in Fig. 3.8A to E. Again, the transport of Gd-DTPA is shown by the expansion of the brighter region into the biofilm.

The calibration protocol was then used to convert the T_1 parameter maps into actual Gd-DTPA concentration maps at time intervals of 2, 22, 72, 122 and 172 minutes as shown in figure 3.8F to J. Again, the expansion of brighter region into the biofilm shows the transport of Gd-DTPA. Figure 3.8K to O shows the two dimensional model generated using a diffusion coefficient of $7.2 \times 10^{-10} \text{ m}^2 \text{ s}^{-1}$, the value calibrated from for diffusive transport through agar. Figure 3.9A shows the comparison of concentration profiles of experimental data along the transect shown in white line in Fig. 3.8F with model data along the same transect Fig. 3.8K. The model using the diffusion coefficient from agar shows slightly slower transport than the experimental data, indicating that transport of Gd-DTPA in the biofilm is faster than in agar. When the model was calibrated using concentration profiles of Gd-DTPA in biofilm, the best fit ($R^2 = 0.92$) was achieved with a diffusion coefficient of $1.04 \times 10^{-9} \text{ m}^2 \text{ s}^{-1}$ as shown in Fig. 3.9B.

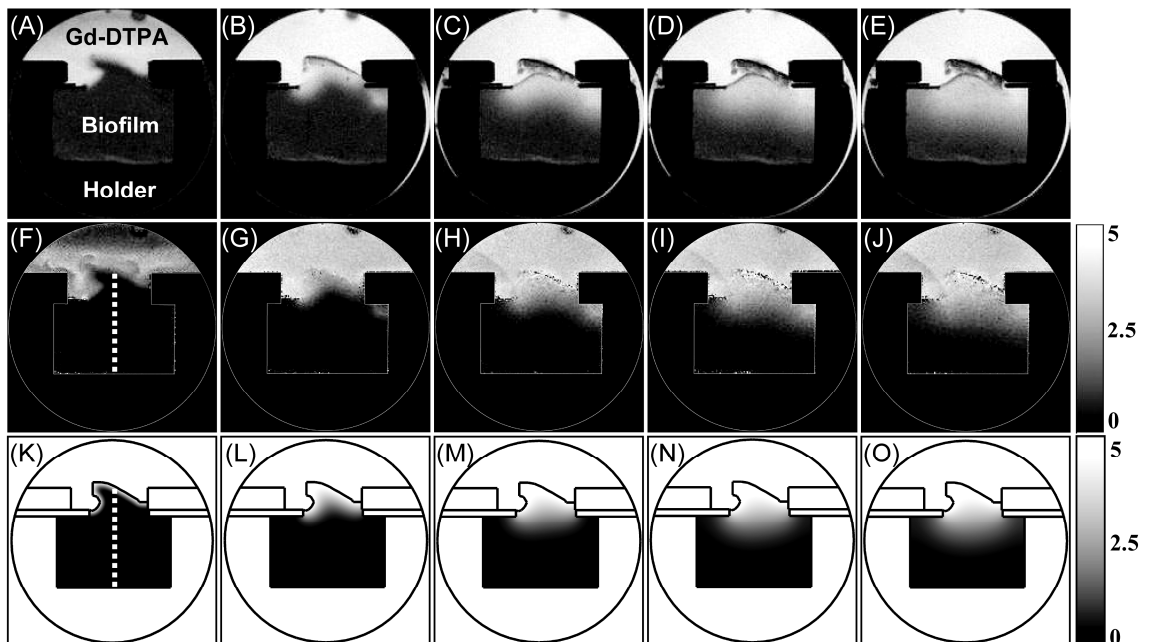


Figure 3.8. Transport of Gd-DTPA into the *Phormidium* biofilm illustrated as T_1 -weighted images acquired at 40° flip angle (A-E), calibrated Gd-DTPA concentration maps (F-J) and diffusion model results (K-O) at time intervals of 2, 22, 72, 122 and 172 minutes. The grey scale indicates the Gd-DTPA concentrations (mM) inside the biofilm.

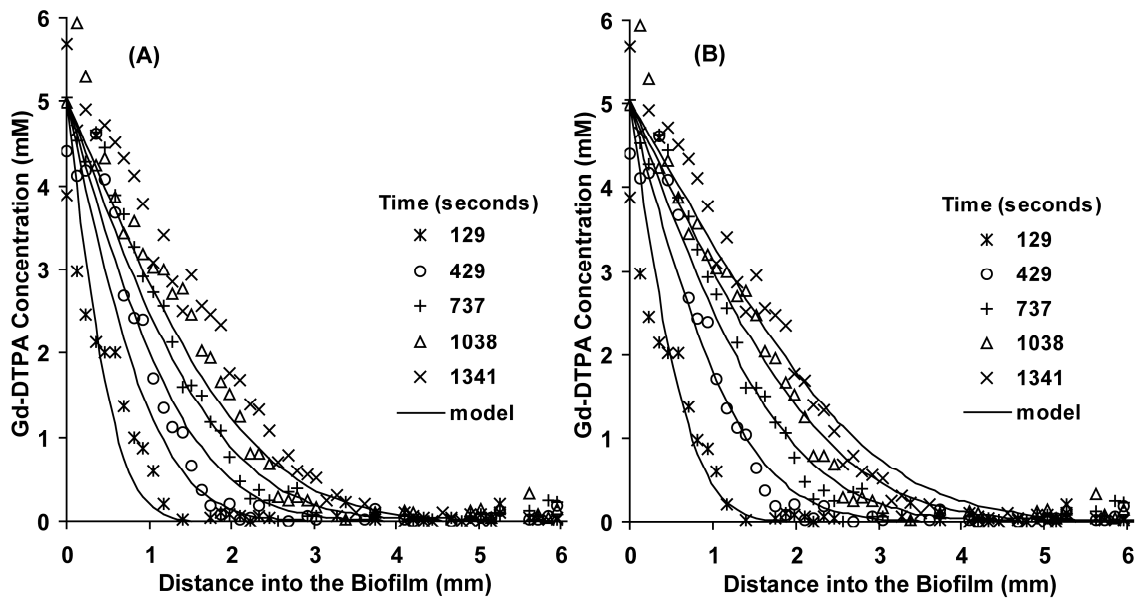


Figure 3.9. Gd-DTPA transport inside the *Phormidium* biofilm is compared between experimental data and (A) model data (modeled at diffusion coefficient of $7.2 \times 10^{-10} \text{ m}^2/\text{s}$) and (B) calibrated diffusion model data. Gd-DTPA concentration profiles were along the transect shown in white line in Fig. 3.8(F and K) at time intervals of 129, 429, 737, 1038 and 1341 seconds. Symbols represent experimental data and solid lines represent model data at respective time intervals.

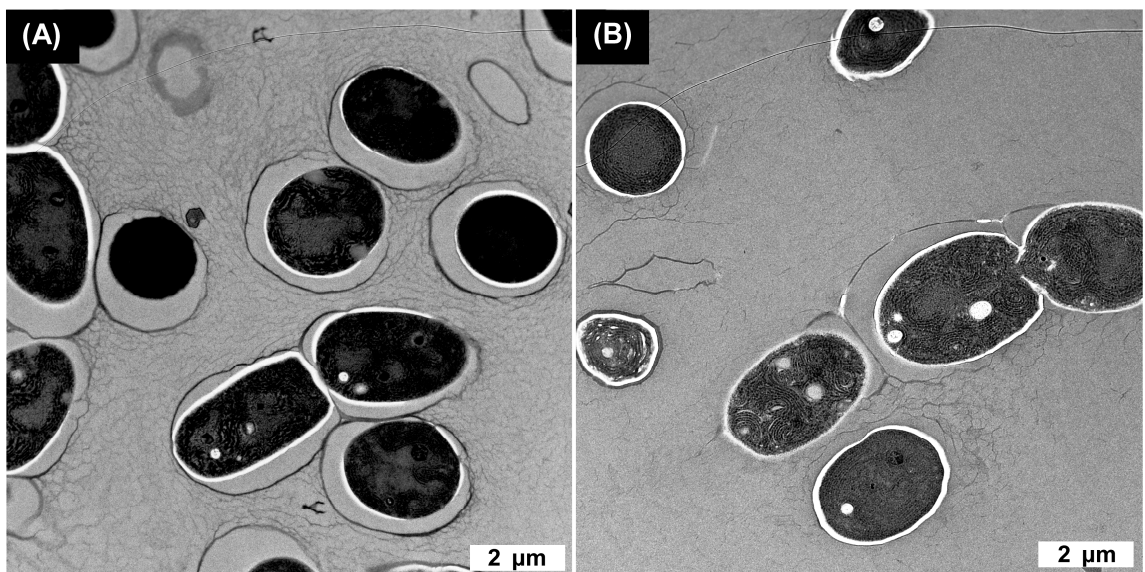


Figure 3.10. Transmission Electron micrograph of freeze-substituted *Phormidium* biofilm sample. (A) Cross section of *Phormidium* filaments embedded in an EPS matrix. The EPS is the fine meshwork seen between cells. (B) Areas where there is little or no EPS between the filaments, thus with voids and interconnected channels between filaments.

3.4.5 Freeze-substitution transmission electron microscopy analysis of biofilm structure

The structural complexity of *Phormidium* biofilm was visualised using freeze-substitution transmission electron microscopy as illustrated in figure 3.10. Transmission electron micrograph (see Fig. 3.10A) shows that *Phormidium* filaments are embedded in an EPS matrix and this was observed in most areas of the biofilm. However in some areas there was little or no EPS between the filaments as shown in figure 3.10B, thus creating voids and interconnected channels between filaments.

3.5 Discussion

In this study, MRI was successful in quantitatively measuring the time-varying spatially distributed concentration of Gd-DTPA as it is transported into the agar and *Phormidium* biofilm. The agar system was used as a simple test system to examine the suitability of the approach. Results from both agar and *Phormidium* biofilm experiments were then compared with simple one and two dimensional models.

As illustrated in figure 3.7B, concentration profiles of Gd-DTPA transport in agar collapsed well onto a single line. Critically, this indicates transport is consistent with (i) diffusion and (ii) diffusion at a constant rate. This corroborates the suitability of this MRI method as such homogeneous diffusion is expected in a homogeneous agar gel. Moreover, the calculated diffusion coefficient of $7.2 \times 10^{-10} \text{ m}^2 \text{ s}^{-1}$ is an acceptable estimate for the diffusivity of Gd-DTPA (molecular mass 547 g mole^{-1}). This is slower than that of much lighter molecules such as water ($D = 2.2 \times 10^{-9} \text{ m}^2 \text{ s}^{-1}$) yet faster than a similar but heavier Gd tagged molecule, Magnevist, ($D = 2.6 \times 10^{-10} \text{ m}^2 \text{ s}^{-1}$; molecular mass 938 g/mole) (Gordon et al., 1999).

This then enabled us to move onto a real biofilm system. Again, this MRI approach successfully tracked the transport of Gd-DTPA into the *Phormidium* biofilm. A simple two dimensional diffusion model that employed the diffusion coefficient calibrated for agar did not match the experimental results (Fig. 3.9A); transport appears to be quicker in the biofilm. When the diffusion model was calibrated against the concentration profiles in the biofilm the best fitting model (Fig. 3.9B) was achieved with a diffusion coefficient of $1.04 \times 10^{-9} \text{ m}^2 \text{ s}^{-1}$. This is an unrealistically high rate of diffusion for Gd-DTPA in the biofilm, since the diffusion coefficient of Gd-DTPA inside the agar is only $7.2 \times 10^{-10} \text{ m}^2 \text{ s}^{-1}$. The agar is a highly permeable, inert gel, designed to give minimal resistance to diffusive transport. Consequently,

the diffusion coefficient determined in agar is expected to be the maximum unrestricted value. Thus, it appears that the transport of Gd-DTPA in the biofilm is not by diffusion alone. It should be noted here, that the thick filamentous biofilm formed by *Phormidium* is a heterogeneous complex three dimensional system. TEM of the biofilm's internal structure reveals that in most areas a dense EPS matrix fills the spaces between *Phormidium* filaments (Fig. 3.10A). However, in other areas there is very little or no EPS fillings these spaces (Fig. 3.10B), thus creating voids and interconnected channels. Previous studies showed that these structural heterogeneities found in biofilms can increase the transport of solutes into and through biofilms via advection (Bishop et al., 1997, de Beer et al., 1997, de Beer et al., 1994, Stewart, 1998, Stewart, 2003). Therefore the component of advective transport of Gd-DTPA in the *Phormidium* biofilm would have increased its transport rate over and above its calculated diffusion coefficient in agar.

Despite the fact that transport in the biofilm is not solely diffusive the calibrated model is a reasonable match to the observed data. This has been observed in biofilm mass transport studies using other techniques where calculated diffusion coefficients are higher than those possible by pure diffusion (de Beer et al., 1997). Thus, the effective diffusion coefficients described in this and other biofilm studies not only embody the impact of factors such as porosity and tortuosity on diffusion, but can also embody components of advection. These effective parameters can be a useful means of quantifying the effects of different transport mechanisms without explicitly representing all of the heterogeneities and flow pathways through a porous medium. The presence of small voids and interconnected channels inside this biofilm cannot be imaged by MRI in this study as the achievable resolution was 150 microns, which is larger than the size of most voids and channels found inside biofilms (de Beer et al., 1994). Ultimately, however, as our ability to image transport at increasingly high spatial resolution evolves it may be possible to disentangle flow mechanisms in a few laboratory based experiments if the sizes of voids and inter connected channels are compatible with achievable higher resolution using MRI. However, for quantifying biofilm transport for any practical applications it may always be necessary to use effective parameters in prudently simplified transport models. Therefore the transport of Gd-DTPA into this *Phormidium* biofilm can be characterised with an effective diffusion coefficient which comprises both its diffusional and advective transport properties.

Usually during the maturation process biofilms adapt to optimize their mass transport behaviours (Beyenal and Lewandowski, 2002). Therefore, conducting mass transport

experiments under unidirectional flow (as in the flow cell) may produce differing mass transport behaviour of the biofilm which was grown under bi-directional flow (on a rocking table). However, these differences do not impact the overall aim of this study which is to demonstrate that paramagnetic tracers can be used to track mass transport in biofilms.

As described earlier, the diffusion of Gd-DTPA is illustrated by the expansion of the brighter region in T_1 -weighted images and in the concentration maps (Fig. 3.8). However, as Gd-DTPA uptake increased a small darker region was observed at the top of the biofilm in the T_1 -weighted images (Fig. 3.8A to E) which continued to expand with time. This is likely a side effect of increasing Gd-DTPA concentration upon the signal intensity. Normally, signal intensity is proportional to the concentration of paramagnetic ions (higher concentrations cause higher signal intensity). However, above a certain threshold concentration, paramagnetic ions can cause a rapid reduction in the signal intensity (Nestle and Kimmich, 1996, Robert, 1997). Apparently, the highest concentrations of Gd-DTPA in the biofilm system are above this threshold and thus generate a darkening, rather than brightening, in the top of the biofilm in the T_1 -weighted images. Importantly, Gd-DTPA concentrations are not calculated directly from these single flip angle T_1 -weighted images. For each image pixel, the signal intensity, $S_{(t)}$, at multiple flip angles is fitted to equation 2 using a non-linear least square algorithm. Thus, the darkening seen in the T_1 -weighted images does not result in an incorrect calculation of lower Gd-DTPA concentration in the top of the biofilm (Fig. 3.9). Although not problematic, this darkening can be overcome by reducing the Gd-DTPA concentration in the in-flow solution so that they stay below the threshold.

The few dark pixels seen in the very top of the biofilm in the concentration maps (Fig 3.8F to J) likely the result from the higher error that is associated with calculating Gd-DTPA concentrations at higher, compared to lower, concentrations. This is because the relationship between T_1 and Gd-DTPA concentration is inversely proportional (equation 3), thus changes in concentration at high Gd-DTPA concentrations cause much smaller shifts in T_1 than at low concentrations.

The resolution gained during this study is 150 microns. This is useful for very thick biofilms which are more common in the natural environment. Biofilms which are commonly used in engineered systems occur on scales of many tens of microns to millimeters and thus a higher resolution is required. The resolution of the MRI image is limited by attainable signal-to-noise ratio. The signal-to-noise ratio increases inversely proportional to the diameter of the RF coil

which detects the MR signal. In this study a commercially available 35 mm diameter RF coil was used. Smaller diameter RF coils, however, are capable of generating higher resolution. Indeed, smaller diameter bespoke RF coils have already been used to examine metabolite production and consumption in biofilms ~100 μm thick, with a resolution of ~ 20 μm (McLean et al., 2008) and water diffusivities with a resolution of ~ 7.5 μm (Renslow et al., 2010). Evidently, the next step here should be to build smaller diameter RF coils which will enable the imaging of paramagnetically labeled molecules in thinner biofilms.

Overall this study illustrates the suitability of this approach in biofilm research to quantify the mass transport rates and pathways of different macromolecules inside biofilm systems. Indeed, a wide range of commercially available paramagnetically tagged molecules and nanoparticles are available to explore the impact of parameters such as molecular mass, charge and molecular geometry or structure on transport in different biofilms. These range from Gd-DTPA (molecular mass 547g mol⁻¹) upto large macromolecules such as Gadolinium labeled albumin (~ 74 kDa) and Gd nanoparticles (<http://www.biopal.com/MRI.htm>). Whilst Gd based tracers are most common, iron oxide based paramagnetic contrast agents, such as USPIO (Ultra-small Superparamagnetic Iron Oxide) can also be used. It is also possible to construct bespoke, tagged molecules with specific properties.

Therefore the use of MRI with paramagnetic tracers has the potential to significantly improve our understanding of the way pollutants and substrate are transported and transformed by real biofilms.

3.6 References

- BEULING, E. E., VAN DUSSCHOTEN, D., LENS, P., VAN DEN HEUVEL, J. C., VAN AS, H. & OTTENGRAF, S. P. P. (1998) Characterization of the diffusive properties of biofilms using pulsed field gradient-nuclear magnetic resonance. *Biotechnology and Bioengineering*, 60, 283-291.
- BEYENAL, H. & LEWANDOWSKI, Z. (2002) Internal and external mass transfer in biofilms grown at various flow velocities. *Biotechnology Progress*, 18, 55-61.
- BISHOP, P. L., GIBBS, J. T. & CUNNINGHAM, B. E. (1997) Relationship between concentration and hydrodynamic boundary layers over biofilms. *Environmental Technology*, 18, 375 - 385.
- BROOKES, J. A., REDPATH, T. W., GILBERT, F. J., MURRAY, A. D. & STAFF, R. T. (1999) Accuracy of T1 measurement in dynamic contrast-enhanced breast MRI using two- and three-dimensional variable flip angle fast low-angle shot. *Jmri-Journal of Magnetic Resonance Imaging*, 9, 163-171.
- CRANK, J. (1979) *The mathematics of diffusion*, Oxford University Press, Oxford, United Kingdom.

- DE BEER, D., STOODLEY, P. & LEWANDOWSKI, Z. (1997) Measurement of local diffusion coefficients in biofilms by microinjection and confocal microscopy. *Biotechnology and Bioengineering*, 53, 151-158.
- DE BEER, D., STOODLEY, P., ROE, F. & LEWANDOWSKI, Z. (1994) Effects of biofilm structures on oxygen distribution and mass transport. *Biotechnology and Bioengineering*, 43, 1131-1138.
- GORDON, M. J., CHU, K. C., MARGARITIS, A., MARTIN, A. J., ETHIER, C. R. & RUTT, B. K. (1999) Measurement of Gd-DTPA diffusion through PVA hydrogel using a novel magnetic resonance imaging method. *Biotechnology and Bioengineering*, 65, 459-467.
- HAACKE, E. M., R. W. BROWN, M. R. THOMPSON, AND R. VENKATESAN (1999) *Magnetic Resonance Imaging: Physical principles and sequence design*, Wiley-Liss.
- HUNTER, R. C. & BEVERIDGE, T. J. (2005) High-resolution visualization of *Pseudomonas aeruginosa* PAO1 Biofilms by freeze-substitution transmission electron microscopy. *Journal of Bacteriology*, 187, 7619-7630.
- LENS, P., VERGELDT, F., LETTINGA, G. & VAN AS, H. (1999) H-1 NMR characterisation of the diffusional properties of methanogenic granular sludge. *Water Science and Technology*, 39, 187-194.
- LOGAN, B. E. & QING, J. (1990) Molecular-size distributions of dissolved organic-matter. *Journal of Environmental Engineering-Asce*, 116, 1046-1062.
- MCLEAN, J. S., ONA, O. N. & MAJORS, P. D. (2008) Correlated biofilm imaging, transport and metabolism measurements via combined nuclear magnetic resonance and confocal microscopy. *Isme Journal*, 2, 121-131.
- NESTLE, N. F. E. I. & KIMMICH, R. (1996) NMR imaging of heavy metal absorption in alginate, immobilized cells, and kombu algal biosorbents. *Biotechnology and Bioengineering*, 51, 538-543.
- PHOENIX, V. R. & HOLMES, W. M. (2008) Magnetic resonance imaging of structure, diffusivity, and copper immobilization in a phototrophic biofilm. *Applied and Environmental Microbiology*, 74, 4934-4943.
- RENSLOW, R. S., MAJORS, P. D., MCLEAN, J. S., FREDRICKSON, J. K., AHMED, B. & BEYENAL, H. (2010) In situ effective diffusion coefficient profiles in live biofilms using pulsed-field gradient nuclear magnetic resonance. *Biotechnology and Bioengineering*, 106, 928-937.
- RIPPKA, R., DERUELLES, J., WATERBURY, J. B., HERDMAN, M. & STANIER, R. Y. (1979) Generic assignments, strain histories and properties of pure cultures of cyanobacteria. *Journal of General Microbiology*, 111, 1-61.
- ROBERT, C. S., AND C. L. ROBERT (1997) *Understanding magnetic resonance imaging*, CRC.
- ROESELERS, G., VAN LOOSDRECHT, M. C. M. & MUYZER, G. (2008) Phototrophic biofilms and their potential applications. *Journal of Applied Phycology*, 20, 227-235.
- SCHMITT-WILLICH, H., BREHM, M., EWERS, C. L. J., MICHL, G., MULLER-FAHRNOW, A., PETROV, O., PLATZEK, J., RADUCHEL, B. & SULZLE, D. (1999) Synthesis and physicochemical characterization of a new gadolinium chelate: The liver-specific magnetic resonance imaging contrast

agent Gd-EOB-DTPA. *Inorganic Chemistry*, 38, 1134-1144.

STANISZ, G. J. & HENKELMAN, R. M. (2000) Gd-DTPA relaxivity depends on macromolecular content. *Magnetic Resonance in Medicine*, 44, 665-667.

STEWART, P. S. (1998) A review of experimental measurements of effective diffusive permeabilities and effective diffusion coefficients in biofilms. *Biotechnology and Bioengineering*, 59, 261-272.

STEWART, P. S. (2003) Diffusion in biofilms. *Journal of Bacteriology*, 185, 1485-1491.

TETLEY, L., BROWN, S. M. A., MCDONALD, V. & COOMBS, G. H. (1998) Ultrastructural analysis of the sporozoite of *Cryptosporidium parvum*. *Microbiology-Uk*, 144, 3249-3255.

VOGT, M., FLEMMING, H. C. & VEEMAN, W. S. (2000) Diffusion in *Pseudomonas aeruginosa* biofilms: a pulsed field gradient NMR study. *Journal of Biotechnology*, 77, 137-146.

WIELAND, A., DE BEER, D., DAMGAARD, L. R., KUHL, M., VAN DUSSCHOTE, D. & VAN AS, H. (2001) Fine-scale measurement of diffusivity in a microbial mat with nuclear magnetic resonance imaging. *Limnology and Oceanography*, 46, 248-259.

Chapter 4

Magnetic resonance imaging of
biofilm mass transport processes and structure
using a simple custom made solenoid RF coil

4

Magnetic resonance imaging of biofilm mass transport processes and structure using a simple custom made solenoid RF coil

4.1 Summary

Investigations of mass transport processes in biofilms using magnetic resonance imaging (MRI) are limited by the spatial resolution that can be achieved. Higher spatial resolutions can be achieved by detecting the MR signal using bespoke RF coils to best suit the sample geometry. In this study a custom made solenoid RF coil, which did not require extensive RF engineering expertise to construct, was used to image the transport of the paramagnetically tagged macromolecule, Gd-DTPA inside a phototrophic biofilm. The bespoke RF coil showed good signal homogeneity and its high sensitivity allowed MR images to be obtained with improved resolutions. The accuracy of MRI transport measurements using the bespoke RF coil was first assessed using a homogeneous test system composed of agar. The measured concentration profiles of Gd-DTPA inside agar showed a close match to a simple diffusion model. However, transport measurements inside the phototrophic biofilm could not be matched to a simple diffusion model, indicating a combination of diffusion and advection of Gd-DTPA within the biofilm. The structural heterogeneity of the biofilm was imaged at resolutions up to 22 x 22 μm , allowing the impact of biofilm architecture on its mass transport behavior to be investigated. The resolution achievable with bespoke RF coils makes them ideal for imaging structure and transport inside biofilms with thicknesses greater than several hundreds of microns (e.g. phototrophic biofilm and granules) which can be too thick for photon based imaging methods. However, this study also highlighted the inevitable tradeoff between the highest achievable spatial resolution and temporal resolution when attempting to image the transport of molecules within biofilms in real time.

4.2 Introduction

The investigation of mass transport of different solutes inside biofilms is essential for effective modeling of biofilm function (Beyenal and Lewandowski, 2002, Bishop et al., 1997, Buffière et al., 1995, de Beer et al., 1994, Wieland et al., 2001). These models can help us understand and optimize biotechnological processes, such as waste water treatment and biofuel production, as well as natural processes such as heavy metal and nanoparticle immobilization in natural aquatic systems.

The non invasive nature of magnetic resonance imaging (MRI) makes it a valuable tool for measuring mass transport inside biofilms as mentioned in section 1.1.3.

The thicknesses of biofilms utilized in most biotechnological processes ranges from tens of microns to several millimeters (Bartacek et al., 2009, Roeselers et al., 2008, Van Loosdrecht and Heijnen, 1993); while natural phototrophic biofilms can develop on centimetre scales such as microbial mats (Wieland et al., 2001). Therefore quantitative MRI measurements of critical biofilm parameters, such as transport rates and reaction rates, require spatial resolutions to suite these scales.

4.2.1 MRI of biofilms

The hydrogen nucleus (^1H) is by far the most widely used in medical MRI, due to the high natural abundance of the isotope and its high magnetogyric ratio, which gives ^1H the greatest sensitivity to the phenomena of nuclear magnetic resonance. Like the human body, biofilms are mostly composed of water (H_2O) so are ideal for use with ^1H MRI. A number of factors affect the magnitude of the ^1H MR signal, including ^1H density and the spin-lattice (T_1) and spin-spin (T_2) relaxation of ^1H nuclei.

The achievable spatial resolution using MRI is limited by three main factors; the magnetic field gradients which are used to encode the MR signal, the transport (mainly the diffusion) of molecules in and out from the voxels and the signal-to-noise ratio (SNR) of the measured MR signal. Strong magnetic field gradients are necessary to achieve higher spatial resolutions, as potential spatial resolution is inversely proportional to the strength of the magnetic field gradients. Also, strong magnetic field gradients help to overcome the diffusion limitation, by allowing image acquisitions with shorter echo times.

The achievable spatial resolutions can still be limited by the signal-to-noise ratio (SNR), even

when strong magnetic field gradients are used. For example, in the initial biofilm experiment (chapter 3) the spatial resolution was not limited by the available gradient strength (i.e. the 1000 mT/m obtained using micro-imaging gradient insert), rather by the SNR of the measured signal.

The MR signal is an oscillating electromotive force (e.m.f) induced in the signal detection coil (RF coil) by the precessing net nuclear magnetization of ^1H nuclei. Onto this signal is the superimposed noise e.m.f arising from the random thermal motion of electrons within the RF coil (Callaghan, 1993). The comparative size of the signal and noise is known as the signal-to-noise ratio (SNR). The spatial resolution that can be achieved is limited by the measured SNR, since the signal available from each voxel decreases with voxel size (i.e. number of ^1H nuclei) (Callaghan, 1993). Consequently, the sensitivity of the receiver electronics (i.e. the SNR of the measured signal) is also important when MR images with higher spatial resolutions are required (Redpath, 1998).

4.2.2 Improving the SNR

The SNR and hence the spatial resolution can be improved by signal averaging; i.e. co-adding the signal from N successive scans to produce a single MR image. Here the true signal adds coherently (proportional to N), while the noise adds in random phase (proportional to $N^{1/2}$), thus the signal-to-noise ratio is proportional to $N^{1/2}$ (i.e. $N / N^{1/2}$) (Callaghan, 1993). This, however, reduces the achievable temporal resolution as signal averaging increases the scan duration.

With improved SNR by signal averaging, the apparent (effective) diffusion coefficient of water inside biofilms can be resolved at high spatial resolutions using pulsed field gradient (PFG) NMR (McLean et al., 2008, Renslow et al., 2010). Here the apparent diffusion coefficient of water was estimated using the measured signal attenuation caused by the random Brownian motion of water molecules which already exist inside the biofilm. In statistical terms this is a steady state process, thus allowing extensive signal averaging to be used to improve spatial resolution without affecting the accuracy of the water diffusion measurements.

PFG analysis is, however, generally limited to water only, as most solutes of interest reside at concentrations that are too low to be detected using PFG or their spin properties makes them incompatible with MRI. An alternative approach is to use paramagnetically tagged molecules

to investigate their transport inside biofilms. This approach has been used to investigate transport of solutes such as trace metals and macromolecules inside granules (Bartacek et al., 2009) and phototropic biofilms (Ramanan et al., 2010) respectively. The transport of paramagnetic solutes is tracked by imaging their concentration dependent affect upon the local MR signal as they migrate into the biofilm; an approach known as dynamic contrast enhanced MRI. In order to capture the dynamic evolution of the solute concentration, rapid real time imaging is required. Ideally, the scan duration should be short compared to the rate of change of solute concentrations. Hence, the use of long scan durations is not desirable, as it will result in time averaged concentration images, complicating data analysis and estimation of transport properties. Therefore, the use of signal averaging is not generally a good option for improving spatial resolution.

Other ways to improve SNR and hence the spatial resolution include using scanners with high magnetic field strengths (Haase et al., 2000) or improving the sensitivity of the MR signal detection, for example by the use of phase array coils (Natt et al., 2005) or cryo-cooled coils (Ginefri et al., 2005). However, these options are not always viable as the choice of MRI scanners are limited due to their high capital and maintenance costs (Werth et al., 2010) and such sophisticated coils are expensive and require extensive engineering expertise to construct.

The SNR is also dependant upon the design of the RF coil used to detect the MR signal. An RF coil, placed closer to the sample, with a high filling factor, detects a larger signal due to the increased magnetic flux linkage between sample and detection coil, resulting in a higher SNR (Redpath, 1998). The filling factor is the ratio between the sizes of the sample and the RF coil, thus samples which fill most of the space in the coil are ideal. Large commercially available RF coils (volume resonators) have previously been used to measure mass transport in large phototrophic biofilms (Phoenix and Holmes, 2008, Ramanan et al., 2010). However, their applications were limited due to the spatial resolution that could be achieved (~ 150 microns) as larger RF coils have the disadvantage of low filling factor (these studies examined biofilm ~1 cm thick using RF coils ~ 3.5 cm in diameter). Therefore, a simpler and cost effective alternative to improve the SNR is to construct a bespoke RF coil to best suit the sample geometry of interest, thus optimizing the filling factor and gaining the maximum resolution achievable for a given biofilm. Different types of microscopy coils have already been used in biofilm research to investigate; metabolite consumption and production (McLean et al., 2008), transport of trace metals in methanogenic granules (Bartacek et al., 2009) and effective water diffusion coefficients inside biofilms (Renslow et al., 2010).

Compared to other common microscopy coil types such as Helmholtz coil and saddle coil, the solenoid coil has the advantages of best NMR sensitivity, high (B_1) field homogeneity and is easy to build with only a few construction rules (Haase et al., 2000). For example, the sensitivity of a solenoid coil is approximately three times that of a saddle coil of the same dimensions. Conversely, a solenoid coil has two disadvantages; limited access to sample, as the coil axis must be perpendicular to the main magnetic field (B_0) and limited practical size of the coil, as the length of the conductor should not exceed one twentieth of the wavelength of RF radiation used (Haase et al., 2000). These disadvantages, however, are not of practical significance when using a solenoid coil to investigate mass transport process inside biofilms with thicknesses ranging between several hundred microns to millimetres.

The main objective of this study was to investigate the mass transport of paramagnetically tagged macro-molecule (Gd-DTPA) inside a phototrophic biofilm with improved spatial resolutions using a custom made solenoid RF coil. Transport of Gd-DTPA inside a thick phototrophic biofilm has been undertaken before as discussed in chapter - 3, but using a commercially available RF coil, which was not optimum for the biofilm being studied. Thus, the spatial resolution was limited (~ 150 microns) due to the SNR restrictions caused by the low filling factor of the RF coil (~ 3.5 cm diameter) with regard to the biofilm (~ 1 cm thick).

This chapter describes the design and use of a solenoid RF coil that has been optimized for quantitative imaging of Gd-DTPA transport inside a laboratory grown *Phormidium* biofilm with thickness of 2.5 mm. This was chosen as a simple model biofilm, as *Phormidium* biofilm readily grows in the laboratory. The paramagnetic complex Gd-DTPA was chosen as this is a commonly used MRI contrast agent. Here also the effect of the paramagnetic property of the tracer upon the MRI signal enables us to not only image the transport of these molecules inside biofilms but also spatially quantify their concentration in real time as discussed in section 2.5. The accuracy of the transport measurement using the custom made RF coil was first tested with a simple test system composed of agar. Then the mass transport of Gd-DTPA inside the biofilm was investigated using the same RF coil. The results from the agar experiment were used to calibrate a two dimensional computational model to determine the diffusion rate of Gd-DTPA inside agar and compared with the previous estimate using a larger, commercially available, RF coil. Finally, the results from the *Phormidim* biofilm experiment were compared with a simple two dimensional diffusion model to see whether Gd-DTPA transport inside the biofilm could be represented by diffusion alone.

4.3 Materials and methods

4.3.1 Agar and phototrophic biofilm

The artificial biofilm was made up of agar (1.5%). Molten agar was poured into a plastic sample tube (4 mm inner-diameter) with a glass rod running through the top. Once set, the rod was removed leaving a hole through which the Gd-DTPA would flow (Fig. 4.1).

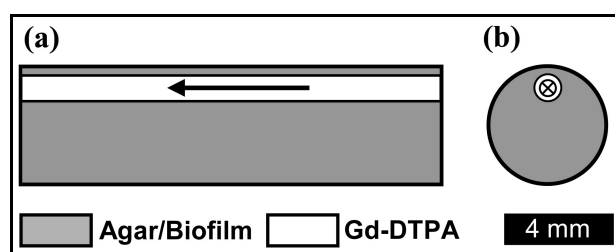


Figure 4.1. Schematic of flow cell containing agar. Cross sections are (a) along the flow cell and (b) across the flow cell.

The phototrophic biofilm used in this study was composed of the cyanobacterium *Phormidium* sp. (strain PP03) from the culture collection of V. R. Phoenix (Phoenix and Holmes, 2008). This phototrophic biofilm was grown in the laboratory inside a plastic sample tube (4 mm inner diameter) with BG-11 +N (BG11 with NaNO₃) nutrient medium (Rippka et al., 1979). The sample tube was initially inoculated with small pieces of *Phormidium* and placed in an incubator and maintained at 28 °C, with a constant light intensity of 25 $\mu\text{mol m}^2 \text{s}^{-1}$. The sample tube containing the phototrophic biofilm was connected via silicon tubing to a BG-11 (+N) nutrient reservoir and slowly pumped with nutrient media at a rate of 0.5 ml min⁻¹ using a peristaltic pump.

4.3.2 Solenoid coil and biofilm frame

The solenoid RF coil was constructed on a rigid purpose built frame made up of three rigid circular polypropylene discs, connected using long plastic threads, to provide it with mechanical stability (see Fig. 4.2). On the right side of the frame (Fig. 4.2a, b), is the flow compartment, which consists of a polypropylene slab with a hole at the centre, to accommodate both solenoid coil and sample tube. The sample tube was carefully placed inside the solenoid coil and fixed to the slab. The slab arrangement was used to hold the solenoid coil and the sample tube rigid during the experiment. On the left side of the frame (Fig. 4.2a, b) is the electronic compartment, which contains the electronic components of the RF resonant circuit. All the components (except the BNC connector, capacitors, connection wires) used to

build the rigid frame were made up with either plastic or polypropylene in order to reduce the magnetic susceptibility and gradient “ringing” effects that metals can cause. A custom made locking mechanism was used to firmly fix the entire frame setup inside the micro-imaging gradients as shown in figure 4.2. Figure 4.3 shows the photograph of the actual custom made biofilm frame.

The solenoid coil was constructed of 0.8 mm diameter copper wire. The solenoid coil has an inner diameter of 5 mm and is 5 mm in height with two and a half turns, which is close to the optimal design of a solenoid coil (Haase et al., 2000).

Figure 4.2(d) shows the RF resonant circuit design used (Holmes et al., 2008, Mispelter. et al., 2006). This consists of two variable air capacitors (C1 and C3) of 0.6 pF to 9.5 pF (Johanson, USA), accessed by tuning rods. C2 is a 2.2 pF ceramic chip capacitor (Temex, France). The solenoid coil was operated in transmit-receive mode using standard scanner electronics.

4.3.3 Estimating the capacitor values of the resonant circuit

The approximate values of inductance of the solenoid coil and capacitance of the tuning and matching capacitors of the resonant circuit were estimated using the resonant circuit theory (Mispelter, 2006).

The inductance of the solenoid coil was estimated using the equation given below.

$$L = 0.4\pi^2 n^2 \frac{r_m^2}{l + e + r_{ext}} AB$$

Equation 1

where n is number of turns of the solenoid coil, r_m is the mean radius, r_{ext} is the outer radius, l is the length of the solenoid and e is the thickness of the conductor (see Fig. 4.4). Values of A and B can be calculated using following equations,

$$A = \frac{10l + 12e + 2r_{ext}}{10l + 10e + 1.4r_{ext}}$$

Equation 2

$$B = 0.5 \log_{10} \left[100 + \frac{14r_{ext}}{2l + 3e} \right]$$

Equation 3

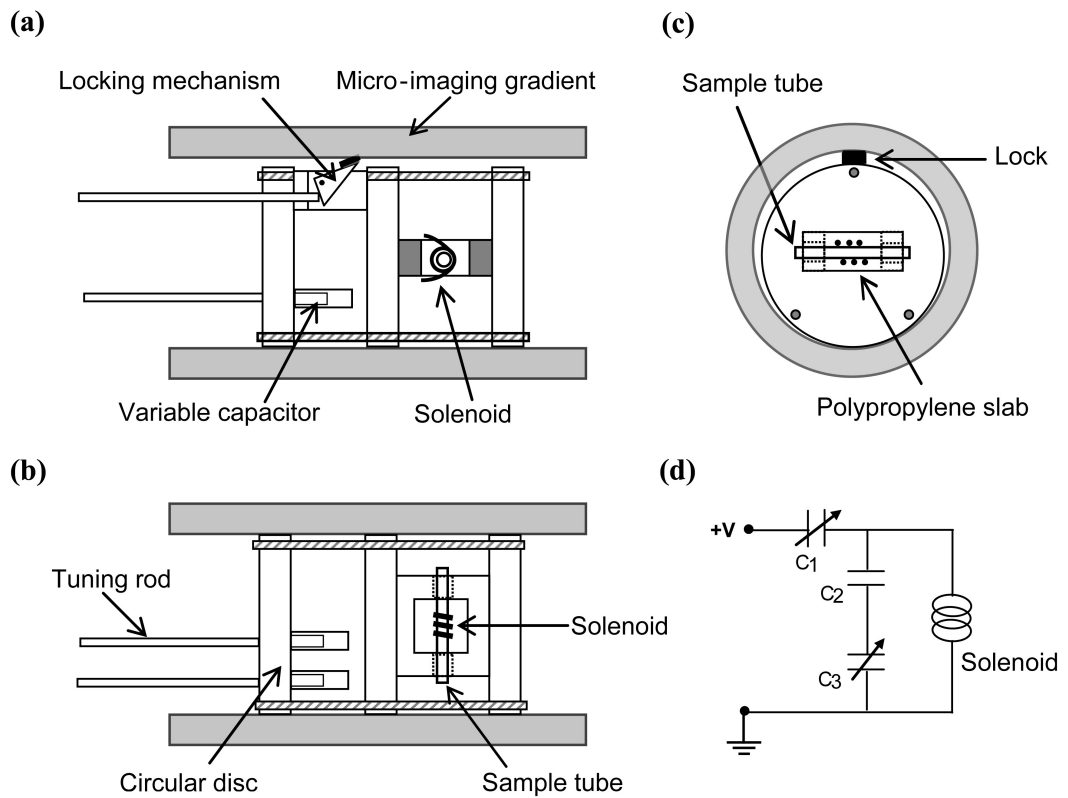


Figure 4.2. Diagram of the support frame with built-in solenoid RF coil and electronic circuit fixed inside the micro-imaging gradient using the locking mechanism. (a) Front, (b) plan and (c) end views of the frame showing how it fits into the 60 mm diameter of the micro-imaging gradient set using the custom made lock mechanism. (d) Resonant circuit design.

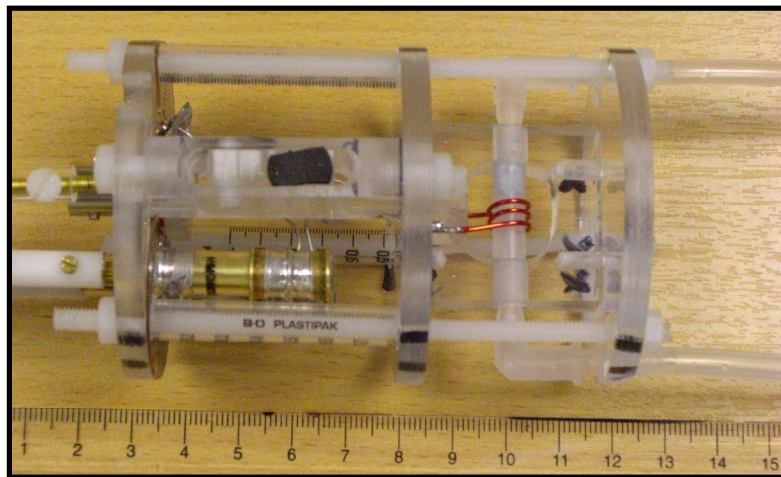


Figure 4.3. Photograph of the actual custom made biofilm frame illustrating the flow compartment and electronic compartment.

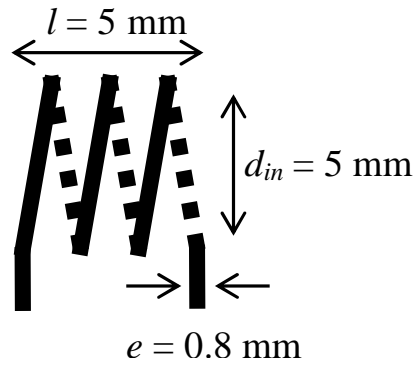


Figure 4.4. Schematic of the solenoid coil used as the RF coil to excite and detect the MR signal.

The calculated inductance of the of the solenoid coil (see Fig. 4.4) using equation 1 was 27 nH.

Capacitance of the tuning capacitor (C_T) and matching capacitor (C_M) of the resonant circuit was calculated using equations 4 and 5 with the following values of $300\text{ MHz} = 2\pi \times 300 \times 10^6$ rad/s for ω_S , the spectrometer resonant frequency, 100 for Q , the quality factor and 50 for Z_0 , the impedance of the resonant circuit.

$$C_T = \frac{Q - U}{\omega_S V}$$

Equation 4

$$C_M = \frac{1}{\omega_S Z_0 U}$$

Equation 5

where values of U, V and r are calculated using following equations,

$$U = \sqrt{\frac{V}{Z_0} - 1}$$

Equation 6

$$V = r(1 + Q^2)$$

Equation 7

$$r = \frac{L \cdot \omega_S}{Q}$$

Equation 8

The estimated values for C_T and C_M are 9.1 pF and 1.06 pF respectively.

Two variable capacitors with capacitance range of 0.6 pF to 9.5 pF were used to construct the resonant circuit as shown in figure 4.2d. However, the maximum resonant frequency of only 200 MHz was observed. This observed lower resonant frequency may be due to the possible addition of resistance, capacitance or inductance by the wires used to connect the solenoid coil to the resonant circuit and its components. Thus, a fixed capacitor was added in series to the tuning capacitor to bring up the resonant frequency. The fixed capacitor of 2.2 pF was chosen after trial and error with other capacitors to bring up the resonant frequency in the range of 300 MHz.

4.3.4 Performance evaluation of the RF coil

The performance of the custom made solenoid RF coil was evaluated by measuring the quality indices such as the field homogeneity and quality factor, Q . The B_1 field homogeneity produced by the RF coil was evaluated by measuring the signal homogeneity of a cylindrical phantom of aqueous Gd-DTPA (1 mM) using a gradient echo pulse sequence.

The quality factor (Q) measurements were done using a network analyzer (Agilent 8712ET) on the laboratory workbench. The Q -factors of the RF coil with and without the phantom were calculated as twice the ratio of the resonant frequency to the frequency bandwidth at -3dB, with the coil tuned and matched to 300 MHz and 50 Ω . The -3dB bandwidth was located at 3dB below the reference level (Haase et al., 2000, Mispelter, 2006).

4.3.5 Flow system

During the agar experiment, the rigid frame containing the agar sample tube was positioned at the centre of the MRI bore. The sample tube containing the agar was first connected via silicon tubing to an 18-M Ω water supply and slowly washed with ultrapure water at a rate of 0.5 ml min⁻¹ using a peristaltic pump. The system was then connected to a 500 ml reservoir of a 1.8 mM Gd-DTPA (molecular mass, 547 g mol⁻¹; Sigma Aldrich) solution, which was pumped through the sample tube at a rate of 0.5 ml min⁻¹. Exactly the same procedures explained for the agar flow system was carried out during the phototrophic biofilm experiment.

4.3.6 MRI

The MRI experiments were performed on a Bruker Avance BioSpec system, using a 30 cm-bore, 7-T superconducting magnet (Bruker BioSpin, Karlsruhe, Germany). A Bruker micro-imaging gradient insert (model BG-6) and 200-A gradient amplifiers were used to provide strong linear magnetic field gradient pulses of up to $1,000 \text{ mT m}^{-1}$, thus allowing the system to perform micro-imaging experiments. The custom made solenoid RF coil with 5-mm-diameter was used to excite and detect the ^1H signal.

4.3.7 Acquisition of T_1 -weighted images

The transport of Gd-DTPA inside both agar and *Phormidium* biofilm was imaged by acquisition of T_1 -weighted images across the sample; perpendicular to flow direction, using a two-dimensional gradient echo pulse sequence, FLASH. Imaging was performed with the following imaging parameters; an echo time (TE) 2.98 ms, a repetition time (TR) 75 ms, field of view was 1 cm x 1 cm, with imaging matrix of 200 x 100 pixels, giving an in-plane resolution of $50 \mu\text{m} \times 100 \mu\text{m}$ with a slice thickness of 1 mm. T_1 -weighted images were acquired with three different excitation pulse flip angles (16° , 45° , and 90°). The imaging time with each flip angle was approximately 23 s, using three signal averages.

4.3.8 Calculation of T_1 parameter maps

The calculation of T_1 parameter maps were done exactly the same way as described in section 3.3.5. Here, however, T_1 -weighted images acquired only at three flip angles in order to reduce the scan duration required to calculate a single T_1 parameter map. The known signal value of zero for 0° flip angle was also used as an additional data point to improve the curve fit as shown in figure 4.5.

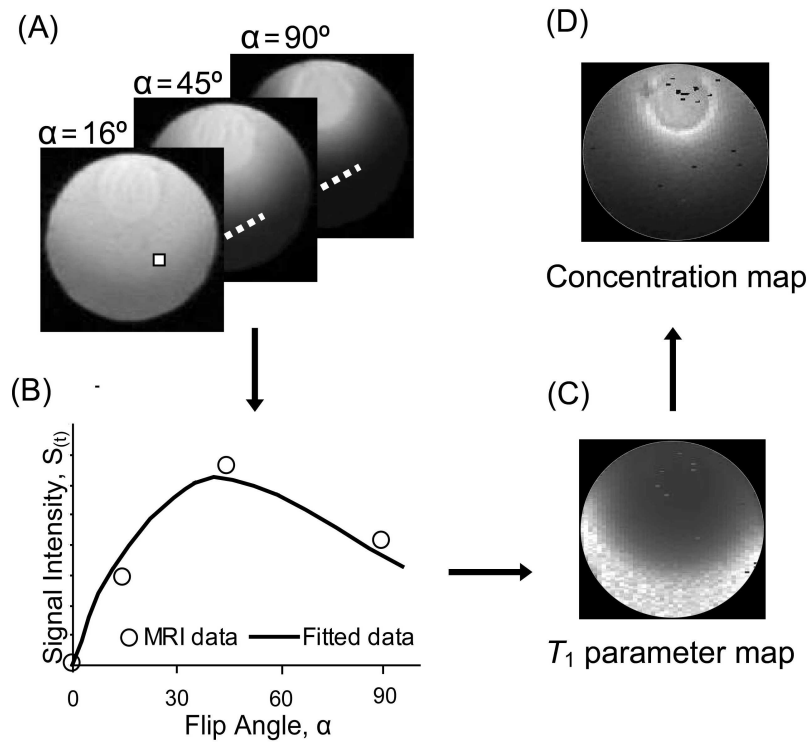


Figure 4.5. (A) For the slice across the agar, T_1 -weighted images are acquired at three different flip angles (16° , 45° and 90°). (B) For each pixel, the variation of signal intensity, $S(t)$ with respect to flip angle (α) was fitted to equation 2 in section 3.3.5, giving a T_1 value. (C) Taking the T_1 value of each pixel yields a T_1 parameter map. (D) The calibrated concentration map of Gd-DTPA inside agar.

4.3.9 Calibration of Gd-DTPA concentrations from T_1 parameter maps

The presence of paramagnetic ions, such as gadolinium (Gd^{3+}), causes a concentration dependent reduction in longitudinal relaxation time (T_1) of neighbouring 1H nuclei. This effect is represented by the equation given below (Haacke, 1999, Stanisz and Henkelman, 2000);

$$[C] = \frac{1}{R} \left\{ \frac{1}{T_{1i}} - \frac{1}{T_{10}} \right\}$$

Equation 9

where T_{10} is the relaxation time in the absence of Gd-DTPA, T_{1i} is the relaxation time in the presence of Gd-DTPA, $[C]$ denotes the concentration of the Gd-DTPA, and R is the relaxivity constant of the Gd-DTPA.

In the current study, T_{10} and T_{1i} are measured variables, as they are taken directly from T_1 parameter maps. R , however, must be determined separately in order to quantify the concentration measurements.

4.3.10 Determination of the relaxivity constant (R) of Gd-DTPA in agar and *Phormidium* biofilm

Relaxivity constant, R depends on the solids content of the sample, with R increasing approximately linearly as the solids content increases as discussed in section 3.3.7.

Thus, the relaxivity constant (R) for agar and the *Phormidium* biofilm was calculated inside the same samples by assuming the Gd-DTPA concentration at the top surface of both agar and biofilm had reached a steady state, which was equal to the concentration of the Gd-DTPA solution pumped during the experiment. Calculated values for T_{10} and T_{1i} from the top surfaces and the known concentration of pumped Gd-DTPA solution (1.8 mM) were used in equation 9 to calculate the value of R .

4.3.11 Measurement of T_2^* values with different Gd-DTPA concentrations

In order to investigate the effect of Gd-DTPA concentration upon T_2^* (apparent transverse relaxation time) values, agar samples were prepared with five different known concentrations of Gd-DTPA and the T_2^* values of each sample were measured using a multiple gradient echo sequence with an echo time (TE) of 2.5 ms and a repetition time (TR) of 3 s.

4.3.12 Modeling the transport of Gd-DTPA inside both agar and *Phormidium* biofilm

To estimate the diffusion coefficient of Gd-DTPA inside agar and determine whether the Gd-DTPA transport inside the biofilm was consistent with diffusion driven transport, the quantitative concentration profiles of Gd-DTPA inside both agar and biofilm were compared with those simulated by a mathematical model of diffusion.

Here the effect of the flow cell boundaries and the irregular domains of agar and biofilm can not be negligible when modelling the Gd-DTPA diffusion process inside both agar and biofilm. However, the degree of symmetry in the shape of agar and biofilm surface along the axis of flow allowed us to use two dimensional diffusion models.

Two dimensional finite element models for diffusion of Gd-DTPA inside agar and biofilm were implemented using COMSOL Multiphysics (3.5a). Diffusion was simulated within the agar and biofilm, i.e. the domains Ω_1 and Ω_2 as shown in figure 4.6, the geometries of which were determined from the MRI images (Fig. 4.8A and 4.10A). The boundaries of domains

were split into two parts (Fig. 4.6) so that $\partial\Omega_1 = \Gamma_1 \cup \Gamma_2$ and $\partial\Omega_2 = \Gamma_3 \cup \Gamma_4$ where Γ_1 and Γ_3 are the surfaces of agar and biofilm which are in contact with the Gd-DTPA solution. Boundaries Γ_2 and Γ_4 are the walls of the sample holder. The concentration of Gd-DTPA in the bulk liquid and hence on the boundaries Γ_1 and Γ_3 was assumed to be a constant, C^* , through time. No transport was permitted through walls, Γ_2 and Γ_4 . Hence the models were defined by;

$$\frac{\partial C(x, y)}{\partial t} = \nabla \cdot (D_{dif} \nabla C(x, y)) \quad x, y \in \Omega_1 (\Omega_2) \quad \text{Equation 10}$$

$$C(x, y) = C^* \quad x, y \in \Gamma_1 (\Gamma_3) \quad \text{Equation 11}$$

$$\frac{\partial C(x, y)}{\partial \bar{n}} = 0 \quad x, y \in \Gamma_2 (\Gamma_4) \quad \text{Equation 12}$$

Here \bar{n} is the vector normal to the boundaries (Γ_2 and Γ_4) and D_{dif} is the diffusion coefficient of Gd-DTPA, which we assume to be constant in time and space. The concentration in the bulk liquid (C^*) was 1.8 mM.

The agar model was used to estimate the diffusion coefficient of Gd-DTPA inside the agar. Concentration profiles along a straight line through the centre of the sample (Fig. 4.8F) were extracted from the MRI data at six discrete time points (1.5, 6, 9, 20, 30 and 50 minutes) and used to calibrate the model and estimate the diffusion coefficient of Gd-DTPA inside agar. The diffusion coefficient was estimated using a golden search algorithm in MATLAB, which called the COMSOL model as a subroutine. The objective function was the sum of square errors between observed and simulated concentrations and an optimum diffusion coefficient was estimated at the minimum value of this objective function.

The biofilm model was simulated using the diffusion coefficient of $6.5 \times 10^{-10} \text{ m}^2 \text{ s}^{-1}$ estimated for Gd-DTPA inside agar in this study. The diffusion coefficient from agar is used here as it is expected to be close to the unattenuated diffusion (as agar is a highly permeable, inert gel designed to give minimal resistance to diffusion). Consequently, transport rates faster than that seen in agar likely indicate a component of advective transport, while slower transport rates are indicative of attenuated diffusion. The biofilm model was undertaken purely for comparative purposes. I did not develop the complexity of the model further here, as this is beyond the scope of this experiment.

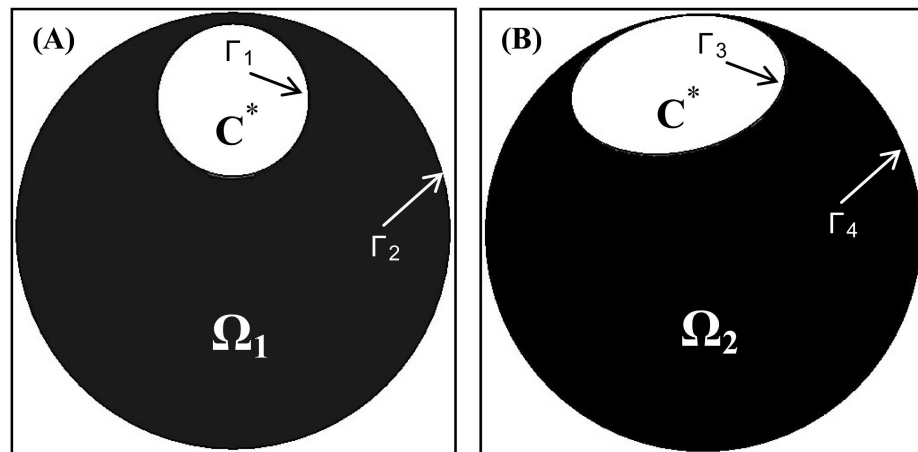


Figure 4.6. Illustrates the two dimensional model of (A) agar and (B) *Phormidium* biofilm constructed using COMSOL Multiphysics.

4.3.13 High resolution MRI of biofilm structure

T_1 , T_2 and diffusion-weighted images were collected to investigate the structure of the biofilm. The T_1 -weighted image was acquired across the sample; perpendicular to the flow direction, using a two-dimensional gradient echo pulse sequence, FLASH. Imaging was performed with the following imaging parameters; an echo time (TE) 4.7 ms, a repetition time (TR) 75 ms, flip angle 90° , field of view was 1 cm x 1 cm, with imaging matrix of 450 x 450 pixels, giving an in-plane resolution of $22 \mu\text{m} \times 22 \mu\text{m}$ with a slice thickness of 1 mm. The imaging time was approximately 9 min, using 16 signal averages.

The T_2 -weighted image was acquired across the sample; perpendicular to the flow direction, using a multislice, multispin echo, two-dimensional imaging sequence. Imaging was performed with the following imaging parameters; an echo time (TE) of 12 ms, a repetition time (TR) of 3500 ms, field of view was 1 cm x 1 cm, with imaging matrix of 256 x 256 pixels, giving an in-plane resolution of $39 \mu\text{m} \times 39 \mu\text{m}$ with a slice thickness of 1 mm. The imaging time was approximately 30 min, using 2 signal averages.

The diffusion-weighted image was acquired across the sample; perpendicular to the flow direction, using a stimulated-echo two-dimensional imaging sequence. Imaging was performed with the following imaging parameters; an echo time of (TE) 15 ms, a repetition time (TR) of 2.5 s, a gradient pulse duration of 2 ms, diffusion time interval of 13.8 ms and diffusion encoding b values of 114.22 and 414.22 s/mm^2 , field of view was 1 cm x 1 cm, with imaging matrix of 256 x 256 pixels, giving an in-plane resolution of $39 \mu\text{m} \times 39 \mu\text{m}$ with a slice thickness of 1 mm. The imaging time was approximately 17 min, using 2 signal averages.

The MR signal attenuation due to the diffusion of water is given by (Renslow et al., 2010);

$$S = S_0 \exp(-bD_{dif})$$

Equation 13

where S and S_0 are respectively the measured signal intensities with and without the applied magnetic field gradient pulses. D_{dif} is the diffusion coefficient of water and b is the diffusion weighted factor. Thus, the spatially resolved apparent diffusion coefficients of water inside the bulk liquid and biofilm were calculated by curve fitting the measured signals with above mentioned b factors to equation 13 using a least squares method. The relative apparent diffusion coefficient map (D_r map) was constructed by normalizing the calculated diffusion coefficient of water inside biofilm to that of water in the bulk liquid.

4.4 Results

4.4.1 Performance evaluation of the RF coil

Figure 4.7 shows the gradient echo images acquired of a cylindrical phantom of aqueous Gd-DTPA (1 mM), relative to the solenoid coil position. The profiles of the normalized signal intensity illustrate the image homogeneity (i.e. B_1 field homogeneity) parallel and perpendicular to the axis of the solenoid. The variations in both vertical and horizontal profiles of the normalized signal intensities perpendicular to the axis of the solenoid are well within the 10% of the maximum or minimum of the signal intensities (Fig. 4.7D and E), indicating an excellent B_1 field homogeneity perpendicular to the axis of the solenoid. However, the signal uniformities parallel to the axis of the solenoid is limited (within 10% of the minimum or maximum), indicating B_1 field homogeneity along the axis of the solenoid is limited to a distance of ± 1 mm from the centre (Fig. 4.7B). The Q-factors of the coil with and without the phantom were measured as 104 and 114.

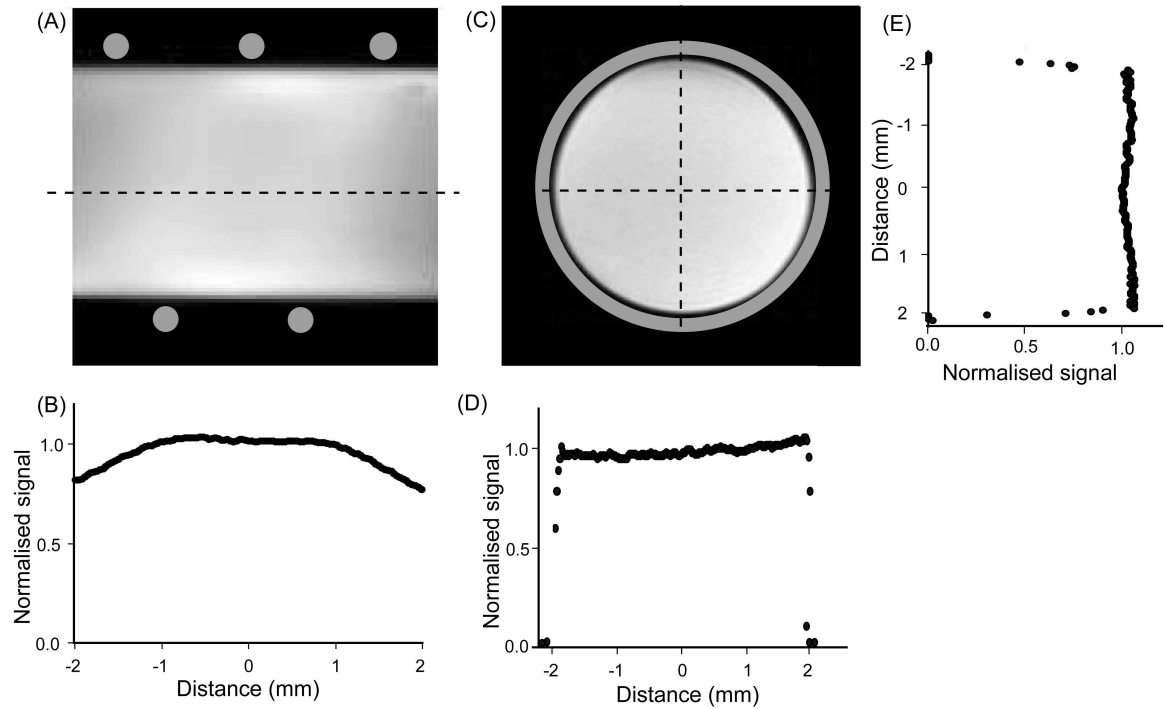


Figure 4.7. Gradient echo images of a cylindrical phantom of aqueous Gd-DTPA. (A) Signal intensity map obtained along the sample tube relative to the solenoid coil. (B) Normalized signal profile along the transect shown by the dotted line in figure 4.7A. (C) Signal intensity map obtained across the sample tube relative to the solenoid coil. (D) Normalized signal profile along the horizontal transect shown by the dotted line in figure 4.7C. (E) Normalized signal profile along the vertical transect shown by the dotted line in figure 4.7C.

4.4.2 Measured T_2^* values with different Gd-DTPA concentrations

Measured T_2^* values of agar samples prepared with five different concentrations of Gd-DTPA are given in table 4.1. Results show that T_2^* and thus $e^{(-T_E/T_2^*)}$ decreases as Gd-DTPA concentration increases.

Gd-DTPA Concentration (mM)	T_2^* (ms)	$e^{(-T_E/T_2^*)}$
0	57	0.95
0.45	37	0.92
0.9	32	0.91
1.35	24	0.88
1.8	20	0.86

Table 4.1. Variation of T_2^* and $e^{(-T_E/T_2^*)}$ values of agar samples with respect to the Gd-DTPA concentrations.

4.4.3 Diffusion of Gd-DTPA inside agar

In order to test the accuracy of the custom made RF coil for imaging transport in biofilms, the transport of Gd-DTPA inside a simple agar test system was imaged and quantified. The transport of Gd-DTPA into the agar was recorded by T_1 -weighted images at regular time intervals as shown in figure 4.8A to E. The presence of Gd-DTPA molecules shortens the T_1 value of the surrounding ^1H nuclei which increases the MRI signal; this is shown as brighter regions in the T_1 -weighted images. Thus the transport of Gd-DTPA is shown by the expansion of the brighter region into the agar (Fig. 4.8A to E). Equation 9 was then used to convert the T_1 parameter maps into actual Gd-DTPA concentration maps as shown in figure 4.8(F to J). Again, the expansion of the brighter region into the biofilm shows the transport of Gd-DTPA. Concentration profiles along the transect shown by the white line (Fig. 4.8F) at six different time intervals are shown in figure 4.9A.

Figure 4.8(K to O) shows the model for Gd-DTPA transport inside agar. The model was simulated with a diffusion coefficient estimated by fitting the model to the experimental data. When the model was fit to the experimental data, the best fit ($R^2 = 0.93$) was achieved with a diffusion coefficient for Gd-DTPA of $6.5 \times 10^{-10} \text{ m}^2 \text{ s}^{-1}$. Figure 4.9B shows the comparison of concentration profiles of experimental data along the transect shown by the white line in figure 4.8F, with the model data along the same transect as that in figure 4.8K.

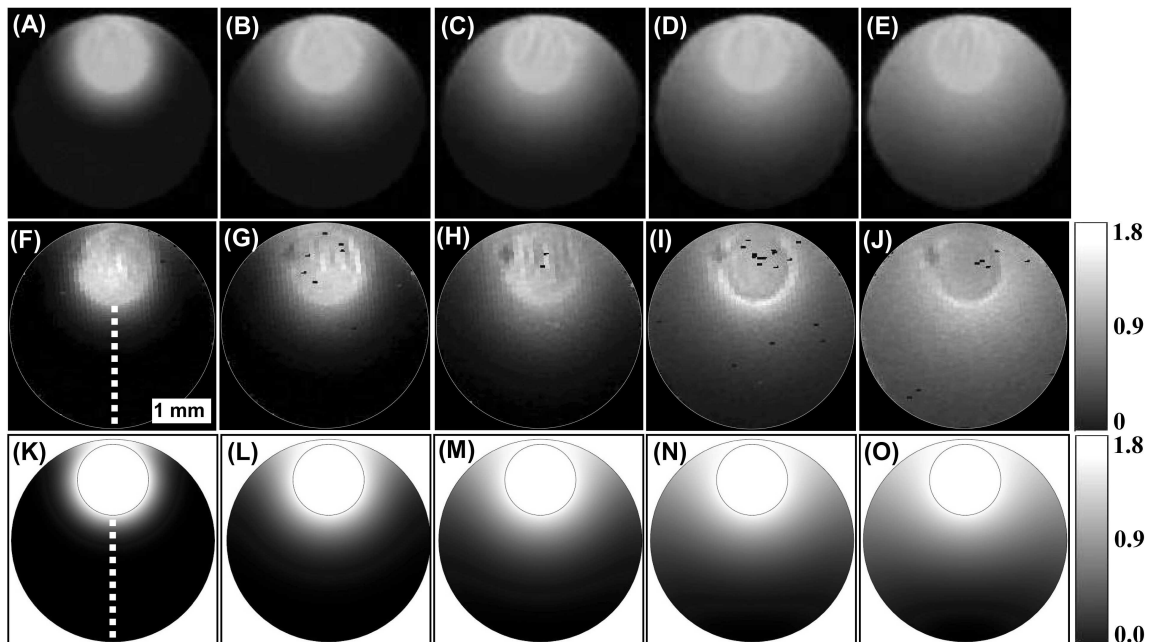


Figure 4.8. Transport of Gd-DTPA into the agar illustrated as T_1 -weighted images (A to E), calibrated Gd-DTPA concentration maps (F to J), and diffusion model results (K to O) at selected time intervals of 1.5, 6, 12, 25, and 55 min. The gray scale indicates the Gd-DTPA concentrations (mM) inside agar.

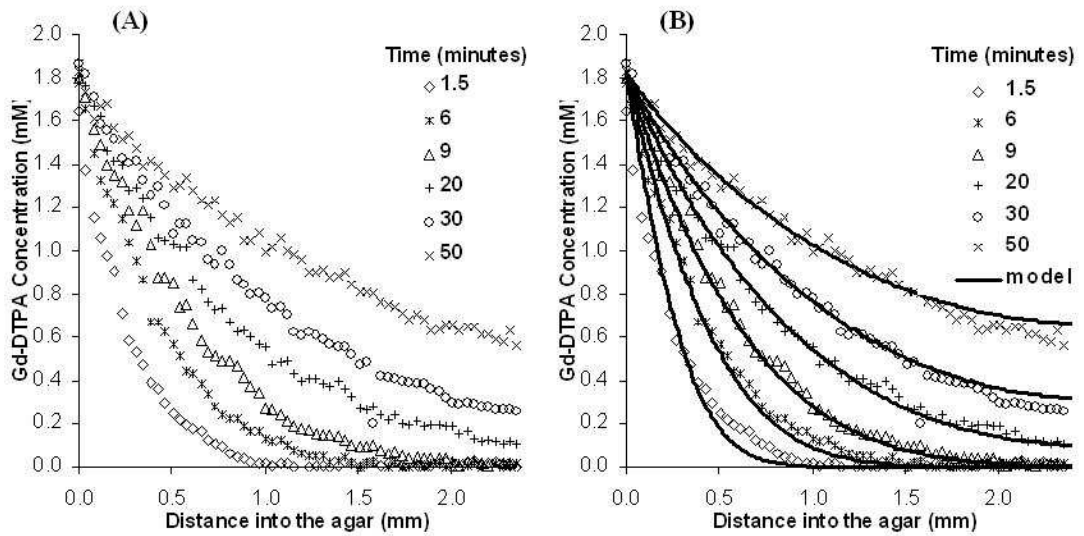


Figure 4.9. (A) Calibrated Gd-DTPA concentration profiles inside agar along the transect shown by the white dotted line in figure 4.8F at selected time intervals of 1.5, 6, 9, 20, 30 and 50 minutes. (B) Comparison between experimental and model data along the transect shown by the white line in figure 4.8F and K at same time intervals. Symbols represent experimental data, and solid lines represent model data at respective time intervals.

4.4.4 Transport of Gd-DTPA into the *Phormidium* biofilm

The transport of Gd-DTPA into the *Phormidium* biofilm was recorded by T_1 -weighted images at regular time intervals as shown in figure 4.10(A to E). Again, the increasing brightness of regions in the biofilm shows the uptake of Gd-DTPA. The calibration protocol (equation 9) was then used to convert the T_1 parameter maps into actual Gd-DTPA concentration maps as shown in figure 4.10(F to J). The transport of Gd-DTPA is shown by the increasing brightness of regions in the biofilm. Calibrated concentration profiles along the transect shown by the white line (Fig. 4.10F) at five different time intervals are shown in figure 4.11.

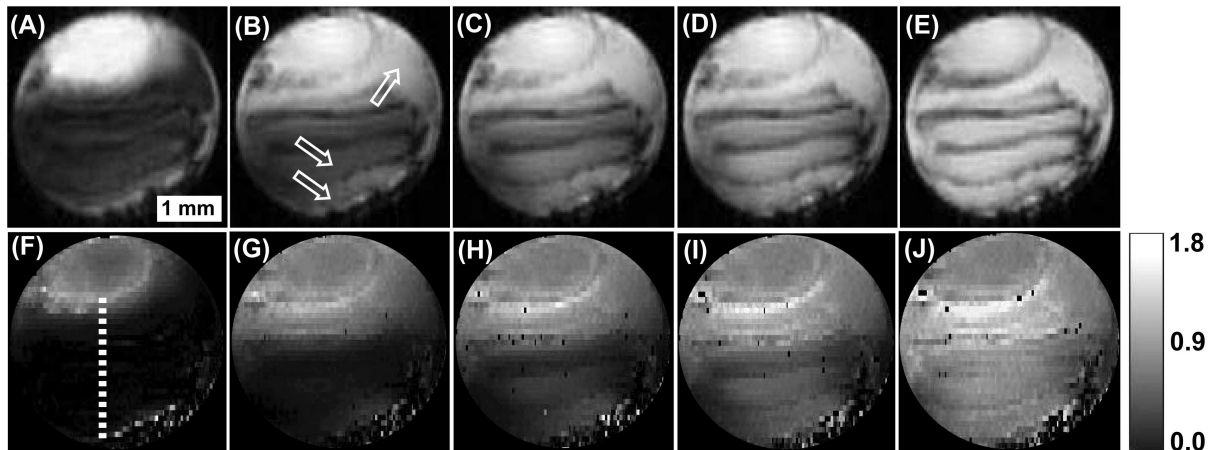


Figure 4.10. Transport of Gd-DTPA into the *Phormidium* biofilm illustrated as T_1 -weighted images (A-E) and concentration maps (F-J) at selected time intervals of 1, 5, 10, 23 and 53 minutes. The grey scale indicates the Gd-DTPA concentrations (mM). Arrows indicate the layers of biofilm where Gd-DTPA uptake is quick compared to rest of the biofilm. (Tube is 4 mm in diameter, biofilm is approximately 2.5 mm thick).

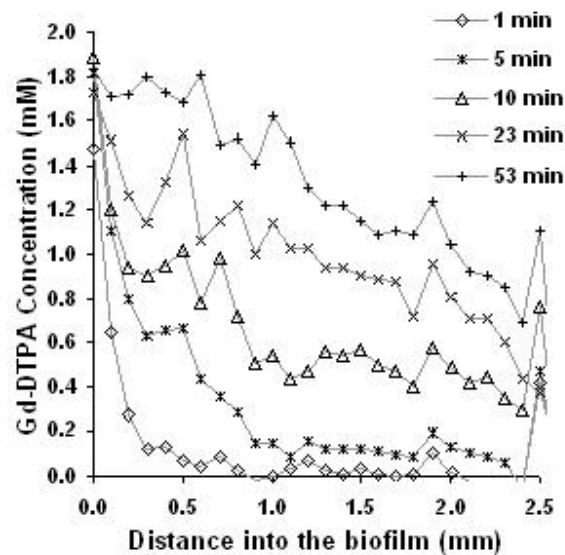


Figure 4.11. Calibrated Gd-DTPA concentrations inside the biofilm along the transect shown by the white dotted line in figure 4.10F at selected time intervals of 1, 5, 10, 23 and 53 minutes.

4.4.5 Simple 2D diffusion model of Gd-DTPA transport into the *Phormidium* biofilm

The transport of Gd-DTPA in the two dimensional diffusion model developed for the *Phormidium* biofilm is shown in figure 4.12(A to E). The model was simulated with the estimated diffusion coefficient of $6.5 \times 10^{-10} \text{ m}^2 \text{ s}^{-1}$ for Gd-DTPA inside agar. Simulated concentration profiles along the transect shown by the white line (Fig. 4.12A) at five different time intervals are compared with those of quantitative experimental data in figure 4.13.

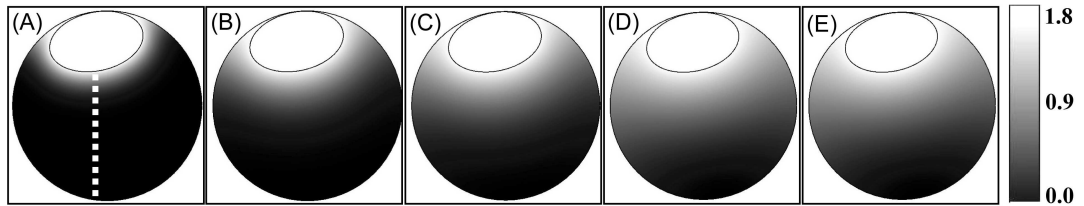


Figure 4.12. Transport of Gd-DTPA into the *Phormidium* biofilm illustrated using the two dimensional diffusion model simulated with the diffusion coefficient of $6.5 \times 10^{-10} \text{ m}^2 \text{ s}^{-1}$ (estimated for agar) at selected time intervals of 1, 5, 10, 23 and 53 minutes. Grey scale indicates the Gd-DTPA concentrations (mM).

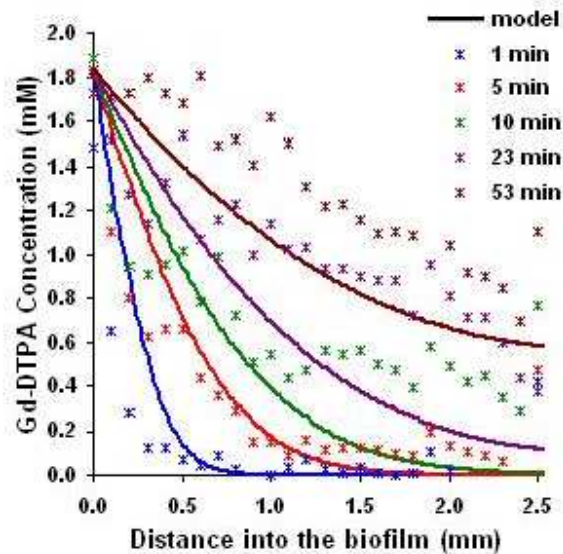


Figure 4.13. Comparison between experimental and model data (modeled at diffusion coefficient of $6.5 \times 10^{-10} \text{ m}^2 \text{ s}^{-1}$) along the transect shown by the white line in figures 4.10F and 4.12A at selected time intervals of 1, 5, 10, 23 and 53 minutes. Symbols represent experimental data, and solid lines represent model data at respective time intervals.

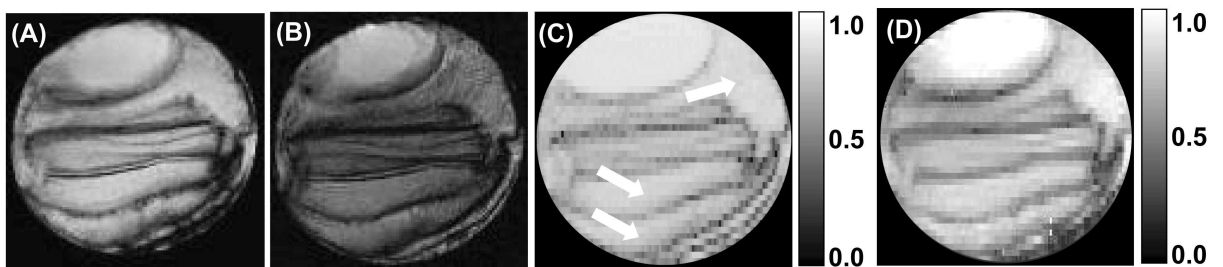


Figure 4.14. (a) T_1 and (b) T_2 -weighted images showing the structural heterogeneity of the biofilm at spatial resolutions of 22 and 39 μm respectively. (c) Map of relative apparent diffusion coefficient (D_r) showing the variations in the calculated water diffusion coefficient inside the biofilm with respect to that of bulk water. Grey scale indicates D_r . Arrows indicate the areas with relatively high water diffusion coefficients compared to the rest of the biofilm. (d) Map of relative water density showing the variations in the water content inside the biofilm with respect to that of bulk water. Grey scale indicates the relative water content.

4.4.6 MRI of biofilm structure

T_1 , T_2 and diffusion-weighted images of the biofilm were acquired to demonstrate the ability of the custom made RF coil to image biofilms with improved spatial resolutions. In figure 4.14, the structural heterogeneity of the biofilm was revealed using (A) T_1 (B) T_2 , (C) relative apparent diffusion coefficient (D_r) map and (D) relative water density map respectively. Both T_1 and T_2 -weighted images show considerable variations in the biofilm structure with layering. D_r varied throughout the biofilm, approximately ranging from 0.9 down to 0.4. The relative water density map; obtained while T_1 parameter maps were calculated, shows variations in the water content inside the biofilm.

4.5 Discussion

In this study, a custom made solenoid RF coil was successfully used to quantify the transport of Gd-DTPA into a *Phormidium* biofilm and image the structural heterogeneity of the biofilm with improved spatial resolutions. Spatial resolutions of 22 microns and 50 microns, achieved during the structural and transport imaging, are almost three times higher than the resolutions previously obtained imaging *Phormidium* biofilms employing larger commercially available RF coils (Phoenix and Holmes, 2008, Ramanan et al., 2010). Moreover, structural images acquired with improved resolution allow biofilm architecture to be related to its transport behaviour.

The accuracy of MRI transport measurements using the bespoke coil was first assessed using a simple test system composed of agar. Here the transport of Gd-DTPA inside agar was quantitatively measured and its diffusion coefficient was determined using a two dimensional mass transport model. As illustrated in figure 4.9B, the concentration profiles of the diffusion model fits well with the experimental data ($R^2 = 0.93$), illustrating transport in agar is by homogenous diffusion, which is expected for a homogeneous porous gel. Moreover, the calculated diffusion coefficient of $6.5 \times 10^{-10} \text{ m}^2 \text{ s}^{-1}$ is an acceptable estimate for the diffusivity of Gd-DTPA (molecular mass, 547 g mol^{-1}) as it is slower than lighter molecules, such as water ($D = 2.2 \times 10^{-9} \text{ m}^2 \text{ s}^{-1}$), yet faster than Magnevist, a similar but heavier Gd-labelled molecule, ($D = 2.6 \times 10^{-10} \text{ m}^2 \text{ s}^{-1}$; molecular mass, 938 g mol^{-1}) (Gordon et al., 1999). This diffusion coefficient is also very close to a previously estimated diffusion coefficient for Gd-DTPA in agar ($7.2 \times 10^{-10} \text{ m}^2 \text{ s}^{-1}$) obtained using a larger (35-mm in diameter) commercially available RF coil (Ramanan et al., 2010). This demonstrates that the custom made RF coil and

the quantification protocol were producing the expected result and could thus be applied to investigate transport of Gd-DTPA inside the *Phormidium* biofilm.

The RF coil was then successfully used to track the transport of Gd-DTPA inside the *Phormidium* biofilm as shown in figure 4.10. However, the concentration profiles of Gd-DTPA inside the biofilm (see Fig. 4.11) demonstrate that transport was not consistent with homogeneous diffusion. The shapes of the concentration curves are complex with numerous peaks and troughs as oppose to a smooth diffusion profile (see Fig. 4.11). Consequently, running the model with different diffusion coefficients cannot produce a suitable fit to the experimental data. When the model is run using the diffusion coefficient from agar (representative of unattenuated diffusion), in some places the model leads the experimental data, while in other areas it lags (Fig. 4.13). These observations indicate that Gd-DTPA transport within this *Phormidium* biofilm is more complex than simple homogeneous diffusion. These discrepancies are likely the result of heterogeneous diffusion and advection.

The map of relative apparent diffusion coefficient of water (D_r) (Fig. 4.14c) illustrates that the diffusion coefficient varies considerably throughout the biofilm. Thin layers which exhibit low D_r values (~ 0.4) correspond to thin, low intensity layers in the relative water density map (Fig. 4.14D). As low values in the water density map (i.e. ^1H density images) are indicative of areas of higher solids content, these low D_r zones must correspond with areas of higher biofilm density. Moreover the observed low intensities of these thin layers in T_2 -weighted images are also indicative of areas with higher solids content as the reduced tumbling rates of water molecules associated with solid surfaces produce lesser MR signal than free water molecules due to the increased T_2 relaxation rate of ^1H nuclei (Callaghan, 1993). The packing density of cells and extracellular polymeric substances (EPS) are known to cause differences in diffusion rates; higher packing density hinders the transport as they act as solid obstructions which increase the tortuosity of the diffusive path length (Stewart, 1998, Zhang and Bishop, 1994). Thus, areas of high solids content are also areas of low D_r .

Gd-DTPA concentration maps (Fig. 4.10F-J) indicate that the bottom two layers (indicated by open arrows) of the biofilm uptake Gd-DTPA quicker than the layer above. This is likely due to the availability of interconnected voids and channels which may have increased the transport of Gd-DTPA into the deeper layers by advection. Correspondingly, the D_r map (Fig 4.14c) shows these lower layers exhibit higher D_r relative to other areas of the biofilm. This again would suggest a more porous and open network, potentially of small channels and

interconnected voids, which could facilitate some advective transport. These structural heterogeneities are common in biofilms; the component of advective transport increasing the transport rate of solutes (including nutrients) over and above that by diffusion alone (Bishop et al., 1997, de Beer et al., 1994, Stewart, 1998). Indeed, these types of cavities have been observed previously in a laboratory grown *Phormidium* sp. biofilm (Ramanan et al., 2010).

The observed brightness along the right hand edge and base of the biofilm in T_1 -weighted image (Fig. 4.10A) suggests that Gd-DTPA transport was not only from the main source point above the biofilm but also from the edges adjacent to the substratum. This may be a channel purposefully created by the biofilm as it adapts to optimize its mass transport behavior during maturation (Beyenal and Lewandowski, 2002) or may simply results from substratum detachment.

Consequently the observed discrepancies between the experimental data and model data are due to advection of Gd-DTPA via available voids and interconnected channels and hindered diffusion of Gd-DTPA caused by the variations in packing density of cells and EPS.

In this study, the complex structure of the biofilm was imaged at resolutions of 22 and 39 μm using both T_1 and T_2 -weighted images respectively (see Fig. 4.14A and B). The observed structural heterogeneity with laminations is a common feature of phototrophic biofilms, resulting from differing cellular densities and orientations (Phoenix and Holmes, 2008). Of course the highest spatial resolution achieved (22 μm) during structural imaging could be used to quantify the transport of Gd-DTPA. However, it should be noted here that the structural image (T_1 -weighted) was acquired using more signal averages compared to those images acquired during the Gd-DTPA transport experiment. These signal averages used during the structural imaging may have compensated the reduction in SNR caused due to the increased spatial resolution (i.e. the SNR will be reduced by reducing the size of the voxel to increase spatial resolution). Higher spatial resolutions with several signal averages are achievable during concentration measurements, but this will result in an increase in scan time and thus reduce the relevance of the concentration measurements (i.e. concentrations will be changing during a single scan and thus the scan will reflect an average of a potentially large change in concentration). Thus, there is always a tradeoff between the highest spatial and temporal resolutions achievable when attempts are made to image the transport of solutes in real time.

In medical applications it is a common practice to improve temporal resolutions by assuming the term, $e^{(-T_E/T_2^*)}$ (see equation 1 in section 3.3.5), does not significantly change by the

uptake of the contrast agent. T_1 parameter maps are thus calculated using a T_1 -weighted image acquired with a single flip angle in conjunction with a proton density image acquired prior to the injection of the contrast agent (Brookes et al., 1999). This way of calculating T_1 parameter maps allows for higher temporal resolutions, as only one T_1 -weighted image with a single flip angle is required to quantify Gd-DTPA concentration at a given time. However, as shown in table 4.1, T_2^* measurements at different Gd-DTPA concentrations revealed that this assumption would not be valid for this study, as $e^{(-T_E/T_2^*)}$ did indeed change over the range of Gd-DTPA concentrations used. Consequently, this study utilized multiple flip angles to determine Gd-DTPA concentrations (Fig. 4.5), at the cost of reduced temporal resolution.

The resolutions achieved with this simple RF coil, tailored to best suit the sample geometry, makes it ideal for imaging biofilms that are on the scale of $\sim 500 \mu\text{m}$ to 5 mm. Photon based imaging methods, such as CLSM and two-photon excitation, are ideal for biofilms on the scale of tens to hundreds of microns, but are limited by biofilm thickness. Biofilm thickness attenuates light penetration, the fluorescent signal and can be hindered by poor penetration of fluorescent dyes into the sample (Barranguet et al., 2004, Paramonova et al., 2007). This can make analysis on thicker biofilms, such as those in granular reactors or phototrophic biofilms challenging (Barranguet et al., 2004, Paramonova et al., 2007). For these thicker biofilms, the use of bespoke microscopy coils for MR imaging might prove to be a valuable tool.

Overall, this study illustrates the suitability of using MRI to quantify mass transport processes of macromolecules within biofilms with bespoke solenoid RF coils. Indeed, the transport of higher molecular mass organics and nanoparticles inside real biofilms and granules could be investigated using RF coils tailored to suit different experimental requirements. One can use either purpose synthesized, tagged molecules with specific properties or the wide range of commercially available paramagnetically tagged molecules and nanoparticles to explore the impact of parameters such as molecular mass, charge, and molecular geometry or structure on transport inside different biofilms.

4.6 References

- BARRANGUET, C., VAN BEUSEKOM, S. A. M., VEUGER, B., NEU, T. R., MANDERS, E. M. M., SINKE, J. J. & ADMIRAAL, W. (2004) Studying undisturbed autotrophic biofilms: still a technical challenge. *Aquatic Microbial Ecology*, 34, 1-9.
- BARTACEK, J., VERGELDT, F. J., GERKEMA, E., JENICEK, P., LENS, P. N. L. & VAN AS, H. (2009) Magnetic resonance microscopy of iron transport in methanogenic granules. *Journal of Magnetic*

Resonance, 200, 303-312.

BEYENAL, H. & LEWANDOWSKI, Z. (2002) Internal and external mass transfer in biofilms grown at various flow velocities. *Biotechnology Progress*, 18, 55-61.

BISHOP, P. L., GIBBS, J. T. & CUNNINGHAM, B. E. (1997) Relationship between concentration and hydrodynamic boundary layers over biofilms. *Environmental Technology*, 18, 375 - 385.

BROOKES, J. A., REDPATH, T. W., GILBERT, F. J., MURRAY, A. D. & STAFF, R. T. (1999) Accuracy of T1 measurement in dynamic contrast-enhanced breast MRI using two- and three-dimensional variable flip angle fast low-angle shot. *Jmri-Journal of Magnetic Resonance Imaging*, 9, 163-171.

BUFFIÈRE, P., STEYER, J. P., FONADE, C. & MOLETTA, R. (1995) Comprehensive modeling of methanogenic biofilms in fluidized bed systems: Mass transfer limitations and multisubstrate aspects. *Biotechnology and Bioengineering*, 48, 725-736.

CALLAGHAN, P. T. (1993) *Principles of nuclear magnetic resonance microscopy*, Clarendon Press.

DE BEER, D., STOODLEY, P., ROE, F. & LEWANDOWSKI, Z. (1994) Effects of biofilm structures on oxygen distribution and mass transport. *Biotechnology and Bioengineering*, 43, 1131-1138.

GINEFRI, J. C., POIRIER-QUINOT, M., ROBERT, P. & DARRASSE, L. (2005) Contrast-enhanced dynamic MRI protocol with improved spatial and time resolution for in vivo microimaging of the mouse with a 1.5-T body scanner and a superconducting surface coil. *Magnetic Resonance Imaging*, 23, 239-243.

GORDON, M. J., CHU, K. C., MARGARITIS, A., MARTIN, A. J., ETHIER, C. R. & RUTT, B. K. (1999) Measurement of Gd-DTPA diffusion through PVA hydrogel using a novel magnetic resonance imaging method. *Biotechnology and Bioengineering*, 65, 459-467.

HAACKE, E. M., R. W. BROWN, M. R. THOMPSON, AND R. VENKATESAN (1999) *Magnetic resonance imaging: physical principles and sequence design*, Wiley-Liss.

HAASE, A., ODOJ, F., VON KIENLIN, M., WARNKING, J., FIDLER, F., WEISSER, A., NITTKA, M., ROMMEL, E., LANZ, T., KALUSCHE, B. & GRISWOLD, M. (2000) NMR probeheads for in vivo applications. *Concepts in Magnetic Resonance*, 12, 361-388.

HOLMES, W. M., MACLELLAN, S., CONDON, B., DUFES, C., EVANS, T. R. J., UCHEGBU, I. F. & SCHATZLEIN, A. G. (2008) High-resolution 3D isotropic MR imaging of mouse flank tumours obtained in vivo with solenoid RF micro-coil. *Physics in Medicine and Biology*, 53, 505-513.

MCLEAN, J. S., ONA, O. N. & MAJORS, P. D. (2008) Correlated biofilm imaging, transport and metabolism measurements via combined nuclear magnetic resonance and confocal microscopy. *Isme Journal*, 2, 121-131.

MISPELTER, J., MIHAELA, L., BRIGUET, A (2006) *NMR probeheads for biophysical and biomedical experiments*.

MISPELTER, J., MIHAELA, L. & BRIGUET, A. (2006) *NMR probeheads for biophysical and biomedical experiments*. London: Imperial College Press.

NATT, O., BEZKOROVAYNYY, V., MICHAELIS, T. & FRAHM, J. (2005) Use of phased array coils for

a determination of absolute metabolite concentrations. *Magnetic Resonance in Medicine*, 53, 3-8.

PARAMONOVA, E., DE JONG, E. D., KROM, B. P., VAN DER MEI, H. C., BUSSCHER, H. J. & SHARMA, P. K. (2007) Low-load compression testing: A novel way of measuring Biofilm thickness. *Applied and Environmental Microbiology*, 73, 7023-7028.

PHOENIX, V. R. & HOLMES, W. M. (2008) Magnetic resonance imaging of structure, diffusivity, and copper immobilization in a phototrophic biofilm. *Applied and Environmental Microbiology*, 74, 4934-4943.

RAMANAN, B., HOLMES, W. M., SLOAN, W. T. & PHOENIX, V. R. (2010) Application of paramagnetically tagged molecules for magnetic resonance imaging of biofilm mass transport processes. *Applied and Environmental Microbiology*, 76, 4027-4036.

REDPATH, T. W. (1998) Signal-to-noise ratio in MRI. *British Journal of Radiology*, 71, 704-707.

RENSLOW, R. S., MAJORS, P. D., MCLEAN, J. S., FREDRICKSON, J. K., AHMED, B. & BEYENAL, H. (2010) In situ effective diffusion Coefficient Profiles in Live Biofilms Using Pulsed-Field Gradient Nuclear Magnetic Resonance. *Biotechnology and Bioengineering*, 106, 928-937.

RIPPKA, R., DERUELLES, J., WATERBURY, J. B., HERDMAN, M. & STANIER, R. Y. (1979) Generic assignments, strain histories and properties of pure cultures of cyanobacteria. *Journal of General Microbiology*, 111, 1-61.

ROESELERS, G., VAN LOOSDRECHT, M. C. M. & MUYZER, G. (2008) Phototrophic biofilms and their potential applications. *Journal of Applied Phycology*, 20, 227-235.

STANISZ, G. J. & HENKELMAN, R. M. (2000) Gd-DTPA relaxivity depends on macromolecular content. *Magnetic Resonance in Medicine*, 44, 665-667.

STEWART, P. S. (1998) A review of experimental measurements of effective diffusive permeabilities and effective diffusion coefficients in biofilms. *Biotechnology and Bioengineering*, 59, 261-272.

VAN LOOSDRECHT, M. C. M. & HEIJNEN, S. J. (1993) Biofilm bioreactors for wastewater treatment. *Trends in Biotechnology*, 11, 117-121.

WERTH, C. J., ZHANG, C. Y., BRUSSEAU, M. L., OOSTROM, M. & BAUMANN, T. (2010) A review of non-invasive imaging methods and applications in contaminant hydrogeology research. *Journal of Contaminant Hydrology*, 113, 1-24.

WIELAND, A., DE BEER, D., DAMGAARD, L. R., KUHL, M., VAN DUSSCHOTE, D. & VAN AS, H. (2001) Fine-scale measurement of diffusivity in a microbial mat with nuclear magnetic resonance imaging. *Limnology and Oceanography*, 46, 248-259.

ZHANG, T. C. & BISHOP, P. L. (1994) Evaluation of tortuosity factors and effective diffusivities in biofilms. *Water Research*, 28, 2279-2287.

Chapter 5

Investigation of nanoparticle transport
inside coarse-grained geological media
using magnetic resonance imaging (MRI)

5

Investigation of nanoparticle transport inside coarse-grained geological media using magnetic resonance imaging (MRI)

5.1 Summary

Quantifying nanoparticle (NP) transport inside saturated porous geological media is imperative for understanding their fate in a range of natural and engineered water systems. While most studies focus upon finer grained systems representative of soils and aquifers, very few examine coarse-grained systems representative of riverbeds and gravel based sustainable urban drainage systems. In this study, we investigated the potential of magnetic resonance imaging (MRI) to image transport behaviours of nanoparticles (NPs) through a saturated coarse-grained system. MRI successfully imaged the transport of superparamagnetic NPs, inside a porous column composed of quartz gravel using T_2 -weighted images. A calibration protocol was then used to convert T_2 -weighted images into spatially resolved quantitative concentration maps of NPs at different time intervals. Averaged concentration profiles of NPs clearly illustrates that transport of a positively charged amine-functionalized NP within the column was slower compared to that of a negatively charged carboxyl-functionalized NP, due to electrostatic attraction between positively charged NP and negatively charged quartz grains. Concentration profiles of NPs were then compared with those of a convection-dispersion model to estimate coefficients of dispersivity and retardation. For the amine functionalized NPs (which exhibited inhibited transport), a better model fit was obtained when permanent attachment (deposition) was incorporated into the model as oppose to non-permanent attachment (retardation). This technology can be used to further explore transport processes of NPs inside coarse-grained porous media, either by using the wide range of commercially available (super)paramagnetically tagged NPs or by using bespoke tagged NPs.

5.2 Introduction

Nanoparticles (NPs) are utilized in a tremendously diverse array of applications, including cosmetics, optics, medical technology, textiles and catalysts (Dawson, 2008, Handy et al., 2008, Theron et al., 2008). As a result of their versatility, the market for nanomaterials continues to grow rapidly and is expected to approach a global value of \$27 billion by 2013 (<http://www.bccresearch.com/report/NAN004J.html>). Problematically, once released into the aquatic environments such as ground and surface water systems NPs can have a diverse range of toxic effects. Ecotoxicological studies demonstrate exposure of aquatic organisms to nanoparticles can produce highly deleterious effects which include vascular and respiratory injury, brain and liver damage, delayed embryonic development and death (Handy et al., 2008, Sánchez et al., 2011). In contrast to the unintentional release of manufactured NPs, due to their high reactivity and high surface area to volume ratio, NPs are also being designed for in-situ remediation of contaminants such as toxic metal ions, radionuclides, organic and inorganic solutes, non-aqueous phase liquids and microorganisms in various water systems (Liu et al., 2005, Sánchez et al., 2011, Zhang, 2003). However, the physicochemical properties such as structure, size, composition and surface charge of NPs and their surrounding environment influence the transport behaviours of NPs (Handy et al., 2008, Tiraferri and Sethi, 2009). Therefore, investigating the influence of such properties upon NP transport is imperative to understand and predict their fate inside saturated porous geological media such as aquifers, soils, riverbeds and engineered drainage systems. Recognizing the importance of investigating NP transport, researchers have already used several methods as described in section 1.2.2. MRI has also already been used to investigate several aspects of porous matrices as disused in section 1.2.3.

The aim of this study was to demonstrate the potential of MRI to image nanoparticle transport through coarse-grained geological media. While most investigations of NP transport focus upon finer grained systems common to aquifers and soils, there is a dearth of information on NP transport on coarser grained systems relevant to riverbeds and the gravel matrices of sustainable urban drainage systems (SUDS). Thus, here, we focus upon NP transport through a coarse-grained gravel matrix.

In this study, a negatively charged *Molday ION (Carboxyl)* and a positively charged *Molday ION (C6Amine)*, which are commercially available iron oxide based MRI compatible NPs, 35 nm in diameter, were used to investigate the effect of surface charge upon their transport

inside a porous column made up with negatively charged rose quartz grains. Here the quartz gravels were used to replicate a natural or engineered aquatic environment containing unconsolidated gravels such as a river bed or SUDS. NPs are released into such aquatic environments via either direct urban runoff (e.g. rainstorm), (Kiser et al., 2009, Wang et al., 2008) or poorly treated effluent discharges from waste water treatment plants (Kiser et al., 2009, Limbach et al., 2008). Consequently, the investigations of transport and retention behaviours of NPs in such systems are vital to design effective remediation strategies.

The iron-oxide core of the NP makes the NP superparamagnetic (Lawaczeck et al., 2004) and thus its presence causes a concentration dependent shortening of the transverse relaxation time (T_2) of surrounding ^1H nuclei of the water (H_2O) molecules. This creates a noticeable reduction of the MRI signal in a T_2 -weighted image. Moreover, the actual concentrations of the NP can be determined, as the reduction in the transverse relaxation rates have a linear relationship with the concentration of the NPs. Therefore, MRI can be used not only to track but also to quantify the transport of NPs inside saturated porous columns.

In this study, we aimed to demonstrate the suitability of using MRI for quantifying NP transport inside porous matrices; hence it's potential for transport analysis of nanoparticles with different physicochemical properties inside complex packed columns. Moreover, the profiles of time varying concentrations of NPs were compared with those of a transport (convection-dispersion) model developed using a finite element modelling software to not only validate the often used homogenous assumption to predict transport inside porous columns but also to check the accuracy of this MRI method in quantifying NP transport.

5.3 Materials and methods

5.3.1 Porous column and nanoparticles

The heterogeneous porous column employed in this study was made up with randomly packed subangular spherical shape rose quartz grains (2.5 mm to 4.5 mm grain size distribution) with a median size of diameter (d_{50}) 3.5 mm (measured using sieve analysis) inside a cylindrical polypropylene column with the dimensions of 4.5 cm internal diameter and 10 cm height (Fig. 5.1a). A porous sintered glass diffuser plate was placed on the inlet end cap to provide an evenly distributed inflow of nanoparticle solution. Prior to the experiment rose quartz grains were washed using deionised water. The column was first filled with deionised water and then

packed with rose quartz grains in order to avoid air bubble formation. Quartz grains were packed only up to the bottom of the top end cap. Quartz grains are negatively charged at experimented pH conditions (Jada et al., 2006). Commercially available iron oxide based MRI compatible NPs (<http://www.biopal.com/>); positively charged *Molday ION*, *C6Amine* (functionalized with surface amine group) and negatively charged *Molday ION*, *Carboxyl* (functionalized with surface carboxyl group), both 35 nm in diameter were used in this study.

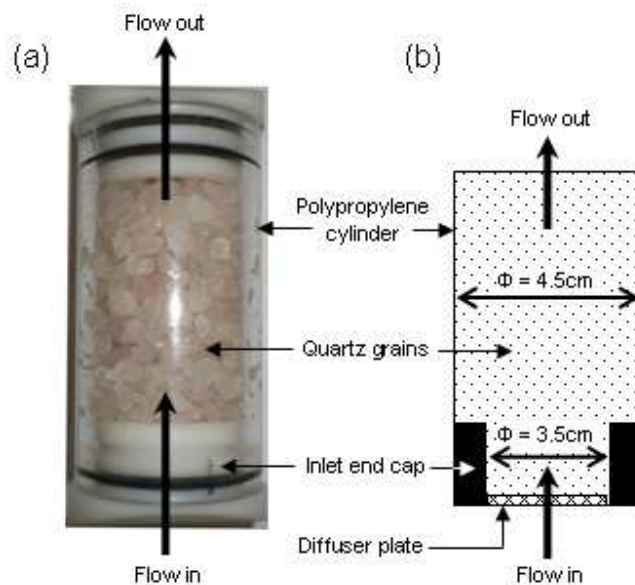


Figure 5.1. (a) The Photograph of the experimented porous column. (b) Cross section of the porous column illustrating the diffuser plate and inlet end cap arrangement.

5.3.2 Transport experiment

The saturated porous column was then vertically positioned at the centre of the MRI bore. The porous column was first connected to an 18-M Ω water supply and slowly washed with deionised water at a flow rate of 1ml/min using a HPLC pump (Agilent, 1100 Series). The system was kept under pressure to avoid air bubble formation inside the column.

During the column experiment, an inlet solution of 0.1mM *Molday ION*, *Carboxyl* was first pumped into the packed column at a flow rate of 1 ml min⁻¹ for approximately 90 minutes and MR imaging was performed every five minutes to record the transport of *Carboxyl* NP. The packed column was then flushed with deionised water for nearly 3 hours in order to remove all the *Carboxyl* NP. An inlet solution of 0.1mM *Molday ION*, *C6Amine* was then pumped into the packed column at flow rate of 1 ml min⁻¹ for approximately 90 minutes and MR imaging was performed every five minutes to record the transport of *C6Amine* NP.

5.3.3 MRI

The MRI experiments were performed on a Bruker Avance BioSpec system, using a 30 cm-bore, 7T superconducting magnet (Bruker BioSpin, Karlsruhe, Germany). A Bruker micro-imaging gradient insert (model BGA-20) and 200-A gradient amplifiers were used to provide strong linear magnetic field gradient pulses of up to 200 mT m^{-1} , thus allowing the system to perform micro-imaging experiments. A Bruker 152 mm diameter birdcage RF volume resonator was used to excite and detect the ^1H signal.

Here, MRI was used to acquire spatially and temporally resolved T_2 -weighted images of the column while nanoparticles were transported through the column. In the absence of *Molday ION* NPs, the T_2 value of ^1H nuclei of water molecules at any location inside the column is influenced by the spin-spin interactions between near by ^1H nuclei, magnetic field inhomogeneities and surface relaxation effects caused due to the presence of quartz gravel. However, the presence of *Molday ION* NPs will alter the T_2 value, the change in the T_2 values upon the uptake of *Molday ION* NPs is then known to be solely due to the presence of NPs. Consequently, T_2 -weighted images can be used to track the transport of *Molday ION* NPs inside the column. T_2 -weighted images acquired before and after introducing NPs can also be used to quantify concentrations of *Molday ION* NPs as the change in the transverse relaxation rates has a linear relationship to the NP concentration.

5.3.4 Acquisition of T_2 -weighted images

The transport of *Molday ION* NPs inside the column was imaged by acquisition of T_2 -weighted images using a two-dimensional Rapid Acquisition Relaxation Enhancement (*RARE*) pulse sequence. Images were obtained along the column (parallel to the flow direction) in 11 adjacent slices (Fig. 5.2a). Experiments were performed with the following imaging parameters; echo time (TE) 60.9 ms, repetition time (TR) 10000 ms with a *RARE* factor of 16, field of view was 9 cm x 6 cm, imaging matrix was 300 x 192 pixels, giving an in-plane resolution of $300 \mu\text{m} \times 300 \mu\text{m}$ with a slice thickness of 1 mm. The imaging time was approximately 2 minutes, using a single signal average. These imaging parameters were kept identical during the entire experiment in order to obtain comparable T_2 -weighted images.

5.3.5 Determination of the relaxivity constant (R) of nanoparticles

Molday ION nanoparticles are classified as a darkening contrast agent acting through the T_2 relaxation process (<http://www.biopal.com/>), and thus their presence inside the porous column causes a concentration dependent linear increase in the transverse relaxation rates of the surrounding ^1H nuclei as described in equation 1.

$$[C] = \frac{1}{R} \left(\frac{1}{T_{2i}} - \frac{1}{T_{20}} \right)$$

Equation 1

where T_{20} is the relaxation time in the absence of NP, T_{2i} is the relaxation time in the presence of NP, $[C]$ denotes the concentration of the NP, and R is the relaxivity constant of the NP.

The relaxivity constants (R) were measured using five NP solutions at different NP concentration prepared for both *Molday ION*, *Carboxyl* and *C6Amine* NPs. T_2 values of each sample were measured using multiple spin echo pulse sequence with the following imaging parameters; echo time (TE) 9.2 ms, repetition time (TR) 15000 ms and 200 echoes with two signal averages. Then, plots of $(1/T_{2i} - 1/T_{20})$ versus NP concentration for both *Carboxyl* and *C6Amine* NPs were plotted separately and the relaxivity constants were determined by fitting equation 1 to the data using linear least squares method.

5.3.6 Calibration of nanoparticle concentration using T_2 -weighted images

The signal intensity, S obtained using a *RARE* pulse sequence is given by (Haacke, 1999);

$$S = S_0 \left[1 - \exp\left(\frac{-TR}{T_1}\right) \right] \exp\left(\frac{-TE}{T_2}\right)$$

Equation 2

where S_0 is the maximum signal intensity, TR denotes the repetition time (the time interval between two successive excitation pulses), TE is the echo time (the time interval between the excitation and signal readout center), T_1 is the longitudinal relaxation time, and T_2 is the transverse relaxation time.

As shown in equation 2, the change in the signal intensity due to the presence of paramagnetic ions is complex and might depend on both T_1 and T_2 relaxation times. However, the *RARE* pulse sequence can be used to produce T_2 -weighted images with carefully chosen image

sequence parameters, such as a sufficient recycle time between scans (TR) and fairly long echo time (TE). In a T_2 -weighted image, the signal decay due to the presence of *Molday ION* NPs at a particular concentration C_i is given by;

$$\frac{S}{S_0} = \exp\left(\frac{-T_E}{T_{2i}}\right)$$

Equation 3

where S/S_0 is the ratio between the signals measured with and without *Molday ION* NPs, known as the normalized signal and T_{2i} is the transverse relaxation time with *Molday ION* NPs at C_i concentration.

Therefore, T_2 -weighted images acquired before and after introducing the NPs can be used to quantify NP concentration using the calibration equation 4; obtained combining equations (1) and (3).

$$C = \left[\left(\ln\left(\frac{S}{S_0}\right) / -T_E \right) - 1/T_{20} \right] \cdot \frac{1}{R}$$

Equation 4

5.3.7 Modelling the transport of NPs inside the porous column

To determine the transport properties of the porous column and NPs such as coefficients of dispersivity and retardation, the NP concentration data obtained using MRI was compared to those simulated by a convection-dispersion mathematical model of NP transport. The shape of the experimented column is variable in space (Fig. 5.2a), and therefore, it is not possible to represent the NP transport by a one-dimensional convection-dispersion equation. However, the cylindrical shape of the column enables us to use a two dimensional axis-symmetric model. The finite element model for NP transport inside the porous column was implemented using COMSOL Multiphysics 3.5a. The model domain, Ω is shown in figure 5.2d, which was determined from the actual column geometry (see Fig. 5.1b).

By assuming the column as homogenous with constant porosity, the transport of NP with retardation was defined by (Fetter, 1994),

$$R \frac{\partial C(x, y)}{\partial t} = \nabla \cdot [D_{dis} \nabla C(x, y)] - U \cdot \nabla C(x, y) \quad x, y \in \Omega$$

Equation 5

$$D_{dis} = \begin{pmatrix} D_T & 0 \\ 0 & D_L \end{pmatrix}$$

Equation 6

$$U = \begin{pmatrix} u & 0 \\ 0 & v \end{pmatrix}$$

Equation 7

where C is the NP concentration, D_T is the transverse dispersion coefficient, D_L is the longitudinal dispersion coefficient, u is the transverse pore velocity, v is the longitudinal pore velocity and R is the retardation coefficient.

For negligible molecular diffusion, lateral and transverse dispersion coefficients can be defined as,

$$D_L = \alpha_L v$$

Equation 8

$$D_T = \alpha_T u$$

Equation 9

where α_L is the longitudinal dispersivity and α_T is the transverse dispersivity of the porous column.

The pore velocity can not be assumed constant throughout the column as the cross sectional area of the column was variable in space (see Fig. 5.1b). Hence, the velocity field inside the column was first determined by solving the momentum balance for NP transport using the Brinkman equation (Pop, 2002) and the continuity equation.

$$-\frac{\eta}{\phi} \nabla^2 U + \nabla P = -\frac{\eta}{k} U$$

Equation 10

$$\nabla \cdot U = 0$$

Equation 11

where U is the velocity, η is the viscosity of the NP solution, k is the permeability of the porous column, ϕ is the porosity of the packed column and P is the pressure.

The permeability value of $1 \times 10^{-7} \text{ m}^2$ is representative of the column made up of unconsolidated well sorted quartz gravel (Bear, 1972). The average porosity value of 0.4 was estimated using the MRI measurements (Fig. 5.6). The Brinkman equation, an extension of Darcy's law, was used to account for any viscous effect that the high hydraulic permeability of

the column may cause; mainly around the corners of the changing geometry interface (Fig. 5.2). However, slip boundary conditions were used at walls of the column in order to represent the plug flow of NPs observed in the MRI data.

The evaluated velocity field was then used in the convection-dispersion equation (equation 5) to determine the transport of NPs. The boundary conditions employed during the simulation are given in table 5.1. The ratio of grain size to column size was large enough that elements in the finite element model of the column were inevitably smaller than a representative elementary volume for the media. This meant that the model was unlikely to capture the finer detail of the movement of fluid and NPs; the aim was to capture the movement of the NP front and the longitudinal gradients in concentration. Thus, transverse dispersivity was assumed high and the longitudinal dispersivity of NPs was calibrated. The concentrations measured by MRI displayed almost no transverse gradients, which bears out this assumption.

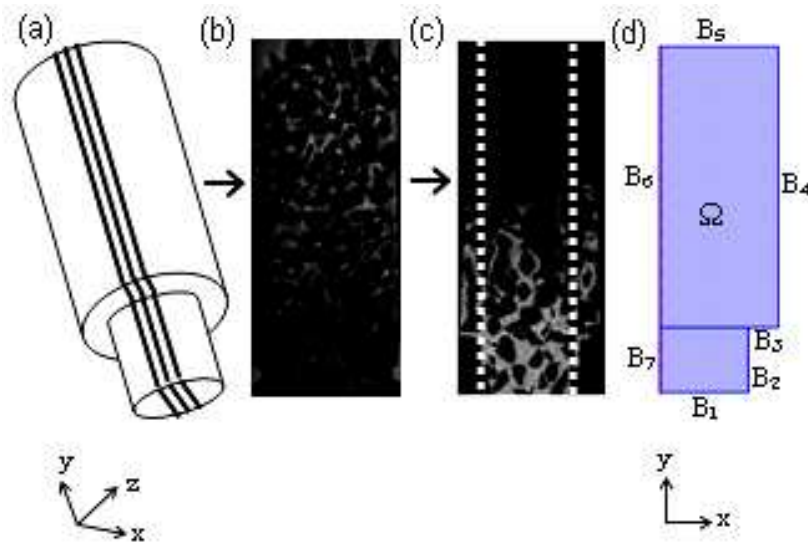


Figure 5.2. (a) For the slice along the porous column, T_2 -weighted image (b) is acquired using two dimensional RARE sequence. Acquired T_2 -weighted images with and without the NPs were used to calibrate the NP concentration map (c) using equation 4. (d) The two dimensional axis symmetry geometry used to model NP transport in the porous column.

First the model was used to estimate the longitudinal dispersivity of the porous column using the quantitative concentration data of *Carboxyl* NP by assuming there is no retardation (i.e. $R = 1$) as both rose quartz and *Carboxyl* NP are negatively charged. The estimated effective dispersivity of the column was then used in the model to estimate the retardation coefficient for the *C6Amine* NP as positively charged *C6Amine* NP is expected to be retarded inside the column made up by negatively charged rose quartz.

Coefficients of dispersivity and retardation were estimated by calibrating the model using respectively the averaged concentration profiles of *Carboxyl* and *C6Amine* NPs along the flow axis (y axis), extracted at seven discrete time points (5, 10, 15, 25, 40, 60 and 80 minutes). The averaged concentration profiles of the NPs along the flow axis were determined by averaging the spatially resolved two dimensional concentration data of NPs from all eleven slices (Fig. 5.2a) and within the area shown by white dotted lines (Fig. 5.2c). The concentration data was averaged only within the region shown in figure 5.2c in order to avoid any edge effect that the change in the geometry of the porous column could cause. Here, the dispersivity and retardation coefficients were estimated using a Golden search algorithm in MATLAB, which called the COMSOL model as a subroutine; where the objective function was the sum of square errors between observed and simulated concentrations. The optimum values of coefficients were estimated at the minimum value of this objective function.

Boundary	Boundary condition	
	Momentum balance	Mass balance
B1	Inlet – velocity	Inlet - concentration
B2	Wall - slip	Wall – insulation
B3	Wall - slip	Wall – insulation
B4	Wall - slip	Wall – insulation
B5	Outlet – pressure	Outlet - convective flux
B6	Symmetry – axial symmetry	Symmetry - axial symmetry
B7	Symmetry – axial symmetry	Symmetry - axial symmetry

Table 5.1. Boundary conditions used in the model to simulate the NP transport inside the column

The variation in the average porosity of the column along the flow axis, for all eleven slices and within the area shown by white dotted lines (see Fig. 5.2c) was determined using T_2 -weighted images obtained with pure water. An algorithm was used to calculate the porosity by dividing the number of water carrying pixels by total number of pixels. 'Pixels on water generate significantly larger MR signals than pixels on the grains. Thus a reasonable threshold for MR signal was used to distinguish water carrying pixels.

It should be noted here that negatively charged quartz grains may cause permanent attachment (deposition) of positively charged *C6Amine* NPs. However, the retardation coefficient, R , calculated above assumes non-permanent attachment. Hence, a permanent attachment (deposition) term (Baumann and Werth, 2005) was explicitly incorporated into the model (see equation 12) to investigate whether any observed discrepancies between the experimental data and model may be due to permanent attachment.

$$R \frac{\partial C(x, y)}{\partial t} = \nabla \cdot [D \nabla C(x, y)] - U \cdot \nabla C(x, y) - kC; \quad x, y \in \Omega$$

Equation 12

where k is the deposition rate constant.

5.4 Results

5.4.1 The relaxivity constant (R) of *Molday ION* NPs

The change in transverse relaxation rates ($1/T_{2i} - 1/T_{20}$) has a linear relationship with the concentration of the NPs as shown in figure 5.3. From the slope of figure 5.3, the relaxivity constant R , for *Carboxyl* and *C6Amine* NPs are determined as $109 \text{ mM}^{-1} \text{ s}^{-1}$ (with 95% confidence interval of $107 - 111 \text{ mM}^{-1} \text{ s}^{-1}$) and $81 \text{ mM}^{-1} \text{ s}^{-1}$ (with 95% confidence intervals of $79 - 83 \text{ mM}^{-1} \text{ s}^{-1}$) respectively.

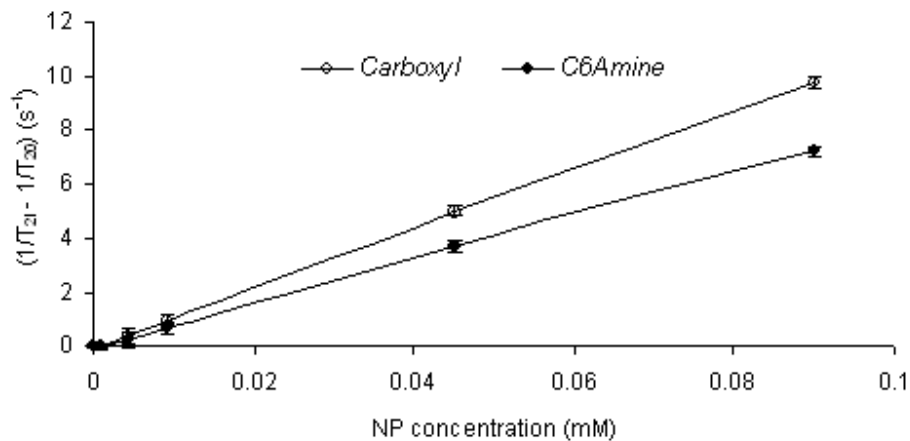


Figure 5.3. Variation in the change of transverse relaxation rates ($1/T_{2i} - 1/T_{20}$) with respect to both *Molday ION Carboxyl* and *C6Amine* NP concentration.

5.4.2 Transport of *Molday ION* nanoparticles inside porous column

The transport of *Molday ION* NPs into the porous column was recorded by T_2 -weighted images. The presence of *Molday ION* NPs are shown less intense (darker) in a T_2 -weighted image, as they reduce the MRI signal and thus the transport of *Carboxyl* NP is shown by expansion of the darker region up into the column (see Fig. 5.4a to c). The quantitative concentration maps of *Carboxyl* NP calibrated using equation 4 are shown in figure 5.4d to f. Here, the expansion of the brighter region up into the column illustrates the transport of NP. Figure 5.4g to i show the convection-dispersion model generated with the estimated

dispersivity using *Carboxyl* NP concentration data. The averaged concentration profiles of both *Carboxyl* and *C6Amine* NPs along the flow direction at selected five different time intervals are shown in figure 5.5. Variation in the averaged porosity (along the flow direction) with respect to the column length is shown in figure 5.6. Here the mean value of the porosity is 0.38 (with 95% confidence interval of 0.32 - 0.44). The porosity was averaged only within the region shown in figure 5.2c in order to avoid any edge effect.

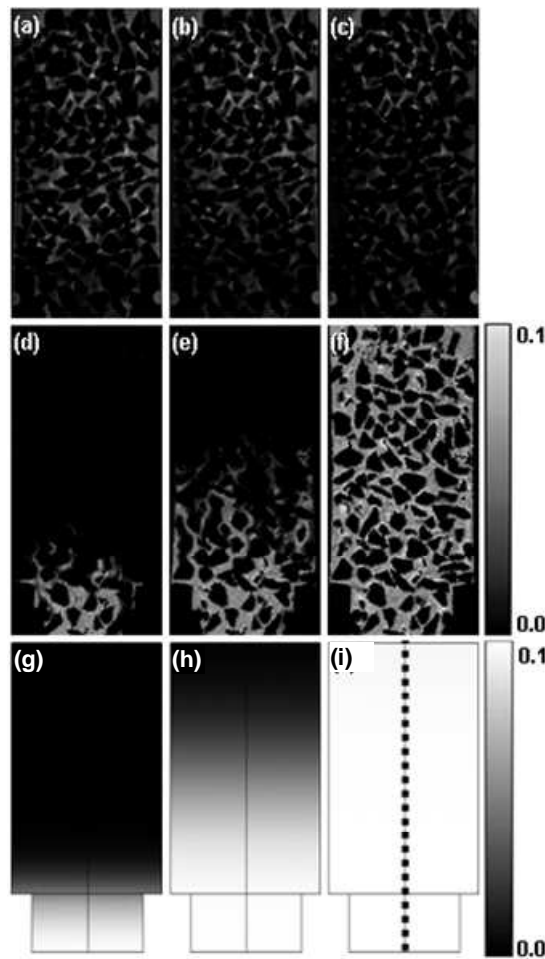


Figure 5.4. (a to c) T_2 -weighted images, (d to f) calibrated concentration maps of *Carboxyl* NP transport inside the column and (g to i) convection-dispersion model results at selected time intervals of 5, 25, and 80 minutes respectively. The gray scale indicates the NP concentration (mM). NP transport direction is from bottom to top.

5.4.3 Comparison of experimental data with model data

Figure 5.7 shows the comparison of averaged concentration profiles of *Carboxyl* NPs along the flow direction, with the model data along the transect shown in Fig. 5.4i. A dispersivity coefficient of 3.5×10^{-3} m for the column was estimated by calibrating the model using

concentration profiles, giving a goodness-of-fit value (R^2) of 0.97. Figures 5.8A and B show the comparison of averaged concentration profiles of *C6Amine* NPs along the flow direction, with the model data along the transect shown in Fig. 5.4i. A retardation coefficient (non-permanent attachment; equation 5) of 1.27 for the *C6Amine* NP was estimated by calibrating the model using concentration profiles, giving a goodness-of-fit value (R^2) of 0.9 (see Fig. 5.8A). When permanent attachment (deposition) was incorporated into the model, a deposition rate constant of 1.09×10^{-4} and retardation coefficient of 1.02 for the *C6Amine* NP was estimated, giving an improved goodness-of-fit value (R^2) of 0.95 (see Fig. 5.8B).

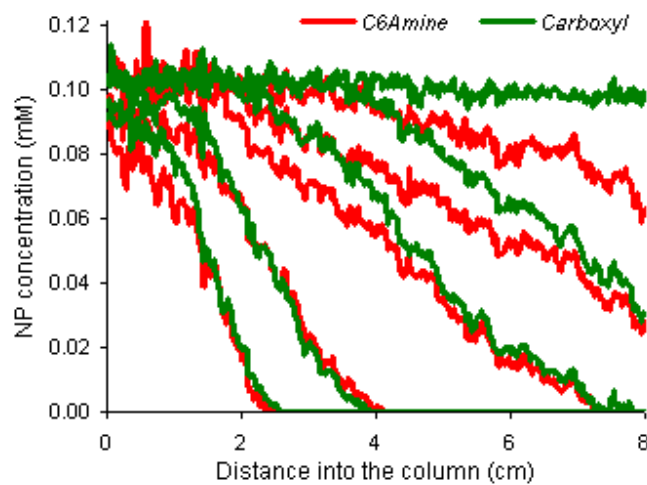


Figure 5.5. Averaged concentration profiles of both *Carboxyl* and *C6Amine* NPs, along the flow direction at selected time intervals of 5, 10, 25, 40 and 80 minutes.



Figure 5.6. Variation in the averaged porosity within the area shown in Fig. 5.2c with respect to the column length.

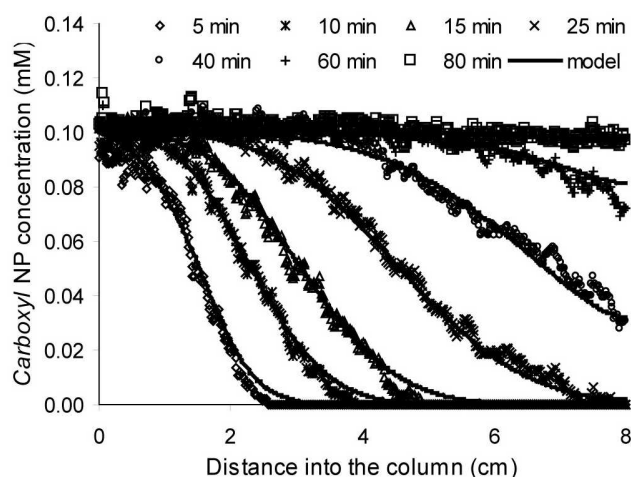


Figure 5.7. Transport of *Molday ION Carboxyl* NPs inside the porous column is compared to the model data in order to estimate the coefficient of dispersivity at time intervals of 5, 10, 15, 25, 40, 60 and 80 minutes. Symbols represent experimental data, and solid lines represent model data.

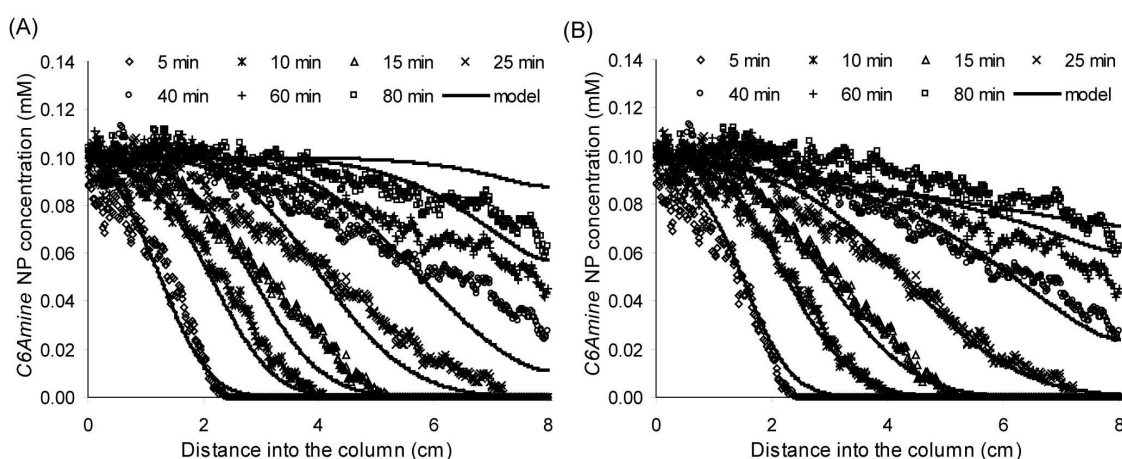


Figure 5.8. Transport of *Molday ION C6Amine* NPs inside the porous column is compared to the model data modeled with (A) retardation and (B) retardation and deposition in order to estimate the coefficients of retardation and deposition constant at time intervals of 5, 10, 15, 25, 40, 60 and 80 minutes. Symbols represent experimental data, and solid lines represent model data.

5.5 Discussion

In this study, MRI was successfully used to quantitatively measuring the time-varying, spatially distributed concentrations of *Molday ION Carboxyl* and *C6Amine* nanoparticles (NPs) as they were transported into a porous column made up with rose quartz grains. As shown in figure 5.5, the averaged concentration profiles for both *Molday ION* NPs clearly illustrates that transport of *C6Amine* NP within the porous column, was slower compared to that of *Carboxyl* NP. This is most likely due to the effect of transport inhibition caused by the adsorption of positively charged *C6Amine* NP onto to the negatively charged quartz grains.

As illustrated in figure 5.7, the concentration profiles of the model match well with the averaged concentration profiles quantified using MRI, illustrating the transport of *Carboxyl* NP inside the column was without retardation as expected for negatively charged *Carboxyl* NP inside a column containing negatively charged rose quartz. The estimated dispersivity of the experimented porous column was 3.5×10^{-3} m, which is similar to the experimental results published elsewhere. Khrapitchev and Callaghan (Khrapitchev and Callaghan, 2003) pool data from a variety of previous studies to derive a relationship between dispersivity and characteristics of porous media. For packed spherical beads with diameter equal to the median diameter (d_{50}) of the rose quartz gravels used here their relationship yields a value of 2.5×10^{-3} m. This corroborates the accuracy of this MRI approach in quantifying NP concentrations inside coarse-grained porous media.

When the *C6Amine* results were modeled using non-permanent attachment, an estimated effective retardation coefficient of 1.27 was estimated, suggesting that transport of *C6Amine* NP was not highly retarded by the rose quartz grains. However, there were discrepancies between this model and the data (goodness-of-fit, R^2 of 0.9) indicating the transport of *C6Amine* inside the porous column can not be explained purely by this model (see Fig. 5.8A). Consequently, a permanent attachment (deposition) term was incorporated into the model, giving a much better fit (goodness-of-fit, R^2 of 0.95) (see Fig. 5.8B). This indicates that electrostatically favourable conditions have caused permanent attachment of *C6Amine* NPs inside the column. When electrostatic conditions are favorable, permanent attachment of NPs onto mineral grains is known to occur (Darlington et al., 2009). Moreover, when deposition is incorporated into the model, the retardation coefficient (non-permanent attachment) drops from 1.27 to 1.02, illustrating the importance of deposition of *C6Amine* NPs inside a column packed with oppositely charged quartz grains.

Overall, this study illustrates the suitability of this approach in water research to spatially resolve the transport behaviours of different NPs inside saturated coarse-grained systems. The spatially and temporally resolved data was successfully described using reaction transport models, giving goodness-of-fit values of 0.95 or better. This illustrated the robustness of this approach, and thus more complex systems requiring, potentially, more complex modelling approaches could now be explored in future. Therefore, the ability of MRI to image NP transport inside packed columns will enable us to build more complex and heterogeneous packed columns, and thus unravel how these heterogeneities impact NP transport. Indeed, a wide range of paramagnetic and superparamagnetic NPs are commercially available to explore

the impact of parameters such as molecular mass, shape and surface charge on their transport. While the current set-up utilizes a typical vertical packed column, the system could easily be modified into a horizontal arrangement similar to a flume, with NP dosed water flowing over the top of the gravel matrix. This would enable better simulation of NP transport in riverbeds.

Therefore, the use of MRI has the potential to significantly improve our understanding of the way NPs are transported inside porous geological media.

5.6 References

- BAUMANN, T. & WERTH, C. J. (2005) Visualization of colloid transport through heterogeneous porous media using magnetic resonance imaging. *Colloids and Surfaces a-Physicochemical and Engineering Aspects*, 265, 2-10.
- BEAR, J. (1972) *Dynamics of fluids in porous media* Dover
- DARLINGTON, T. K., NEIGH, A. M., SPENCER, M. T., NGUYEN, O. T. & OLDENBURG, S. J. (2009) Nanoparticle characteristics affecting environmental fate and transport through soil. *Environmental Toxicology and Chemistry*, 28, 1191-1199.
- DAWSON, T. L. (2008) Nanomaterials for textile processing and photonic applications. *Coloration Technology*, 124, 261-272.
- FETTER, C. W. (1994) *Applied hydrogeology*, Prentice Hall.
- HAACKE, E. M., BROWN, R. W., THOMPSON, M. R., AND VENKATESAN, R. (1999) *Magnetic resonance imaging: physical principles and sequence design*, Wiley-Liss.
- HANDY, R. D., VON DER KAMMER, F., LEAD, J. R., HASSELLOV, M., OWEN, R. & CRANE, M. (2008) The ecotoxicology and chemistry of manufactured nanoparticles. *Ecotoxicology*, 17, 287-314.
- [HTTP://WWW.BCCRESEARCH.COM/REPORT/NAN004J.HTML](http://www.bccresearch.com/report/nan004j.html).
- [HTTP://WWW.BIOPAL.COM/](http://www.biopal.com/).
- JADA, A., AKBOUR, R. A. & DOUCH, J. (2006) Surface charge and adsorption from water onto quartz sand of humic acid. *Chemosphere*, 64, 1287-1295.
- KHRAPITCHEV, A. A. & CALLAGHAN, P. T. (2003) Reversible and irreversible dispersion in a porous medium. *Physics of Fluids*, 15, 2649-2660.
- KISER, M. A., WESTERHOFF, P., BENN, T., WANG, Y., PEREZ-RIVERA, J. & HRISTOVSKI, K. (2009) Titanium nanomaterial removal and release from wastewater treatment plants. *Environmental Science & Technology*, 43, 6757-6763.
- LAWACZECK, R., MENZEL, M. & PIETSCH, H. (2004) Superparamagnetic iron oxide particles: contrast media for magnetic resonance imaging. *Applied Organometallic Chemistry*, 18, 506-513.
- LIMBACH, L. K., BEREITER, R., MUELLER, E., KREBS, R., GAELLI, R. & STARK, W. J. (2008)

Removal of oxide nanoparticles in a model wastewater treatment plant: Influence of agglomeration and surfactants on clearing efficiency. *Environmental Science & Technology*, 42, 5828-5833.

LIU, Y. Q., MAJETICH, S. A., TILTON, R. D., SHOLL, D. S. & LOWRY, G. V. (2005) TCE dechlorination rates, pathways, and efficiency of nanoscale iron particles with different properties. *Environmental Science & Technology*, 39, 1338-1345.

POP, I., INGHAM, D. B. (2002) *Transport phenomena in porous media II*, A Pergamon Title

SÁNCHEZ, A., RECILLAS, S., FONT, X., CASALS, E., GONZÁLEZ, E. & PUNTES, V. (2011) Ecotoxicity of, and remediation with, engineered inorganic nanoparticles in the environment. *TrAC Trends in Analytical Chemistry*, 30, 507-516.

THERON, J., WALKER, J. A. & CLOETE, T. E. (2008) Nanotechnology and water treatment: Applications and emerging opportunities. *Critical Reviews in Microbiology*, 34, 43-69.

TIRAFERRI, A. & SETHI, R. (2009) Enhanced transport of zerovalent iron nanoparticles in saturated porous media by guar gum. *Journal of Nanoparticle Research*, 11, 635-645.

WANG, Y. G., LI, Y. S., FORTNER, J. D., HUGHES, J. B., ABRIOLA, L. M. & PENNELL, K. D. (2008) Transport and retention of nanoscale C-60 aggregates in water-saturated porous media. *Environmental Science & Technology*, 42, 3588-3594.

ZHANG, W. X. (2003) Nanoscale iron particles for environmental remediation: An overview. *Journal of Nanoparticle Research*, 5, 323-332.

Chapter 6

Investigation of copper immobilisation inside artificial
biofilms using magnetic resonance imaging (MRI)

6

Investigation of copper immobilisation inside artificial biofilm using magnetic resonance imaging (MRI)

6.1 Summary

Quantifying transport and reaction rates of heavy metals inside biofilms is important to develop representative models of metal immobilization in industrial wastewater treatment systems and in natural biofilms. In this study, magnetic resonance imaging (MRI) was used to quantify the transport of copper inside artificial biofilms made up with different ratios of agar and the bacteria *Bacillus subtilis*. MRI successfully imaged the transport of copper inside artificial biofilms using T_2 -weighted images. A calibration protocol was then used to convert T_2 -weighted images into spatially resolved quantitative concentration maps of copper at different time intervals. Comparing the experimental data obtained at 6, 12, 18 and 24 hours with two-dimensional adsorption-diffusion models revealed that copper was transported inside artificial biofilms composed of 5 % and 50 % bacteria with diffusion coefficients of $7.9 \times 10^{-10} \text{ m}^2 \text{ s}^{-1}$ and $4.4 \times 10^{-10} \text{ m}^2 \text{ s}^{-1}$ respectively and log stability (adsorption) constants of 4.45 and 4.55 respectively. However, the model lagged the experimental data at early time intervals, and lead at later time intervals. When each time interval was modelled separately, allowing the diffusion coefficient (D) to vary, D was observed to increase throughout the duration of the experiment. Indeed, the phenomenon of increasingly broadening diffusive reaction front for copper has been observed previously inside other metal adsorption matrices. An explicitly incorporated concentration dependent diffusion coefficient with respect to the total copper concentration (adsorbed and free) showed improvements in the model fits. However, its relevance and the influence of other possible effects such as cell lysis and electro static interactions needs to be further investigated in order to enhance models of adsorption-diffusion processes in metal immobilizing biofilms.

6.2 Introduction

Despite the importance of heavy metals in industrial processes, their presence in effluents is a pronounced threat to the environment and to human health (Le Cloirec et al., 2003, Singh and Cameotra, 2004, Volesky, 1994). Unlike organic wastes which are eventually degraded to harmless substances, heavy metals are more persistent and can create chronic illnesses in humans and animals via a range of exposure routes (e.g. circulation through food chains) (Dogru et al., 2007, Singh and Cameotra, 2004, Volesky, 1994). Therefore, proper removal of heavy metal species is an essential part of waste management. As an efficient, cost effective and environmental friendly means of removing heavy metals from waste water, using biofilms in bioremediation of heavy metals via biosorption is a promising alternative to conventional heavy metal removal processes such as chemical precipitation, chemical oxidation or reduction, ion exchange, reverse osmosis, electrochemical treatment and evaporation (Le Cloirec et al., 2003, Volesky, 1994). Due to their ubiquitous nature, biofilms also play a role in scavenging heavy metals in the natural environment.

Biofilms, which are the common mode of life for bacteria, have been used to remove large quantities of heavy metals from both natural and industrial environments by sorption (Le Cloirec et al., 2003, Mullen et al., 1989), mainly via complexation of metals to the bacterial surface (Phoenix and Holmes, 2008). In addition to the reaction kinetics between metals and bacterial surfaces, the immobilization of metals inside biofilms is also influenced by the rate at which these metals are transported into the biofilm. Due to differences (e.g. composition, density and porosity) between biofilm types and the heterogeneous nature of individual biofilms, reaction kinetics and transport properties of heavy metals could significantly vary both inside individual biofilms and between biofilm types. Therefore, a clear understanding of reaction kinetics and transport is essential when attempts are made to optimize the performance of metal sequestration processes using biofilms.

Using MRI in metal immobilization experiments enables visualization of the transport of metals inside biofilms, due to the effect of their paramagnetism upon the MR signal (Bartacek et al., 2009, Nestle, 2002, Phoenix and Holmes, 2008). Moreover, as this effect is concentration dependent, it is possible to use variation in MR relaxation (T_1 or T_2) of neighbouring ^1H nuclei to quantify the concentration of heavy metals.

The objectives of this study are to apply MRI to quantitatively map copper transport and its immobilization inside artificial biofilms in real time and then to determine whether an

equilibrium model, the Langmuir adsorption isotherm, could adequately describe this process. Investigating the suitability of adsorption isotherms will help us to determine the best approaches for modelling reaction-transport of metals in biofilms. Unlike linear adsorption isotherms, Langmuir adsorption isotherms consider saturation effects and have previously shown good correlation with adsorption of heavy metals inside natural phototrophic biofilms (Phoenix and Holmes, 2008). Since biofilms exhibit heterogeneous physicochemical properties such as spatially varying transport and reaction rates, it is convenient to use artificial biofilms as an ideal test system before moving onto more complex real biofilms (Strathmann et al., 2000). For this study of heavy metal uptake, we utilized *Bacillus subtilis*, a gram positive bacterium. These bacteria have the ability to accumulate high amounts of heavy metals due to their high adsorptive capacity, which is attributable to the carboxyl and phosphoryl functional groups found on their cell walls (Dogru et al., 2007).

Moreover, the quantitative maps of copper concentration using MRI are then compared to a two-dimensional adsorption-diffusion model (incorporating Langmuir adsorption) to estimate mass transfer kinetic parameters, such as the log stability (adsorption) constants and diffusion coefficients of copper inside the artificial biofilms.

6.3 Materials and methods

6.3.1 Bacteria

The model bacteria used in this experiment were *Bacillus subtilis* which is a gram positive bacteria. *B. subtilis* (strain NR1129, supplied by Nicola Stanley-Wall, University of Dundee) were grown to late exponential phase at 23°C and 110 rpm in Tryptic soy broth. Cells were washed four times in ultrapure water, and bacteria were separated from the water by centrifugation.

6.3.2 Artificial biofilms

The artificial biofilms were made up of either 5:95 or 50:50 ratios of the bacteria and agar (1.5%). Thus, replicating bacterial cells suspended in an extracellular polymer matrix. After preparing the agar, the bacteria were mixed in. The molten mixture was then poured into a modified 30-ml plastic syringe and allowed to cool, such that it produced an artificial biofilm with an approximate semi-circular cross-section (see Fig. 6.1).

6.3.3 Flow systems

During the artificial biofilm experiments, the reaction cell containing the artificial biofilm was positioned in the center of the magnet. The reaction cell was first connected via silicon tubing to an 18-M Ω water supply and slowly washed with ultrapure water. The system was then connected to a 4-liter reservoir of a 10 mg l⁻¹ Cu²⁺ solution, prepared using CuSO₄·5H₂O. A peristaltic pump was used to pump the solution at a rate of 0.7 ml min⁻¹ (Fig. 6.1). The Cu²⁺ solution effluent was pumped back into the reservoir.



Figure 6.1. Schematic of the flow cell containing the artificial biofilm. Cross sections are (a) along the flow cell and (b) across the flow cell.

6.3.4 MRI

The MRI experiments were performed on a Bruker Avance BioSpec system, using a 30 cm-bore, 7T superconducting magnet (Bruker BioSpin, Karlsruhe, Germany). A Bruker micro-imaging gradient insert (model BG-6) and 200-A gradient amplifiers were used to provide strong linear magnetic field gradient pulses of up to 1000 mT m⁻¹, thus allowing the system to perform micro-imaging experiments. A Bruker 35 mm diameter birdcage RF volume resonator was used to excite and detect the ¹H signal.

6.3.5 Acquisition of T_2 - weighted images

The transport of copper inside the artificial biofilm was imaged by acquisition of T_2 -weighted images in the axial plane by using a multispin echo, two-dimensional imaging sequence; 64 consecutive spin echoes were acquired with an echo time of 6.8 ms and a recovery time of 7 s. T_2 -weighted images were obtained across the sample, with a slice thickness of 1 mm. The field of view was 26 mm x 26 mm, using an imaging matrix of 130 pixels x 130 pixels, giving an in-plane resolution of 200 μ m x 200 μ m. Two signal averages were taken, giving a total imaging time of 30 minutes.

6.3.6 Calculation of T_2 parameter maps

T_2 parameter maps were calculated from the series of 64 T_2 -weighted images (Fig. 6.2A) by fitting the signal decay for each individual pixel to an exponential function (Haacke, 1999) (see Fig. 6.2B),

$$S_{(t)} = S_{(0)} \cdot \exp^{-t/T_2} + B$$

Equation 1

where $S_{(t)}$ is the MR signal at time t , $S_{(0)}$ is the MR signal at time zero, T_2 is the transverse relaxation time and B is a baseline offset parameter. It was found that all the signal decay curves were well fitted by such a single exponential function. This procedure was applied to estimate the T_2 value of every pixel within the slice of the two-dimensional image (see Fig. 6.2C). The presence of paramagnetic metals, such as copper, causes a reduction in T_2 . Consequently, construction of T_2 parameter maps during copper uptake can be used to reveal the location and concentration of copper.

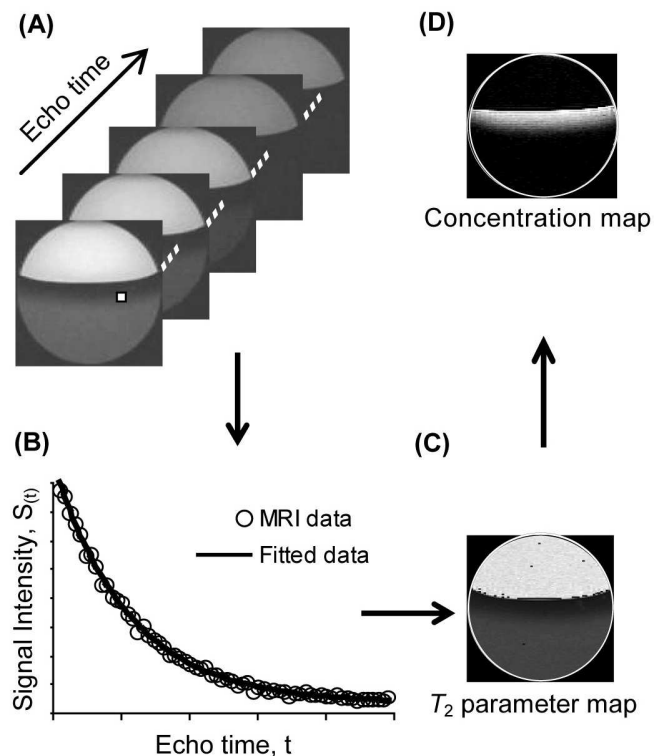


Figure 6.2 (A) For the slice across the biofilm, T_2 -weighted images are acquired with increasing echo time. (B) For each pixel, the decay of the MRI signal was fitted to an exponential function, giving a T_2 value. (C) Taking the T_2 values for each pixel yields a T_2 parameter map. (D) The calibrated concentration map of Gd-DTPA inside artificial biofilm.

6.3.7 Calibration of copper concentrations from T_2 parameter maps

The presence of paramagnetic ions, such as Cu^{2+} , causes a concentration dependent reduction in T_2 , represented by the following equation (Haacke, 1999, Stanisiz and Henkelman, 2000, Phoenix and Holmes, 2008).

$$[C] = \frac{1}{R} \left(\frac{1}{T_{2i}} - \frac{1}{T_{20}} \right)$$

Equation 2

where T_{20} is the relaxation time in the absence of ions, T_{2i} is the relaxation time in the presence of ions, $[C]$ denotes the concentration of the copper ions, and R is the relaxivity constant of the Cu^{2+} .

In this study, T_{2i} and T_{20} are measured variables, as they are taken directly from T_2 parameter maps. R , however, is unknown and must be separately determined to enable the calculations of $[C]$.

6.3.8 Determination of relaxivity constant (R) of copper in artificial biofilms

The relaxivity value, R depends on the solids content of the sample as discussed in section 3.3.7. Therefore, estimating the solids content related R value of copper would enable more accurate determination of its concentrations inside artificial biofilms.

The effect of solids content on copper relaxivity has already been investigated by Phoenix and Holmes (Phoenix and Holmes, 2008); hence the appropriate R values for artificial biofilm samples were taken from their results. Note, the study by Phoenix and Holmes utilized similar agar and bacteria composites to those used here to investigate the impact of solids content, thus their results are of direct relevance to this study. These resulting R values were then used in equation 2 to calculate the copper concentrations inside the artificial biofilm from the MRI data collected during the experiment.

6.3.9 Modeling the adsorption-diffusion of copper inside artificial biofilms

To determine whether the measured copper concentration profiles using MRI were commensurate with an adsorption-diffusion process, they were compared with a mathematical

model.

Consider the adsorbate, A , (e.g. copper Cu^{2+}) diffuses into a homogeneous medium, agar which contains a uniform distribution of adsorbent sites, S , (e.g. immobile bacterial sites). The adsorption of an adsorbate A , onto an adsorbent site S , can then be described with the following simple reversible reaction:



Equation 3

By assuming no interaction between adsorbate on different sites, the adsorption process can be described by the Langmuir adsorption isotherm (Bartlett and Gardner, 1996).

The adsorption constant (equilibrium constant), K , is equal to

$$K = \frac{k_f}{k_b} = \frac{[AS]}{[A][S]}$$

Equation 4

where k_f and k_b are the forward and backward rate constants.

For the one-dimensional case, taking x as the distance into a medium of thickness L , time t , and the fraction of sites occupied (at a specified distance and time) θ , the diffusion adsorption equation for adsorbate, copper, is given by

$$D_{dif} \frac{\partial^2 C}{\partial x^2} - k_f C(1 - \theta)N + k_b \theta N = \frac{\partial C}{\partial t}$$

Equation 5

where $C(x, t)$ is the concentration of the diffusing copper, D_{dif} is its diffusion coefficient inside the medium, and N is the concentration of the binding sites within the medium. Consideration of the kinetics at the reaction sites gives;

$$N \frac{\partial \theta}{\partial t} = k_f C(1 - \theta)N - k_b \theta N$$

Equation 6

Then combining equations 5 and 6 gives

$$D_{dif} \frac{\partial^2 C}{\partial x^2} - \frac{\partial C}{\partial t} = N \frac{\partial \theta}{\partial t}$$

Equation 7

Equations 6 and 7 are coupled nonlinear partial differential equations. These equations were

solved within the artificial biofilm, the domain Ω shown in Fig. 6.3, using a two dimensional model, implemented using finite element package COMSOL Multiphysics (3.5a). Here the degree of symmetry in the shape of the agar along the axis of flow enabling a two dimensional model to be used. The boundary of the domain was split into two parts (Fig. 6.3) so that $\partial\Omega = \Gamma_1 \cup \Gamma_2$ where Γ_1 is the top surface of the agar and Γ_2 is the wall of the plastic holder in which the artificial biofilm was placed. The concentration of Cu^{2+} in the bulk liquid and hence on the boundary Γ_1 was assumed to be a constant, C^* , through time. No transport was permitted through wall boundaries, Γ_2 . Hence the model was defined by equations 6 and 7 and the following boundary conditions;

$$C(x, y) = C^* \quad x, y \in \Gamma_1 \quad \text{Equation 8}$$

$$\frac{\partial C(x, y)}{\partial \bar{n}} = 0 \quad x, y \in \Gamma_2 \quad \text{Equation 9}$$

Here \bar{n} is the vector normal to the boundaries (Γ_2), and C^* is the concentration of Cu^{2+} in the bulk liquid above the artificial biofilm.

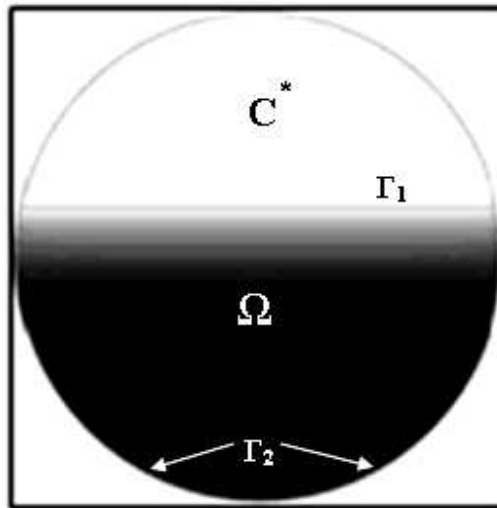


Figure 6.3. Illustration of the two dimensional model of artificial biofilm constructed using COMSOL Multiphysics.

Based on the results from MRI analysis, values for variable N representative of each artificial biofilm were put into the model. Details of estimating the values of variables are provided in the following section. The model was then calibrated using the experimental data to estimate the values of K , D_{dif} , and k_f . Optimum values of these parameters were estimated using a golden search algorithm in MATLAB, which called the COMSOL model as a subroutine. The

objective function was the sum of square errors between observed and simulated concentrations and the optimum values for K , D_{dif} and k_f were estimated at the minimum value of this objective function.

6.3.10 Estimating the values for variables used in the model

The concentration of Cu^{2+} in the overlying fluid (C^*) was set at 1.57×10^{-4} M as this concentration (i.e. 10 mg/l) of Cu solution was continuously pumped over the artificial biofilm throughout the experiment. The concentration of reactive sites, N , was determined as the sum of metal-complexed sites (AS) and uncomplexed sites (S) at maximum adsorption capacity after 24 hours of time interval. The metal-complexed sites (AS) was determined from the MRI data and taken to be the average maximum adsorbed Cu^{2+} concentration inside the biofilm (see Fig. 6.6) (1.88×10^{-2} M, i.e. 1200 mg/l in the 50:50 bacteria:agar system and 5.5×10^{-3} M, i.e. 350 mg/l in the 5:95 system), while S was calculated using equation 4, with value of A equal to C^* and value of K was evaluated using the above mentioned parameter estimation method.

6.3.11 Concentration dependent diffusion of copper inside artificial biofilms

It is a common practice to assume a constant diffusion coefficient when models are used to investigate transport behaviours of solutes inside biofilms. However, studies have showed that diffusion coefficient of solutes is concentration dependent in many practical systems related to adsorption and diffusion-reaction process (Lin, 1992, Nestle and Kimmich, 1996, Ruthven, 2004, Scott and Karanjkar, 1995).

Therefore, the concept of concentration dependent diffusion coefficient was incorporated in the model in order to investigate whether this would improve the fit between the experimental data and the model data for these artificial biofilms.

The concentration dependence of diffusion coefficient of copper can be represented by either a linear (equation 10) or an exponential (equation 11) function as given below (Lin, 1992).

$$D_{dif} = D_0(1 + b(c / c_0)) \quad \text{Equation 10}$$

$$D_{dif} = D_0(\exp(bc / c_0)) \quad \text{Equation 11}$$

where D_0 is the base diffusion coefficient and c_0 is the reference concentration maintained at

the top of the biofilm (C^*) and b is the unknown constant.

Models representing the concentration dependent diffusion of copper (equations 10 and 11) were calibrated using the experimental data. The influence of concentration dependent diffusion of copper upon models was investigated using the goodness-of-fit values (R^2).

The physical reason behind the concept of concentration dependent diffusion coefficient is unclear. Thus, the effect of both free and total concentration upon the diffusion coefficient was investigated. The main driving force for the diffusive transport is the gradient of chemical potential, rather than the gradient of concentration (Ruthven, 2004). Therefore, the adsorbed copper concentration may also have an effect on the diffusion of copper, in addition to free copper.

6.4 Results

6.4.1 Transport of copper inside artificial biofilms

The transport of copper into the artificial biofilm made up of 5:95 mix of agar and bacteria at time intervals of 6, 12, 18 and 24 hours was recorded by T_2 -weighted images, as shown in Fig. 6.4A-D. The presence of copper reduces the T_2 values, hence the reaction transport of copper into the artificial biofilm is shown by the expansion of darker region over time down into the artificial biofilm. Then by applying the calibration protocol (equation 2) described above, T_2 parameter maps were converted into copper concentration maps as shown in Fig. 6.4E-H. Here, the expansion of the brighter region down into the biofilm shows the transport of copper. Figure 6.4I-L shows the two-dimensional model for adsorption and diffusion of copper inside the artificial biofilm generated using the estimated values for D_{dif} , K and k_f (see table 6.1) at given time intervals.

The transport of copper into the artificial biofilm made up of 50:50 mix of agar and bacteria at time intervals of 6, 12, 18 and 24 hours was recorded by T_2 -weighted images, as shown in Fig. 6.5A-D. The presence of copper reduces the T_2 values, hence the reaction transport of copper into the artificial biofilm is shown by the expansion of darker region over time down into the artificial biofilm. Then by applying the calibration protocol (equation 2) described above, T_2 parameter maps were converted into copper concentration maps as shown in Fig. 6.5E-H. Here, the expansion of the brighter region down into the biofilm shows the transport of copper. Figure 6.5I-L shows the two-dimensional model for diffusion and adsorption of

copper inside the artificial biofilm generated using the estimated values for D_{dif} , K and k_f (see table 6.1) at given time intervals.

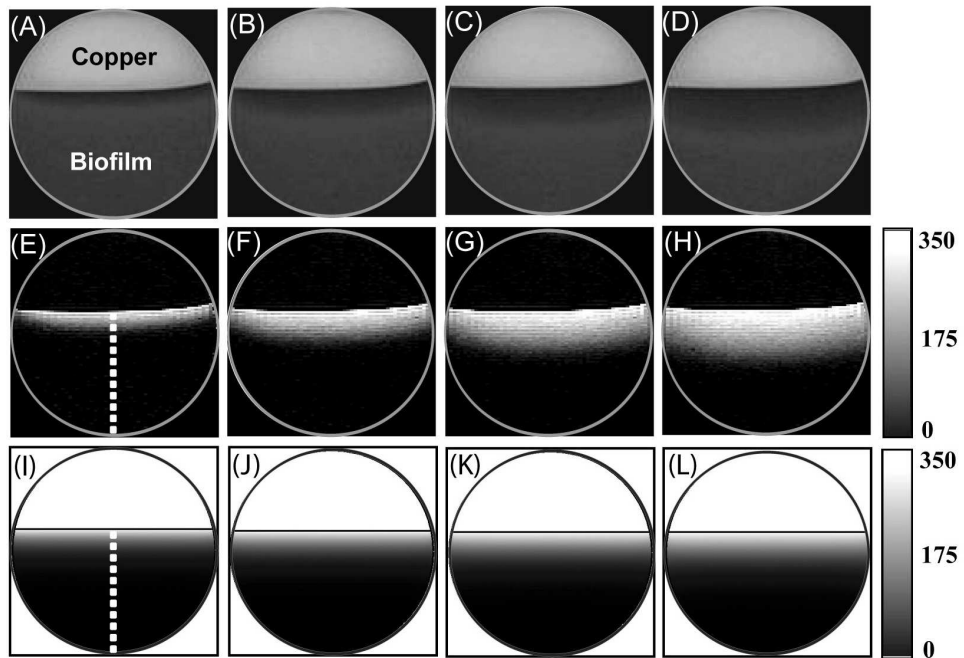


Figure 6.4. Transport of copper into the artificial biofilm of 5:95 mix illustrated as T_2 -weighted images (A-D), calibrated copper concentration maps (E-H), and diffusion-adsorption model results (I-L) at time intervals of 6, 12, 18 and 24 hours. The gray scale indicates the copper concentrations (mg/l) inside the biofilm.

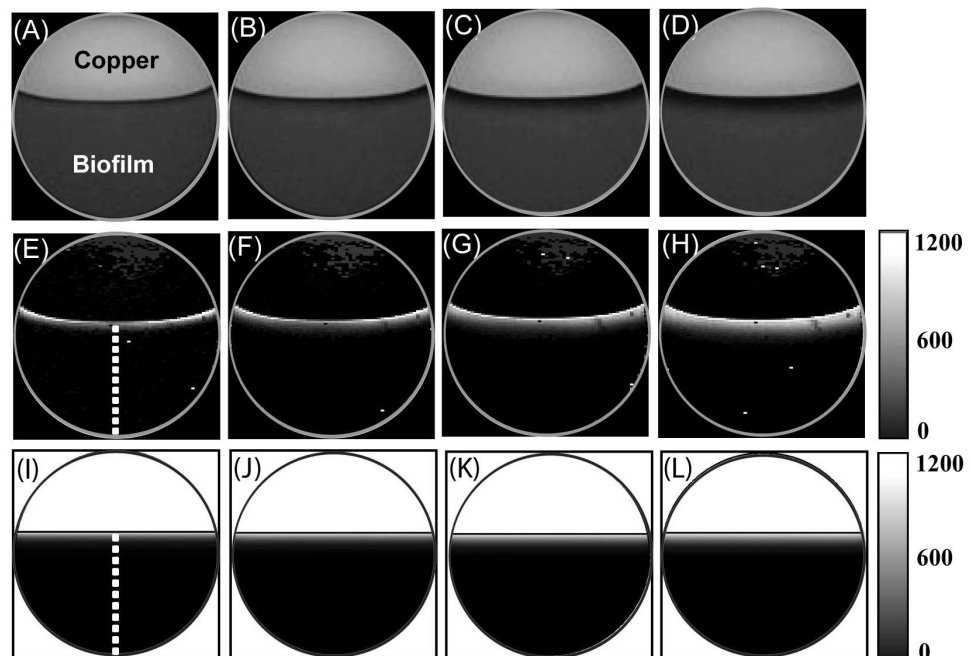


Figure 6.5. Transport of copper into the artificial biofilm of 50:50 mix illustrated as T_2 -weighted images (A-D), calibrated copper concentration maps (E-H), and diffusion-adsorption model results (I-L) at time intervals of 6, 12, 18 and 24 hours. The gray scale indicates the copper concentrations (mg/l) inside the biofilm.

Concentration profiles along the transect shown by the white line (Fig. 6.4E and Fig. 6.5E) at time intervals of 6, 12, 18 and 24 hours for both agar and bacteria mixes are shown in figures 6.6A and B.

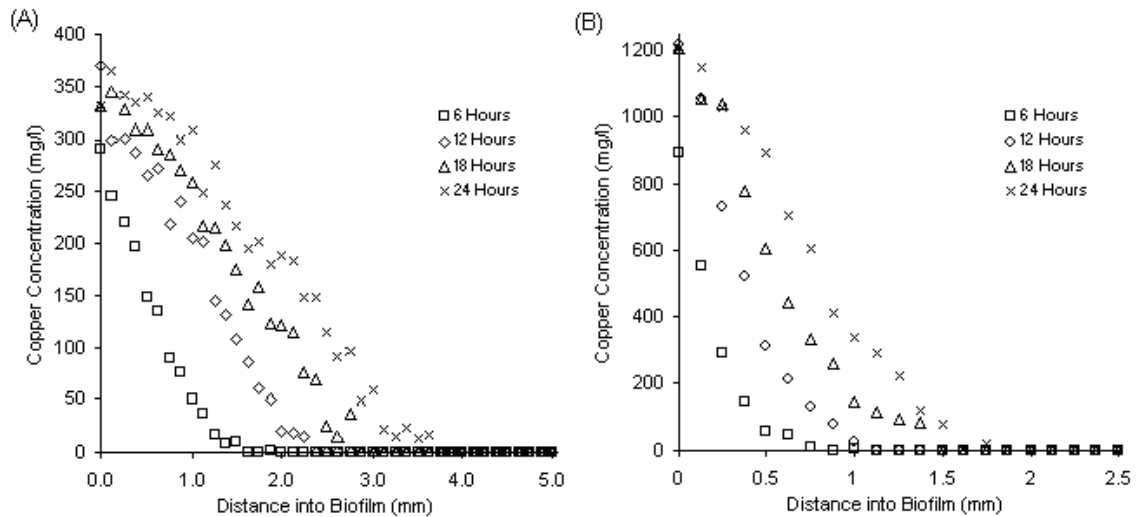


Figure 6.6. Calibrated copper concentration profiles at time intervals of 6, 12, 18, and 24 hours along the transect shown by the white dotted line in Fig. 6.4E for (A) 5:95 and Fig. 6.5E for (B) 50:50 mix of artificial biofilm. Note the difference in scale between graphs on x and y axis.

6.4.2 Models describing the transport of copper inside artificial biofilms

6.4.2.1 Transport of copper modelled with constant diffusion coefficients

Figure 6.7, compares the concentration profiles of copper with the model data along the transect shown by the white line in Fig. 6.4I and Fig. 6.5I for both artificial biofilms. The estimated values for K , D_{dif} and k_f are given in table 6.1 along with the goodness-of-fit (R^2) values.

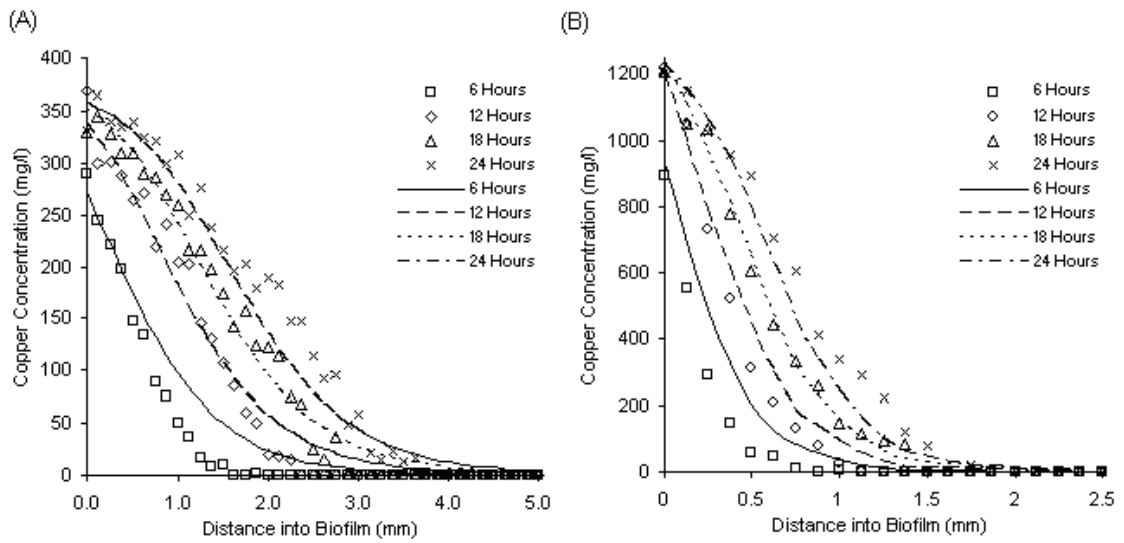


Figure 6.7. Comparison of experimental data with the adsorption-diffusion model data for artificial biofilms made up with (A) 5:95 and (B) 50:50 bacterial pellets and agar mix at time intervals of 6, 12, 18, and 24 hours along the transect shown by the white dotted line in Fig. 6.4E,I and 6.5 E,I. Symbols represent experimental data, and solid lines represent model data at respective time intervals.

Artificial-biofilm mix (bacteria:agar)	K (l/mg)	D_{dif} (m^2/s)	k_f (mg/l)	R^2
5:50	4.45	7.9×10^{-10}	0.34	95.76
50:50	4.55	4.4×10^{-10}	0.32	97.16

Table 6.1. Estimated values of log stability constant, K (for adsorption), constant diffusion coefficient, D_{dif} , forward constant rate, k_f and goodness of fit, R^2 when the model is calibrated for both artificial biofilms (5:95 and 50:50 mix) by considering experimental data obtained at 6, 12, 18 and 24 hour time intervals together.

6.4.2.2 Transport of copper modelled with different diffusion coefficients at different time intervals

Figure 6.8 and 6.9, shows the comparison of experimental data and model data (along the same transects shown in figures 6.4E, I and figures 6.5E, I) when diffusion coefficients were separately estimated at each time interval for both the artificial biofilms by using previously estimated values for K and k_f (see table 6.1). The estimated values for D_{dif} at different time intervals for both artificial biofilms are given in tables 6.2 and 6.3 along with the goodness-of-fit (R^2) values.

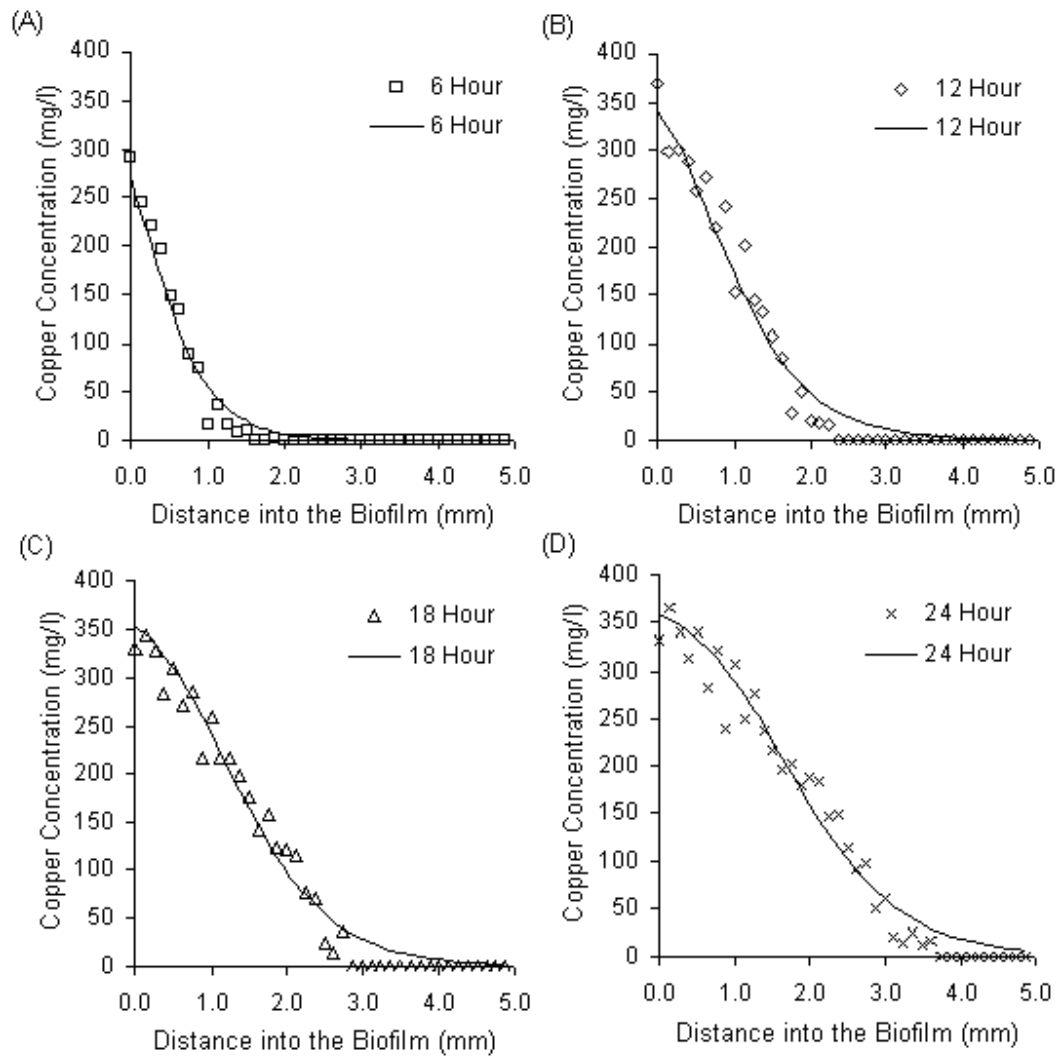


Figure 6.8. Comparison of experimental data (5:95 mix) to the model data modelled with diffusion coefficients estimated separately for each time interval by using previously estimated values for K and k_f (see table 6.1). Symbols represent experimental data, and solid lines represent model data at respective time intervals.

Time interval	6 Hour	12 Hour	18 Hour	24 Hour
D_{dif} (m^2/s)	4.3×10^{-10}	6.5×10^{-10}	7.9×10^{-10}	9.9×10^{-10}
R^2	97.71	97.09	97.64	97.03

Table 6.2. Estimated value of constant diffusion coefficient, D_{dif} and goodness of fit, R^2 when model is calibrated for (5:95) artificial biofilm by considering experimental data separately at 6, 12, 18 and 24 hour time intervals.

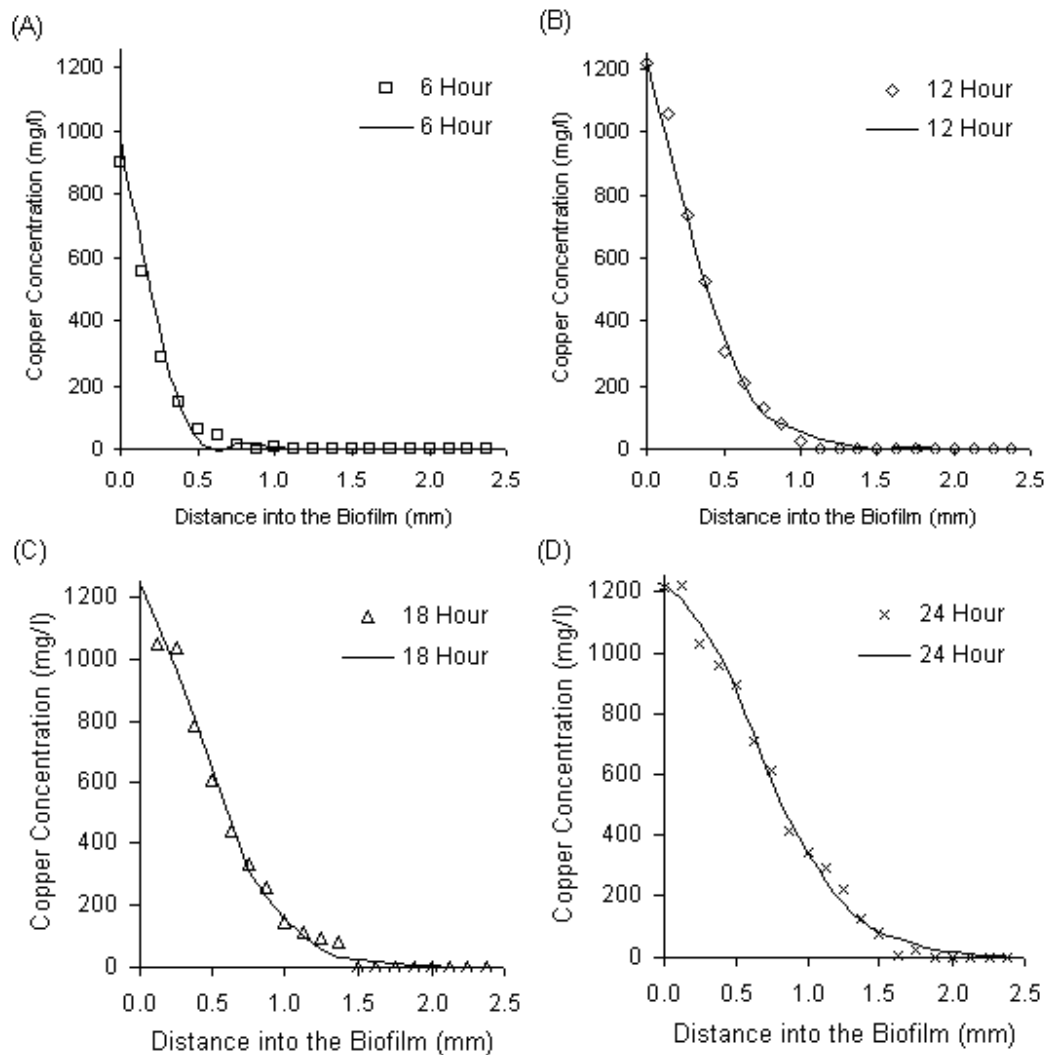


Figure 6.9. Comparison of experimental data (50:50 mix) to the model data modelled with diffusion coefficients estimated separately for each time interval by using previously estimated values for K and k_f (see table 6.1). Symbols represent experimental data, and solid lines represent model data at respective time intervals.

Time interval	6 Hour	12 Hour	18 Hour	24 Hour
D_{dif} (m^2/s)	1.8×10^{-10}	3×10^{-10}	4.2×10^{-10}	5.5×10^{-10}
R^2	98.37	99.51	99.32	99.44

Table 6.3. Estimated value of constant diffusion coefficient, D_{dif} and goodness of fit, R^2 when model is calibrated for (50:50) artificial biofilm by considering experimental data separately at 6, 12, 18 and 24 hour time intervals.

6.4.2.3 Transport of copper modelled with concentration dependent diffusion coefficient

Figure 6.10 and 6.11, shows the comparison of experimental data and model data (along the same transects shown in figures 6.4E, I and 6.5E, I) modelled using a systematic variation in D_{dif} ; i.e. proportional to the concentration of copper (equations 10 and 11) by using previously

estimated values for K and k_f (see table 6.1). Here figures 6.10A, 6.10B, 6.11A and 6.11B show the comparison when the concentration dependent diffusion coefficient with respect to the free concentration of copper is used, while figures 6.10C, 6.10D, 6.11C and 6.11D show the comparison when concentration dependent diffusion coefficient with respect to the total (adsorbed and free) concentration of copper is used. Comparison between the linear and exponential relationship for concentration dependant diffusion coefficient for both biofilms are shown in figures (6.10A, 6.10C, 6.11A and 6.11C) and (6.10B, 6.10D, 6.11B and 6.11D) respectively. The estimated values for D_0 and values of constant, b for both artificial biofilms are given in tables 6.4 and 6.5 along with the goodness-of-fit (R^2) values.

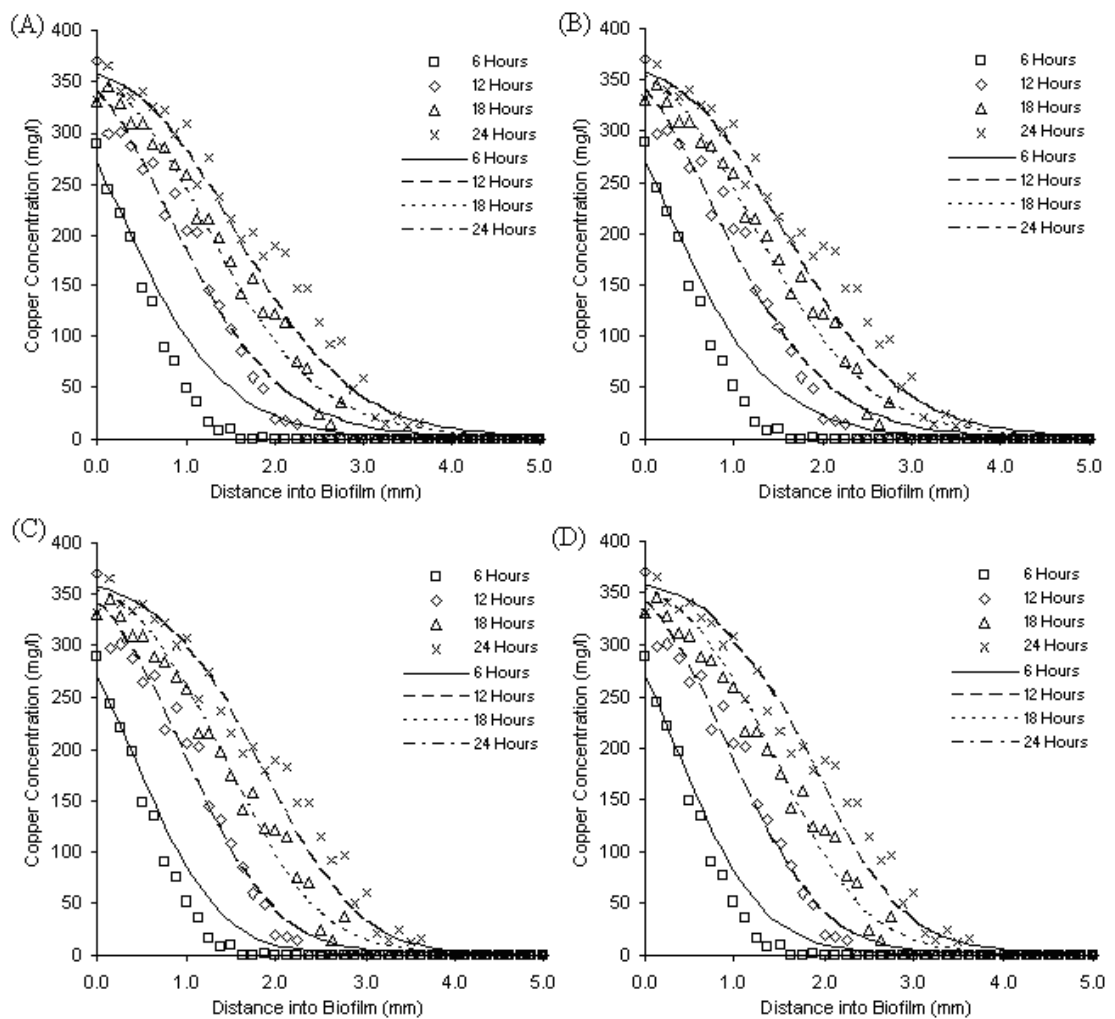


Figure 6.10. Comparison of experimental data to the model data modelled with concentration dependent diffusion coefficients for Cu^{2+} inside the artificial biofilm made up with 5:95 agar and bacteria mix at time intervals of 6, 12, 18, and 24 hours along the transect shown by the white dotted line in Fig. 6.4E and I. Diffusion coefficient as a (A) linear and (B) exponential function with respect to the free copper concentration. Diffusion coefficient as a (C) linear and (D) exponential function with respect to the total copper concentration. Symbols represent experimental data, and solid lines represent model data at respective time intervals.

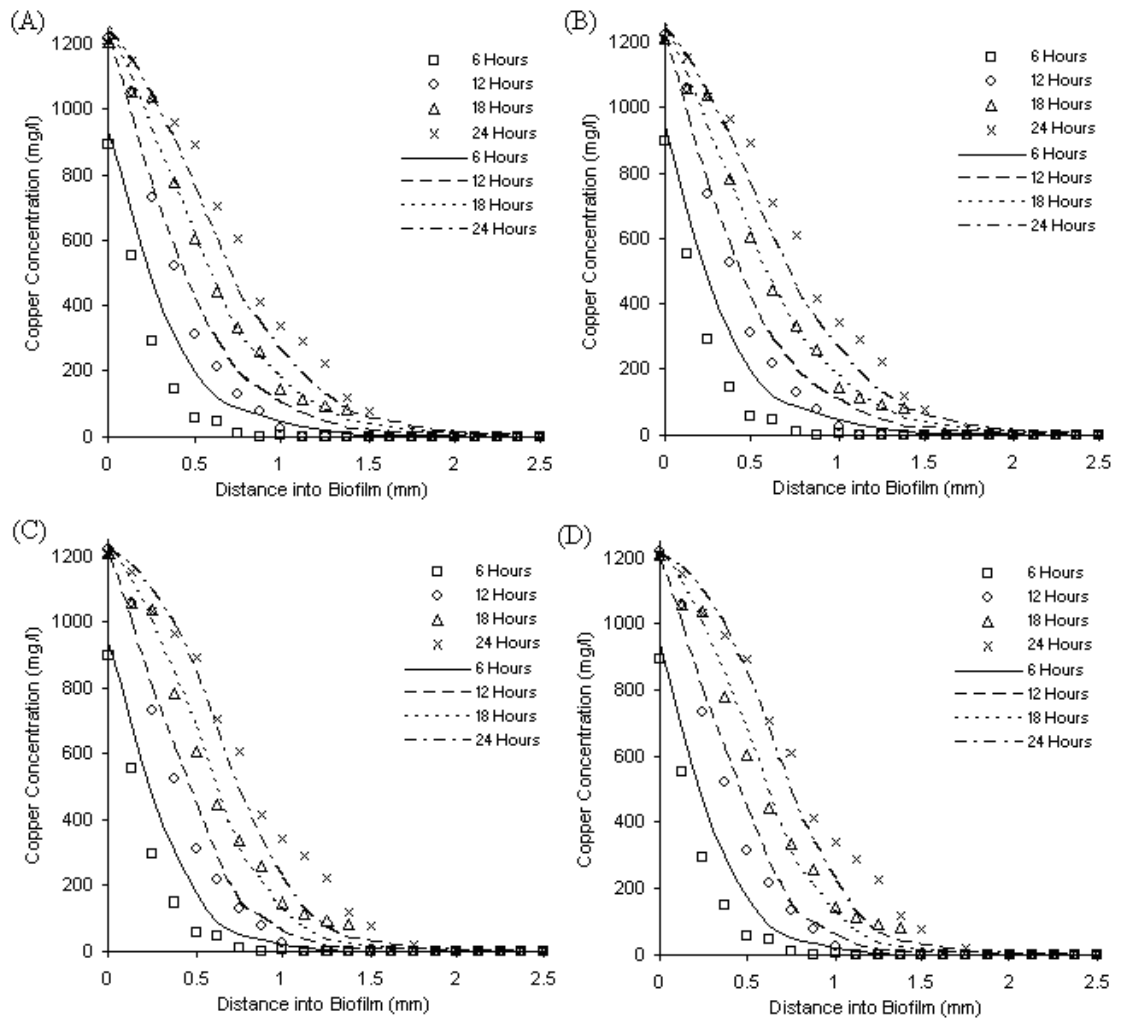


Figure 6.11. Comparison of experimental data to the model data modelled with concentration dependent diffusion coefficients for Cu^{2+} inside the artificial biofilm made up with 50:50 agar and bacteria mix at time intervals of 6, 12, 18, and 24 hours along the transect shown by the white dotted line in Fig. 6.5E and I. Diffusion coefficient as a (A) linear and (B) exponential function with respect to the free copper concentration. Diffusion coefficient as a (C) linear and (D) exponential function with respect to the total copper concentration. Symbols represent experimental data, and solid lines represent model data at respective time intervals.

Concentration dependent diffusion coefficient	D_0 (m ² /s)	B	R ²
with respect to liquid phase			
(i) Linear function	7.99x10 ⁻¹⁰	0.198	95.78
(ii) Exponential function	8.06x10 ⁻¹⁰	0.1708	95.78
with respect to total phase			
(i) Linear function	3.57x10 ⁻¹⁰	0.0877	96.94
(ii) Exponential function	4.12x10 ⁻¹⁰	0.0414	96.85

Table 6.4. Estimated values of base diffusion coefficient, D_0 , unknown constant, b and goodness of fit value, R^2 when model for (5:95 bacteria and agar mix) is calibrated using linear and exponential functions for concentration dependent diffusion coefficient with respect to both free and total copper concentrations. Here experimental data obtained at 6th, 12th, 18th and 24th hour time intervals are considered together for model calibration. Previously obtained values for K and k_f were used (table 6.1).

Concentration dependent diffusion coefficient	D_0 (m ² /s)	b	R ²
with respect to liquid phase			
(i) Linear function	5.88x10 ⁻¹⁰	-0.4029	97.35
(ii) Exponential function	5.94x10 ⁻¹⁰	-0.4931	97.35
with respect to total phase			
(i) Linear function	2.73x10 ⁻¹⁰	0.0093	97.43
(ii) Exponential function	2.78x10 ⁻¹⁰	0.0067	97.46

Table 6.5. Estimated values of base diffusion coefficient, D_0 , unknown constant, b and goodness of fit value, R^2 when model for (50:50 bacteria and agar mix) is calibrated using linear and exponential functions for concentration dependent diffusion coefficient with respect to both free and total copper concentrations. Here experimental data obtained at 6th, 12th, 18th and 24th hour time intervals are considered together for model calibration. Previously obtained values for K and k_f were used (table 6.1).

6.5 Discussion

In this study, MRI was successfully used to quantitatively measure the time-varying, spatially distributed concentration of copper as it was transported into artificial biofilms made up with two different compositions of agar and bacteria. The quantitative concentrations were then used to estimate reaction and transport parameters, such as coefficients of adsorption and diffusion, by using an adsorption-diffusion model.

Figures 6.6A and B clearly illustrate that increase in the bacterial concentration has increased the adsorption capacity of the artificial biofilm, while the transport of copper inside that biofilm was significantly retarded (also see Fig. 6.4 and Fig. 6.5) as increased adsorption of copper is expected to reduce its transport rate. Of course one should expect approximately a ten fold increase in the amount of copper adsorbed inside the biofilm made up with 50% bacteria compared to that of the biofilm made up with 5% bacteria. However, only a four times increase in the adsorbed copper levels are observed (see Fig. 6.6). This may be due to

the possible interaction between functional groups on the bacterial surfaces in the high bacterial density system. As the bacteria are more closely packed, functional groups from one cell can interact with, and mask, functional groups from another cell. For example, positively charged amine groups (R-NH_3^+) from one cell could mask negatively charged carboxyls (R-CO_2^-) from another. Functional group masking has been observed in dense bacteria/mineral composites, where the functional groups on the surface of minerals and bacteria mask each other (Kulczycki et al., 2005). This effect may well have reduced the number of sites available for copper adsorption. Significantly, this indicates that bacterial density in biofilms may not always correlate linearly with the number of metal adsorption sites available. In terms of optimal density for maximising metal adsorption in a designed biofilm, it appears there may be a threshold density above which little extra adsorption is generated. This, however, has no effect in the accuracy of the adsorption-diffusion model as the number of adsorption sites was estimated from the maximum amount of copper adsorbed.

The two-dimensional adsorption-diffusion model calibrated using all experimental data obtained at all time intervals, did not perfectly match the experimental data as shown in figures 6.7A and B. For both artificial biofilms, the model leads the experimental data at earlier time intervals, and then lags behind at later time intervals.

Despite the fact that the adsorption-diffusion model does not perfectly represent the transport of copper inside artificial biofilms, the calculated values for log stability constant for adsorption and diffusion coefficient (see table 6.1) are acceptable estimates. The estimated log stability constants, K , of 4.45 and 4.55 for copper adsorption onto 5% and 50% *B. subtilis* artificial biofilms respectively, are close to the previously reported value of 4.3 for copper adsorption onto planktonic *B. subtilis* (Fein et al., 1997). In addition the estimated diffusion coefficient, D , of $7.9 \times 10^{-10} \text{ m}^2 \text{ s}^{-1}$ and $4.4 \times 10^{-10} \text{ m}^2 \text{ s}^{-1}$ for 5% and 50% *B. subtilis* artificial biofilms respectively, are reasonable estimates for diffusion coefficients of copper inside these systems. The diffusion coefficient value for Cu in 5% bacteria matrix is close to the previously reported diffusion coefficient of $7.8 \times 10^{-10} \text{ m}^2 \text{ s}^{-1}$ for Cu^{2+} in an infinitely dilute solution at 25°C (Quickenden and Xu, 1996). Agar is a highly permeable, inert gel designed to give minimal resistance to diffusion and the small concentration of bacteria (5%) clearly does not alter porosity and tortuosity enough to alter copper's diffusion coefficient. In contrast, when high bacterial density is used, this clearly impacts porosity and tortuosity sufficiently to reduce copper's diffusion coefficient.

When data was fit using a constant D , in both artificial biofilms the model lead the data at earlier time intervals, but lagged behind at later time intervals. This may be suggesting that at least one of the fit parameters was evidently changing over the course of the experiment. In response to this, the data was re-modelled allowing D to vary. The best model fits to the experimental data were observed (see Fig. 6.8 and 6.9) when diffusion coefficients were separately estimated for each time intervals by using previously estimated values for K and k_f (see table 6.1). Interestingly, the estimated diffusion coefficients for both biofilms (5:95 and 50:50 mix) increased with time (see table 6.2 and 6.3).

It should be noted here that the prolonged exposure to the observed elevated copper concentrations (due to adsorption) may have stressed the *Bacillus subtilis* bacteria and resulted in cell lysis and sporulation. Previous studies of copper adsorption onto planktonic species of *Bacillus subtilis* and *Escherichia coli* bacteria (Navarrete et al., 2010) and inside *Escherichia coli* biofilms (Hu et al., 2007) have shown that copper in excess amounts is toxic to microorganisms, causing cell lysis (death). This could have increased the amount of copper sequestered by the artificial biofilm, as upon cell lysis the cell generally bursts, releasing internal components that have the ability to bind copper (Navarrete et al., 2010). However, the estimated log stability constants using the experimental data would have already accounted for the copper adsorption onto lysed cell components.

Of course the lysed cell components likely have the ability to move inside the artificial biofilm. This will increase the net flux of copper through the biofilm compared to that expected by the adsorption-diffusion alone as the sequestered copper on lysed cell components becomes mobile. However, this effect is not incorporated in the adsorption-diffusion model; thus may be causing the model to fit the experimental data with increasing diffusion coefficients at increasing time intervals. However, the observed behaviour of increasingly broadening diffusive reaction front for copper inside the artificial biofilm was also reported in previous studies of copper immobilisation inside biological and non-biological biosorbents such as immobilized yeast cells, alginate gels and Kombu leaves (Nestle, 2002). Thus, the hypothesis of increasing diffusion coefficients caused due to the mobility of sequestered copper onto lysed cell components is speculative at the moment.

Previous studies on metal biosorption by biofilm coated activated carbon (Scott and Karanjkar, 1995) showed a concentration dependent trend in the diffusion coefficient; i.e. increase in diffusion coefficients with metal loading or uptake. This observed increase in the

estimated effective diffusion coefficients with respect to the metal uptake may be due to the saturation effect of the metal uptake onto adsorbents. However, the effect of saturation dependent diffusion coefficients have been implicitly incorporated by the Langmuir isotherm used to represent copper transport inside the artificial biofilm (Nestle and Kimmich, 1996). However, Lin (Lin, 1992) suggested that explicitly incorporated concentration dependence of diffusion coefficients to the isotherms better represents most adsorption-diffusion processes.

Consequently, the data was remodelled, but this time using a systematic variation in D ; proportional to the concentration of copper (as shown in equations 10 and 11). Small improvements in the model fits were observed when the model was calibrated using concentration dependent diffusion coefficient for copper (see tables 6.4 and 6.5). However, concentration dependent diffusion coefficient with respect to the total concentration of copper (adsorbed and free) showed better correspondence with the experimental data for both biofilms, compared to just using free copper alone (although the improvement in R^2 was only ~ 0.1 at a 50:50 mix). It was not clear whether the linear or exponential relationship for concentration dependant diffusion (equations 10 and 11) was more appropriate for this system. Overall, this indicates that the amount of copper accumulated onto the cell walls may have an effect upon the transport behaviour of copper inside biofilms as well as the free copper in solution. However, the physical explanation for the observed better agreement between experimental data and model with a concentration dependent diffusion coefficient with respect to the total copper concentration needs further investigations.

Despite the improvements in fit, concentration dependant diffusion could not generate a full agreement between model and data. This indicates that the copper dependant diffusion relationships (equations 10 and 11) need further refinement, or that other mechanisms need to be considered as discussed below.

The fact that model fits well with the experimental data for constant reaction rates (K and k_f) and varying transport rates (D) at increasing time intervals may indicate, that transport rate of copper may have changed by some other phenomenon unaccounted in the model. For example, the electrostatic interactions between the ionic solutes (Cu^{2+}) and ionic constituents of biofilms may have changed the transport rates of solutes inside biofilms. Previous studies on surface charge characterisation of planktonic *Bacillus subtilis* bacteria (Yee et al., 2004) have shown that deprotonation of surface functional groups forms electrical potential which extends across the cell walls and bulk solution. Thus, models including Nerst-Planck equations

to incorporate the electro static interactions between bacterial pellets and copper ions may help us interpret the experimental data more accurately. Nestle and Kimmich (Nestle, 2002) have showed that models incorporating Nerst-Planck equation and reaction kinetics better described the copper adsorption in alginate gels.

The observed discrepancies between the experimental and model data may be the result of one or a combination of the above mentioned factors. Since the behaviour of heavy metal transport inside biofilms are seldom reported, the influence of the above mentioned factors upon the discrepancies between the experimental and model data remain unclear. The results herein, therefore, suggest that the above mentioned factors should be further investigated and considered when attempts are made to understand the reaction kinetics of heavy metal immobilisation inside biofilms.

Therefore, the use of MRI especially to investigate metal transport inside artificial biofilms has the potential to significantly improve our understanding of the way heavy metals are sequestered inside biofilms.

6.6 References

- BARTACEK, J., VERGELDT, F. J., GERKEMA, E., JENICEK, P., LENS, P. N. L. & VAN AS, H. (2009) Magnetic resonance microscopy of iron transport in methanogenic granules. *Journal of Magnetic Resonance*, 200, 303-312.
- BARTLETT, P. N. & GARDNER, J. W. (1996) Diffusion and binding of molecules to sites within homogeneous thin films. *Philosophical Transactions of the Royal Society of London Series a-Mathematical Physical and Engineering Sciences*, 354, 35-57.
- DOGRU, M., GUL-GUVEN, R. & ERDOGAN, S. (2007) The use of *Bacillus subtilis* immobilized on Amberlite XAD-4 as a new biosorbent in trace metal determination. *Journal of Hazardous Materials*, 149, 166-173.
- FEIN, J. B., DAUGHNEY, C. J., YEE, N. & DAVIS, T. A. (1997) A chemical equilibrium model for metal adsorption onto bacterial surfaces. *Geochimica Et Cosmochimica Acta*, 61, 3319-3328.
- HAACKE, E. M., R. W. BROWN, M. R. THOMPSON, AND R. VENKATESAN (1999) *Magnetic resonance imaging: physical principles and sequence design*, Wiley-Liss.
- HU, Z. Q., JIN, J., ABRUNA, H. D., HOUSTON, P. L., HAY, A. G., GHIORSE, W. C., SHULER, M. L., HIDALGO, G. & LION, L. W. (2007) Spatial distributions of copper in microbial biofilms by scanning electrochemical microscopy. *Environmental Science & Technology*, 41, 936-941.
- KULCZYCKI, E., FOWLE, D. A., FORTIN, D. & FERRIS, F. G. (2005) Sorption of cadmium and lead by bacteria-ferrihydrite composites. *Geomicrobiology Journal*, 22, 299-310.

- LE CLOIREC, P., ANDRES, Y., FAUR-BRASQUET, C. & GERENTE, C. (2003) Engineered biofilms for metal ion removal. *Reviews in Environmental Science and Bio/Technology*, 2, 177-192.
- LIN, S. H. (1992) Nonlinear diffusion and adsorption in heterogeneous systems by the orthogonal collocation method. *Journal of the Chemical Society-Faraday Transactions*, 88, 1573-1576.
- MULLEN, M. D., WOLF, D. C., FERRIS, F. G., BEVERIDGE, T. J., FLEMMING, C. A. & BAILEY, G. W. (1989) Bacterial sorption of heavy-metals. *Applied and Environmental Microbiology*, 55, 3143-3149.
- NAVARRETE, J. U., BORROK, D. M., VIVEROS, M. & ELLZEY, J. T. (2010) Copper isotope fractionation during surface adsorption and intracellular incorporation by bacteria. *Geochimica Et Cosmochimica Acta*, 75, 784-799.
- NESTLE, N. (2002) NMR studies on heavy metal immobilization in biosorbents and mineral matrices. *Re/Views in Environmental Science and Bio/Technology*, 1, 215-225.
- NESTLE, N. & KIMMICH, R. (1996) Concentration-dependent diffusion coefficients and sorption isotherms. Application to ion exchange processes as an example. *Journal of Physical Chemistry*, 100, 12569-12573.
- PHOENIX, V. R. & HOLMES, W. M. (2008) Magnetic resonance imaging of structure, diffusivity, and copper immobilization in a phototrophic biofilm. *Applied and Environmental Microbiology*, 74, 4934-4943.
- QUICKENDEN, T. I. & XU, Q. Z. (1996) Toward a reliable value for the diffusion coefficient of cupric ion in aqueous solution. *Journal of the Electrochemical Society*, 143, 1248-1253.
- RUTHVEN, D. M. (2004) Sorption kinetics for diffusion-controlled systems with a strongly concentration-dependent diffusivity. *Chemical Engineering Science*, 59, 4531-4545.
- SCOTT, J. A. & KARANJKAR, A. M. (1995) Adsorption-isotherms and diffusion-coefficients for metals biosorbed by biofilm coated granular activated carbon. *Biotechnology Letters*, 17, 1267-1270.
- SINGH, P. & CAMEOTRA, S. S. (2004) Enhancement of metal bioremediation by use of microbial surfactants. *Biochemical and Biophysical Research Communications*, 319, 291-297.
- STANISZ, G. J. & HENKELMAN, R. M. (2000) Gd-DTPA relaxivity depends on macromolecular content. *Magnetic Resonance in Medicine*, 44, 665-667.
- STRATHMANN, M., GRIEBE, T. & FLEMMING, H. C. (2000) Artificial biofilm model - a useful tool for biofilm research. *Applied Microbiology and Biotechnology*, 54, 231-237.
- VOLESKY, B. (1994) Advances in biosorption of metals - selection of biomass types. *Fems Microbiology Reviews*, 14, 291-302.
- YEE, N., FOWLE, D. A. & FERRIS, F. G. (2004) A Donnan potential model for metal sorption onto *Bacillus subtilis*. *Geochimica Et Cosmochimica Acta*, 68, 3657-3664.

Chapter 7

Concluding remarks

7

Concluding remarks

7.1 Summary of conclusions

Quantifying mass transport in environmental systems is key to understand the fate and remediation of environmental pollutants and waste products.

The transport rates of different molecules or ions inside biofilms can significantly control the performance of pollutant capture and degradation processes (chapter 1), and thus quantifying mass transport is an essential part of understanding (and enhancing) the function of natural and engineered biofilms.

In addition to interaction with biological systems, pollutant fate can be influenced by interactions with abiological systems. Consequently, imaging transport of pollutants through porous geological media is key to understand their transport and fate in systems such as soils, aquifers, river beds and sustainable urban drainage systems.

The particular question that was addressed in this research is how transport of macromolecules, nanoparticles and heavy metals can be quantified inside biofilms and porous packed columns. MRI is chosen as it can image inside systems that are opaque to other methods. Moreover, MRI can spatially resolve data in a non-invasive manner; the system is unperturbed by the analysis.

The property of (super)paramagnetic molecules, heavy metals and ions affecting the MR signal was exploited not only to track their transport but also to quantify their concentrations inside biofilms and porous packed columns (chapters 3, 4, 5 and 6). Mathematical models were then calibrated using experimental data to estimate transport and reaction rates.

The work described in previous chapters addresses the importance of understanding the transport processes of different molecules inside biofilms and porous packed columns, with

the following conclusions being derived.

In chapters 3 and 4, MRI was successfully used to investigate the transport of Gd-DTPA, a commonly used MRI contrast agent inside phototrophic biofilms with thicknesses of 10 mm and 2.5 mm. The comparison of spatially distributed, time-varying concentrations of Gd-DTPA inside the biofilms with diffusion models illustrates that transport of Gd-DTPA is via both diffusion and advection in the biofilms used here. Moreover, this illustrates the potential of using MRI to image the transport of mid to high molecular mass pollutants by using paramagnetically tagged molecules as pollutant surrogates.

In chapter 4, the ability of the bespoke RF coil to image biofilms with improved spatial resolution revealed the influence of biofilm architecture upon its mass transport behaviour. This simple to construct and cost effective custom made RF coil is a promising option to investigate structural and mass transport behaviours of biofilms which can be too thick (e.g. phototrophic biofilm and granules) for photon based imaging methods.

In chapter 5, the ability to image inside opaque systems was further exploited to image nanoparticle transport inside a coarse-grained packed column. The quantitative concentration profiles of carboxyl terminated and amine-terminated nanoparticles inside the packed column were compared with that of a convection-dispersion model to estimate the coefficients of dispersivity, retardation and deposition. This corroborated the robustness of this approach to spatially and temporally quantify NP transport inside geological media. Thus more complex systems can be explored which simple breakthrough curve analysis may struggle to describe. This illustrates the potential of this technique for imaging spatial variation in transport heterogeneity that are unobservable by traditional approaches.

In chapter 6, MRI was successfully used to quantify the adsorption-diffusion transport of copper, a well know toxic heavy metal, inside an artificial biofilm. The comparison between experimental data and model data (modelled using a Langmuir isotherm to represent the adsorption-diffusion of copper) generated good results for the diffusion coefficient and adsorption constant. However, discrepancies between the model and experimental data showed that transport of copper was more complex than expected. From this it is suggested concentration dependant diffusion coefficients or incorporation of transport by mobile organic complexes may be required to improve heavy metal adsorption models in biofilms.

Hence it is concluded that MRI together with the use of the MRI compatible

(super)paramagnetic molecules constitute a highly versatile, non-destructive method for imaging pollutant transport inside opaque biofilms and saturated porous packed columns.

Therefore, the use of MRI has the potential to significantly improve our understanding of the way macromolecules, nanoparticles and heavy metals are transported inside natural and engineered systems.

It should be noted here that R^2 has been used to measure the goodness of the fit of the models which are discussed in chapters 2-6. Here R^2 is computed from the sum of the squares of the distances of the experimental data from the best fit curve (given by the model). R^2 is used to measure the goodness of fit when the model is assumed *a priori*. Thus R^2 can be used to determine the combination of parameters that yield a simulation that minimizes the difference between simulated and measured variables. It cannot be used to assess the statistical significance of a model in comparison to some null hypothesis in the way one might do with a regression analysis, where p-values are routinely used to assess the likelihood of seeing a test statistic at least as extreme as that observed given an assumption that some null hypothesis is true. With regression the null hypothesis is normally assumed to be that there is no trend in the data. When fitting a complex finite element model to a physical process like diffusion and (or) advection it is not possible to define a neat null hypothesis to use in a significance test. Rather one can only compare a suite of potential models. R^2 values are useful in this respect. However, it may be the case that several combinations of parameter values give similarly good fits or that there is little difference in the R^2 value for very large ranges of parameter values. To assess this requires a more detailed analysis either in the form of a sensitivity analysis or in a more directed way using a Bayesian inference framework. In Bayesian approach a distribution of possible parameter values are assumed, which can be naive and assume no prior knowledge of what the parameters might be, or can use prior information. Multiple simulations of the model are then run with parameters selected from these distributions using sophisticated algorithms that systematically explore the parameter space. Posterior distributions are then generated for all uncertain variables/parameters in the model which give the modified likelihood of the variables/parameters given the data and the model. From these is possible to derive statistics like the Bayesian information criterion (BIC) and deviance information criterion (DIC) which measure goodness of fit and can be used to compare models. In a Bayesian approach these are particularly useful in that they penalise models that are over parameterised and hence reward the most parsimonious models that fit the data.

7.2 The future research of MRI of environmental systems

The present work contributes to strengthen the foundation of investigating mass transport processes in environmental systems using MRI. A promising next step is to investigate the influence of various physicochemical properties of molecules such as molecular mass, size and surface charge upon their transport behaviours inside biofilms and geological porous media by using either commercially available (super)paramagnetic MRI contrast agents or bespoke (super)paramagnetically labelled real molecules of interest. For example, commercially available Gadopolylysine (<http://www.biopal.com/>), gadolinium-labelled molecules with a range of molecular masses (e.g. 10 kDa, 22 kDa, 50 kDa, 110 kDa and 225 kDa) can be used to investigate the influence of molecular mass upon their transport inside biofilms. *Galbumin*, another commercially available (<http://www.biopal.com/>) gadolinium-labelled molecule, 740 kDa in mass can also be used to compare the transport behaviour of even higher molecular mass molecules.

Similarly, while two *Molday ION* nanoparticle contrast agents have already been used here (chapter 5), these are available in other forms with a wide range of surface charge characteristics (see table 7.1), and thus can be used to investigate the influence of surface charge upon nanoparticle transport inside porous packed columns. Also, *FeREX*, another commercially available (<http://www.biopal.com/>) MRI contrast agent, 50-150 nm in diameter, could be used to investigate the influence of nanoparticle size upon their transport inside packed columns.

<i>Molday ION</i> type	~ Size (nm)	~ Zeta potential (mV)
Molday ION	30	-4.8
Molday ION (-)	30	-15
Molday ION C6Amine	35	48
Molday ION Carboxyl	35	-38
Molday ION Rhodamine B	35	35

Table 7.1. List of commercially available *Molday ION* contrast agents; source (<http://www.biopal.com/>).

Moreover, it may be possible to label actual environmental pollutants (rather than surrogates) for transport imaging. Indeed, there is a considerable expertise in paramagnetic labelling to track tumor targeting molecules, investigate drug delivery to specific organs (Saito et al., 2004) and now to image virus transport in mammals (Raty et al., 2006). For example, viral nanoparticle MRI contrast agents with improved relaxation properties have already been

developed by conjugation of more than 500 gadolinium chelate groups (e.g. Gd-DTPA) onto a viral capsid (Anderson et al., 2006). This suggests that labelling of real pollutants with (super)paramagnetic tags may be possible. However, (super)paramagnetic labelling is not a straightforward process and the ability to tag real pollutants would need considerable further investigation such as investigating the MRI compatibility of pollutants with and without (super)paramagnetic tags and investigating the chemical properties of pollutants to allow better labelling of (super)paramagnetic tags.

There is a growing concern of the fate of nanoparticles inside biofilms. Waste water treatment plants use biofilms to remove nanoparticle (NP) pollutants found in household and industrial waste water while biofilms found in the natural environment also remove nanoparticle pollutants which reach the natural water bodies by direct urban runoff and untreated wastewater effluents. Therefore, there is clearly a need to investigate the fate of nanoparticles inside both thick natural biofilms and biofilms used in waste water treatment plants. Here, the bespoke RF coil can be used to investigate NP transport inside biofilms with improved resolutions. This can be further extended by investigating how the biofilm growth inside porous geological media affects the transport behaviours of NPs. Indeed, in this study, a clean biofilm (bacteria) free coarse grained media was used. However, in natural systems such as aquifers and river beds, biofilms can coat grain surfaces and block pore throats. While this may alter the hydrodynamic regime, the bacteria's reactive surface may sequester nanoparticles; e.g. (Glasauer et al., 2001). Consequently, biofilms are likely to retard nanoparticle transport.

Laboratory grown biofilms and the use of MRI compatible mineral grains in packed columns offer the advantage of that they can be imaged easily with MRI. However, the presence of metal impurities in some industrial and natural biofilms, and packed columns made up with grains found in the natural environment can hinder MR imaging either by shorting the relaxation times or causing magnetic susceptibility artifacts. The limitation in detecting the MR signal arising due to the shorting of relaxation times may be overcome by using ultra-short echo time imaging methods. In medicine, ultra-short echo time MR imaging allows the detection of signal components with T_2 relaxation times on the order of only a few hundred microseconds, which are found in highly ordered tissues such as tendons and ligaments and cannot be detected with conventional imaging techniques in which the echo time is limited to few milliseconds (Rahmer et al., 2006). Hence, samples that are hard to image due to shorter relaxation times can be tried using these advanced MR imaging techniques.

However, variations in the magnetic susceptibility of samples such as packed columns made up with naturally found grains, cause serious MR imaging artefacts. The magnetic susceptibility of a material is a measure of its ability to become magnetized in an external magnetic field. Thus, the susceptibility differences found in different components of a sample (e.g. water and grains of a packed column) cause inhomogeneities in the imaging gradient field across the sample, thus resulting geometrical distortion of the boundary interfaces (Farahani et al., 1990). Susceptibility artefacts could be reduced when MRI scanners with low main magnetic fields are used (Farahani et al., 1990). However, MR imaging at low main magnetic fields reduces the achievable signal-to-noise ratio (SNR). Therefore, the trade off between SNR and susceptibility artefacts should be considered when low main magnetic field scanners are used to quantify pollutant transport inside porous packed columns.

It should also be noted here that models used in this study were capable of estimating only the bulk transport and reaction rates of molecules inside biofilms and porous columns regardless to the usual spatial heterogeneities found in such systems. For example, many natural and engineered systems of interest, such as biofilms and saturated porous matrices display heterogeneity in structure (Lorente and Bejan, 2006, de Beer et al., 1994), hydrodynamics (de Beer et al., 1994), geochemistry (Bhattacharjee et al., 2002) and microbiology (Kim et al., 2010, de Beer et al., 1994). Consequently, models incorporating spatial variations of physical and chemical (or reactive) properties of these systems must be considered if the spatially resolved quantitative concentration data obtained using MRI is to be fully utilised.

The biofilm structure, mainly the shape was used as an input into the model (chapters 3 and 4). In these chapters, biofilm structures were assumed as homogeneous and transport of molecules was simulated only for diffusion. The observed variations between experimental and model data were then discussed by using previously observed heterogeneities in the structure and hydrodynamics of biofilms. This modelling approach did not impact the aims of this thesis which are to introduce the capability of MRI in quantifying environmental processes and using mathematical models to estimate effective transport and reaction rates of pollutants to test the accuracy of the MRI methodology. Researchers, however, have shown that heterogeneities found in biofilms can be modelled when the actions and interactions of the biomass units with each other and the environment is linked using bottom-up approach models such as biomass based models and individual based models (Kreft et al., 2001). Here, structure (e.g. EPS matrix, pores and channels), hydrodynamics (e.g. diffusion and advection) and microbiology (e.g. microbial colonies) of biofilms are emergent properties depending on the existing

environment such as microbial properties and nutrient availability (Kreft et al., 2001). Therefore, comparing spatially quantified MRI data to a biofilm, modelled using such bottom-up approaches would allow us estimating spatially resolved transport and reaction rates.

The transport of nanoparticles (NPs) inside porous packed column was also simulated by assuming the system as homogenous (chapter 5). However, more complex systems may not allow the assumption of homogeneity. Therefore, incorporating heterogeneities into the models is likely essential to understand the experimental data from more complex systems. For, example the usual flow heterogeneities found in heterogeneously packed columns can be deduced by using MRI itself. Researchers have used MRI to map flow velocities inside porous media (Mantle et al., 2001). Thus, using MRI to spatially resolve both flow velocities and concentrations is a promising next step to improve models. Moreover, incorporating biofilm models into reaction-transport models of porous matrices will enable us to investigate influence of biofilm growth upon nanoparticle transport. Combined approaches have already been used by researchers to predicting biofouling in reverse osmosis membranes (Pintelon et al, 2010).

7.3 References

- ANDERSON, E. A., ISAACMAN, S., PEABODY, D. S., WANG, E. Y., CANARY, J. W. & KIRSHENBAUM, K. (2006) Viral nanoparticles donning a paramagnetic coat: Conjugation of MRI contrast agents to the MS2 capsid. *Nano Letters*, 6, 1160-1164.
- BHATTACHARJEE, S., RYAN, J. N. & ELIMELECH, M. (2002) Virus transport in physically and geochemically heterogeneous subsurface porous media. *Journal of Contaminant Hydrology*, 57, 161-187.
- DE BEER, D., STOODLEY, P., ROE, F. & LEWANDOWSKI, Z. (1994) Effects of biofilm structures on oxygen distribution and mass transport. *Biotechnology and Bioengineering*, 43, 1131-1138.
- FARAHANI, K., SINHA, U., SINHA, S., CHIU, L. C. L. & LUFKIN, R. B. (1990) Effect of field-strength on susceptibility artifacts in magnetic-resonance-imaging. *Computerized Medical Imaging and Graphics*, 14, 409-413.
- GLASAUER, S., LANGLEY, S. & BEVERIDGE, T. J. (2001) Sorption of Fe (hydr)oxides to the surface of *Shewanella putrefaciens*: Cell-bound fine-grained minerals are not always formed de novo. *Applied and Environmental Microbiology*, 67, 5544-5550.
- [HTTP://WWW.BIOPAL.COM/](http://www.biopal.com/).
- KIM, J. W., CHOI, H. & PACHEPSKY, Y. A. (2010) Biofilm morphology as related to the porous media clogging. *Water Research*, 44, 1193-1201.

- KREFT, J. U., PICIOREANU, C., WIMPENNY, J. W. T. & VAN LOOSDRECHT, M. C. M. (2001) Individual-based modelling of biofilms. *Microbiology-Sgm*, 147, 2897-2912.
- LORENTE, S. & BEJAN, A. (2006) Heterogeneous porous media as multiscale structures for maximum flow access. *Journal of Applied Physics*, 100, 8.
- MANTLE, M. D., SEDERMAN, A. J. & GLADDEN, L. F. (2001) Single- and two-phase flow in fixed-bed reactors: MRI flow visualisation and lattice-Boltzmann simulations. *Chemical Engineering Science*, 56, 523-529.
- PINTELON, T. R. R., CREBER, S. A., VON DER SCHULENBURG, D. A. G. & JOHNS, M. L. (2010) Validation of 3D Simulations of Reverse Osmosis Membrane Biofouling. *Biotechnology and Bioengineering*, 106, 677-689.
- RAHMER, J., BORNERT, P., GROEN, J. & BOS, C. (2006) Three-dimensional radial ultrashort echo-time imaging with T-2 adapted sampling. *Magnetic Resonance in Medicine*, 55, 1075-1082.
- RATY, J. K., LIIMATAINEN, T., WIRTH, T., AIRENNE, K. J., IHALAINEN, T. O., HUHTALA, T., HAMERLYNCK, E., VIHINEN-RANTA, M., NARVANEN, A., YLA-HERTTUALA, S. & HAKUMAKI, J. M. (2006) Magnetic resonance imaging of viral particle biodistribution in vivo. *Gene Therapy*, 13, 1440-1446.
- SAITO, R., BRINGAS, J. R., MCKNIGHT, T. R., WENDLAND, M. F., MAMOT, C., DRUMMOND, D. C., KIRPOTIN, D. B., PARK, J. W., BERGER, M. S. & BANKIEWIEZ, K. S. (2004) Distribution of liposomes into brain and rat brain tumor models by convection-enhanced delivery monitored with magnetic resonance imaging. *Cancer Research*, 64, 2572-2579.

Appendix

Appendix

A-1. IDL and MATLAB codes used in chapter 3

A-1.1. Construction of T_1 parameter maps and concentration maps using IDL

The procedures implemented in IDL in order to compute T_1 parameter maps and concentration maps are described in sections 3.3.5 and 3.3.6 respectively.

The IDL codes used to construct T_1 parameter maps and concentration maps are listed below. The code is annotated with comments that refer to the illustration of its processing as shown in figure. 3.3.

A-1.1.1. IDL codes for construction of T_1 parameter maps

```
Function T1_parametermap,data,s1,s2,s3
;the raw data matrix, the signal maps (data) with dimensions of s1 (number of pixels along x direction),
s2 (number of pixels along y direction) and s3 (number of flip angles).

signal=fltarr(s3) ;array to store signals at each flip angle
weights=fltarr(s3) ;array to store weights used during the curve fitting procedure
weights[*]=1.0 ;assign one (1) as value for weights
angle = [5.0,20.0,40.0,60.0,90.0] ;array with used flip angles

T1image=make_array(s1,s2,/float) ;an array with pixels along x and y directions
for i=0,s1-1 do begin
for j=0,s2-1 do begin
signal(0:s3-1)=float(data(i,j,0:s3-1))
If signal[0] gt -2.0 then begin
a=[100000,0.5] ;initial guesses
res=curvefit(angle,signal,weights,a,sigma,/NODERIVATIVE,function_name='anglefit')
T1image(i,j)=a(1)*1000
endif else begin
T1image(i,j)=0.0
endelse
endifor
endifor

maxlimit=T1image lt 2000
minlimit= T1image gt 0
T1image=T1image * maxlimit *minlimit
;trims the T1 parameter map with maximum and minimum values for T1.

return,T1image ;T1 parameter map
end
```

The curve fit function, `anglefit`, called as a sub routine in the above given function (`T1_parametermap`) is given below;

```

pro anglefit,angle,a,f
TR =75.0e-3 ;repetition time (TR) of the pulse sequence
x=angle
u= a[0]*sin(x*2.0*PI/360.0)-a[0]*sin(x*2.0*PI/360.0)*exp(-TR/a[1])
v= 1.0-cos(x*2.0*PI/360.0) * exp(-TR/a[1])
f= u/v ;signal equation for gradient echo pulse sequence
end

```

A-1.1.2. IDL codes for construction of concentration maps

Function concmap,data,s1,s2,points
;the raw data matrix, the T1 parameter maps (data) with dimensions of s1 (number of pixels along x direction), s2 (number of pixels along y direction) and points (number of time intervals).

R=1.06483E-05 ;relaxivity constant of the Gd-DTPA

```

concmap=fltarr(s1,s2,points)
T20=fltarr(s1,s2) ;T1 parameter map obtained without Gd-DTPA
T2=fltarr(s1,s2) ;T1 parameter map obtained with Gd-DTPA

```

```

T20=reform(data(*,*,0),s1,s2) ;reformation of the data matrix
R20=1.0/T20

```

```

for k=0,points-1 do begin
T2=reform( data(*,*,k),s1,s2)
R2= 1.0/T2
temp = ( R2-R20 )/(R)
concmap[* ,*,k]=reform(temp,s1,s2,1) ;reformation of the data matrix
endfor

```

```

maxlimit=concmap lt 1000
minlimit= concmap gt 0
concmap=concmap * maxlimit *minlimit
;trims the concentration map with maximum and minimum values for concentration

```

```

return,concmap
end

```

A-1.2. Estimating diffusion coefficient of Gd-DTPA inside agar and biofilm using MATLAB

The diffusion coefficient of Gd-DTPA inside agar was estimated using the curve fitting toolbox available in MATLAB. The concentration data with respect to their respective x/\sqrt{t} were first loaded as inputs into the curve fitting toolbox. The curve fitting procedure for input data was then executed using standard graphical user interface of the curve fitting toolbox. The data were curve fitted to the solution of the diffusion equation for a semi-infinite one dimensional domain (see equation 4 in chapter 3).

The transport of Gd-DTPA with an arbitrary (e.g. an initial guess) diffusion coefficient was first simulated for biofilm using the model implemented in COMSOL as described in section

3.3.9. The model was then saved as an m-file. The saved m-file was then modified to incorporate an optimization routine (e.g. golden search algorithm), which called the COMSOL model as a subroutine. The optimum diffusion coefficient was estimated at the minimum value of the objective function of the optimization routine. The objective function was the sum of square errors between observed and simulated concentrations. The MATLAB codes used for estimating diffusion coefficient of Gd-DTPA inside biofilm is listed below.

A-1.2.1. MATLAB codes used to estimate the diffusion coefficient of Gd-DTPA inside biofilm

```
function diffusion_Gadolinium_phormidiumbiofilm
[d,fval] = fminsearch(@ram_objective,5.5e-10,optimset('Tolx',1e-12,'Maxiter',10000))
end

function obj = ram_objective(d)

load exp_Gd_Phormidium %loads the experimental data

%%%%%%%%%%%%%%%%%%%%%%%%%%%%%%%%%%%%%%%%%%%%%%%%%%%%%%%%%%%%%%%%%%%%%%%%
%start of the COMSOL m-file
% COMSOL Multiphysics Model M-file
% Generated by COMSOL 3.5a (COMSOL 3.5.0.603, $Date: 2008/12/03 17:02:19 $)
% Some geometry objects are stored in a separate file.
% The name of this file is given by the variable 'flbinaryfile'.

flclear fem

% COMSOL version
clear vrsn
vrsn.name = 'COMSOL 3.5';
vrsn.ext = 'a';
vrsn.major = 0;
vrsn.build = 603;
vrsn.rcs = '$Name: $';
vrsn.date = '$Date: 2008/12/03 17:02:19 $';
fem.version = vrsn;

flbinaryfile='optimize_alltime.mphm';

% Geometry
clear draw
g3=flbinary('g3','draw',flbinaryfile);
draw.s.objs = {g3};
draw.s.name = {'CO1'};
draw.s.tags = {'g3'};
fem.draw = draw;
fem.geom = geomcsg(fem);

% Initialize mesh
fem.mesh=meshinit(fem, ...
    'hauto',5);
```

```

% Refine mesh
fem.mesh=meshrefine(fem, ...
                    'mcase',0, ...
                    'rmethod','regular');

% (Default values are not included)

% Application mode 1
clear appl
appl.mode.class = 'Diffusion';
appl.module = 'CHEM';
appl.assignsuffix = '_chdi';
clear bnd
bnd.c0 = {0,1000};
bnd.type = {'N0','C'};
bnd.ind = [1,1,2,2,1,2,2,1];
appl.bnd = bnd;
clear equ
equ.D = d(1); % diffusion coefficient as a variable to optimise
equ.ind = [1];
appl.equ = equ;
fem.appl{1} = appl;
fem.frame = {'ref'};
fem.border = 1;
fem.outform = 'general';
clear units;
units.basesystem = 'SI';
fem.units = units;

% ODE Settings
clear ode
clear units;
units.basesystem = 'SI';
ode.units = units;
fem.ode=ode;

% Multiphysics
fem=multiphysics(fem);

% Extend mesh
fem.xmesh=mesnextend(fem);

% Solve problem
fem.sol=femtime(fem, ...
               'solcomp',{'c'}, ...
               'outcomp',{'c'}, ...
               'blocksize','auto', ...
               'tlist',[0,129,429,737,1038,1341], ... %experimental time intervals
               'tout','tlist');

% Save current fem structure for restart purposes
fem0=fem;

% Plot solution
postplot(fem, ...
         'tridata',{'c','cont','internal','unit','mol/m^3'}, ...
         'trimap','Rainbow', ...
         'solnum','end', ...
         'title','Time=540 Surface: Concentration, c [mol/m^3]', ...

```

```

'axis',[-0.002694,0.002694,-0.0027001000000000004,0.0017001000000000002]);

% Plot in cross-section or along domain
postcrossplot(fem,1,[0 0;-1.084202e-19 -0.0025], ...
'lindata','c', ...
'title','Concentration, c [mol/m^3]', ...
'axislabel',{'Arc-length','Concentration','c [mol/m^3]'});
%end of the COMSOL m-file
%%%%%%%%%%%%%%%%%%%%%%%%%%%%%%%%%%%%%%%%%%%%%%%%%%%%%%%%%%%%%%%%%%%%%%%%
%%%%%%%%%%%%%%%%%%%%%%%%%%%%%%%%%%%%%%%%%%%%%%%%%%%%%%%%%%%%%%%%%%%%%%%%

% interpretation of model results along the transect of interest
conc1 = postinterp(fem,'c',[x];-(y/1000)],[solnum',2);
conc2 = postinterp(fem,'c',[x];-(y/1000)],[solnum',3);
conc3 = postinterp(fem,'c',[x];-(y/1000)],[solnum',4);
conc4 = postinterp(fem,'c',[x];-(y/1000)],[solnum',5);
conc5 = postinterp(fem,'c',[x];-(y/1000)],[solnum',6);

%define the objective function
obj = sum((c1-(conc1')).^2)+sum((c2-(conc2')).^2)+sum((c3-(conc3')).^2)+sum((c4-
(conc4')).^2)+sum((c5-(conc5')).^2)
%%%%%%%%%%%%%%%%%%%%%%%%%%%%%%%%%%%%%%%%%%%%%%%%%%%%%%%%%%%%%%%%%%%%%%%%
%%%%%%%%%%%%%%%%%%%%%%%%%%%%%%%%%%%%%%%%%%%%%%%%%%%%%%%%%%%%%%%%%%%%%%%%

%calculating the mean of the experimental data
mc1 = mean(c1(1:65,1)*ones(1,65));
mc2 = mean(c2(1:65,1)*ones(1,65));
mc3 = mean(c3(1:65,1)*ones(1,65));
mc4 = mean(c4(1:65,1)*ones(1,65));
mc5 = mean(c5(1:65,1)*ones(1,65));

%sum of squares of the differences between respective the experimenatl and model data points
SSreg = sum(((c1(1:65,1))-(conc1(1,1:65)))'.^2) + sum(((c2(1:65,1))-(conc2(1,1:65)))'.^2) +
sum(((c3(1:65,1))-(conc3(1,1:65)))'.^2) + sum(((c4(1:65,1))-(conc4(1,1:65)))'.^2) + sum(((c5(1:65,1))-
(conc5(1,1:65)))'.^2);
%sum of squares of the differences between the experimenatl data points and the mean of the
experimental data
SStot = sum(((c1(1:65,1))-(mc1'))'.^2) + sum(((c2(1:65,1))-(mc2'))'.^2) + sum(((c3(1:65,1))-(mc3'))'.^2) +
sum(((c4(1:65,1))-(mc4'))'.^2) + sum(((c5(1:65,1))-(mc5'))'.^2)
%goodness of fit value (R2)
R2 = (1 - (SSreg/SStot))*100
%%%%%%%%%%%%%%%%%%%%%%%%%%%%%%%%%%%%%%%%%%%%%%%%%%%%%%%%%%%%%%%%%%%%%%%%
%%%%%%%%%%%%%%%%%%%%%%%%%%%%%%%%%%%%%%%%%%%%%%%%%%%%%%%%%%%%%%%%%%%%%%%%
%plot experimental data VS distance and model VS distance
plot(y,c1,y,conc1,y,c2,y,conc2,y,c3,y,conc3,y,c4,y,conc4,y,c5,y,conc5)

%value of the optimised diffusion coefficient
d(1)

%save the results
save results

end

```

A-2. IDL and MATLAB codes used in chapter 4

A-2.1. Construction of T_1 parameter maps and concentration maps using IDL

The procedures implemented in IDL in order to compute T_1 parameter maps and concentration maps are described in section 4.3.8 and 4.3.9 respectively.

The IDL codes used to construct T_1 parameter maps for agar and biofilm are similar to the codes listed in section A-1.1.1, except that T_1 weighted images were acquired only at three flip angles. The known signal value of zero at 0° flip angle was also used as an additional data point to improve the curve fit results (see figure 4.5).

The IDL codes used to construct concentration maps are similar to the codes listed in section A-1.1.2. Appropriate relaxivity constant (R) values for both agar and biofilm were used during the calculation of concentration maps.

A-2.2. Construction of apparent diffusion coefficient (ADC) map using IDL

The procedures implemented in IDL in order to compute the relative apparent diffusion coefficient map are described in section 4.3.13.

The IDL codes used to construct apparent diffusion coefficient map are listed below.

A-2.2.1. IDL codes for construction of diffusion maps

```
function diffusion_map,data,s1,s2,s3

signal=fltarr(s3)
weights=fltarr(s3)
weights[*]=1.0

b = [114.22, 414.22]

diffimage=make_array(s1,s2,/float)
for i=0,s1-1 do begin
for j=0,s2-1 do begin
signal(0:s3-1)=float(data(i,j,0:s3-1))
If signal[0] gt -2.0 then begin
a=[1000000,2e-3]
res=curvefit(b,signal,weights,a,sigma,/NODERIVATIVE,function_name='diffit')
diffimage(i,j)=a(1)*1e-6
endif else begin
diffimage(i,j)=0.0
endelse
endifor
endifor

maxlimit=diffimage lt 10e-9
minlimit= diffimage gt 1e-10
diffimage=diffimage * maxlimit *minlimit

return,diffimage
end
```

The curve fit function, `diffit`, called as a sub routine in the above given function (`diffusion_map`) is given below;

```
pro diffit,b,a,f
x=b
f= a[0]*exp(-a[1]*x)
end
```

A-2.3. Estimating diffusion coefficient of Gd-DTPA inside agar and biofilm using MATLAB

The transport of Gd-DTPA inside agar was simulated using a model implemented in COMSOL as described in sections 4.3.12.

Similar procedures used to estimate the diffusion coefficient of Gd-DTPA inside biofilm as described in section A-1.2.1 were used to estimate the diffusion coefficient of Gd-DTPA inside agar and biofilm.

A-3. IDL and MATLAB codes used in chapter 5

A-3.1. Construction of the concentration maps using IDL

The procedures implemented in IDL in order to compute concentration maps are described in section 5.3.6.

A-3-2. Estimating the concentration of nanoparticles averaged along the flow axis using IDL

The IDL codes used to estimate the concentration of nanoparticles averaged along the flow axis is given below.

A-3.2.1. IDL codes for the construction of concentration maps and estimation of concentration averaged along the flow axis.

```
function conc_pro_average_multislice_1time_2part,data,s1,s2,s3,s4,time

aver_conc = make_array(s1,/float)
conc_image=make_array(s1,s2,/float)
conc = make_array(s1,/float)
nodes = make_array(s1,/float)
tot_conc = 0.0
for k=s3,s4 do begin
l= time
s = data(*,*,k,l)
s0 = data(*,*,k,0)
for i=0,432 do begin
```

```

signal_tot = 0.0
p = 0.0
for j=35,135 do begin
If s0(i,j) gt 25000.0 then begin ;if s[0]<25000, then assume that is from rock.
conc_image(i,j)= (alog(s(i,j)/s0(i,j)))/(-Te)-R20)/R ;carboxyl and C6Amine
signal_tot_new = signal_tot + T1image(i,j)
p_new = p + 1.0
endif else begin
conc_image(i,j)=0.0
signal_tot_new = signal_tot
p_new = p
endelse
signal_tot = signal_tot_new
p = p_new
endfor
conc(i) = signal_tot/p
nodes(i) = p
endfor

for i=433,s1-1 do begin
signal_tot = 0.0
p = 0.0
for j=35,135 do begin
If s0(i,j) gt 25000.0 then begin ;if s[0]<25000, then assume that is from rock.
conc_image(i,j)= (alog(s(i,j)/s0(i,j)))/(-Te)-R20)/R ;carboxyl and C6Amine
signal_tot_new = signal_tot + T1image(i,j)
p_new = p + 1.0
endif else begin
conc_image(i,j)=0.0
signal_tot_new = signal_tot
p_new = p
endelse
signal_tot = signal_tot_new
p = p_new
endfor
conc(i) = signal_tot/p
nodes(i) = p
endfor
tot_conc_new = tot_conc + conc
tot_conc = tot_conc_new
endfor

aver_conc = tot_conc/(s4-s3+1)

maxlimit=conc_image lt 1
minlimit= conc_image gt 0
T1image=conc_image * maxlimit *minlimit

return,aver_conc
end

```

A-3.3. Estimating the porosity of the column along the flow axis using IDL

The IDL codes used to estimate the porosity of the column averaged along the flow axis is given below.

A-3.3.1. IDL codes for estimating porosity averaged along the flow axis

```

function porosity_average_multislice_1time_2part,data,s1,s2,s3,s4,time

aver_porosity = make_array(s1,/float)
total_nodes = fttarr(512)
total_nodes(0:428) = 101
total_nodes(429:511) = 101

nodes = make_array(s1,/float)
tot_nodes = 0.0

for k=s3,s4 do begin
l= time
for i=0,428 do begin
p = 0.0
for j=35,135 do begin
If s0(i,j) gt 25000.0 then begin ;if s[0]<25000, then assume that is from rock.
p_new = p + 1.0
endif else begin
p_new = p
endelse
p = p_new
endfor
nodes(i) = p
endfor

for i=429,s1-1 do begin
p = 0.0
for j=35,135 do begin
If s0(i,j) gt 25000.0 then begin ;if s[0]<25000, then assume that is from rock.
p_new = p + 1.0
endif else begin
p_new = p
endelse
p = p_new
endfor
nodes(i) = p
endfor
tot_nodes_new = tot_nodes + nodes
tot_nodes = tot_nodes_new
endfor

aver_nodes = tot_nodes/(s4-s3+1)
aver_porosity = aver_nodes/total_nodes

maxlimit=T1image lt 1
minlimit= T1image gt 0
T1image=T1image * maxlimit *minlimit

return, aver_porosity
end

```

A-3.4. Estimating coefficients of dispersion, retardation and decay of nanoparticles inside porous column using MATLAB

The transport of nanoparticles inside the porous column was simulated using a model implemented in COMSOL as described in sections 5.3.7.

Similar procedures used to estimate the diffusion coefficient of Gd-DTPA inside biofilm as described in section A-1.2.1 were used to estimate the coefficients of interest for nanoparticles inside the porous column.

A-4. IDL and MATLAB codes used in chapter 6

A-4.1 Construction of T_2 parameter maps and concentration maps using IDL

The procedures implemented in IDL in order to compute the T_2 parameter maps and concentration maps are described in section 6.3.6 and 6.3.7 respectively.

The IDL codes used to construct T_2 parameter maps and concentration maps are listed below. The code is annotated with comments that refer to the illustration of its processing as shown in figure 6.2.

A-4.1.1 IDL codes for construction of T_2 parameter maps

```
function T2_parametermap,data,te,s1,s2,s3
;the raw data matrix, the signal maps (data) with dimensions of s1 (number of pixels along x direction),
s2 (number of pixels along y direction) and s3 (number of flip angles).

signal=fltarr(s3)
weights=fltarr(s3)
weights[*]=1.0

te_array=(findgen(s3)+1)*te
t2image=make_array(s1,s2,/float)
for i=0,s1-1 do begin
for j=0,s2-1 do begin
signal(0:s3-1)=float(data(i,j,0:s3-1))
If signal[0] gt 1000 then begin
a=[(data(i,j,0)), -1.0/16,3000]
res=curvefit(te_array,signal,weights,a,sigma,/NODERIVATIVE,function_name='expfit')
t2image(i,j)=-1.0/(a(1))
endif else begin
t2image(i,j)=0.0
endelse
endfor
endfor

maxlimit=T2image lt 400
minlimit= T2image gt 0
T2image=T2image * maxlimit *minlimit

return,t2image
end
```

The curve fit function, `expfit`, called as a sub routine in the above given function (`T2_parametermap`) is given below;

```
pro expfit, x,a,f
bx=exp(a[1]*x)
f=a[0] *bx +a[2]
end
```

A-4.1.2 IDL codes for construction of concentration maps

The IDL codes used for the construction of concentration maps are similar to the codes listed in section A-1.1.2. Appropriate relaxivity constant (R) values for both 5% and 50% bacterial and agar mix were used during the calculation of concentration maps.

A-4.2 Estimating coefficients of adsorption and diffusion of copper inside artificial biofilm using MATLAB

The adsorption-diffusion transport of copper with arbitrary (e.g. an initial guess) adsorption constant and diffusion coefficient was first simulated for biofilm using the model implemented in COMSOL as described in section 6.3.9.

Similar procedures used to estimate the diffusion coefficient of Gd-DTPA inside biofilm as described in section A-1.2.1 were used to estimate the coefficients of diffusion and adsorption for copper inside artificial biofilms.

Papers and Presentations

- RAMANAN, B., HOLMES, W. M., SLOAN, W. T. & PHOENIX, V. R. (2010) Application of paramagnetically tagged molecules for magnetic resonance imaging of biofilm mass transport processes. *Applied and Environmental Microbiology*, 76, 4027-4036.
- PHOENIX, V. R., HOLMES, W. M. & RAMANAN, B. (2008) Magnetic resonance imaging (MRI) of heavy-metal transport and fate in an artificial biofilm. *Mineralogical Magazine*, 72, 483-486
- RAMANAN, B., HOLMES, W. M., SLOAN, W. T. & PHOENIX, V. R. Investigation of nanoparticle transport inside coarse-grained geological media using magnetic resonance imaging (MRI) (Revised, corrections pending to *Environmental Science and Technology*).
- RAMANAN, B., HOLMES, W. M., SLOAN, W. T. & PHOENIX, V. R. Magnetic resonance imaging of mass transport inside biofilms using a simple custom made solenoid RF coil. (In preparation)

- Symposium “Chemical Process Meets Medicine over MRI” organised by The Rank Prize Funds, UK, 25th-28th March, 2011 at the Lake District, UK.
- Emerging Environmental Technologies for Sustainable Development (EPSRC workshop), 2nd-4th of March, 2009 at Indian Institute of Technology, Delhi, India.
- Processes in Biofilms: Fundamentals to Applications, 14th-16th of September, 2009 at University of California, Davis, USA.

- Environmental Geochemistry poster competition organised by the “*Anglo American plc*” (second place with £2000 prize money).